The University Of Sheffield.

The Aerodynamics of Fixed and Variable Pitch Vertical Axis Wind Turbines

Mohamed Mohamed Elsakka

A thesis submitted in partial fulfilment of the requirements for the degree of Doctor of Philosophy

The University of Sheffield
Faculty of Engineering
Department of Mechanical Engineering

Submission Date

March, 2020

DECLARATION

The work presented in this thesis is that of the author and has not been submitted for any other award or degree at the University of Sheffield or any other university or institution. Where other sources of information or help from other parties have been used this has been acknowledged.

ACKNOWLEDGEMENTS

First and foremost, I would like to thank Allah, the God, for giving me the strength, ability and opportunity to undertake this research study.

I would like to express my profound gratitude and sincere thankfulness to my supervisors, Professor Lin Ma, Professor Derek Ingham, and Professor Mohamed Pourkashanian for their continuous support and useful suggestions throughout this research study.

I am also grateful to the Egyptian Cultural Affairs and Missions Sector along with Port Said University for their financial support.

Last but not least, I would like to thank my parents for their support throughout my life. In addition, I would like to thank my wife and my son.

PUBLICATIONS

Published papers:

M.M. Elsakka, D.B. Ingham, L. Ma and M. Pourkashanian, CFD Analysis of the Angle of Attack for a Vertical Axis Wind Turbine Blade. *Energy conversion and management*, vol. 182, pp. 154-165, 2019.

Zhang, T.T., **Elsakka, M.**, Huang, W., Wang, Z.G., Ingham, D.B., Ma, L. and Pourkashanian, M., "Winglet Design for Vertical Axis Wind Turbines Based on a Design of Experiment and CFD Approach," *Energy Conversion and Management*, vol. 195, pp. 712–726, 2019.

M.M. Elsakka, D.B. Ingham, L. Ma and M. Pourkashanian, "Effects of Turbulence Modelling on the Predictions of the Pressure Distribution around the Wing of a Small Scale Vertical Axis Wind Turbine." *7th European Conference on Computational Fluid Dynamics (ECFD 7)*, Glasgow, UK, 2018.

Future publication under review:

M.M. Elsakka, D.B. Ingham, L. Ma and M. Pourkashanian, "Comparison of the CFD predictions of VAWT performance against detailed pressure measurement"

Future publications in preparation:

M.M. Elsakka, L. Ma, D.B. Ingham, and M. Pourkashanian, "The Effect of the Targeted Maximum Angle of Attack on the Performance of a VAWT under Different Variable Pitch Scenarios"

M.M. Elsakka, L. Ma , D.B. Ingham and M. Pourkashanian, "Response Surface Optimisation for the Design Exploration of VAWT based on CFD simulations"

ABSTRACT

Due to the challenging wind potential and the increasing energy demand, it is important to design the future wind turbines to operate efficiently at low wind speeds. The focus of this thesis is about the small scale straight-bladed Vertical Axis Wind Turbine (VAWT) due to its competitive advantages and promising market. This thesis aims to provide an in-depth understanding of the aerodynamics of small VAWTs and the effect of blade pitch in the turbine performance at low wind speed conditions. Moreover, this thesis proposes a novel procedure for the analysis of turbine performance and the estimation of the Angle of Attack (AOA). This enables the design of the most appropriate fixed pitch and variable pitch configurations.

Based on the unsteady Reynolds-Averaged Navier-Stokes (uRANS), the state-of-the-art Computational Fluid Dynamics (CFD) simulation is utilised as a modelling approach and this enables high fidelity analysis with a reasonable computational cost. In order to find the most appropriate CFD methodology for the modelling of a VAWT, detailed verification and validation studies are carried out and this includes the comparisons of the CFD predictions against detailed instantaneous experimental data. These comparisons include both the 2D and 3D simulations based on two highly recommended turbulence models in the literature, namely the SST k-ω model and the SST k-ω with the γ Intermittency transition model. Moreover, this thesis proposes a novel procedure for the analysis of turbine performance and the estimation of the Angele of Attack (AOA). The Response Surface Methodology (RSM) is utilised for the optimisation of the fixed pitch configuration while several parametric studies are carried out to select the best variable pitch configuration. In addition, the effects of the implementation of winglets on the turbine performance are investigated for different aspect ratios.

Under the current setup, the CFD predictions based on the SST k-ω model are found to have a good agreement with the experimental data at the midspan section. However, the trend of the 2D CFD predictions, based on the SST k-ω with the γ Intermittency transition model, deviates from the experimental data. The proposed procedure for the analysis of a VAWT is found to assist in obtaining a better understanding of the performance of a VAWT based on the analysis of the performance of the aerofoil-

shaped blades. Moreover, the use of RSM optimisation assists not only in identifying the optimal fixed pitch configuration but also in exploring the effects of the different design parameters on the turbine performance. The parametric study of the variable pitch configuration reveals that the targeted maximum angle of attack has a substantial effect on the performance of the variable pitch configuration. In addition, the implementation of an optimised winglet on the blade tips is found to improve the turbine performance, especially for low aspect ratios. While the good selection of the fixed pitch angle is found to improve the performance, the implementation of an appropriate variable pitch profile is found to have a significant improvement in the turbine performance.

In contrast with the initial design in the reference case, the optimisation of the fixed pitch configuration leads to improve the power coefficient by about 2.9% in the 2D case and 34.5% in the 3D case. In addition, the variable pitch investigation leads to a further power coefficient improvements of about 18.4% in the 2D case and 28.6% in the 3D case in contrast with the optimised fixed pitch configuration. Furthermore, the implementation of the optimised winglet leads to improve the power coefficient in the 3D case by about 4.8% for the optimized fixed pitch configuration and 3.5% for the best variable pitch configuration.

LIST OF CONTENTS

LIST OF FIGURES

List of figures in the main text:

List of figures in the Appendices:

LIST OF TABLES

NOMENCLATURE

Symbols

A	Face area, [m^2]
A_c	Blade area based on the chord, [m^2]
AR_D	Aspect Ratio based on the diameter
A_x	Projected area in the x-direction that is aligned with the undisturbed flow direction, [m^2]
A_y	Projected area in the y-direction, [m^2]
C	Main blade chord, [m]
C_m	Instantaneous torque coefficient
$\bar{C}_m$	Average torque coefficient
$\hat{C}_m$	Maximum torque coefficient
C_P	Power coefficient
$C_{P,5}$	Power coefficients at wind velocity of 5 m/s
$C_{P,7}$	Power coefficients at wind velocity of 7 m/s
$C_{P,2D}$	Power coefficient based on 2D simulations
$C_{P,3D}$	Power coefficient based on 3D simulations
c_{tip}	Tip chord, [m]
F_N	Normal force, [N]
F_R	Resultants force, [N]
F_T	Tangential force, [N]
F_x	Force in x-direction, [N]
F_y	Force in y-direction, [N]
H	Total blade height, [m]
h/2	Blade half span, [m]
i and j	Tensor indices
k	Turbulence kinetic energy, [m^2/s^2]
ℓ_a and ℓ_b	Parameters of the computational domain dimensions, [m]
l_e	Eccentric length, [m]
l_m, l_c, and l_s	Fixed lengths in the four bar mechanism, [m]
L_{tip}	Tip straight extension, [m]
M_P	Pressure torque contributions of the arbitrary cell face, [N.m]
M_τ	Shear torque contributions of the arbitrary cell face, [N.m]
N	Number of cycles
N_b	Number of the blades
O	Main rotor centre point
OA209	ONERA Aerospace aerofoil No. 209

O_e	Eccentric rotational point
P	Single blade power, [W]
p	Pressure, [Pa]
Q	Predicted quantity
R_{cant}	Radius of the winglet cant, [m]
T	Torque, [N.m]
V	Approaching wind velocity, [m/s]
V_∞	Undisturbed wind flow velocity, [m/s]
V_r	Local incident relative velocity, [m/s]
X	Horizontal distance between the face centre and the origin of the computational domain, [m]
$x, y, and\ z$	The principal cartesian directions where x is the streamwise direction, y is the lateral direction, and z is the spanwise direction.
x_1, x_2, and x_3	Polynomial of sinusoidal function's coefficients
Y	Vertical distance between the face centre and the origin of the computational domain, [m]
y+	Dimensionless wall distance

Greek symbols

∇	Divergence operator
α	Angle of Attack or AOA, [°]
β	Fixed pitch angle, [°]
γ_{tip}	Ratio between the tip chord and the blade chord
δ_{ij}	Kronecker delta function
ζ	Targeted Maximum AOA or TMAOA, [°]
θ	Variable pitch angle, [°]
θ_p	Orientation angle in the four-bar mechanism, [°]
θ_{sweep}	Sweep angle, [°]
μ	Dynamic viscosity, [Pa.s]
μ_t	Turbulence eddy viscosity, [Pa.s]
ρ	The air density, [kg/m^3]
σ	Solidity
σ_t	Winglet twist angle, [°]
τ	Shear stress, [N/m^2]
τ_{w_x}	Wall shear stress component in the x-direction, [N/m^2]
τ_{w_y}	Wall shear stress component in the y-direction, [N/m^2]
ϕ	Azimuthal position, [°]
ψ	Relative velocity angle, [°]

ω	The rotational velocity, [rad/s]
Ω_{cant}	Angle of the winglet cant, [°]

Abbreviations

2D	Two-dimensional
3D	Three-dimensional
AC	After Christ
AOA	Angle of Attack
AR	Aspect Ratio
ASI	Aerospace Systems, Inc
BC	Before Christ
BEM	Blade Element Momentum
BSR	Blade Speed Ratio
CAGR	Compound Annual Growth Rate
CCD	Central Composite Design
CFD	Computational Fluid Dynamics
DDES	Delayed Detached Eddy Simulations
DES	Detached Eddy Simulations
DMST	Double Multiple Streamtube, also DMS
DoE	Design of Experiments
FP	Fixed Pitch
FP-VAWT	Fixed Pitch Vertical Axis Wind Turbine
GIS	Grid Induced Separation
GR	Growth Rate
HAWT	Horizontal Axis Wind Turbine
HPC	High-Performance Computing
IDDES	Improved Delayed Detached Eddy Simulations
IEA	International Energy Agency
LES	Large Eddy Simulation
MOGA	Multi-Objective Genetic Algorithm
NACA	National Advisory Committee for Aeronautics
QUICK	Quadratic Upwind Interpolation for Convective Kinematics
RANS	Reynolds-Averaged Navier-Stokes
RF	Refinement Factor
RMSE	Root Mean Square Error
RNG	Re-Normalisation Group
RSM	Response Surface Methodology
RSO	Response Surface Optimisation

SAS	Scale Adaptive Simulations
SBES	Stress-Blended Eddy Simulation
SRS	Scale-Resolving Simulation
SST	Shear Stress Transport
TMAOA	Targeted Maximum Angle of Attack
TSR	Tip Speed Ratio
TVR	Turbulent Viscosity Ratio
UDF	User Defined Function
uRANS	Unsteady Reynolds-Averaged Navier-Stokes
VAWT	Vertical Axis Wind Turbine
VP	Variable Pitch
VPP	Variable Pitch Profile
VP-VAWT	Variable Pitch Vertical Axis Wind Turbine
WM-LES	Wall-Modelled Large Eddy Simulation

1 INTRODUCTION AND OBJECTIVES

1.1 Energy demand and wind energy

Throughout history, there has been a strong dependency between the energy demand and evolution of civilisation. The modern human urbanisation and modernisation are driven by energy in both the developed and the developing communities. In a world of increasing population, the global energy demand is continuously increasing. According to the International Energy Agency (IEA), this global demand will increase by more than one-fourth by 2040 [1]. In order to meet the increasing demand while limiting the greenhouse gas emissions, a proper energy mix is required, and this incorporates geothermal, tidal, solar and wind energy along with other conventional energy sources.

Wind energy is one of the most promising alternative energy sources. The wind is purely renewable and is maintained and dominated by solar energy mainly through the uneven solar radiation across the earth that forms the temperature gradient between the equator and the poles. This forms a pressure gradient where the cold and hot air streams are circulated due to buoyancy forces [2]. The wind turbines haven't the problem of either emitting the greenhouse gases, such as fossil fuel power plants, or having radiative waste, such as nuclear power plants. Therefore, increasing the wind energy share of the installed capacity assists in reducing climate change and environmental pollution. The wind energy potential is not limited to the day time like solar energy potential. However, the wind energy potential depends on the location and changes with the seasons over the year. Hence, a proper energy mix is essential to cover the energy demand regardless of the uncertainty in the wind and solar energy potentials. In order to get the most benefits from the wind energy resources, there is a need to develop and employ efficient wind turbine designs as a part of a sustainable energy mix in order to meet the growing energy demand.

1.2 The challenging wind potential

In order to design a wind turbine for the future, attention should be paid to the available wind resources on the Earth. Several numerical simulations have been carried out to estimate the global wind resources. However, Vaisala [3] introduced a high-resolution numerical assessment of the global wind based on a measured database. Figure 1.1

shows the world onshore wind map at a height of 80 m above the ground and this corresponds to the typical hub height of modern large scale HAWT wind turbines. The map shows that the majority of continental and near-shore regions are exposed to low and moderate wind speeds. The concepts of low and moderate wind speeds are relative and are not well-defined. However, an annual average wind speed lower than 7.5 m/s is considered low according to the International Electrotechnical Commission (IEC) [4].

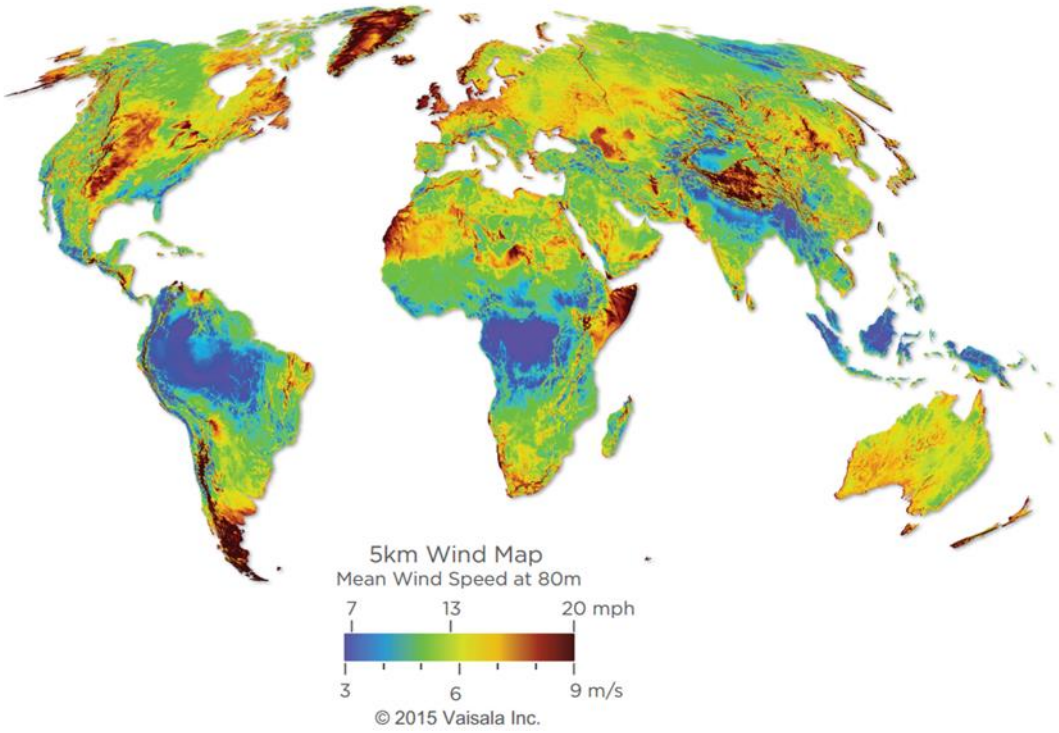

Figure 1.1 World onshore wind map at a height of 80 m [3].

On the national level, the majority of the countries have either limited regions or even no regions with high wind potential. Even in countries with higher energy potential, there is a need for a turbine to work better at low and moderate speeds. The reason is that sites with higher wind quality are used first. So, the sites with less wind quality are left for future utilisations. Therefore, future designs for a wind turbine will need to operate at lower wind speeds than their older generations. This fact drives the wind turbine manufacturers except that, in the next few years, about one-third of the worldwide installed wind capacity will be installed in low to moderate wind speed sites [5]. According to Barnes et al. [6], the utilisation of low wind speed sites is expected to increase by several governmental and industrial researchers across the world,

including the United States, Canada, Europe, China, India, and Brazil. In conclusion, there is a need to develop future wind turbine designs that are specifically tailored to operate efficiently and economically at low wind speed, particularly lower than 7.5 m/s.

1.3 Wind turbines types

Wind turbines are classified into Horizontal Axis Wind Turbines (HAWTs) and Vertical Axis Wind Turbines (VAWTs). Due to their simpler and more steady aerodynamics, the HAWTs have received intensive research and developments over the decades. Currently, VAWTs power coefficients lack behind that of the HAWTs, but increasing research has been established in order to enhance VAWTs performance. Consequently, the wind energy market is led by HAWT technology. However, the global market of the VAWTs is growing and is expected to have a Compound Annual Growth Rate (CAGR) of about 4.3% between 2019 and 2025 [7].

VAWTs can be classified into Savonius and Darrieus designs [8], [9]. The Darrieus VAWTs are based on the aerofoil-shaped blades that are mainly driven by the lift forces and offers better performance in contrast to the drag driven Savonius designs [8]. The early-developed Darrieus VAWTs had curved blades and eggbeater-shaped rotor, also referred to as troposkein-rotor. In addition, some modern designs incorporate a helical shaped blade. However, the majority of modern VAWTs utilise straight blades due to the lower manufacturing costs.

From the market perspective, the wind turbines are classified into the small scale and large scale turbines and each category has its own market share. The small scale turbines have some distinct advantages that make them considered as a sustainable viable option [10]. In contrast with the large scale grid-connected turbines, the small scale turbines can be installed near the consumption locations or even installed on the customer property and hence reduce the load on the grid. It is also suitable for the installation in micro-grids to serve small communities in the off-grid locations. However, small scale turbines have small capacities and are not suitable for energy-demanding applications. VAWTs produce cyclical variations in the torque and normal force which can lead to difficulty in transmission and blade fatigue control in particular for small VAWTs. The small scale turbines gain increasing interest in the use in small stand-alone applications such as road lighting [11], [12] and hybrid wind-solar

desalination units [13]–[15]. The small scale turbines are not meant to replace the large scale turbines, but both of them should be incorporated into a sustainable energy mix.

In contrast to HAWTs, small VAWTs have some important features, especially for the use in the urban environment, and this includes their better response to the high turbulence level of incoming flow and the rapid change in the urban flow conditions [16], [17]. In addition, the VAWT concept has a lower noise emission due to its lower rotational speed and better integration with the building environment. Another major advantage is that VAWTs can intake the wind from any direction without any yawing mechanism. In conclusion, the small VAWT is considered as a viable sustainable prime-mover with a promising market. However, the current designs of VAWTs have lower power coefficients in contrast with HAWTs.

1.4 Fundamentals of straight-bladed Darrieus VAWTs

The straight-bladed Darrieus VAWTs features simple blade shape and easy construction and this type of VAWT is the focus of this thesis. For simplicity, the term VAWT is used, in this thesis, to refer to the straight-bladed Darrieus VAWTs unless otherwise specified. A typical VAWT consists of a shaft and a number of aerofoil-shaped blades. These are connected together by means of struts or supporting arms. While the number of blades varies from one turbine to another, increasing the number of blades leads to better start-up characteristics. However, it is common to have an odd number of blades, particularly three or five blades, as this reduces the torque ripple. Figure 1.2 shows an illustration of a three-bladed turbine with a turbine diameter of D, a blade chord length of C, and turbine height of h. In this context, the turbine height refers to the blade length that is known as the blade span. The aspect ratio concept is used to evaluate the turbine height in a dimensionless form. In this thesis, the turbine height is normalised by the turbine diameter in the form of the Aspect Ratio based on the diameter, $AR_D=h/D$. The majority of the small scale VAWT designs in the market have low aspect ratios. Hence, the effects of the tip losses are considerably high and the blades suffer from a strong tip vortex. This suggests that the use of a proper tip device may be essential for low aspect ratio VAWTs. This may include the implementation of a winglet shaped tip that is proven to enhance the performance of the finite wing in the aviation application under certain operating conditions.

The performance of a VAWT depends on its swept area that is illustrated in Figure 1.2 and is defined as follows:

$$\text{Swept area} = h * D \tag{1.1}$$

As a lift-type turbine, the performance of VAWT strongly depends on its solidity. The solidity, σ, represents the ratio between the total reference area of the blade and the swept area of the turbine and is defined as follows:

$$\sigma = \frac{N_b \times (C \times h)}{D \times h} = \frac{N_b \times C}{D} \tag{1.2}$$

where N_b is the number of the blades.

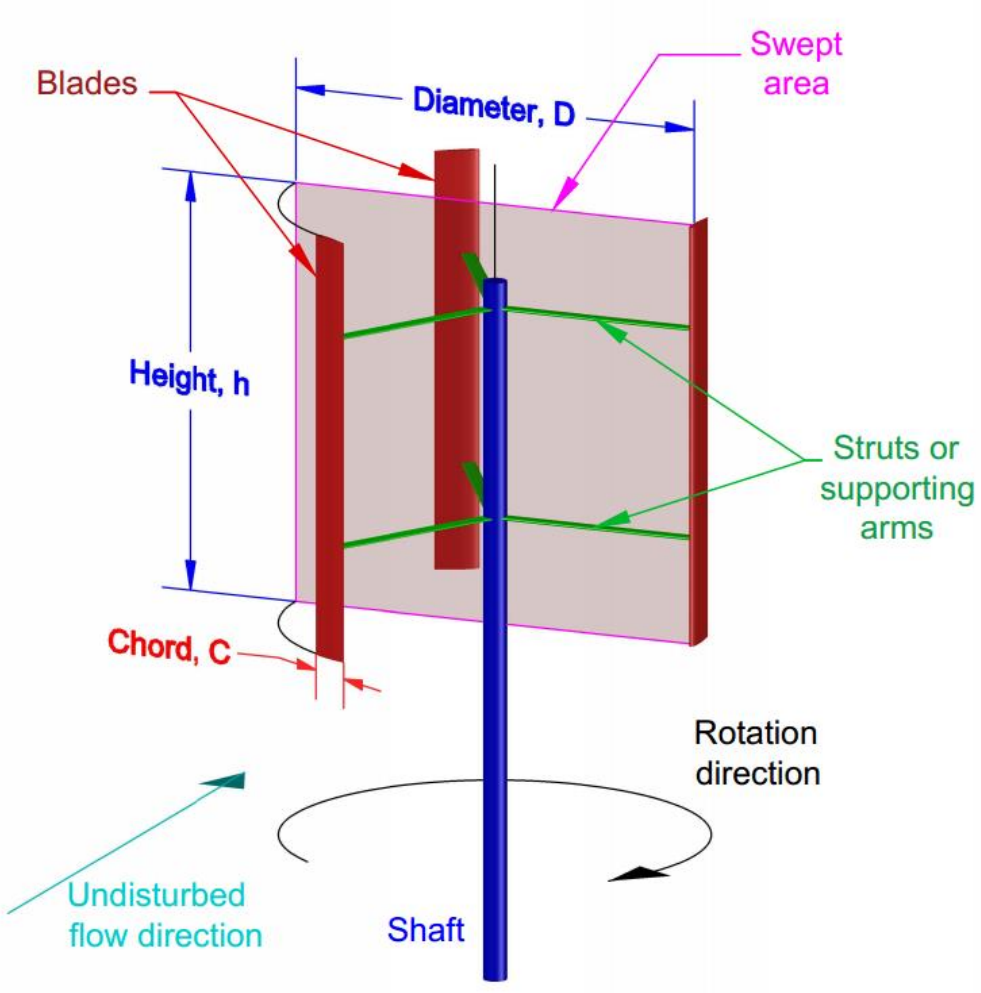

Figure 1.2 An illustration of a three-bladed VAWT. This clarifies the different components of the VAWT in addition to its main terminologies.

The Blade Speed Ratio (BSR) represents the ratio between the tangential velocity of the blade and the undisturbed flow velocity. It is commonly referred to as the Tip

Speed Ratio (TSR). The TSR is one of the most influential parameters that affects the turbine performance and is defined as follows:

$$\mathrm{TSR} = \frac{\omega * \mathrm{R}}{\mathrm{V}} \tag{1.3}$$

where ω is the rotational velocity in rad/s, R is the turbine radius and V is the undisturbed wind flow velocity.

Due to the rotation of the VAWT blades around its axis that is perpendicular to the approaching wind direction, the aerofoil-shaped blade encounters a time-variant Angle of Attack (AOA), also referred to as α. Figure 1.3 illustrates the AOA and the theoretical velocity triangle near the aerofoil at an arbitrary azimuthal position, ϕ. Based on this velocity triangle, the theoretical AOA can be derived as follows:

$$\alpha = \tan^{-1}\frac{\mathrm{V}\times\sin(\phi)}{\mathrm{V}\times\mathrm{TSR}+\mathrm{V}\times\cos(\phi)} = \tan^{-1}\frac{\sin(\phi)}{\mathrm{TSR}+\cos(\phi)} \tag{1.4}$$

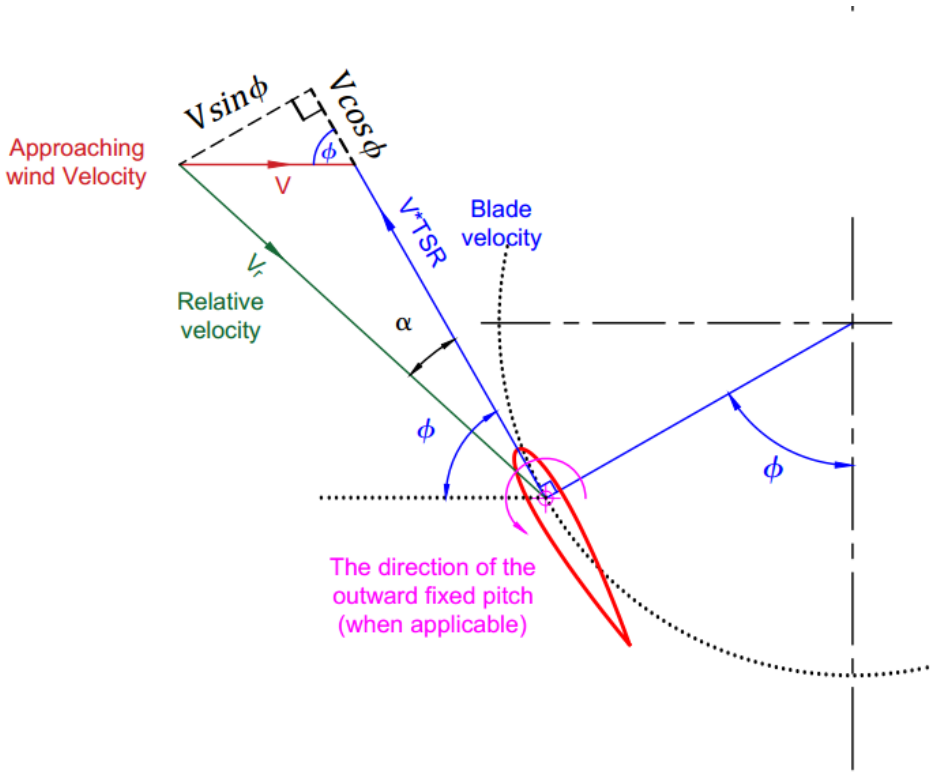

Figure 1.3 A schematic for the velocity triangle near the blade at an arbitrary azimuthal position.

Due to the relative flow passing over the aerofoil-shaped blade, the aerodynamic forces are generated. Figure 1.4 illustrates the different aerodynamic forces acting on the

blade at an arbitrary azimuthal position. These aerodynamic forces include the lift, L, that acts perpendicular to the relative flow direction and the drag, D, that acts parallel to the relative flow direction. The resultants force, F_R, can be analysed into the tangential force, F_T, and normal force, F_N, when projected onto the tangential and radial directions, respectively. Considering a single blade, the tangential force generates the single blade driving torque, $T=F_T*R$, and consequently the single blade power, $P=T*\omega$. These parameters can be expressed in dimensionless forms as follows:

$$\text{Lift coefficient, } C_L = {}^{L}/_{0.5\,\rho \times\ (h \times C) \times\ V^2} \tag{1.5}$$

$$\text{Drag coefficient, } C_D = {}^{D}/_{0.5\,\rho \times\ (h \times C) \times\ V^2} \tag{1.6}$$

$$\text{Torque coefficient, } C_m = {}^{T}/_{0.5\,\rho \times\ (h \times D) \times\ V^2 \times R} \tag{1.7}$$

$$\text{Power coefficient, } C_P = {}^{P}/_{0.5\,\rho \times (h \times D) \times V^3} \tag{1.8}$$

where ρ is the air density.

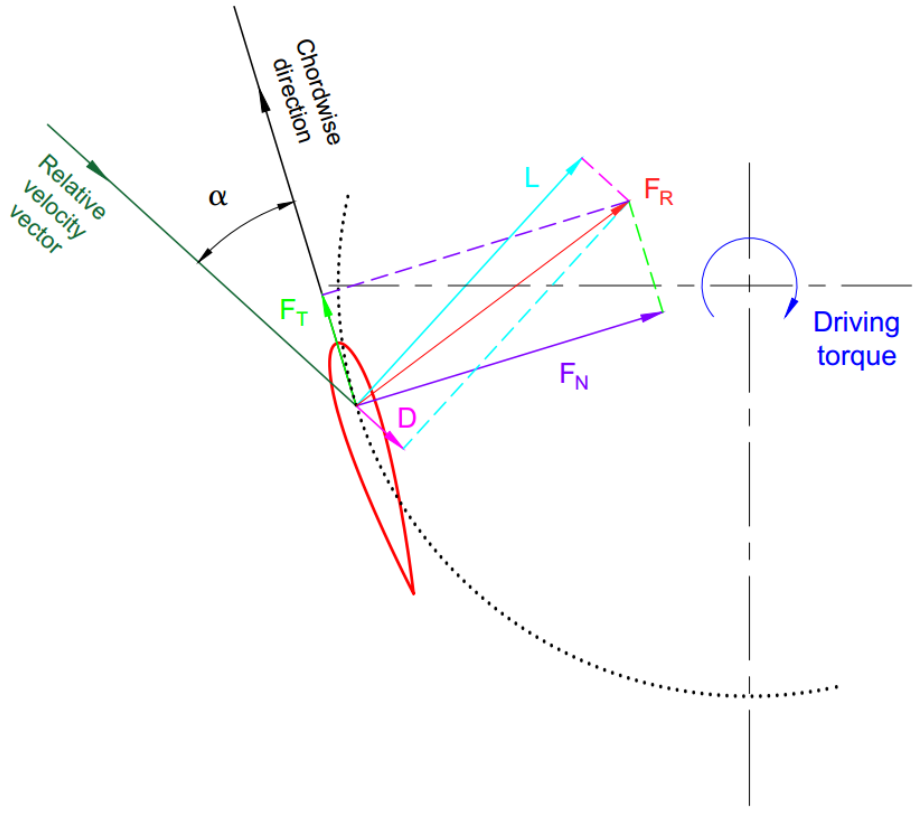

Figure 1.4 A schematic for the aerodynamic forces on the blade at an arbitrary azimuthal position. The blade is mounted at the aerodynamic centre at ¼ of the chord from the leading edge.

The performance of a VAWT can be evaluated in the form of its dimensionless coefficients such as the power coefficient and/or the torque coefficient. However, the VAWT is driven by its aerofoil profiled blades and its performance can be evaluated in terms of the lift and drag coefficients as well. The understanding of the blade performance assists in obtaining a better understanding of the overall turbine performance. The most significant parameter that affects the performance of the aerofoil profiled blades is the AOA. Figure 1.5 shows the distribution of the theoretical AOA, based on Equation (1.4), over the entire cycle for different TSRs. It is clear that the VAWT encounters high AOA, especially when operated at low TSR. However, in order to have sufficient torque and a better start-up performance, the small scale VAWTs usually have a considerably high solidity and consequently operate at relatively low TSR. In order to improve the blade performance and consequently the overall performance of a small scale VAWT, both the fixed pitch and variable pitch concepts have been introduced mainly to reduce the AOAs to more favourable values. Figure 1.3 illustrates the direction of the outward fixed pitch about the blade mount point. In a fixed pitch configuration, a constant pitch angle is imposed over the entire cycle and this assists in obtaining a more favourable AOA over some parts of the cycle. Considering an outward fixed pitch angle, β, the AOA is reduced as follows:

$$\alpha = \tan^{-1}\frac{\sin(\phi)}{\mathrm{TSR}+\cos(\phi)} - \beta \tag{1.9}$$

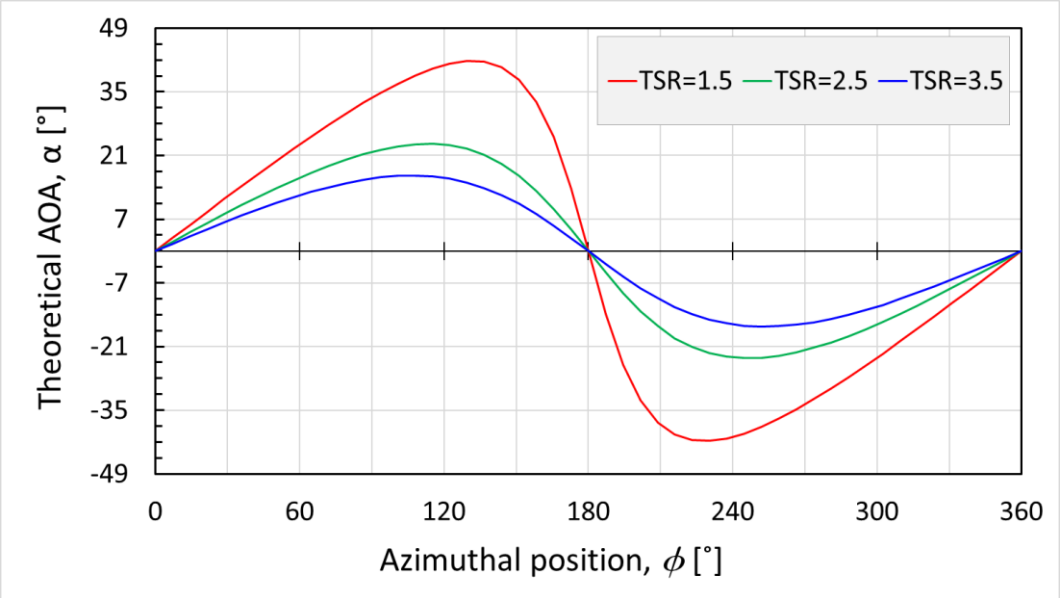

Figure 1.5 The effect of the TSR on the theoretical AOA over an entire cycle with the azimuthal angle between 0° and 360°, based on Equation (1.4).

In a variable pitch configuration, a time-variant change in the pitch angle is imposed and this assists in obtaining more control on the AOA distribution over the cycle. Despite the need for a pitch mechanism that increases the complexity of the turbine, the variable pitch concept is considered as a promising tool in improving the VAWT performance. Although the variable pitch configurations loss the advantage of being omnidirectional, it is only required to adjust the reference point of the pitch mechanism instead of yawing the whole turbine.

In conclusion, the most influential parameters on the VAWT performance includes the solidity, the TSR and pitch angle. The understanding of the performance of an aerofoil-shaped blade assists in obtaining a better understanding of the overall turbine performance. The AOA has a significant effect on the VAWT performance and hence modifying the AOA based on the fixed pitch and the variable pitch could assist in improving the overall turbine performance. In addition, there is a need to quantify the effect of the winglet on the performance of the VAWT for different aspect ratios.

1.5 Motivations, aims, and objectives

In the light of the continuously increasing energy demand and the challenging wind potential, it is viable to develop the future wind turbines to obtain high performance at low wind speeds. The small scale straight-bladed VAWT is selected as the scope of this thesis based on its competitive advantages and promising market. Due to the prospective performance enhancement both the fixed pitch and variable pitch VAWT configurations are considered.

The state-of-the-art Computational Fluid Dynamics (CFD) simulations is chosen as a modelling approach due to its high fidelity and reasonable computational cost. The three most influential parameters, namely the solidity, TSR, and fixed pitch angle, are chosen for the investigation of the fixed pitch configuration using the optimisation approach in order to gain more insight into the effect of the selected parameters on the VAWT performance. Several parametric studies are carried out to investigate the performance of variable pitch configurations. This investigation is extended to test the key 3D aspects of the VAWT in the fixed and variable pitch configurations.

The main aim of this thesis is to provide an in-depth understanding of the aerodynamics and the effect of blade pitch of small VAWTs in order to improve the

performance of the turbine at low wind speed conditions. In other words, the aims of this thesis are not limited to the design of the most appropriate fixed pitch and variable pitch configurations. However, this thesis is extended to provide appropriate methodologies for the modelling of VAWTs and the analysis of its performance. In addition, it is intended to provide a better understanding of the aerodynamics of VAWTs and how the VAWT performance is developed and why a certain configuration outperforms another. These aims are achieved through the fulfilment of the following specific research objectives:

- Construction of numerically-verified 2D and 3D CFD models which are capable to provide accurate experimentally-validated predictions.
- Analysis of the relation between the complex VAWT performance and the aerodynamics of its aerofoil-shaped blades.
- Design optimisation of a fixed pitch small scale VAWT for low wind speeds based on three input parameters that include the tip speed ratio, solidity, and fixed pitch angle. The objective function is to maximise the power coefficient at wind speeds of 7 m/s and 5 m/s, with a higher priority to the 7 m/s case.
- Identification of the most appropriate variable pitch configuration based on the investigation of how the different aspects of the variable pitch profile affect the performance.
- Investigation of the effect of 3D design aspects of the fixed pitch and variable pitch VAWTs on their performance. These aspects include the aspect ratio and the shape of the blade tip.

1.6 Thesis outline

The structure of the thesis is arranged into nine chapters as follows:

Chapter 1 introduces the relevant background and motivations for this thesis. This illustrates the role of wind energy in fulfilling the increasing energy demand and how the challenging wind potential directs the future designs of the wind turbine. The market viability of the small scale VAWT is clarified and the fundamentals of the VAWT and its design parameters are introduced.

In **Chapter 2**, the literature on the design and modelling of VAWTs is critically reviewed with more emphasis on the variable pitch VAWTs. The relevant literature is analysed from different perspectives and this includes the different types of variable pitch, the available variable pitch mechanisms, and the different variable pitch profiles. In addition, the principal findings of the recent numerical and experimental studies are discussed. By the end of this chapter, the research gaps and potential future works are identified.

Chapter 3 outlines the principles of the overall methodologies that have been implemented in this thesis. It sheds much light on the principles of Computational Fluid Dynamics (CFD) and the Response Surface Optimisation (RSO).

Chapter 4 describes the details of the proposed 2D and 3D CFD models. In this chapter, the numerical verifications of the models are carried out based on several sensitivity analyses which include the time step independency and the mesh independency study. In addition, the solution periodicity, the selection of the domain size, and the effect of the discretisation schemes are discussed for the two selected turbulence models.

The validation of the 2D and 3D CFD predictions against the detailed experimental data is presented in **Chapter 5** based on qualitative and quantitative assessments. This includes the comparisons of the detailed pressure coefficient distributions around the blade at different azimuthal angles in addition to the comparisons of the instantaneous torque coefficient.

In order to obtain a better understanding of the VAWT performance, a new procedure for the analysis of the VAWT is proposed in **Chapter 6** based on the relation between the VAWT performance and the performance of its aerofoil-shaped blades. This analysis procedure relies on a novel method for the estimation of the AOA.

Chapter 7 presents the details of the design optimisation of the fixed pitch VAWT. In addition, the effects of the aspect ratio and the shape of the blade tip on the performance of the VAWT are discussed.

Chapter 8 starts with a discussion of the effect of the fixed pitch angle on the VAWT performance. Then, more emphasis is given to the different parameters that affect the

performance of the variable pitch VAWT. This includes the investigation of four different variable pitch profiles. Moreover, the effects of the targeted maximum angle of attack and the preset fixed pitch angle are discussed. In addition, the power required to overcome the aerodynamic torque during the pitch motion is quantified.

Chapter 9 summarises the main findings and conclusions. In addition, some recommendations and potential future works are proposed.

2 LITERATURE REVIEW

2.1 Overview

This literature review starts with a brief survey of the history of wind energy utilisation and the evolution of the wind turbine concept until the modern VAWT. Then, the key research findings in the aerodynamics and performance of a fixed pitch VAWT is surveyed and critically analysed. Then, more emphasis is given to the relatively more complex variable pitch VAWT. This includes a critical discussion of the different types of variable pitch control, the different variable pitch mechanisms, and the modelling methodologies. In addition, the key research in the kinematically similar variable pitch vertical axis tidal turbines is discussed. Furthermore, the previous studies on the optimisations of the VAWT are discussed. Then, the flow physics of the aerofoils and finite wing aerodynamics are emphasised. Finally, the research gaps and the areas that need further research are summarised.

2.2 History of wind energy

The first reported utilisation of wind energy dates back to the dawn of history in Egypt where sails were implemented to drive boats since 4000 BC [18]. The early wind turbines were known as windmills due to the fact that cereal grinding was the most important application of these turbines. The windmill concept appeared in the wind-driven toy-like application by Hero in his pneumatic book that dates back to the first century AC [19]. Hero described a pneumatic device that operates with a small horizontal axis windmill. However, there is no evidence that this concept was developed for a practical wind turbine [20].

The first practical windmills were used by the 7th century AC in the Persian region [19], [20]. These turbines were reported to be vertical axis windmills that were developed for grinding, irrigation, and rice pounding applications [20]. Some turbines based on this concept have survived up to the present time and have continued in operation [19]. Figure 2.1 shows a photograph of the surviving windmills in Nashtifan. The horizontal axis windmills appeared in Europe in the 12th century AC [20] and were impressively spread in the 13th century [21]. The early horizontal axis windmills had a yawing capability and their sails developed later from the flat sails to twisted aerofoil-like

shaped sails [21]. One of the remarkable developments in wind turbines is the American multi-bladed turbine, also referred to as fan mills. When the new settlers moved to the west of the American land, they found great treeless plains with relatively lower wind speeds. They needed an alternative to the traditional windmill that could operate at lower wind speeds and requires less wood and less attention from the owners [21]. The main application was the water pumping for their pastures using the relatively slow piston pumps. Therefore, the high solidity multi-bladed design that is yawed by a tail vane was found to be a suitable solution that was spread during the 1850s [21].

Figure 2.1 The surviving windmills in Nashtifan. Photograph by Ali Vaseghnia, distributed under a CC BY-SA 4.0 license.

The prominent turning point in the wind energy utilisation was the implementation of an electrical generator that replaced the windmill concept with the wind turbine that extracts the electricity from the wind energy. The first fully functional wind turbine was introduced and implemented in 1888 by Charles Brush to generate electricity and charge batteries [21]. After decades of investigations, the HAWTs have a more efficient streamlined design while the three-bladed HAWT is considered as the flagship design of the modern turbines market.

The majority of modern VAWTs use either the Darrieus or Savonius concepts. Darrieus Marie [22] introduced his lift type VAWT in a patent filed in 1926 that had aerofoil-shaped blades. His patent illustrated both the eggbeater-shaped rotor, also referred to as troposkein-shaped as shown in Figure 2.2. In addition, he introduced the straight blade rotor, also referred later as the H-Darrieus VAWT or straight-bladed Darrieus VAWT. Savonius Johannes [23] filed his patent of a drag type VAWT in 1925. He illustrated a rotor with two curved vanes that formed an S-like passage as shown in Figure 2.3. The vertical axis windmill first appeared in Europe in the 15th century with a four-bladed rotor whose blades were curved [21], [24], similar to the more recent Savonius turbine. However, Savonius work is still remarkable in the development of drag-type VAWTs.

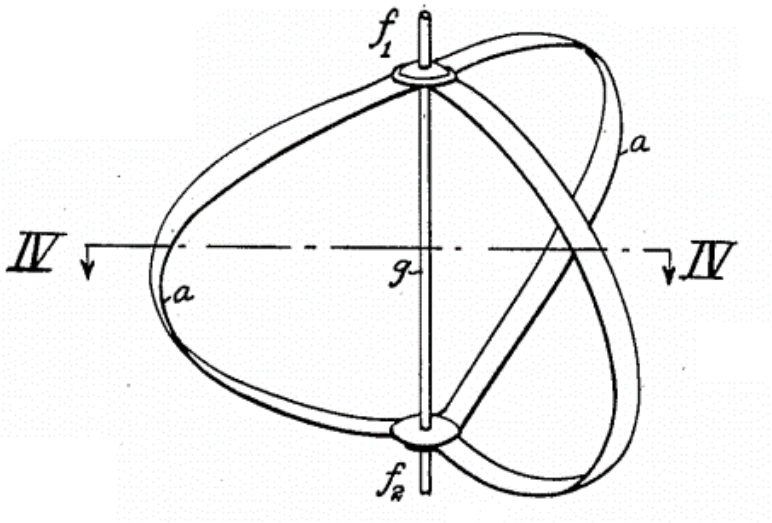

Figure 2.2 Schematic of a Darrieus eggbeater-shaped rotor as presented in his patent [22]**.**

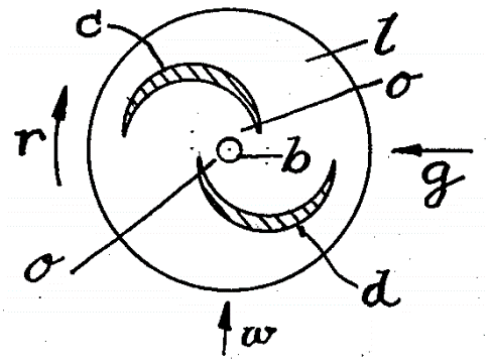

Figure 2.3 Illustration of the curved vanes of a Savonius rotor as presented in the original patent [23]**.**

The Darrieus VAWTs have generally a higher power coefficient and higher optimal TSR in contrast with the Savonius. However, the Savonius VAWT has a better start-up and can operate at lower wind speed [25]. Due to its higher power coefficient, Darrieus VAWT is selected as the focus of this thesis. For simplicity, the terms VAWT is used, in this thesis, to refer to the straight-bladed Darrieus VAWTs unless otherwise specified. In recent years, the matured Darrieus VAWT concept appeared to begin a new era [26], while a gradual increase in the research concerned with VAWTs is remarked [27]. While the early-developed VAWTs had fixed blades, the concept of the articulated blades with cyclic pitch motion was introduced by Darrieus himself in his patent [22] as shown in Figure 2.4. Darrieus described them as pivotally mounted blades. Currently, modern Darrieus VAWTs can be classified into Fixed Pitch VAWT (FP-VAWT) and Variable Pitch VAWT (VP-VAWT).

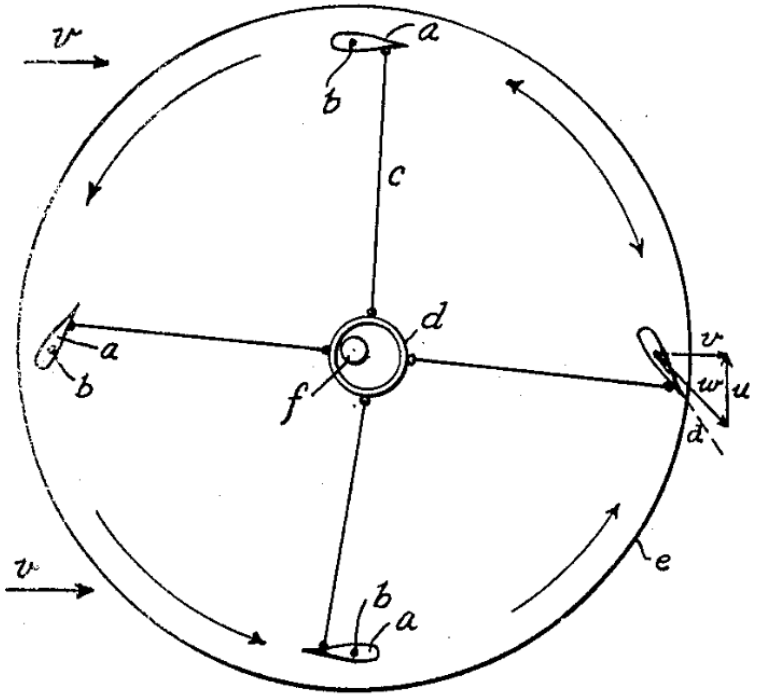

Figure 2.4 Schematic of a variable pitch VAWT as presented in the patent filed by Darrieus [22]**.**

2.3 The key findings in the FP-VAWT research

Gosselin et al. [28] carried out a remarkable parametric study to evaluate the effect of different parameters on the VAWT performance based on CFD simulations. These parameters include the tip speed ratio, the solidity based on the turbine radius, the

fixed pitch angle, the blade profile based on the NACA 4-digit series, and the Reynolds number. While several studies have been investigated with some of these parameters separately, the importance of the Gosselin et al. [28] study is that it provides consistent comparisons based on the same numerical setup.

Gosselin et al. [28] remarked that both the TSR and the solidity have significant effects on the power coefficient, as shown in Figure 2.5. Their results illustrate how the maximum power coefficient decreases for higher solidities. Moreover, the TSR at the maximum power coefficient is lower for high solidity turbines. For a particular solidity, the power coefficient reduces at relatively high TSRs. These findings are in agreement with the finding of Li et al. [29] based on their experimental data, Rezaeiha et al. [30] based on the CFD simulations, and Valappil et al. [31] based on the vortex method. The significance of the TSR is due to its effect on the local AOA around the blade and consequently the performance of the blade and the whole turbine. The early-developed VAWT had a low solidity and produces relatively higher power coefficient at high TSR. However, the low solidity VAWT produce lower torque and has poor self-starting behaviour [32]. It is observed that the modern designs of VAWTs usually have a relatively high solidity.

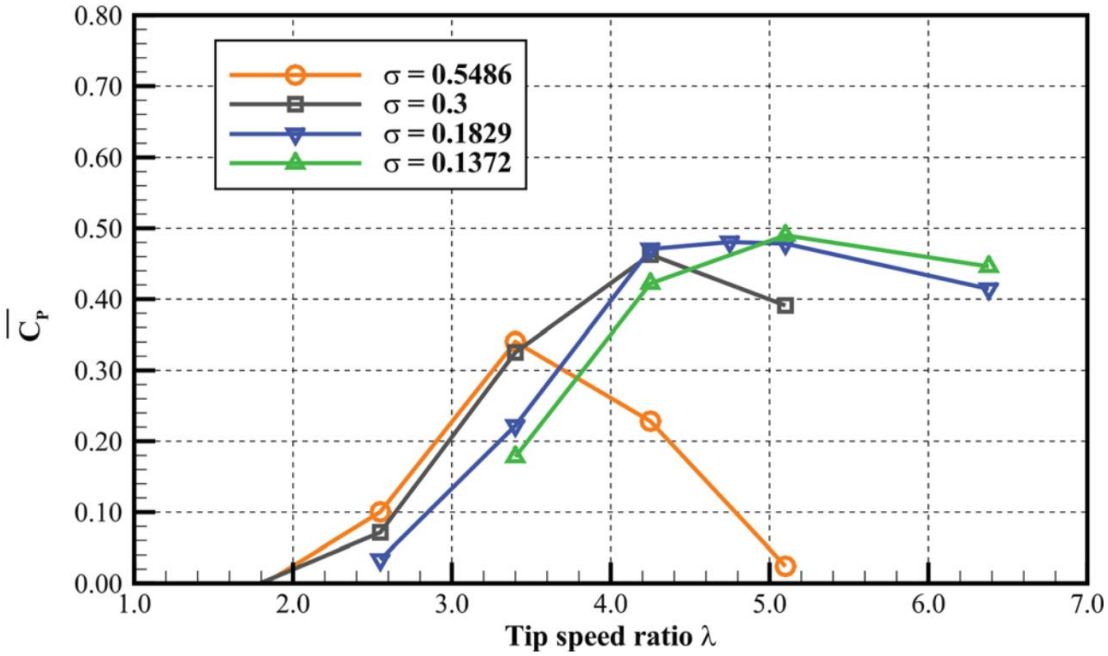

Figure 2.5 The effect of the TSR and the solidity, σ, on the power coefficient [28]**. In this particular Figure, the power coefficient and tip speed ratio are referred to as $\overline{C_p}$ and λ, respectively.**

For a particular solidity, Gosselin et al. [38] found that the number of blades, in the range between 3 and 9, have a small effect on the power coefficient. A similar conclusion is reported by Delafin et al. [33] and Hwang et al. [34]. It is noticed that several studies [35]–[37] changed the number of blades with a constant chord, and hence the solidity increases with the increase in the number of blades. These studies conclude that the number of blades has a considerable effect on the power coefficient. However, due to the fact that the effects of the solidity are not isolated in these studies, their conclusions appear to be related to the change in the solidity rather than the effect of the number of blades itself.

The two-bladed rotor has high torque ripple and bad stating-up behaviour. Increasing the number of blades leads to a significantly more uniform torque output and a better starting-up behaviour. The number of blades also affects the fluctuation of the thrust and lateral forces and hence the fatigue load on the tower and foundation. However, increasing the number of blades increases the number of supporting arm and hence increase the parasitic losses due to the drag on the supporting structure [28], [33]. Due to the nature of the torque ripple, an odd number of blades is usually preferred. While the early VAWTs were equipped with two-bladed rotors [28], most of the latter designs have three or five blades.

As mentioned above, VAWTs with relatively high solidity are preferred to their higher torque production and better start-up characteristics. However, these VAWTs produce its maximum power coefficient at moderate TSRs and hence their blades encounter high AOAs. In order to improve the performance of VAWT at moderate TSR, the fixed pitch concept is introduced to reduce the maximum AOA at the upstream part of the cycle. Gosselin et al. [38] found that the outward fixed pitch angle has a significant effect on the power coefficient, especially in moderate TSR, as shown in Figure 2.6. Due to the kinematics of VAWT, the amplitude of the AOA reduces with the increase in TSR and hence there is no advantage of using the fixed pitch at high TSR. Several studies [38]–[40] have reported the significant effect of the fixed pitch angle on the VAWT performance. However, the optimal fixed pitch angle is not constant and it appears to be dependent on the TSR and the turbine geometry.

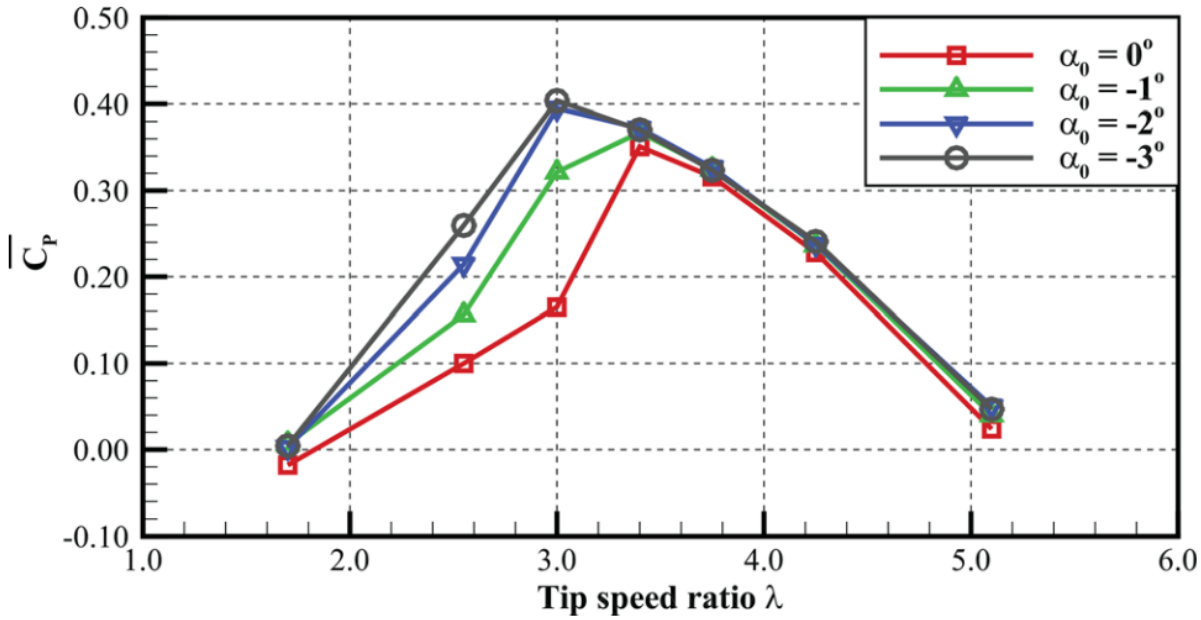

Figure 2.6 The effect of the fixed pitch angle on the power coefficient for a range of TSRs [28]. **In this particular Figure, the fixed pitch angle, power coefficient, and tip speed ratio are referred to as α_0, $\overline{C_p}$, and λ, respectively.**

It was reported that the power coefficient is independent of the Reynolds number, Re, at high Re ≥ 500,000 [41]. However, for small scale VAWTs, that usually operate at low Reynolds number, it has a significant influence on the power coefficient since most of the aerofoils have poor performance at low Reynolds number [42]. For a constant wind speed and operating TSR, the Reynolds number for the blade depends mainly on the chord length and consequently on the turbine scale and hence Reynolds number cannot be considered among the independent design parameters.

The VAWTs are driven by the torque produced by the aerodynamic forces on their aerofoil-shaped blades. The aerofoil shape of the blades affects the generated aerodynamic forces and hence the overall performance of VAWT. The shape of the aerofoil not only affect the power coefficient of the turbine but also affect its starting-up capability [43]. There are a tremendous amount of studies that either tested several exsiting aerofoils [44]–[51] or specifically optimised new aerofoils for VAWT [52]–[56]. However, their conclusions are not identical and there is no unique selection for the aerofoil that has the best performance. The thickness of the aerofoil is an important parameter. A good aerofoil for a VAWT should have a relatively moderate thickness. It should be thick enough to delay the stall and sustain a high AOA but not very thick in

order to avoid the excessive drag [44]. For the symmetrical NACA 4-digit aerofoil series, several studies [28], [45], [47], [51], [57] suggested that the NACA0015 with 15% thickness to chord ratio provides superior performance. However, these conclusions about the NACA0015 aerofoil cannot be generalised and some other studies have different conclusions [48], [58]. The suitability of a certain aerofoil to a certain VAWT depends on the Reynolds number and the maximum AOA and consequently is related to the wind speed, the TSR, and the size of the VAWT. Therefore, the selection of the best aerofoil cannot be generalised.

There are some interesting research to improve the VAWT performance by implementing slotted aerofoils [59], auxiliary flaps [60], [61], Gurney flaps [62], [63], tubercle leading edge [64], [65], J-shape aerofoils [66], [67], omni-directional guide vanes [68], [69], upstream deflector [70], active flow control [71], [72], vortex generators [73]. However, it is expected that the utilisation of fixed and variable pitch has more prominent effects in improving the turbine performance.

The VAWTs use finite aerofoil-shaped blades and hence a finite aspect ratio. These finite blades suffer from tip losses due to the flow leakage over the tips and this reduces the performance near the tips of the blades. The effect of the tip losses on the overall turbine performance is reduced when the blade length is increased. Therefore, the aspect ratio is reported to have a considerable effect on VAWT performance [28], [74]–[76]. In addition to its influence on the performance, reducing the aspect ratio is found to reduce the starting-up capabilities of the VAWT [32]. On the contrary, Brusca et al. [77] suggested that reducing the aspect ratio is associated with maximising the power coefficient. The reason behind their inconsistent conclusion is that their results are based on a Multiple Stream Tube model that neglect the tip losses and the three-dimensional nature of the flow around the VAWT. Zanforlin and Deluca [74] investigated the effect of the aspect ratio on the performance of VAWTs with different sizes and they concluded that aspect ratio lower than 0.8 should be avoided. Although several studies [28], [74]–[76] have investigated the effects of the aspect ratio on the VAWT performance up to an aspect ratio of 3, there is a lack in the investigation of aspect ratios higher than 3. However, increasing the aspect ratio in order to improve the performance is not always possible due to space constraints and structural design aspects.

In order to reduce the tip losses and improve the performance of VAWT with a certain aspect ratio, tip devices, such as endplates [78] and winglets [79], could be implemented. Zhang et al. [79] carried out an optimisation study to design an optimised winglet for a VAWT with an aspect ratio of about 0.6. Their results showed that the implementation of optimised winglets leads to an improvement of the power coefficient with about 6.7% at the optimal TSR in contrast with the case without winglet. However, there is a lack of information about the improvement of the performance due to the winglet for a VAWT with high aspect ratios in order to assess the importance of the winglet at different aspect ratios.

In conclusion, the solidity, TSR, and fixed pitch angle are found to be among the most influential parameters on the VAWT performance performance and these three parameters have been investigated later in Chapter 7. There is no single aerofoil that will generally give the best performance for all VAWT configurations. However, the NACA0015 aerofoil appears to be a very good candidate. More investigations are required in order to have a better insight into the effects of the aspect ratio and the winglets on the performance of VAWTS, especially for high aspect ratio configurations.

2.4 **The estimation of the AOA**

The distribution of the relative AOA of the approaching flow near the blade over the cycle has a significant effect on the performance of the blade and hence the whole turbine. The AOA can be simply estimated using Equation (1.4) assuming that the approaching wind velocity to the blade is constant and parallel to the undisturbed wind flow velocity. This simple calculation ignores the effects of the rotor on the flow and in particular the blade-wake interactions existing in the VAWT operation, which can lead to a significant error in the prediction of the performance of the turbine blades. While this simplified calculation of the AOA is widely used [65], [80]–[86], a more realistic estimation of the AOA is needed that takes into account the variation of the magnitude and direction of the approaching wind velocity vector to the blade at different azimuthal positions. Kozak [87] calculated the AOA based on the CFD data using two different methods and these are based on the calculated lift coefficient or the pressure ratio between the suction and pressure sides of the blades. However, his validation of these methods was limited to the study of a pitching motion with a geometric AOA

between 0° and 8°. Bianchini et al. [88] used the CFD data for the estimation of the AOA based on the location of the suction pressure peak by comparing it to the location of the pressure coefficient peak obtained by the panel method. In order to account for the virtual camber effect, the original aerofoil coordinates are transformed to a virtual aerofoil and then the panel method is used for the pressure coefficient calculations [88]. Although this method has a good agreement with the Blade Element Momentum (BEM) results, it involves many intermediate tasks. Edwards et al. [89] presented an estimation method of the corrected AOA based on the cycle-averaged CFD velocity flow-field. This method involves discarding the distorted velocity near the blade trajectory then interpolating the flow-field. While this method provides a good estimation of the AOA, it ignores the instantaneous variation of the velocity flow-field and involves many intermediate tasks. Gosselin et al. [28] claimed a good estimation of the AOA using CFD data based on the velocity vector at a single point located on the tangential trajectory at a distance of two-chord lengths in front of the blade. However, a distance of two-chord lengths appears to be large, especially for high solidity turbines where the chord to radius ratio is quite high.

It is noted that most of the estimation methods of the AOA that are available in the literature have two common drawbacks, namely (i) the lack of a reference for comparison and validation of the methods and thus can lead to relatively large errors, and (ii) the need for extensive post-processing. This thesis presents a new method for the accurate estimation of the AOA which uses the CFD simulated flow-field data at two well-selected reference points around the blade. This is essential for the understanding of how a certain fixed or variable pitch configuration affects the AOA and hence the overall turbine performance which have been helpful in the research work in Chapters 7 and 8.

2.5 Progress in VP-VAWT research

It is observed that the majority of the modern designs of VAWTs have a relatively high solidity in order to increase the torque production and start-up capabilities. The blades, of such high solidity turbines, encounter high AOA and the variable pitch is proven to enhance the turbine overall performance by reducing the local AOA. However, the variable pitch is found to assist in improving the performances of low-

solidity turbines at high TSR by increasing the AOA instead [90]. The different aspects of the design and analysis of the VP-VAWT are discussed in the following subsections.

2.5.1 Types of variable pitch

The control of the variable pitch for turbine blades can be classified to be active or passive control. Both have been investigated to enhance the VAWTs performance. In this section, the criterion used to distinguish between active and passive pitch controls is whether the pitch control could secure a prescribed pitch profile based on specific kinematics or the pitch control is dependent on the aerodynamic and inertial effects. This criterion is in contradiction to the one used to distinguish between the active and passive circulation control that is based on whether external energy is needed in active circulation control or no auxiliary power is required for passive control [91].

2.5.1.1 Active-controlled variable pitch using actuators

The actuated active control requires an energy expenditure or an actuator that changes the blade pitch either in a prescribed base or a reactive controlled manner that alerts the pitch distribution according to the flow conditions. Either of the prescribed active control or reactive control has the advantage of easy implementation of arbitrary pitch profiles. In addition, reactive control could be used to alert the pitch profile to suit the incident flow conditions. However, all actuated active controls need an auxiliary power that then takes from the turbine output power and may affect the overall efficiency of the turbine. Also, the actuated active control of a VAWT needs to continuously alert the angles of the blades with a high pitch rate during the VAWT rotation. This continuous pitch control requires an expensive high-frequency actuator and control circuit that could significantly increase the cost of the system and make it not suitable for small units.

2.5.1.2 Active-controlled variable pitch based on variable pitch mechanisms

The active control, based on the kinematics of certain mechanisms, have the advantage of providing prescribed pitch profiles that only depends on the azimuthal position. However, some of these mechanisms have a sort of control parameters that could be used to alter the pitch profiles to suit different flow conditions. Further discussions of the pitch mechanisms are presented in Section 2.5.2.

2.5.1.3 **Passive controlled variable pitch**

The passive pitch control, also referred to as self-pitch, does not need an auxiliary power or actuator. The blades are attached to some sort of springs and balancing weights that react on the aerodynamic and inertial forces exerted on the blades. However, the blades are free to pitch around a pivot under the combined effect of inertial, centrifugal and aerodynamic forces. Also, the maximum pitch could be restricted by means of stoppers. Due to the dependence on the centrifugal forces, this design suffers from the sensitivity to the rotational speed, and it could not be easily optimised for different operation speeds [92].

2.5.2 **Variable pitch mechanisms**

2.5.2.1 **The double crank four-bar linkage**

The double crank four-bar linkage, also referred to as cycloidal turbine, is considered as the state-of-the-art pitch mechanism [93]. This mechanism has been used in air vehicles but to produce thrust in a simple, reliable and controllable way [93]. The mechanism kinematics is based on the eccentricity between the main rotor rotational point, O and the eccentric rotational point, O_e, as shown in Figure 2.7. While l_m, l_c, and l_s are fixed lengths, the kinematics are controlled by an adjustable eccentric length, l_e and its orientation, θ_p. However, the majority of the researchers fix θ_p *to be zero* and use a fixed value of l_e. The lengths of the links could be selected using the multi-body simulation approach to achieve the desired pitch amplitude [92]. For zero orientation angle, the eccentric link will be parallel to the wind direction. Therefore, it could be attached to a vane that maintains the alignment with the incident wind and acts as a yawing mechanism without the need to yaw the whole turbine [92].

Firdaus et al. [94] carried out a numerical and experimental study on the implementation of the variable pitch using the four-bar mechanism. Their results showed that the reduction in the AOA, using the variable pitch, contributed to enhancing the torque coefficient and hence the turbine performance. This enhancement was obtained in the upwind region in addition to some parts of the downstream region. Xisto et al. [93], [95] performed a study for VP-VAWTs based on the four-bar mechanism. They found that a high amplitude of variable pitch could

enhance the power coefficient at lower TSRs, 0.5< TSR <1.5. Their results showed that the use of a higher number of blades is associated with obtaining a higher torque at low TSRs and therefore better start-up characteristics.

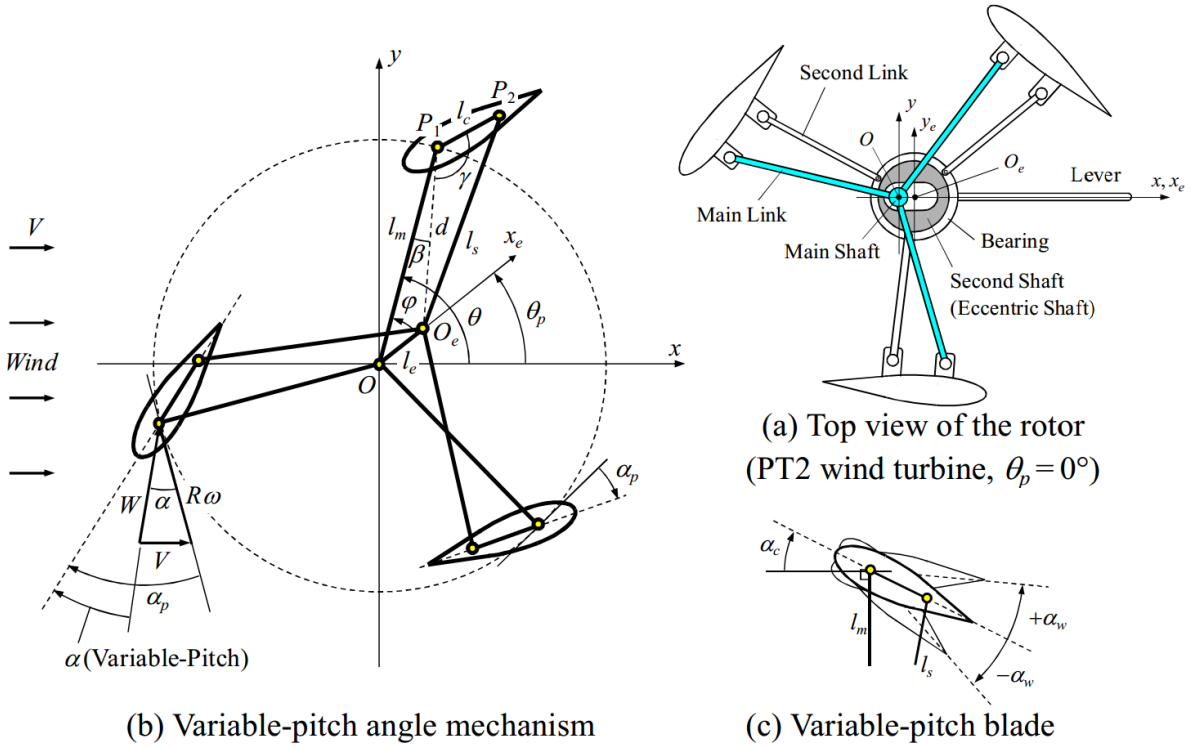

Figure 2.7 Schematic diagram of a double crank four-bar linkage used for variable pitch [96]**.**

The kinematics of the four-bar mechanism with zero time-averaged pitch profile gives an equal maximum pitch amplitude in both of the upstream and downstream parts of the cycle. These kinematics are associated with a strong coupling between the performance in the upstream and downstream parts, as it was reported that the increase of the power extracted in the upstream part is associated with decreasing the power extracted in the downstream part [97]. It was suggested to use more versatile pitch profiles with nonzero time-averaged pitch angle that could offer non-symmetrical pitch angles across the upstream and downstream parts [97]. VP-VAWTs, based on a double crank four-bar linkage, shows a higher power coefficient in contrast with the FP-VAWTs. However, the blade pitch angle is restricted to the cycloidal motion kinematics that could not give the optimal tangential force at each azimuthal position [98].

2.5.2.2 **Cam based mechanisms**

The cooperation between Aerospace Systems, Inc. (ASI) and Pinson Energy Corporation introduced the ASI/Pinson turbine that is one of the earliest variable pitch turbine designs [99]. It used the tilt-cam mechanism to control the blade pitch angle. In addition, the tilt-cam mechanism was capable of reversing the blade pitch to slow down the rotor in high wind speeds [99]. Erickson et al. [100] introduced a reconfigurable cam and control rod to impose a first-order sinusoidal pitch profile as shown in Figure 2.8. The use of this mechanism enables one to control the mean blade pitch, blade pitch amplitude, and phase angle. While the mean pitch is controlled by a control rod, the pitch amplitude is controlled using a set of interchangeable cams. In addition, the phase angle is applied to the cam axis. Their results showed that an improvement of about 35% in the efficiency could be achieved using a sinusoidal pitch. Although their investigation was limited by imposing the first-order sinusoidal pitch, the cam based mechanisms are promising and could be used to impose a more variant pitch profile.

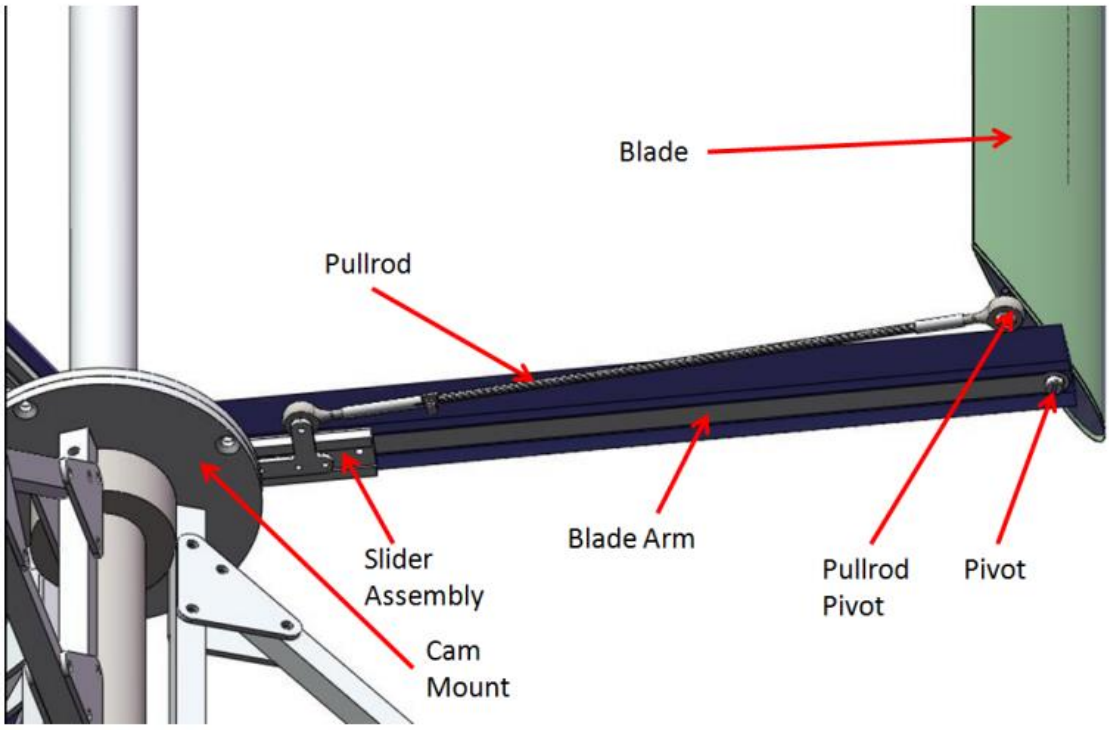

Figure 2.8 Schematic of the cam and control rod mechanism [100].

Kayan [101] utilised two different mechanisms to implement different variable pitch profiles into a vertical axis hydro-turbine. The first mechanism was based on a circular

grooved disk or cam and the second was based on a profiled grooved disk. Figure 2.9 shows the profiled grooved disk that they had used. The eccentricity of the circular disk and the phase angle of the profiled disk were used as control parameters to alter the pitch profile. These results showed the ability of both mechanisms to achieve a self-starting at low flow velocities. However, the mechanism based on the profiled grooved disk showed a significantly higher power coefficient Kayan [101].

Figure 2.9 Photograph of the profiled grooved disk [101]**.**

2.5.2.3 **Continuous uniform blade pitch mechanisms**

Cooper and Kennedy [102] developed a novel concept for VAWTs, called the Wollongong turbine or collective pitch controlled turbine [103], as shown in Figure 2.10. The concept is to rotate each blade continuously about its axis at half the speed of the main rotor axis. Therefore, when the turbine rotor completes one cycle, the blade is pitched by 180° in a continuous uniform pitch speed. This concept requires that the cross-section of the blades to be symmetrical about their axes, such as an elliptical [102], [104] or rectangular [105], [106] cross-section. There are several mechanisms to obtain the continuous blade pitch kinematics, such as: (a) bevel gears [102], (b) spur gears [107], (c) belts and pulleys [103], [106], (d) chain and sprocket [108], [109], etc. In

addition, Diaz and Pinto [110] utilised an electrical actuator to apply the continuous pitching for each individual blade.

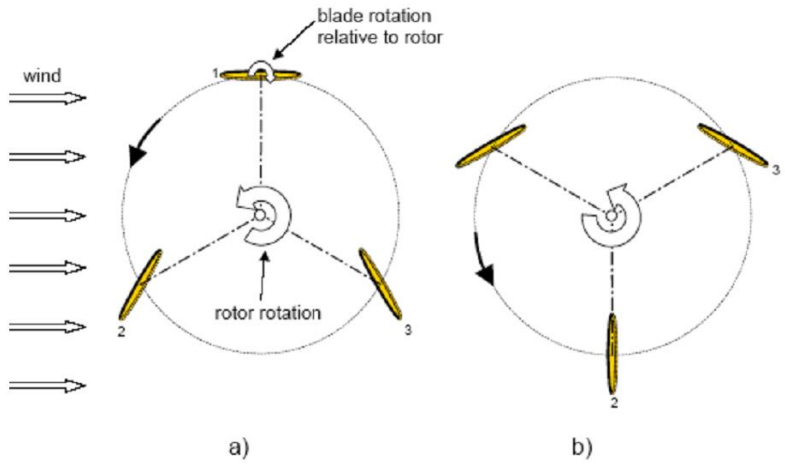

Figure 2.10 Schematic of the kinematics of continuous uniform blade pitch [102].

Zhang et al. [103] found that, for collective pitch control, both solidity and number of blades affected the power coefficient, while the maximum power coefficient for four-bladed configurations could be obtained at a TSR of 0.7. On the other hand, Bayeul-Laine et al. [104], [111] predicted a maximum power coefficient at a TSR of 0.4 for a three-bladed configuration. Their simulation results showed that the Reynolds number has only a small influence on the turbine performance, while the turbine configuration minimises the interactions between a turbine blade and the wake of neighbouring blades. In addition, they reported that a well-chosen staggered angle between the wind direction and the initial reference blade could enhance the performance of the turbine.

The continuous uniform pitching turbine is reported to have a better performance than both the FP-VAWT [104] and the Savonius drag type turbine [105] and this is in addition to increasing the start-up torque by about six times that of the Savonius turbine [105]. Moreover, it is found that the device produced useful power only for low TSRs, < 1 [102].

2.5.2.4 **Actuated active individual pitch control**

An energy expenditure, or an actuator, is required for the active individual control to impose the desired pitch profile. The aim of the individual pitch is to maximise the tangential force of each blade [98] and hence the turbine power. Zhang et al. [112] used a set of servomotors to adjust each individual blade angle. Each blade was connected

to a servomotor by a synchronous belt while the servo motor was controlled to achieve the optimal pitch angles. Liu et al. [113] used a set of stepper motors and worm gears to introduce a real-time variable pitch. Hwang et al. [114] used servomotors to actively control the pitch angle and to implement a set of different pitch profiles for different TSRs. Their experiments suffer from flow unsteadiness due to the use of an artificial wind from a propeller fan. However, their results showed that the individual active control could be used to introduce an optimal pitch for different TSRs, including the start-up operation. Liang et al. [115] implemented both continuous blade pitch and active pitch control using controlled servomotors. It was found that an individual pitch control could achieve an enhanced torque coefficient that is up to 2.5 times that of the FP-VAWT. Active individual pitch control is the most flexible way to apply an arbitrary optimised-pitch profile. However, attention should be given to the precision, as any hysteresis error will affect the pitch profile and hence the overall performance [116].

2.5.2.5 **Passive control variable pitch mechanism**

The passive control of a VAWT blade aims to combine the inertial, centrifugal, and aerodynamic forces in order to achieve a suitable variable pitch profile under the effects of all or some of the following: the inertia of the blade, add inertia from external weights, springs, and motion limiters. Kirke and Lazauskas [117] proposed a passive variable pitch mechanism based on spring and stabiliser mass which has been found to improve the turbine performance. Pawsey [118] suggested a novel passive pitch mechanism that utilises a flexible stem to act as a spring and a motion limiter at the same time as shown in Figure 2.11. This design is found to improve the turbine start-up but it reduces the turbine overall performance. In general, a passive pitch mechanism is not fully controlled and requires extensive iterative tests in order to have a suitable mechanism.

2.5.3 **Variable pitch profiles**

2.5.3.1 **Variable pitch profile based on the cycloidal kinematics**

The cycloidal motion obtained by the four-bar mechanism is controlled by the adjustable eccentric length and its orientation. These control parameters give a variety of cyclic pitch profiles with different amplitudes and offset angles [96], [119]. In addition, the geometric AOA, along the cycle, depends also on the TSR [96]. Xisto et al. [95]

expressed the kinematics of the pitch motion by a set of equations. These equations are rewritten here in order to fit the definition and symbols in Figure 2.7 as follows:

$$\alpha_{\mathrm{p}} = \frac{\pi}{2} - \sin^{-1}\left(\frac{l_e}{a}\cos[\phi + \theta_p]\right) - \cos^{-1}\left(\frac{a^2+l_c^2-l_s^2}{2al_c}\right) \tag{2.1}$$

$$a^2 = l_e^2 + R^2 - 2l_eR\cos\left(\phi + \theta_p + \frac{\pi}{2}\right) \tag{2.2}$$

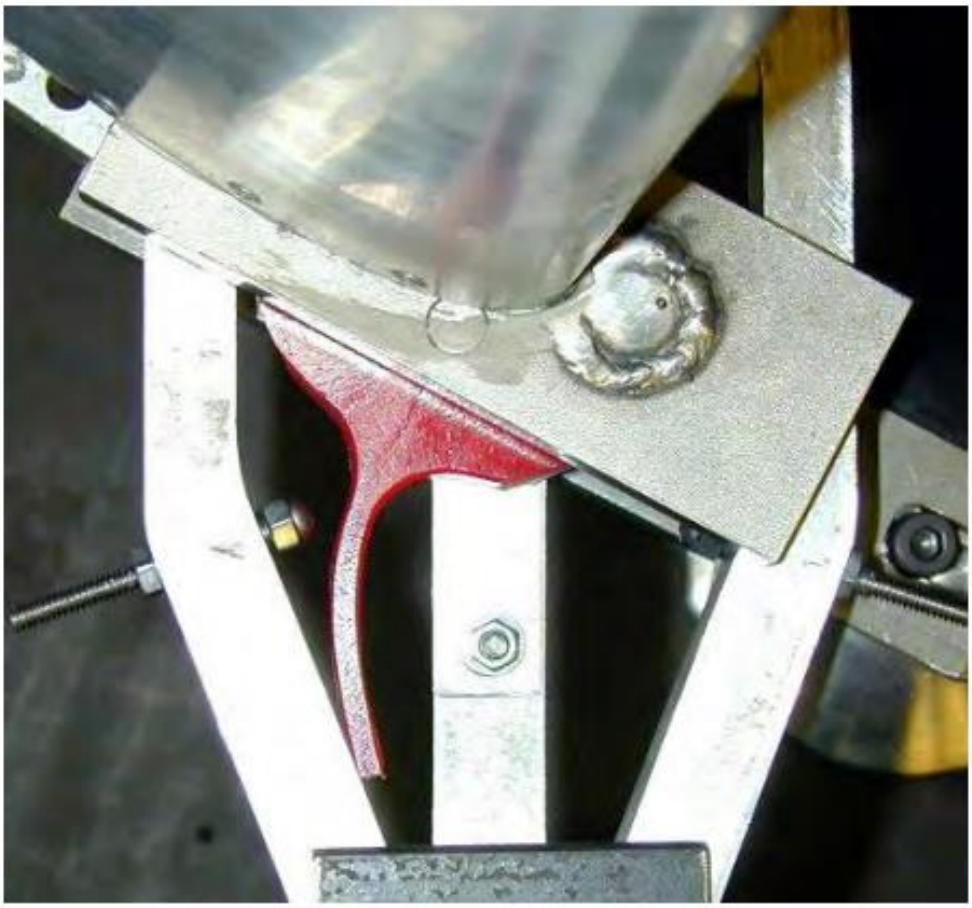

Figure 2.11 A photograph for a passive pitch mechanism based on a flexible stem [118]**.**

2.5.3.2 **Variable pitch profiles based on trigonometric functions**

The first-order sinusoidal pitch was suggested by Erickson et al. [100] and it was achieved using a cam based mechanism. It is found that it achieves about 35% efficiency enhancement, and also it is capable of self-starting. Liu et al. [113] implemented a sinusoidal variable pitch profile with a low angular amplitude, typically 3°. Although this angular amplitude is not expected to be optimal for a low TSR turbine, this result showed a slight improvement in the instantaneous power coefficient in the upstream

region. So far, the sinusoidal and cycloidal motions are the most commonly used variable pitch profiles [120].

Paraschivoiu et al. [121] suggested a polynomial of trigonometric functions for the pitch profile as follows:

$$\boldsymbol{\theta = x_1 \cos \phi + x_2 (\sin \phi)^{X_3}} \tag{2.3}$$

where the coefficients $x_1, x_2,$ and x_3 are to be optimised with a Genetic Algorithm optimiser coupled with an analytical momentum model. The optimised pitch profile increased the calculated annual energy production by about 30 %. However, the improvement in the performance strongly depends on the wind velocity and dynamic stall. Furthermore, Xu et al. [122] propose an optimised variable pitch profile based on a series of sinusoidal functions. Gosselin et al. [123] investigated the performance of VAWTs with a piecewise variable pitch profile based on a proposed trigonometric function. Their results showed an interesting coupling between the energy extraction in the upstream and downstream regions. Thereby, when a high power extraction is achieved upstream, the amount of power that could be extracted from the downstream region is reduced.

2.5.3.3 **Variable pitch profile based on the conditional elimination of high AOA**

Staelens et al. [124] proposed a variable pitch profile in which the pitch motion is applied only if the amplitude of the theoretical AOA exceeds the static stall angle. This eliminates the high AOA region and maintains a constant theoretical AOA over a wide region of the cycle. Zhang et al. [112] implemented this variable pitch profile and they found that the turbine performance is significantly enhanced in the upstream part of the cycle in contrast with the performance of the fixed pitch configuration. However, they did not find improvement in the performance in the downstream part of the cycle. This suggests that it might be appropriate to apply the variable pitch only in the upstream part of the cycle.

Finally, regardless of the implemented variable pitch profile, the static stall angle of the aerofoil is commonly considered as the critical AOA [90], [115], [120], [124]–[126] and this raises the question whether or not the static stall angle is a real measure for the favourable AOA in the design of the VP-VAWT.

2.5.4 **Numerical modelling of variable pitch turbines**

In addition to the experimental procedures on a wind tunnel scale or in field-tests, there are multi-fidelity numerical methods for predicting and analysing the performance of VAWTs. The Double Multiple Streamtube (DMS or DMST) method offers a simple and computationally inexpensive analysis tool. Also, the vortex method also has a relatively moderate computational cost based on potential flow while it can be easily extended to 3D by considering the blade tip vortices. The majority of the Blade Element Momentum (BEM) and the vortex methods neglect the viscous effects while being highly dependent on the implementation of the stall models [127]. CFD is considered to some extent the highest-fidelity analysis tool that is widely used for VAWT modelling. On the other hand, CFD has a relatively higher computational cost. Further discussions of the implementations, strengths, and weaknesses of these methods are presented in the following sub-sections.

2.5.4.1 **Double Multiple Streamtube model**

The DMST model is basically a momentum model that integrates both the momentum theory and blade element theory. As a development of the single streamtube model, in which the whole turbine is enclosed by a single stream tube, the multiple streamtube models involves several adjacent streamtubes. Each tube has its incidence velocity and induction factor. The idea of the DMST is a further development of the multiple streamtube models in which the actuator disk is modelled twice in order to represent the upstream and downstream path of the blades [128].

Soraghan et al. [129] developed one of the most comprehensive DMST models, named StrathDMS, that features an interception method for the induction factor calculations. This model includes a tip loss correction, based on the Prandtl's tip loss factor, along with an empirical dynamic stall adoption. In addition, the effect of the stream tube expansion and flow curvature have been adopted. The results of StrathDMS have been emphasised against two sets of real experimental data and shows good assessments of the turbine performance. Rathi [130] developed a graphical output function into MATLAB based on the DMST model. The graphical output enables the visualisation of the lift and drag directions and amplitude along the cycle that could explicitly show how the variable pitch could improve the local aerodynamic forces. On the other hand,

DMST is reported to have achieved a good prediction for low solidity turbines, while it has a poor prediction for high solidity turbines [128].

Chougule et al. [131] performed a DMST numerical investigation on the performance of the double aerofoil configuration in variable pitch VAWTs. The double aerofoil consisted of the slat and the main aerofoil. Their results showed that the implementation of the variable pitch in the double blade configuration could achieve about 20% improvement in the power coefficient.

2.5.4.2 **Vortex method**

The vortex model is based on potential flow in which the vortex sheet segment is tracked in the wake region using a Lagrangian approach. In addition, the vortex method includes the viscous effect in the vicinity of the blade and its wake [132]. The vortex method can handle more complex geometries in contrast with the blade element or momentum models but, of course, with more complexity and computational cost [118]. Pawsey [118] developed a vortex model to account for the passive variable pitch. His predictions based on both the vortex model and the momentum model showed good agreements with the experimental data. Moreover, the vortex method was able to handle the turbulent wind which the momentum methods could not consider [118].

2.5.4.3 **Computational Fluid Dynamics**

CFD offers a high fidelity along with a deep insight into the flow around VAWTs. Straight-bladed VAWT can be modelled using both 2D and 3D CFD simulations. The 2D CFD modelling is reported to be relatively accurate [105] and to require a moderate computational cost. However, the 2D CFD modelling of VAWTs cannot render the drag in the connecting rods and pitching mechanism and this cannot be neglected at high TSRs. In addition, VAWTs with low Aspect Ratio (AR) blades suffers from a high percentage of blade tip losses, and therefore it cannot be treated in 2D modelling [133]. The following subsections shed more light on the literature of VP-VAWT research in terms of the modelling of the variable pitch motion and the effects of turbulence modelling.

2.5.4.3.1 Mesh motion approaches

The sliding mesh method is found to be effectively suitable for VP-VAWT simulations [27]. This approach is widely used for simulating the VAWTs in both 2D [93], [103], [105], [115] and 3D [133] analyses. In this method, the computational domain is divided into several subdomains while using circular sliding mesh interfaces around each blade as well as around the rotor. The CFD solver rotates the rotor subdomain to account for the turbine rotation and rotates the blade subdomain to account for the blade pitch. Figure 2.12 shows a typical mesh with several subdomains and sliding interfaces.

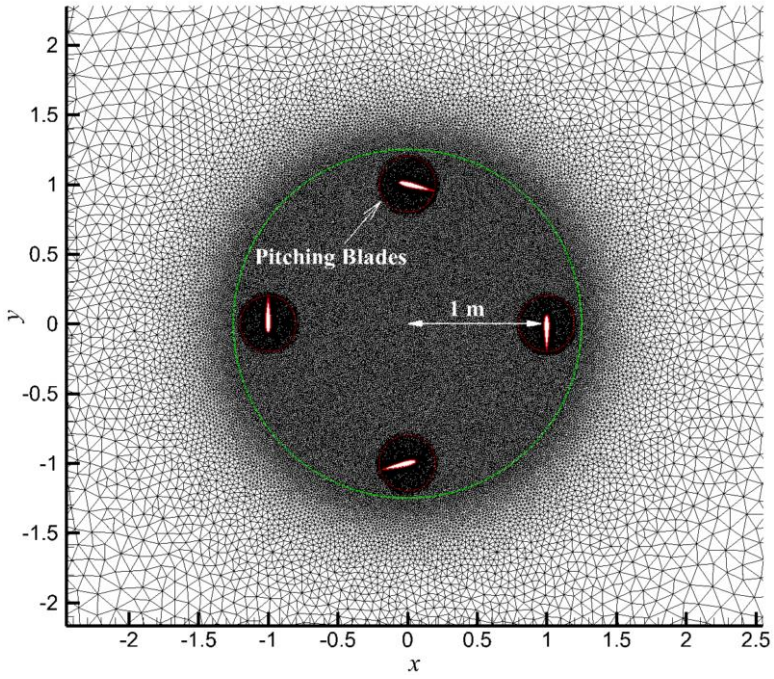

Figure 2.12 A typical computational mesh with several sub-domains and sliding mesh interfaces [93]**.**

Paillard et al. [134], [135] implemented a mixed rotation and deformation meshing approach to simulate a variable pitch vertical axis tidal turbine using the CFX-Solver. The sliding mesh was used to implement the rotation of the main rotor while using mesh deformation to account for the blades pitch motion. They used a structure-shaped mesh that was deformed by the solver in each time step according to the blades pitch motion as shown in Figure 2.13. However, this approach appears to be limited to low pitch amplitude due to the limitations of mesh deformation.

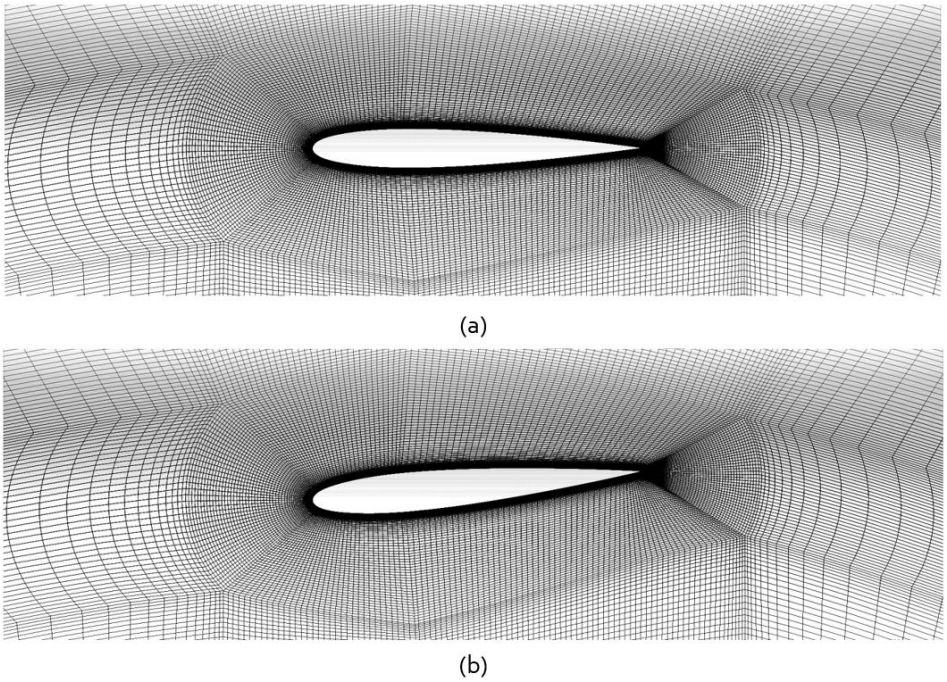

Figure 2.13 A structured mesh near the turbine blade (a) without and (b) with mesh deformation [134]**.**

Another meshing methodology is to simulate both the blade pitch and the turbine rotation using the overset meshing approach [97], [136]. Benedict et al. [97] simulated the VP-VAWT using an overset solver based on RANS equations, known as OVERTURNS. This solver features the overset meshing capability and was successfully used to represent the VP-VAWT using a 2D-overset structured mesh as shown in Figure 2.14. Their overset mesh topology combined a C-type mesh around each blade and a background O-type mesh to represent the flow domain away from the blades. The connectivity between the different parts of the mesh is obtained using an implicit approach, referred to as the hole cutting method [97].

Although the overset meshing offers a robust and a unique approach to obtaining a structure-shaped mesh of the domain, currently it is not well-developed on most of the commercial and open-source CFD solvers. However, some new releases of CFD solvers start to offer the overset mesh capabilities, namely ANSYS FLUENT [137], STAR-CCM+ [138]. In conclusion, the sliding mesh method is the most robust and widely employed method for the modelling of the variable pitch motion in the CFD simulations of VP-VAWTs.

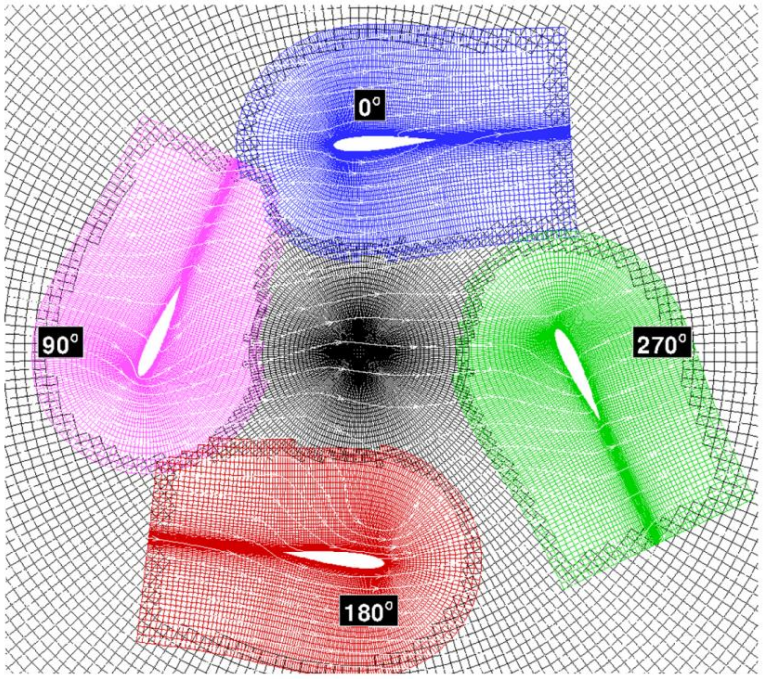

Figure 2.14 A typical overset meshing topology [97].

2.5.4.3.2 Turbulence modelling

Paillard et al. [135] studied the effect of three different viscous models in their CFD modelling of VP-VAWT. Their investigation includes the laminar model, SST k-ω turbulence model, and SST transition model. They found that the laminar model is associated with high oscillations and early stall predictions, and therefore it was concluded that the use of the laminar model was not suitable for their simulations. On the other hand, their simulations using the transition model showed some contradictory results, since the transition model results were associated with deeper stall and large recirculation zones. Moreover, they found that the transition model over-predicts the stall induced separation. They expected that either the inlet turbulence level needs to be adjusted or the transition model is not suitable for their cases. However, their results showed that the non-transition model, namely SST k-ω, could give good agreement with the experimental data. Firdaus et al. [94] performed a 2D-CFD study of the VP-VAWT that included the effect of different turbulence models, including RNG k-ε, Realizable k-ε, and SST k-ω. Their RNG k-ε results tended to have a better agreement with the experimental data in contrast with the other investigated turbulence models. However, all the models appeared to significantly over predict the turbine performance due to ignoring the three-dimensionality of the flow.

In contrast with the above-mentioned investigations of the turbulence models effects on the predictions of VP-VAWT, more extensive studies have been carried out for the FP-VAWT. Howell et al. [139] compared both 2D and 3D CFD predictions of the power curve against the experimental data at low Reynolds number, as low as 30,000, based on the RNG k–ε turbulence model. The geometry of the straight blade Darrieus VAWT is symmetrical about its mid-span section and hence the use of symmetric boundary conditions enables the modelling of only one-half of the geometry in order to reduce the computational cost without sacrificing the accuracy for 3D simulations [139]. Their results showed that the 2D predictions of the power coefficient are significantly over-estimated while the 3D predictions had a good agreement with the experimental data in both trend and magnitude. However, the 3D predictions of the power coefficient showed some under-estimations in contrast with the experimental data at relatively high TSRs.

Siddiqui et al. [140] quantified the differences in the predictions of the 2D and 3D CFD simulations with and without the consideration of the supporting structure based on the Realizable k-ε model. They found that the 2D results had an over-prediction by about 32% in the overall performance coefficient in contrast with the 3D simulations that resolved the supporting structure and tip losses. Franchina et al. [141] compared the 2D and 3D predictions of the velocity magnitude and turbulence intensity in the VAWT wake based on the SST k-ω with low Reynolds number correlations against the experimental data. They considered the use of a transitional turbulence model beyond the scope of their investigation. Their 2D results showed a clear overestimation of the velocity in the wake region. While there are few comparative studies between the 2D and 3D predictions, almost each of these studies uses a specific turbulence model based on either its reputation or based on a recommendation from previous 2D studies. Hence, there is a lack of the assessment of how the quality of the turbulence models' predictions are different between the 2D and 3D cases.

Daróczy et al. [142] carried out a 2D comparative CFD study based on six different turbulence models against four sets of experimental data. However, all these experimental data sets are limited to the power coefficient variations with the TSR. They found that the results of the k-ε Realizable model have consistence agreements with the four experimental data, while the results of the SST k-ω model did not match

well with one of the four sets of experimental data. They suggested that further 3D assessments are needed before the final selection of the suitable turbulence model. Several studies compare the suitability of the different turbulence model for vertical axis water turbines [143]–[146] and they obtained different conclusions about the most appropriate turbulence model for the vertical axis water turbine simulation.

Almohammadi et al. [147] compared the 2D CFD predictions based on the SST k-ω and the SST transition turbulence model. They concluded that the transitional effect is essential for the prediction of the dynamic stall. However, their conclusion is based on the interpretation of the differences between the numerical results rather than a comparison with detailed experimental data. Rezaeiha et al. [148] presented a critical 2D CFD comparison of seven commonly-used turbulence models mainly against the experimental data of the strength of the circulation of the vortex, time-averaged streamwise velocity in the wake region and the power coefficient over TSR. They concluded that the SST k-ω model and its transitional variants are most suitable for unsteady Reynolds-Averaged Navier-Stokes (uRANS) simulations. These transitional variants includes the three-equations SST k-ω with the γ transition turbulence model and the four-equations SST transition model. However, according to ANSYS [167], the SST transition model is not recommended for the domains with moving walls.

It is noticed that the majority of the turbulence model comparisons are based on the experimental data of the cycle-averaged power coefficient at different TSR. However, the cycle-averaged power coefficient is an integral quantity that may involve counteracting terms that affect the conclusion. Therefore, the use of more detailed experimental data will assist to have a better assessment of the quality of the turbulence models' predictions. It can be concluded that the SST k-ω model and the SST k-ω with the γ transition turbulence model are appropriate for the turbulence modelling of VAWTs based on the uRANS equations.

2.5.4.3.3 Scale-Resolving Simulation

The majority of the CFD research on VAWT are based on RANS turbulence models. However, some investigations, mainly for FP-VAWT, were carried out using several Scale-Resolving Simulation (SRS) models that aim to resolve the whole or a part of the turbulence spectrum at least outside the wall boundary layer [149]. This includes the

Large Eddy Simulation (LES) [133], Wall-Modelled Large Eddy Simulation (WM-LES) [150], Scale Adaptive Simulations (SAS) [151], [152], Detached Eddy Simulations (DES) [153], Delayed Detached Eddy Simulations (DDES) [154], Improved Delayed Detached Eddy Simulations (IDDES) [155], [156], and Stress-Blended Eddy Simulation (SBES) [152], [157]. There is a lack of comprehensive comparative studies with different SRS models that would analyse the differences between their predictions and their computational costs in order to define the most appropriate SRS model for VAWT simulations. However, in general, the SBES model is currently recommended due to its advantages in contrast with the other SRS models [149], [158].

The LES simulations are very computationally expensive and only applicable to 3D simulations. Hence, it is extremely difficult to rely on the LES for optimisation and extensive parametric studies. In contrast with the LES, the other SRS models are compatible with 2D simulations. However, the other SRS models are more computationally demanding, in contrast with RANS turbulence models. While the LES, DES, and DDES suffer from Grid Induced Separation (GIS), the recently introduced SBES assists in eliminating the GIS problem [157]. All the SRS, except LES, relay on the RANS turbulence models in the wall boundary layers while implementing LES-like approaches for the free shear flows away from walls [149], [158]. Therefore, the selection of the underlying RANS turbulence model is observed to have some influence on the predictions of the different SRS models [159]. While the current study focuses on the implementation of RANS turbulence models, it is recommended to carry out a comprehensive comparative study between the predictions of SRS models and RANS models against detailed experimental data, especially when focusing on the wind turbine wake and blade wake interactions.

2.5.4.3.4 Summary of the numerical methods

Table 2.1 shows a tabulated literature review of the research that have included numerical modelling methods for VP-VAWT with different fidelity. Comments on their merits and demerits are included.

Table 2.1 Tabulated literature review of the numerical modelling of VP-VAWTs.

No.	Authors	Features	Merits	Demerits
1	*Woods et al.* [160] *Zhang et al.* [106]	Low-order model equivalent to single streamtube model	The fast execution time of the code	Low order computational model
2	*Abdelkader and Abdelmawla* [128], [161] *Chougule and Nielsen* [92] *Chougule et al.* [131] *Farthing* [162] *Paraschivoiu et al.* [121] *Rathi* [130] *Soraghan et al.* [129] *Staelens et al.* [124] *Zhaoet al.* [120]	Double Multiple Streamtube	The fast execution time of the code	-Inviscid Momentum Model -miscalculates the AOA in upwind stroke and mispredict of dynamic stall - highly dependent on the implementation of the stall models
3	*Erickson et al.* [100]	2D hybrid dynamic vortex and BEM	Low computational cost	Could not account for the dynamic stall and is not suitable for high solidity or low TSR
4	*Horb et al.* [163] *Pawsey* [118] *Zhao et al.* [132]	Vortex method	-Low computational cost -Could be extended to 3D	Usually depends on inhouse codes and the quality of the predictions depends on the assumption in the code.
5	*Bayeul-Laine et al.* [104], [111], [164] *Benedict et al.* [97] *Cheng et al.* [165] *Firdaus* [109] *Firdaus et al.* [94], [166] *Hwang et al.*[114] *Liang et al.* [115] *Li-xun et al.* [116] *Mao et al.* [105] *Paillard et al.* [135] *Sagharichi et al.* [167] *Shrivastava* [98] *Xisto et al.* [93], [95] *Yao and Yang* [27] *Zhang et al.* [112], [103]	2D CFD Unsteady Reynolds-averaged Navier–Stokes (uRANS)	Moderate computational cost	Exclude the 3D effects and limited to high Aspect Ratio (AR)
6	*Gosselin et al.* [123]	3D RANS CFD	High fidelity	Higher computational cost
7	*Elkhoury M et al.* [133]	3D CFD large eddy simulation (LES)	Highest fidelity	Highest computational cost

2.5.5 **Experimental investigations and prototyping of VP-VAWTs**

In order to investigate the performance of VP-VAWTs at different TSRs and flow conditions both the flow driven [97], [100], [109], [168], [169] and the motor-driven configurations [96], [119] were used. In the motor-driven configuration, the turbine is mounted to a driving motor, while the rotational speed of the turbine is prescribed by controlling the motor speed. In the flow-driven configuration, the turbine is allowed to spin by the incoming flow, while the rotational speed is controlled by means of a mechanical, magnetic or electrical load. Araya and Dabriri [170] compared the near wake characteristics of a fixed pitch hydro-turbine with the two driving configurations. Their results showed that, in some circumstance, the flow driven test rig may not be able to accelerate to some extent to achieve a certain TSR due to the resonance in the mechanism [97].

More in-depth attention should be paid to the parasitic power dissipated on the drag resistance of the pitch mechanism's linkage and the component of the supporting strut. Benedict et al. [97] reported that the parasitic losses were significant in their experimental tests.

Several experimental investigations have been carried for VP-VAWTs in open jet wind tunnels [96], [97], [115], [119], [168], closed-circuit wind tunnels [100], [109], [169], and field tests [102], [166]. The closed test section wind tunnel experiments suffer from the effect of blockage [100]. However, Battisti et al. [171] studied the effect of blockage around an FP-VAWT in both open and closed test sections. Their assessment of several theoretical models for the blockage corrections showed that these models were not able to correctly estimate the effect of blockage.

A brief review of the experimental investigations that are available in the literature is shown in Table 2.2. These investigations are compared according to the implemented variable pitch mechanism, the wind tunnel type, and the driving configuration. Currently, most of VP-VAWTs prototypes were not commercialised. However, a British company, called Vertogen, is currently seeking to commercialise its prototype [172].

Table 2.2 Tabulated literature review of the experimental investigations (* denotes that the value is converted to SI units).

No.	Authors	Pitch Control Mechanism	Experimental Setup
1	*Erickson et al.* [100]	Reconfigurable cam and control rod mechanism	Flow-driven rotor in MIT's Wright Brothers Wind Tunnel
2	*Cooper and Kennedy* [102]	Continuous uniform pitch mechanism	Field test
3	*Firdaus* [109]		Flow-driven rotor in Closed-circuit wind tunnel A= 1.25×1.25 m^2
4	*Hwang et al.* [166]	Servo motor controlled four-bar-linkage	Field test
5	*Benedict et al.* [97]	Four-bar-linkage	Flow-driven rotor in Open-circuit wind tunnel A=0.56×0.56* m^2
6	*Kiwata et al.* [96]		Motor-driven rotor in Open-circuit wind tunnel A= 1.2×1.2 m2 + Field test at no load
7	*Mills et al.* [168]		Flow-driven rotor in Open-circuit wind tunnel A=0.56×0.56* m^3
8	*Yamada et al.* [119]		Motor-driven rotor in Open-circuit wind tunnel A= 1.2×1.2 m^2
9	*Liang et al.* [115]	Individual active pitch control using servo motor	Simple axial flow fans as an open jet wind tunnel A= 2×2 m^2
10	*Kirke and Lazauskas* [169]	Passive pitch based on aerodynamic and inertial forces	Flow-driven rotor in Closed-circuit wind tunnel A= 2×3 m^2
11	*Kirke and Paillard* [173]	Four-bar-linkage	Truck-mounted prototype in a field test

2.5.6 **Variable pitch water current turbines**

The use of the vertical axis turbine concept for tidal currents has the advantages of omnidirectionality in addition to keeping the gearbox and the generator above the water surface. The implementation of variable pitch on vertical axis water current turbines was reported to achieve an improvement of up to 20% in the power coefficient [101]. The hydro-turbines, with either active pitch control [101] or passive

pitch control [174], were found to be capable of self-starting due to the good starting torque. The good start-up capability eliminates the need for start-up devices and overcomes the typical start-up problem in the fixed pitch counterpart [174].

2.6 Optimisation

As mentioned in Section 2.3, there are several studies that aimed to optimise new aerofoils specifically designed for VAWT [52]–[56]. These studies [52]–[56] utilised the Genetic Algorithm to optimise the aerofoil shape for the VAWT. The Genetic Algorithm is found to be highly effective and robust in addition to being simple to be implemented [54]. However, the Genetic Algorithm is oriented to finding the optimal design and can not provide a clear idea of the effect of the different geometric aspects on the performance.

Several studies have been carried out to optimise the variable pitch profile for VAWT. Paraschivoiu et al. [121] used a genetic algorithm optimiser based on a DMST model to optimise the variable pitch profile. They predicted that 30% improvement in the annual energy production could be achieved using the optimised pitch profile. Kozak [87] implemented a brute-force procedure to optimise the variable pitch profile based on a DMST model. Furthermore, Hwang et al. [34] used the genetic algorithm to optimise the variable pitch profile for a Vertical Axis Water Turbine based on CFD simulations.

It is noticed that the majority of the optimisation studies, that are related to FP-VAWTs, focused on optimising the blade profiles. When considering the TSR, solidity, and fixed pitch angle as the most influential parameters on the VAWT performance, there is a lack of studies that focus on the effects of these important design parameters in the optimisation of FP-VAWTs. On the other hand, the majority of the optimisation studies, that are related to FP-VAWTs, are based on direct optimisation using the Genetic Algorithm. However, the use of optimisations based on a metamodel, i.e. surrogate model, such as the Response Surface Methodology [175], is expected to be effective in the design optimisation of FP-VAWTs in addition to providing a deep insight into the effects of the different design parameters on the performance of FP-VAWTs.

2.7 **Flow physics**

VAWTs rely on the aerofoil-profiled blade in producing the driving torque. Hence, the understanding of the aerofoil performance is crucial for the understanding of VAWT performance. The main performance parameters of an aerofoil are the lift and drag coefficients which represent the dimensionless form of the lift and drag forces respectively, as defined before in Section 1.4. In some applications, the moment coefficient about the aerofoil aerodynamic centre is considered. In the static condition, the lift and drag coefficients depend mainly on the aerofoil shape, the AOA and Reynolds number. In the static conditions, the lift coefficient is generally increased with the AOA until the critical AOA at which the lift coefficient starts to decrease dramatically. This decrease in the lift coefficient is referred to as stall and the corresponding critical AOA is referred to as the static stall angle. However, the lift and drag coefficients for an aerofoil that undergoes a dynamic pitch motion are different from the corresponding static values. The behaviour of the aerofoil in the dynamic motion depends on the Reynolds number, the pitch frequency, and the pitch profile.

Figure 2.15 shows comparisons of the lift, drag, and moment coefficients under the static and dynamic conditions, illustrating both the static and dynamic stall. In contrast with the static condition, it is clear how the behaviour of the aerodynamic coefficients in the dynamic condition is different, especially when the AOA exceeds the static stall angle in the upstroke at stage No. 1. Between stages 1 and 2, a vortex starts to appear near the leading edge, as illustrated in the vorticity contours, and this leads to a reduction in the pressure on the suction side and hence an increase in the lift coefficient in contrast with the static case. Between stages 2 and 3, the vortices increase in the size and convect in the downstream direction and this leads to a further increase in the lift coefficient. However, this is associated with increasing drag coefficient. It is noticed that the moment stall appears between stage 2 and 3 as the vortices move near the trailing edge.

Stage 3 represents the maximum dynamic lift coefficient. By increasing the AOA further, the lift stall occurs as the vortices detach from the suction surface between stages 3 and 4. If the AOA is increased further, loads suffer from chaotic fluctuations due to the vortex shedding between stages 4 and 5. By reaching the maximum AOA at

the end of the upstroke, the aerofoil undergoes a pitch down motion that reduces the AOA along the downstroke.

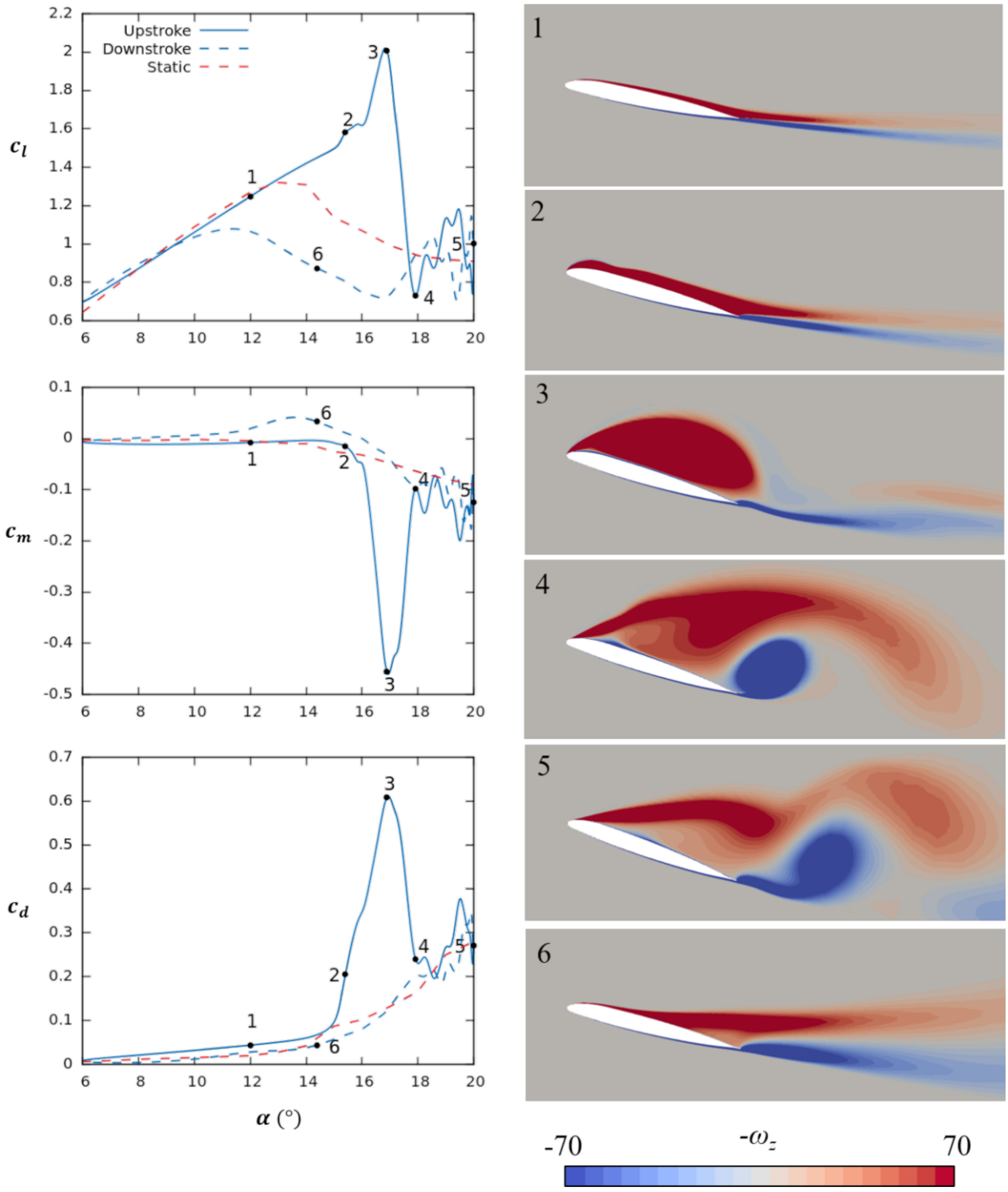

Figure 2.15 A comparisons between the lift, drag, and moment coefficients under the static and dynamic conditions, illustrating both the static and dynamic stall for the OA209 airfoil at a Reynolds number of 1.15 × 10^6 and a reduced frequency of 0.05. In addition, the vorticity contours are presented at the different stages of the dynamic pitch motion [176].

In the downstroke, the aerofoil encounters a deep stall condition with a reduced lift coefficient until the AOA is reduced enough to allow for the reattachment of the flow near the leading edge at stage 6. The reattachment process continues with decreasing the AOA and the cyclic motion is repeated once the AOA reaches its minimum value. Further details about the stages of the dynamic stall are available in [176], [177].

The rotor of a straight-bladed VAWT has a finite aspect ratio and includes a number of finite blades. Figure 2.16 shows an illustration of a finite blade. Due to the difference in the pressure between the suction side (low-pressure side) and the pressure side (high-pressure side) near the tips of the finite blade, the so-called tip vortices are formed as the flow escape from the high-pressure side to the low-pressure side as shown in Figure 2.16. Wang and Zhao [178] investigated the behaviour of the finite blade under the dynamic stall conditions. Based on their simulations, Figure 2.17 shows the isosurfaces of the vorticity magnitude around the finite blade at different AOA. It is observed that the dynamic stall vortices are more intensive near the mid-section of the blade and that the stall effect is reduced near the tip. Wang and Zhao suggested that this behaviour may be due to the reduction in the pressure difference between the sides of the blade near the tips due to the tip vortices [178]. It is concluded that the tip vortices have an effect in alleviating the stall near the blade tips. However, the tip vortices reduce the blade performance and it is suggested reducing the tip vortices by means of tip device, such as winglets [78], [79] and endplates [28], [78].

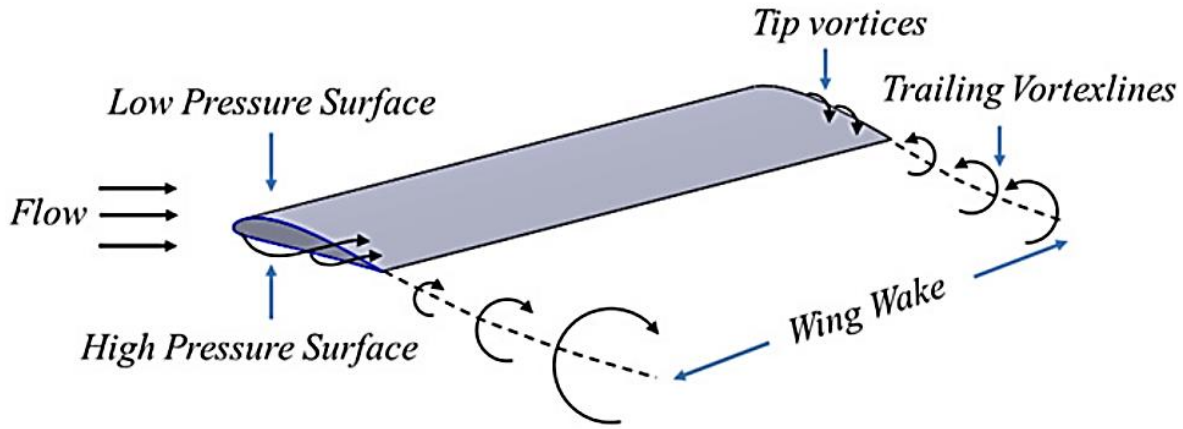

Figure 2.16 An illustration of the tip vortices near the tips of a finite blade [179]**.**

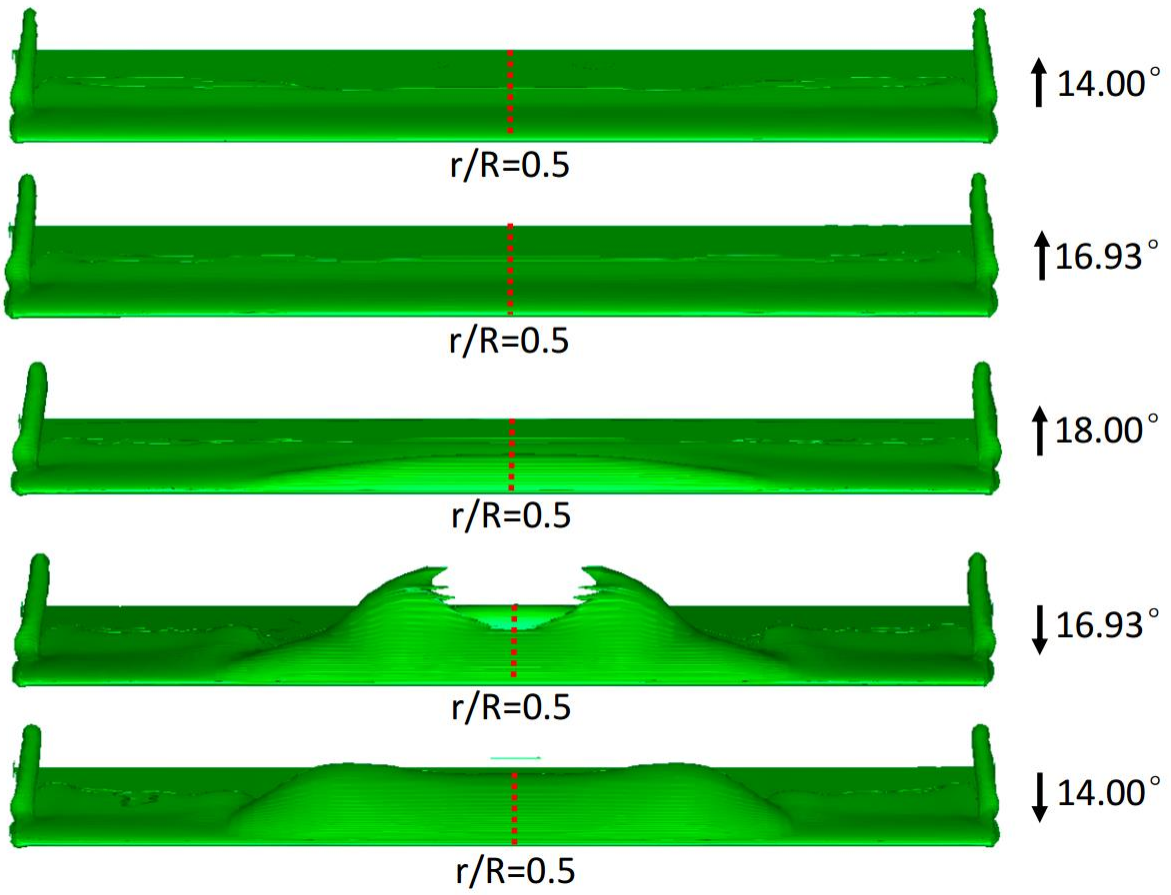

Figure 2.17 The isosurfaces of the vorticity magnitude around a finite blade at different AOA under a harmonic pitch motion. The upwards arrow ↑ denotes the angle in the upstroke, while the downward arrow ↓ denotes the angle in the downstroke [178]**.**

2.8 Challenges, gaps, and potential future work

Based on the critical discussions in the introduction and the literature review, the following the challenges, gaps, and potential future work are revealed and some of them are intended to be covered in this thesis:

- In order to design a VAWT for the future, several challenges should be tackled. Due to the challenging wind potential, it is essential to design future turbines to operate at relatively low wind speeds. In addition, the power coefficient of VAWTs, that is currently behind that of HAWT, needs to be enhanced in order to maximise the power output from the VAWT for a certain swept area and hence increase the feasibility of the utilisation of the VAWT concept.

- While the majority of the investigations in the literature rely on time-averaged quantities to validate the numerical models, it is crucial to assess the numerical predictions against detailed experimental instantaneous data.
- The AOA of the flow in the vicinity of VAWT blade has a significant influence on the overall performance of the VAWT. However, the available methods for the estimation of the AOA are either inaccurate or require extensive post-processing. Therefore, there is a need to develop accurate and robust methods for the estimation of the AOA for VAWTs.
- The majority of the optimisation studies related to VAWTs aims to optimise the aerofoil shape of the blades. However, there is a lack of research in the optimisation of the important geometric and kinematic aspects of the rotor, such as the TSR, solidity, and fixed pitch angle.
- The current understanding of the favourable AOA for a VP-VAWT is not clear and there are several studies that rely on the static stall angle as an indication for the favourable AOA. It is viable to investigate the influence of the targeted favourable AOA on the performance of VP-VAWT under different variable pitch scenarios.
- There is a lack of knowledge regarding the power required to implement the pitch motion, and hence it is important to quantify these power requirements. Several aspects affect this power requirement and this includes the power required to overcome the aerodynamic forces in addition to the power required to overcome the friction and inertia of the pitch mechanism. However, the power required to overcome the friction and inertia is subjected to the structural design aspect of the VP-VAWT.
- While the implementation of winglet at the blade tips is found to improve the turbine performance, there is a need for an assessment of the effect of the winglet on the performance of VAWTs at different aspect ratios.
- It is essential to design the variable pitch mechanisms to be less bulky to avoid the high parasitic losses that were found in some of the existing mechanisms due to the drag effects.

- Finally, the low-speed VAWT is subjected to lower aerodynamic loads and hence needs to be lighter and less sturdy and hence could be built to be more economical. This needs a new special structural design.

In conclusion, the above-mentioned gaps show some insufficiency in the current understanding of the aerodynamics and the effect of some aspects of blade pitch on the VAWT performance. In addition, these gaps shed more light on some insufficiencies in the modelling and design approaches for VAWT. As clarified in Section 1.5, the main aim of this thesis is to provide an in-depth understanding of the aerodynamics and the effect of blade pitch of small VAWTs in order to improve the performance of the turbine at low wind speed conditions. In order to fulfil the aerodynamic-related gaps, this thesis, as outlined in Section 1.6, provides an improved optimal design of VAWTs at low wind speeds based on design exploration and optimisation algorithms. In addition, it relies on detailed experimental instantaneous data for the validation of the computational model while providing a comprehensive verification study for the different numerical aspects of the computational model. Furthermore, a novel method for the accurate estimation of the AOA is presented. In order to gain a better in-depth understanding of the VAWT performance, a novel procedure for the analysis of VAWT performance is proposed based on the interception of the aerodynamic performance characteristics of the aerofoil-shaped blades. In addition, the effects of the different aspects of the fixed and variable pitch design on the VAWT performance are investigated.

3 METHODOLOGY

3.1 Overview

This chapter discusses the different methods that have been used for the modelling of VAWTs in the literature. Moreover, it sheds more light on the principles of Computational Fluid Dynamics (CFD), which is selected as a modelling methodology in this thesis. The concept of turbulence modelling and the basic turbulence models are briefly summarised. In addition, the different design approaches are discussed while the principles of the optimisation approach are clarified. The aim of this chapter is to outline the principles of the overall methodologies that have been implemented in order to meet the main aim and objectives of this thesis. However, the details of the implemented modelling and optimisation methodologies are clarified in more depth in Chapters 4 and 7, respectively.

In order to achieve the aims and objectives in Section 1.5, several methodologies are implemented. Firstly the CFD modelling methodology is implemented to construct a validated and numerically verified computational model that represents the two-bladed turbine presented by Li et al. [97]. The same CFD modelling methodology is applied to the other parts of the thesis. Due to the high torque ripple and poor start-up behaviour of the two-bladed configuration, it is decided to design a three-bladed fixed pitch configuration. In order to improve the performance of the new three-bladed fixed pitch configuration, the optimisation approached is implemented. The design optimisation method is used to indicate the optimal three-bladed fixed pitch configuration. In order to improve the performance further, a parametric study is then carried out to investigate the different aspects of the variable pitch design in order to identify the best variable pitch configuration. The optimal winglet design, that was optimised by Zhang et al. [79], is adopted for both the optimal fixed pitch configuration and the best variable pitch configuration in order to quantify the effect of the winglet on the performance at different aspect ratios. Figure 3.1 shows a schematic of the workflow and methodologies that are implemented to achieve the intended objectives.

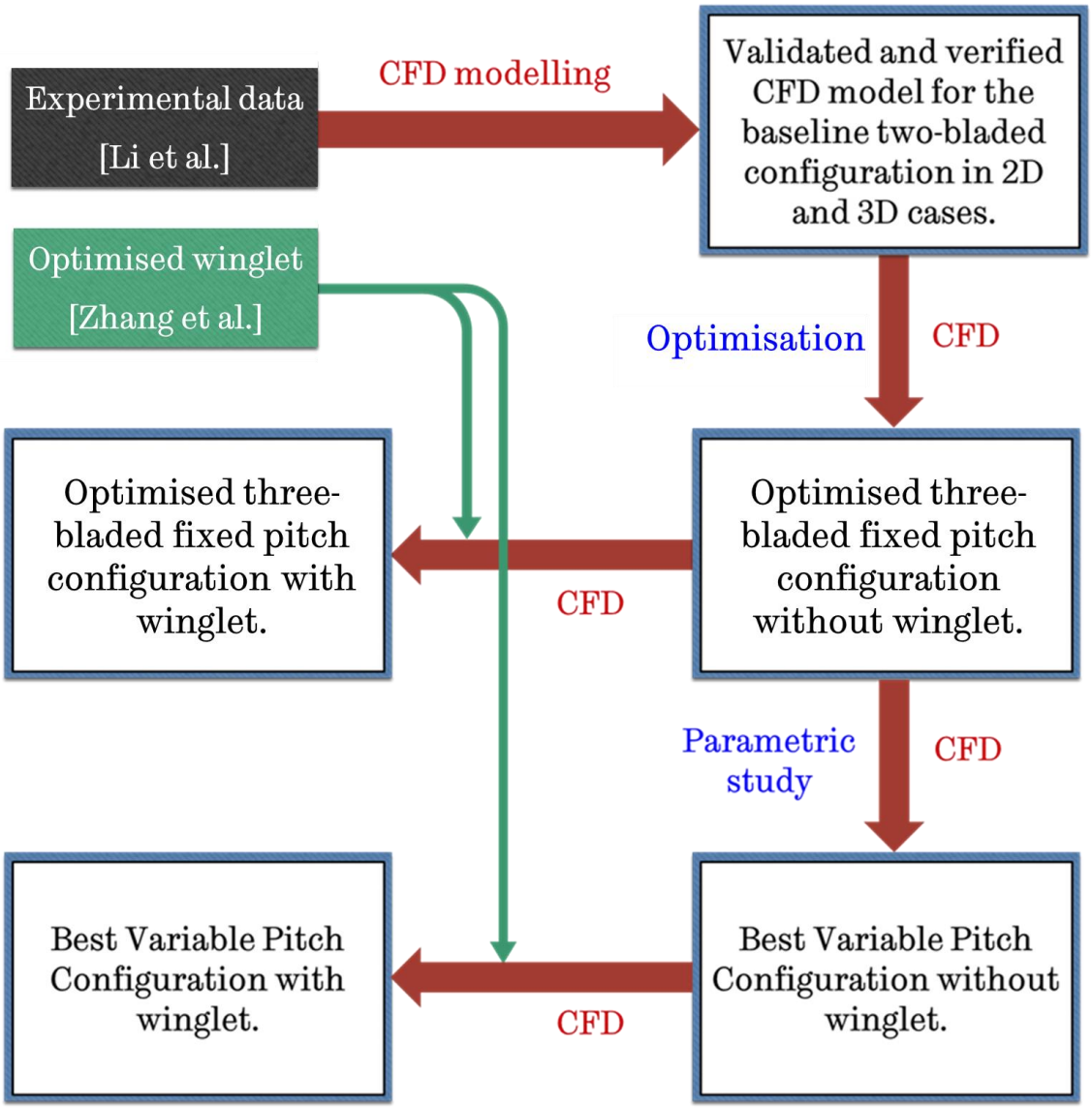

Figure 3.1 A schematic of the workflow and the implemented methodologies. More details about the experimental data and the optimised winglet are available in the work carried out by Li et al. [180] **and Zhang et al.** [79]**, respectively.**

3.2 Modelling approaches

In addition to the experimental modelling in both wind tunnels and open field tests, a range of other numerical modelling approaches with different fidelity has also been used to predict the performance of VAWTs. This includes the Double Multiple Stream Tube (DMST) [129], [181]–[183] and the vortex method [184]–[187]. In addition, Computational Fluid Dynamics (CFD) has been frequently used for turbine flow analysis and optimisation [17]–[19]. CFD has been found to be a powerful tool for the analysis, design, and optimisation of the VAWT blades [188] that enable more accurate

predictions and detailed visualisation [189]. Due to the simple geometry of the straight blade Darrieus VAWT, it can be modelled using 2D CFD simulations. Currently, most of the CFD modelling of VAWTs is based on a 2D analysis [189]. However, most VAWT designs have a low aspect ratio in which the 3D behaviour of the VAWT is considerable. This includes the effects of the blade tip vortex and the effect of the supporting structure. The 2D CFD simulations ignore the important contributions of the 3D effects and can result in significant conceptual errors. Despite being computationally expensive, the 3D CFD simulations account for the 3D behaviour of the VAWTs and provides a more realistic modelling of the VAWTs. However, considering the trade-off between the accuracy and computational cost, the 2D CFD simulations are considered a suitable tool for the design optimisations and extensive parametric studies. In addition, detailed 3D CFD simulations are essential in testing the final designs before building physical prototypes. The 3D CFD simulations are required for testing and developing the 3D features of VAWTs, including the supporting structure, tip devices, and/or non-straight blades.

In this thesis, the 2D CFD modelling is utilised for the optimisation of the FP-VAWT, the investigation of the AOA and the analysis of the relation between the blade aerodynamic performance and the turbine performance, in addition to the investigation of the different aspect of variable pitch on the VAWT performance. Moreover, the 3D CFD modelling is utilised for the investigation of the 3D aspect of the design of the VAWT and this includes the effect of supporting arms, the effect of the winglet as a tip device, the effect of the turbine aspect ratio on its performance, etc. More details about the principles of the CFD modelling of the VAWT are presented in Section 3.4. Moreover, the details of the implemented 2D and 3D CFD models are clarified in Chapter 4.

3.3 **Design approaches**

In general, there are two main design approaches to investigate the effect of a set of design parameters on the performance of a VAWT. The first approach is based on parametric studies in which the effect of a certain parameter is investigated while keeping the other parameters as constants. The second approach is based on the design optimisations in which an optimisation technique is implemented to investigate the effect of different parameters at the same time. While the majority of the VAWT

performance investigations are based on parametric studies, there is a considerable amount of research that focuses on the optimisation of the aerofoil shape for VAWTs rather than the optimisation of the whole rotor, as discussed in detail in Section 2.5.6.

The utilisation of the optimisation techniques to optimise the whole rotor is expected to assist in reducing the computational cost and providing valuable information about the sensitivity of the VAWT performance to the changes in the different design parameters. In contrast with the parametric studies, the optimisation approaches have the advantage of being more effective and reducing the number of required simulations when dealing with multiple design parameters. Therefore, the optimisation is preferred when dealing with multiple design parameters at the same time while the straight forward parametric studies are sufficient in testing the effects of a single parameter separately.

In this thesis, the optimisation approach is implemented for the design of an optimised FP-VAWT configuration based on three input parameters that include the solidity, TSR, and fixed pitch angle. More details about the principles of the optimisation approach in Section 3.7. Moreover, the details of the implementation of the optimisation approach in the design of FP-VAWT are clarified in Chapter 4.

Furthermore, a set of straight forward parametric studies are carried out in order to test the effect of the turbine aspect ratio and the implementation of winglet on the turbine performance. Moreover, parametric studies are carried out for the investigation of the effect of the favourable AOA and the preset fixed pitch angle on the performance of a VP-VAWT.

3.4 **Computational Fluid Dynamics**

The Computational Fluid Dynamics (CFD) can be partially described as the art of solving the governing equations of the fluid flow numerically in order to obtain the numerical description of the flow-field [190]. CFD has made substantial developments over the recent decades and has great benefits from the advancement of the computing hardware. One of the prominent turning points in the CFD technology is the development of the general-purpose open-source and commercial CFD software. This enables the CFD analysts to save the time of rewriting codes for the governing equations for each fluid flow problem by using the developed general-purpose CFD

software. The industry-leading general-purpose CFD software, FLUENT, is selected to be used in the current study. In addition to its capabilities in the modelling of a wide range of fluid flow problems with different numerical methods, FLUENT allows the CFD analysts to customise the software with some additional features using the so-called User Defined Functions (UDFs).

The CFD simulation consists of three intermediate steps. The first step is the pre-processing in which the computational domain is constructed and discretised in the form of the computational mesh or grid. In addition, the fluid properties, initial conditions, and boundary conditions are defined. The second step is the solution in which the governing equations are solved iteratively in order to obtain the predicted results. The third step is the post-processing in which the predicted results are visualised in different forms that may include contour plots, streamlines, and vector plots.

The majority of engineering flow problems involves turbulent flow with a wide range of turbulence spectrum. As discussed in Section 2.5.4.3.3, there is a wide range of simulation methods that model part or the whole turbulence spectrum. The current study is based on uRANS approach and uses the turbulence model concept to model the majority of the turbulence spectrum. The flow around the VAWT under the current setup is incompressible and is considered to be isothermal. Therefore, the fluid flow is covered by the uRANS equation and the continuity equation for incompressible flow.

The continuity equation for incompressible flow can be expressed in a tensor form as follows:

$$\frac{\partial u_i}{\partial x_i} = 0 \tag{3.1}$$

where $i = 1, 2, 3$ for the three dimensional case.

Considering Newtonian fluid, the unsteady Reynolds-Averaged Navier-Stokes (uRANS) equations for incompressible flow, neglecting the gravity effects, can be expressed as follows:

$$\rho \frac{\partial u_i}{\partial t} + \rho u_j \frac{\partial u_i}{\partial x_j} = -\frac{\partial p}{\partial x_i} + \mu \frac{\partial}{\partial x_j}\left(\frac{\partial u_i}{\partial x_j} + \frac{\partial u_j}{\partial x_i}\right) + \frac{\partial}{\partial x_j}\left(-\rho \overline{\acute{u}_i \acute{u}_j}\right) \tag{3.2}$$

where ρ is the density, p is the pressure, μ is the dynamic viscosity, $i = 1, 2, 3$ and $j = 1, 2, 3$.

In contrast with the Navier-Stokes equations, the uRANS equations include an extra term, and this is referred to as Reynolds stress, $\tau_{ij} = -\rho\overline{\acute{u}_i\acute{u}_j}$. This tensor is a function of the turbulence velocity fluctuations and it is essential to be modelled using the so-called turbulence models in order to solve the uRANS equations or its steady version, i.e RANS. More details about the turbulence modelling are presented in Section 3.5.

3.5 Turbulence Modelling

The purpose of the turbulence model is to model Reynolds stress tensor as discussed in Section 3.4. There is two way to achieve this purpose. The first is adapted in the Reynolds Stress Model in which seven equations are solved including six equations for the distinguished Reynolds stress terms in addition to the dissipation-rate equation. This model is the most computational demanding among all RANS turbulence models. The second way to model the Reynolds stress tensor relies on Boussinesq's turbulence viscosity hypothesis that suggests that the Reynolds stress is proportional to the rate of the deformation as follows:

$$\tau_{ij} = -\rho\overline{\acute{u}_i\acute{u}_j} = \mu_t\left(\frac{\partial u_i}{\partial x_j} + \frac{\partial u_j}{\partial x_i}\right) - \frac{2}{3}\rho k\delta_{ij} \tag{3.3}$$

where μ_t is the eddy viscosity, also referred to as turbulence viscosity, k is the normalised turbulence kinetic energy, and δ_{ij} is referred to as the Kronecker delta function that is defined as $\delta_{ij} = 1$ if $i = j$ and $\delta_{ij} = 0$ otherwise.

In order to calculate the Reynolds stress tensor, it is essential to calculate the turbulence eddy viscosity. The $k - \varepsilon$ turbulence model uses two transport equations to calculate the turbulence kinetic energy, k, and the rate of dissipation of turbulence kinetic energy, ε, and the turbulence eddy viscosity can be calculated as follows:

$$\mu_t = \rho C_\mu \frac{k^2}{\varepsilon} \tag{3.4}$$

where C_μ is a dimensionless constant.

The $k - \varepsilon$ turbulence model is one of the commonly used turbulence models in industrial applications, especially in internal flow applications [191]. This model is

considered to be robust and computational economic while being reasonably accurate for a range of turbulence flow problems. However, the predictions of the separation based on the $k-\varepsilon$ turbulence model are generally delayed and reduced in size [191].

The $k-\varepsilon$ turbulence model relies on the following transport equations for the calculation the turbulence parameters, i.e k and ε:

$$\frac{\partial}{\partial t}(\rho k)+\frac{\partial}{\partial x_i}(\rho k u_i)=\frac{\partial}{\partial x_j}\left[\left(\mu+\frac{\mu_t}{\sigma_k}\right)\frac{\partial k}{\partial x_j}\right]+G_k+G_b-\rho\varepsilon-Y_M+S_k \tag{3.5}$$

and

$$\frac{\partial}{\partial t}(\rho \varepsilon)+\frac{\partial}{\partial x_i}(\rho \varepsilon u_i)=\frac{\partial}{\partial x_j}\left[\left(\mu+\frac{\mu_t}{\sigma_\varepsilon}\right)\frac{\partial \varepsilon}{\partial x_j}\right]+C_{1\varepsilon}\frac{\varepsilon}{k}(G_k+C_{3\varepsilon}G_b)-C_{2\varepsilon}\rho\frac{\varepsilon^2}{k}+S_\varepsilon \tag{3.6}$$

where G_k refers to the turbulence production, G_b represents the effect of buoyancy, Y_M represents a correction factor for compressible flows, $C_{1\varepsilon}, C_{2\varepsilon}, \text{and } C_{3\varepsilon}$ are constants, σ_k and σ_ε represent the turbulence Prandtl numbers for k and ε, S_k and S_ε are additional customisable user-defined source terms. The detailed explanations of the transport equations and their calculation procedure are available in [192].

The $k-\omega$ turbulence model is an alternative to the $k-\varepsilon$ turbulence model that uses two transport equations to calculate the turbulence kinetic energy, k, and the turbulence frequency, $\omega=\varepsilon/k$, and the eddy viscosity can be calculated, for high Reynolds number, as follows:

$$\mu_t=\rho\frac{k}{\omega} \tag{3.7}$$

The $k-\omega$ turbulence model provides a better prediction of the separation and boundary layer flow in the case of adverse pressure gradients. However, the predictions based on this model is relatively sensitive to the values of k and ω in the freestream region outside the shear layer.

The $k-\omega$ turbulence model relies on the following transport equations for the calculation the turbulence parameters, i.e k and ω.

$$\frac{\partial}{\partial t}(\rho k)+\frac{\partial}{\partial x_i}(\rho k u_i)=\frac{\partial}{\partial x_j}\left[\left(\mu+\frac{\mu_t}{\sigma_k}\right)\frac{\partial k}{\partial x_j}\right]+G_k-Y_k+S_k \tag{3.8}$$

and

$$\frac{\partial}{\partial t}(\rho\omega) + \frac{\partial}{\partial x_i}(\rho\omega u_i) = \frac{\partial}{\partial x_j}\left[\left(\mu + \frac{\mu_t}{\sigma_\omega}\right)\frac{\partial \omega}{\partial x_j}\right] + G_\omega - Y_\omega + S_\omega \quad (3.9)$$

where G_ω is the generation of ω, Y_k and Y_ω are the dissipation of k and ω due to the effect of turbulence, and S_ω is an additional customisable user-defined source term. The detailed explanations of the transport equations and their calculation procedure are available in [192].

The Shear Stress Transport (SST) $k-\omega$ turbulence model is proposed as a hybrid model that uses a blend function to transform from the $k-\varepsilon$ turbulence model the region far from the walls into the $k-\omega$ turbulence model in the regions near the walls. This model utilises the advantage of the $k-\varepsilon$ turbulence model in the free steam regions while eliminating its poor performance in the adverse pressure gradient.

The $k-\varepsilon$ turbulence model is modified to fit the $k-\omega$ formulations and hence the transport equations is very similar to that of $k-\omega$ turbulence model and is expressed as follows:

$$\frac{\partial}{\partial t}(\rho k) + \frac{\partial}{\partial x_i}(\rho k u_i) = \frac{\partial}{\partial x_j}\left[\left(\mu + \frac{\mu_t}{\sigma_k}\right)\frac{\partial k}{\partial x_j}\right] + G_k - Y_k + S_k \quad (3.10)$$

and

$$\frac{\partial}{\partial t}(\rho\omega) + \frac{\partial}{\partial x_i}(\rho\omega u_i) = \frac{\partial}{\partial x_j}\left[\left(\mu + \frac{\mu_t}{\sigma_\omega}\right)\frac{\partial \omega}{\partial x_j}\right] + G_\omega - Y_\omega + D_\omega + S_\omega \quad (3.11)$$

where D_ω is the cross-diffusion term.

In the case of SST $k-\omega$ turbulence model, the σ_k and σ_ω is calculated based on blending functions. The detailed explanations of the transport equations and their calculation procedure are available in [192].

In order to account for the laminar to turbulent transition, the four-equation SST transition model is proposed [193]. In contrast with the SST $k-\omega$ turbulence model, the SST transition model includes two extra transport equations for the momentum thickness Reynolds number, Re_θ and the intermittency, γ. The SST transition model is often referred to as the γ- Re_θ model. The Re_θ equation is used to force the transition-onset Re_θ to follow the value obtained from the experimental correlations, while the γ equation is used to trigger the transition process. This model relies on experimental-correlation that is extracted based on a large number of experimental observations.

Despite the fact that this model is calibrated for a wide range of test cases with different flow conditions, it is found that recalibrating the local correlation parameters, based on more relevant specific experimental data, can lead to more-accurate predictions [194], [195]. The four-equation SST transition model cannot be considered as Galilean invariant and is not recommended where the computational domain includes moving walls [192], which is the case of VAWTs. In this context, the equations that are considered as Galilean invariant remains the same in any inertial frame. However, the issue of not being a Galilean invariant is related to the Re_θ equation as reported by Menter et al. [193].

The two additional transport equations for γ and Re_θ are expressed as follows:

$$\frac{\partial}{\partial t}(\rho\gamma) + \frac{\partial}{\partial x_j}(\rho\gamma u_j) = P_{\gamma 1} - E_{\gamma 1} + P_{\gamma 2} - E_{\gamma 2} + \frac{\partial}{\partial x_j}\left[\left(\mu + \frac{\mu_t}{\sigma_\gamma}\right)\frac{\partial \gamma}{\partial x_j}\right] \tag{3.12}$$

and

$$\frac{\partial}{\partial t}(\rho \mathrm{Re}_\theta) + \frac{\partial}{\partial x_j}(\rho \mathrm{Re}_\theta u_j) = P_{\theta t} + \frac{\partial}{\partial x_j}\left[\sigma_{\theta t}(\mu + \mu_t)\frac{\partial \mathrm{Re}_\theta}{\partial x_j}\right] \tag{3.13}$$

where $P_{\gamma 1}$and $E_{\gamma 1}$ are the transition source terms, $P_{\gamma 2}$and $E_{\gamma 2}$ are the relaminisation source terms, $P_{\theta t}$ is a source term, and σ_γ and $\sigma_{\theta t}$ are constants that equals to 1 and 2, respectively.

All the source terms in Equations (3.12) and (3.13) are functions of the transition parameters that are derived from empirical correlation. The detailed explanations of the transport equations and their calculation procedure are available in Ref. [192].

The three-equation SST $k-\omega$ with the γ transition model, also referred to as the γ transition model or intermittency transition model, is considered as a further development of the four-equation SST transition model. The SST $k-\omega$ with the γ transition model avoids the need for the Re_θ transport equation while solving the γ transport equation. This leads to a reduction in the computational costs. In addition, this eliminates the dependency of Re_θ on the velocity and hence the SST $k-\omega$ with the γ transition model is considered as Galilean invariant. In contrast to the SST transition model, the γ transition model is recommended when the computational domain includes walls that have relative motions to the main reference frame. In addition,

among the available transition models, the γ transition model is the only one that is capable of accounting for the transition due to crossflow instability [191].

The additional transport equation for γ is expressed as follows:

$$\frac{\partial}{\partial t}(\rho\gamma) + \frac{\partial}{\partial x_j}(\rho\gamma u_j) = P_\gamma - E_\gamma + \frac{\partial}{\partial x_j}\left[\left(\mu + \frac{\mu_t}{\sigma_\gamma}\right)\frac{\partial \gamma}{\partial x_j}\right] \tag{3.14}$$

The detailed explanations of the transport equation and its calculation procedure are available in [192].

3.6 Model verification and validation

For any numerical model, there is a range of sources of error, including numerical and conceptual errors, and this affects the accuracy of the model predictions. According to Roache [196], it is valuable to distinguish between validation and verification. The verifications aim to assess the numerical errors and focuses on "solving the equations right" [196] whether or not the obtained solution and the used equations represent the physical problem. On the other hand, the validations aim to assess the conceptual modelling errors and focus on "solving the right equations" [196]. For CFD modelling, the validation is usually performed by comparing the CFD predictions against the experimental data. However, before validating the CFD predictions, it is necessary to verify the computational model first. The goal of the verification study is to ensure that the effects of the different numerical aspects of the computational model on the predicted results are minimal. These numerical aspects include the time-step size, the mesh size and order of accuracy of the discretisation scheme. Considering the need to reduce the computational cost, the validation of the above-mentioned numerical aspects is usually carried in the form of independency studies. This aims to identify the minimum requirements for each numerical aspect so that any further improvement in the numerical aspects will lead to negligible effects on the predictions. When the physical model involves a cyclic motion, it is essential to verify that the computational model encounters a sufficient number of cycles so that the discrepancies from the initial boundary conditions are eliminated and that a time-periodic solution is obtained. In some scenarios, some of the conceptual aspects of the numerical model may need to be verified. For example, the selected locations of the hypothetical model boundaries may need to be verified. These boundaries represent the size of the

computational domain and the hypothetical interface between the selected computational model and the surroundings.

In the current study, the CFD model is verified to ensure that there isn't any significant effect on the CFD predictions can be found by improving the mesh element size, the time step size, the computational domain size, or the number of cycles. More details about the verification study are presented in Chapter 4. Moreover, the current CFD model is validated against detailed experimental data published by Li et al. [180]. These data include the pressure coefficient around the blade midsection that have been measured using a high-frequency pressure scanner. In addition, the pressure contribution to the instantaneous power coefficient is also included in the experimental data. More details about the validation of the current CFD model is presented in Chapter 5.

3.7 Optimisation

3.7.1 Optimisation methods from the engineering design perspective

There is a wide range of optimisation methods that suit different disciplines. However, form a practical perspective in engineering design, there are two main approaches for the optimisations and these include the direct approach and the metamodel-based approach [197]. Figure 3.2 illustrates the workflow of the two approaches. In the direct approach, the optimiser is coupled directly with the numerical model and a full numerical simulation is executed in each optimisation loop. However, the optimiser in the metamodel-based optimisation is coupled with a metamodel that provides a fast assessment of the output parameters in each optimisation loop. In order to do so, the output parameters' data for the initial sample is collected from the simulations based on the numerical model and then is used to construct the metamodel. The metamodel is a surrogate model that represents the relation between the input and output parameters and is simply defined as "the model of a model" [197]. In other words, the metamodel represents the response of the system in terms of the values of the output parameters as related to the values of input parameters.

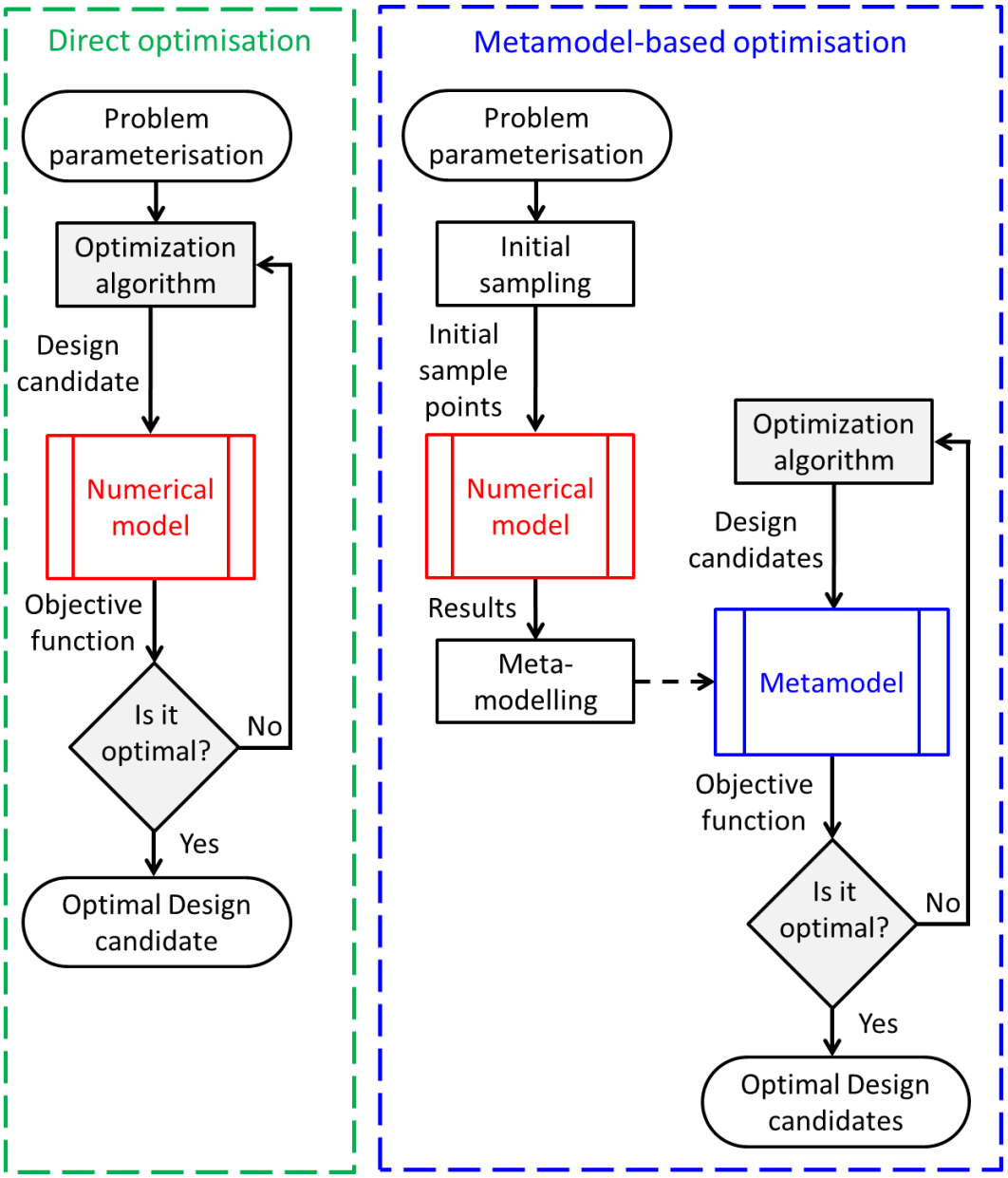

Figure 3.2 The workflow for the direct optimisation and metamodel-based optimisation approaches

Currently, engineering design is based on sophisticated computational demanding simulations, such as CFD and Finite Element Analysis (FEA), and these are time-consuming and, in some situations, require much detailed attention from the user. This makes it difficult to rely on the direct optimisation technique where the metamodel-based approach shows its advantages as it relies on the metamodel that represents the system response in a fast real-time manner with a minimal low computational cost. In addition, metamodel-based optimisation can be used to provide multiple design alternatives while the direct optimisation usually leads to a single optimal design.

Furthermore, the direct optimisation is oriented towards finding the optimal design in a sequential procedure without any insight on the relation between the different input and output parameters. On the other hand, from an engineering design perspective, the metamodel-based optimisation approach enriches the design process with more detail about the relations between the input and output parameters and their sensitivity [198].

The metamodel, surrogate model, and Response Surface terms are used interchangeably to describe the model that represents the relation between the input and output parameters. However, in this thesis, the Response Surface is often used and the metamodel-based optimisation approach is often referred to as the Response Surface Methodology (RSM) or the Response Surface Optimisation (RSO).

3.7.2 **Response Surface Optimisation**

In order to carry out the RSO, three main intermediate steps are required that include the initial sampling, the construction of the response surface, and the implementation of the optimisation algorithm. The method behind the initial sampling is often referred to as the Design of Experiments (DoE). In addition, before starting with the RSO, the design problem should be parameterised. Figure 3.3 illustrates the intermediate steps of the RSO method and the following subsections shed more light on these intermediate steps. However, more details about the implementation of the RSO on the FP-VAWT are available in Chapter 7.

3.7.2.1 **Design parameters**

It is essential to parameterise the design problem into a set of design parameters. The parameters can be classified as input parameters and output parameters. The input parameters represent the independent design variable that affects the performance of the system or the component under the investigation. The output parameters represent the depended design variables that often describe the performance of the system or component. The input parameters may include the geometric aspect of the design and/or the loads and boundary conditions. There are two types of input parameters, in particular the continuous and discrete parameters. The value of a continuous parameter can be any value within a specific range, for example, the chord length of a turbine blade. The value of a discrete parameter is limited to a set of

predefined values that is often an integer value, such as the number of blades in a turbine. Based on the input parameters, the design space is defined as the multidimensional space bounded by the ranges of the selected input parameters.

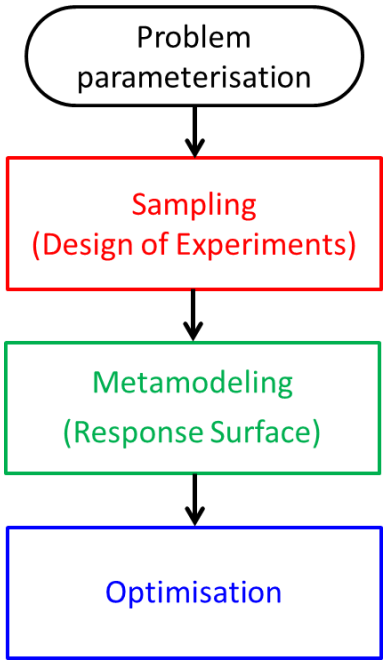

Figure 3.3 An illustration of the steps of the RSO.

3.7.2.2 Design of experiments

The DoE is a technique that assists in the efficient distribution of the location of the initial sampling points throughout the design space. In this context, efficient distribution means reducing the number of sampling points while improving the accuracy of the response surface. There is a range of different DoE methods including the Central Composite Design (CCD), Optimal Space-Filling Design (OSF), Box-Behnken Design, and Latin Hypercube Sampling Design (LHS). However, the CCD is probably the most widely used method for DoE [199] and is selected for the current study. The CCD is a fractional factorial design that is distributed around the centre of the design space and can be classified into three basic types: circumscribed, inscribed, and face-centred CCDs. Figure 3.4 illustrates these basic types of CCD for a design space with three generic parameters with a range between -1 to 1.

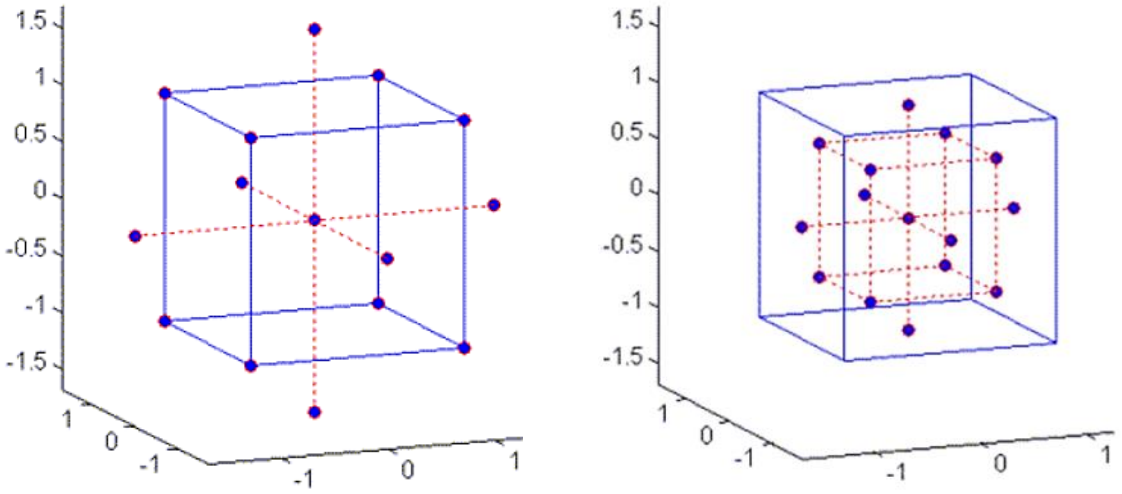

(a) Circumscribed CCD

(b) Inscribed CCD

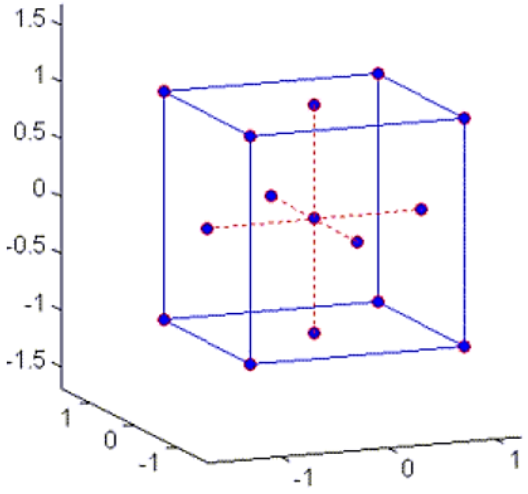

(c) Face-centred CCD

Figure 3.4 The basic types of CCD [175].

It is noticed that the face-centred CCD is a three-level design while both the circumscribed and inscribed CCDs have five-levels. Both the circumscribed and inscribed can be implemented in a rotatable configuration so that the non-central points are located at a constant distance from the centre of the domain regardless of their direction and hence have the same error expectations [175]. In contrast with the basic CCDs, a better fit with the Response Surface can be achieved by adding more levels for each parameter using the so-called enhanced CCDs. Figure 3.5 shows a comparison between the rotatable inscribed CCD and the enhanced rotatable inscribed CCD for a design space with two parameters with a range between -1 to 1. It is noticed that the enhanced rotatable CCD provides a good coverage of the design space except in the region near the corner points. Hence, the combination between

the enhanced rotatable inscribed CCD and additional corner points is suggested and implemented in this thesis as clarified in detail in Section 7.4.

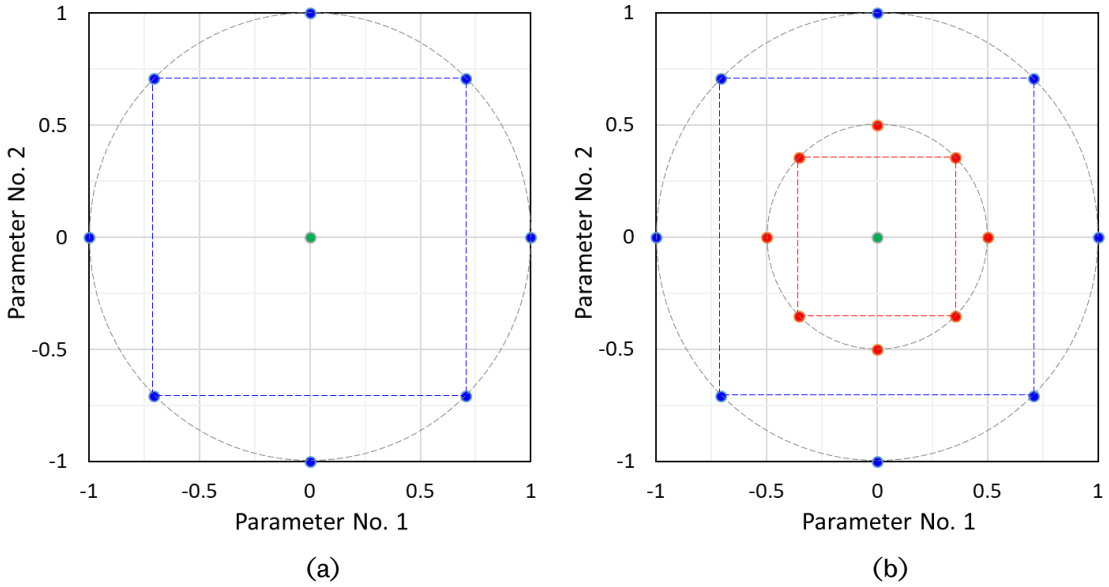

Figure 3.5 The locations of the design points for (a) the rotatable inscribed CCD and (b) the enhanced rotatable inscribed CCD.

3.7.2.3 Response Surface

After the real simulations for the initial sample and the extraction of the corresponding values of the output parameters, the Response Surface is constructed for each output parameter. There are different types of response surfaces including the multidimensional interpolation, regression, and neural network. The advantage of the interpolation-based Response Surface is that it perfectly fits with all the data in the initial sample and provides an improved response quality [175]. Therefore, the Kriging method is used in this thesis as an advanced multidimensional interpolation as clarified in detail in Section 7.5.

3.7.2.4 Optimisation

The optimisation step in the RSO is to carry out an optimisation algorithm aiming to identify the optimal design. The optimisation algorithms are iterative procedures that are executed to compare various design candidates in order to satisfy the optimisation objectives and comply with the design constraints. The design candidate is a specific design identified by specific values of input parameters that meets the optimisation objectives. The objective function is the function or parameter to be optimised. The optimisation objectives are the aims of the optimisation and can include maximising,

minimising, or seeking a specific value of the objective functions. The optimisation algorithms can be classified to be a single-objective or multi-objective depending on their capability to deal-with more than one objective. There is a wide range of optimisation algorithms including screening, evolutionary algorithm, and gradient-based algorithm. In this thesis, the Multi-Objective Genetic Algorithm (MOGA) is chosen as an evolutionary algorithm that has advanced capabilities in identifying the global optimal designs under multi-objective scenarios [175]. More details about the implementation of the MOGA in the optimisation of the FP-VAWT are presented in Section 7.6.

3.8 Summary

In conclusion, the CFD modelling approach based on uRANS turbulence modelling is selected for the current study. Two highly recommended turbulence models in the literature are selected, and these include the SST k-ω turbulence model and the SST k-ω with the γ transition turbulence model. While this chapter outlines the principles of the CFD methodology, the details of the implemented CFD model are clarified in more depth in Chapters 4. Moreover, the Response Surface method is selected for the optimisation of the fixed pitch configuration due to its ability to handle multiple design parameters in an efficient way. More details about the implementation of the Response Surface method in the optimisation of the fixed pitch configuration is presented in Chapter 7. The parametric study method is selected for the investigation of the variable pitch configuration as clarified in details in Chapter 8.

4 MODELLING OF VAWTS

4.1 Overview

While the validation of a computational model aims to assess the conceptual modelling errors and how this model represents the physical problem, the verification of the model focuses on the numerical errors and the effects of the numerical aspects on the predictions. According to Roache [196], the validation is described as "solving the right equations" while the verification is about "solving the equations right". This chapter focuses on the verification of the numerical aspects of the 2D and 3D CFD models. More details about the validations of these models are available in Chapter 5. The aims of the current chapter include building a 2D CFD model of the VAWT based on a structure-shaped mesh. The verification of the numerical aspects of the computational model is accomplished by several sensitivity tests. These include the study of the solution periodicity, domain size effects, time-step size independence, mesh independence, and the effects of the order of the spatial and temporal discretisation. Based on the 2D mesh sensitivity study, the significant mesh attributes are clarified. A computationally affordable 3D model is built based on the conclusions from the 2D study and this 3D model is verified for mesh independency.

A two-bladed FP-VAWT, with 6° of preset fixed pitch based on the NACA 0015 aerofoil, is selected for the verification and validation of the current 2D and 3D CFD models due to the ample experimental data obtained by Li et al. [180]. The selected turbine has a diameter of 1.7m, a chord length of 0.225 m, and a span of 1.02 m. In the selected test case, the turbine operates at a TSR of 2.29 that is associated with the maximum power coefficient in the experimental data. Figure 4.1 shows a schematic of the turbine geometry at an arbitrary azimuthal location and clarifies the reference azimuthal location, i.e. ϕ=0°. The VAWT encounters a cyclic rotational motion in which the azimuthal angle changes from ϕ=0° to ϕ=360° in each cycle. As illustrated in Figure 4.1, each cycle is divided into an upstream part between ϕ=0° and ϕ=180° and a downstream part between ϕ=180° and ϕ=360°.

In this chapter, and in order to have a relatively comparable assessment, the single blade instantaneous torque coefficient is selected for the analysis of the 2D predictions

while the contribution of the mid-span section of a single blade into the instantaneous torque coefficient is selected for the analysis of the 3D predictions. The 3D predictions at the mid-span are less sensitive to the 3D effects and are relatively comparable to the 2D results.

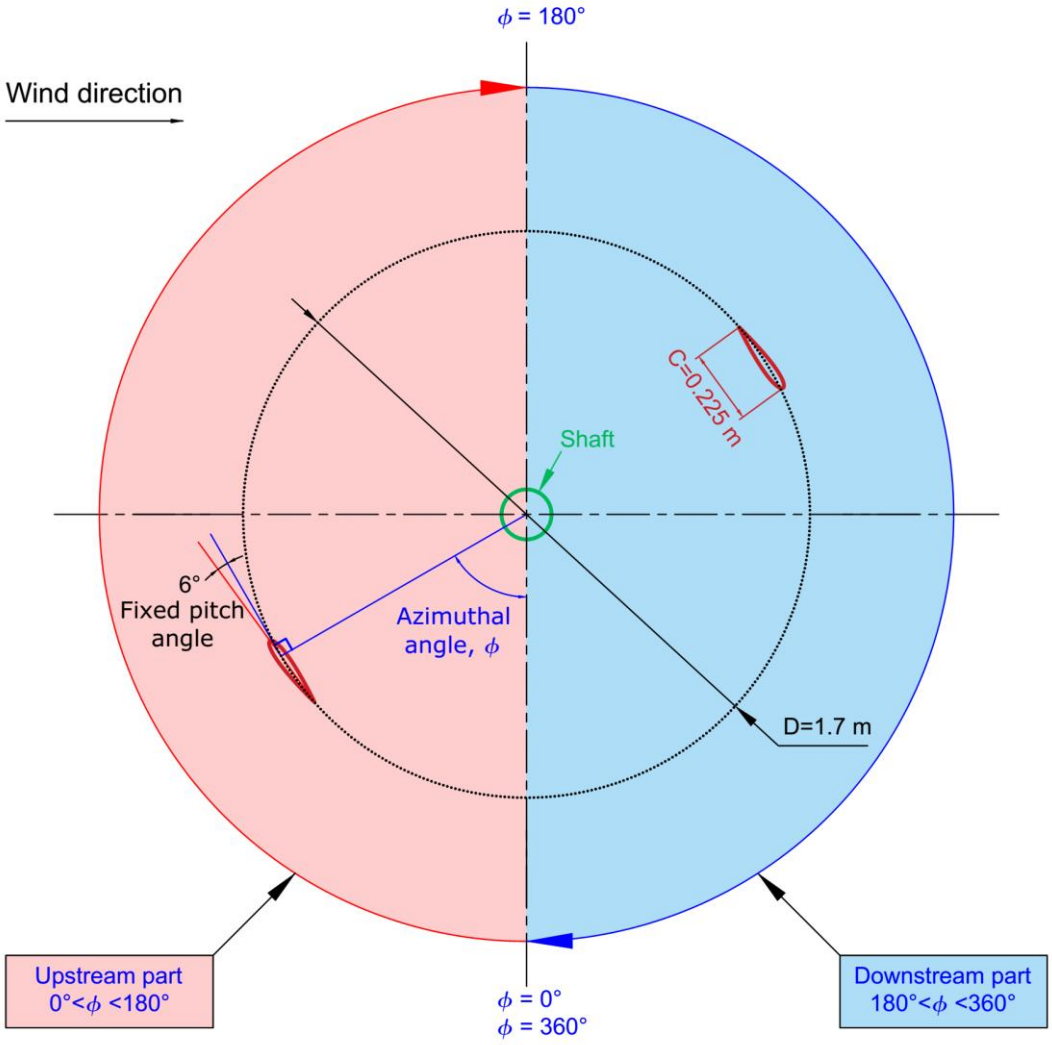

Figure 4.1 A 2D schematic of the two-bladed turbine with 6° of fixed pitch at an arbitrary azimuthal location.

In this chapter, and in order to quantify the significance of a certain attribute on a predicted quantity, Q, a sensitivity parameter is defined as:

$$\text{Sensitivity} = \frac{Q|_{based\ on\ the\ new\ attribute} - Q|_{based\ on\ the\ baseline\ attribute}}{Q|_{based\ on\ the\ baseline\ attribute}} \times 100\% \qquad (4.1)$$

The aim is to have a sensitivity less than 1% in the 2D case and 2% in the 3D case to any change between the selected baseline models and any higher-order or higher-fidelity setting or attributes.

4.2 2D CFD modelling

4.2.1 Numerical methods and model description

The 2D CFD simulation is widely used for the modelling of the VP-VAWTs due to its reasonable accuracy and moderate computational cost. The 2D simulations ideally represent a turbine with an infinite blade height and could not account for the blade tip losses, the parasitic resistance of the supporting struts and the fully 3D behaviour of the VAWTs. However, more discussion about the ability of the 2D simulations on the prediction of the turbine performance at the mid-span section of the turbine blade is available in Section 5.2.

The simulations have been performed using a commercial CFD solver, namely ANSYS FLUENT version No. 18.2, and the 2D double-precision version of ANSYS FLUENT is utilised in the transient mode. The pressure-based coupled solver algorithm is implemented. In contrast with the segregated solver, the coupled solver is able to accommodate higher Courant number and hence larger time step size [191] that could significantly reduce the computational cost. The second-order implicit transient formulation is enabled for improved accuracy [191]. The solver is allowed to perform 30 iterations per each time step and this is found to be generally sufficient to reduce all the normalised residuals to, at least, five orders of magnitudes for the main flow variable and, at least, four orders of magnitudes for the turbulence model variable. The second-order upwind scheme is implemented for the discretisation of the momentum and the turbulence model equations.

The sliding mesh method is used to model both of the turbine rotation and blade pitch motion, when applicable. The angular velocity of both the pitch motion and the turbine rotation is imposed on the corresponding subdomain using an interpreted User Defined Function (UDF) that is integrated into the solver. A typical example of the used UDF is provided in Appendix A. In order to account for the time-dependent behaviour of the flow around the turbine, a fine temporal resolution of 540 time-steps per cycle is carefully chosen as discussed in Section 4.2.5.

Despite the fact that there has been a continuous development and enhancement of the turbulence models, none of these models could be generalised to be suitable for all problems. Each model has its strength and weakness that should be taken into

consideration. For the present study, the blades of the turbine encounter a relatively low Reynolds number regime with an average of about 247,000 based on the blade chord length. Therefore, the assessment of the behaviour of one of the transition models is essential. The three equations SST k-ω with the γ transition turbulence model is chosen to account for the laminar to turbulent transition, as it is recommended for the domains with moving walls [192]. Moreover, the SST k-ω turbulence model is used as a non-transition model that has been suggested by Paillard et al. [135]. The present tests showed that the SST k-ω with the γ transition requires more computational time than the non-transition SST k-ω model. Particularly for the reference mesh and time step size, the SST k-ω with the γ transition case needs about 10 % more wall clock time in contrast to the SST k-ω model. Due to the differences in the complexity between the transition and the non-transition models, the predictions of each model are investigated separately as discussed in the following sections.

4.2.2 **Computational domain and meshing topology**

In order to capture the details of the flow around the turbine, a rectangular-shaped computational domain is constructed. The selected domain is extended to 10-diameters in each direction from the rotation axis, except in the downstream direction where it is extended to 20-diameters. More details about the selection of the computational domain size are available in Section 4.2.4. The domain is assembled using the ANSYS DesignModeler, while the NACA0015 aerofoil coordinates are obtained using the XFOIL 6.96 database for the NACA 4-digit series. The trailing edge is rounded to eliminate the effect of the accelerating flow over the sharp corners of a blunt trailing edge. However, the rounding radius to chord ratio, about 0.19 %, is too small to have a significant effect on the aerofoil performance. The details of the computational domain and the boundary conditions are illustrated in Figure 4.2.

The implementation of the sliding mesh method requires dividing the computational domain into several subdomains which include a stationary subdomain for the region far from the turbine, a rotating subdomain for the region around the turbine, in addition to small circular subdomains around each blade to account for blade pitch, when applicable. The connections between these subdomains are achieved by means of circular non-conformal mesh interfaces around each of the rotating and blade-

pitching subdomains. The upper and lower edges of the domain are modelled with the symmetric boundary condition that enforces zero-gradients across its normal direction. The upstream edge is modelled with a velocity inlet boundary condition with a streamwise component of 7 m/s and turbulence intensity of 0.5 % in order to match the values in the experiments carried out by Li et al. [180]. A relatively high Turbulent Viscosity Ratio (TVR) of 100 is used at the inlet. However, it is found that the value of TVR at inlet has an insignificant effect on the predicted results as discussed in Appendix B. The downstream boundary is set as a pressure outlet boundary condition with zero gauge pressure. The blade profiles and the turbine axis are considered as walls with zero velocity relative to the adjacent cell zones.

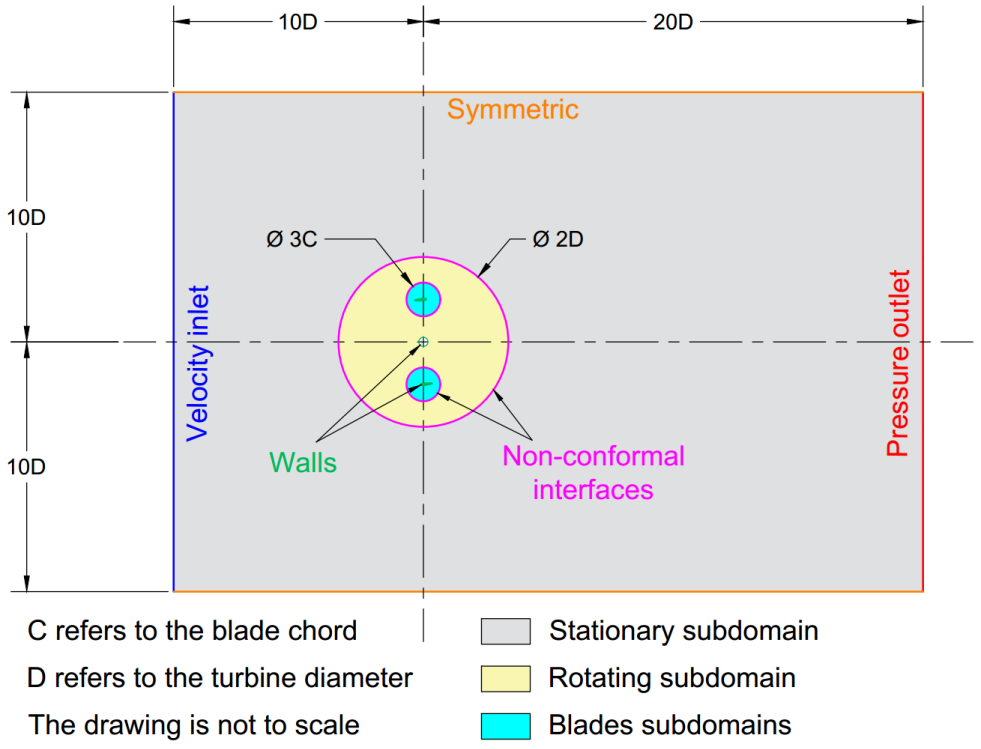

Figure 4.2 Boundary conditions and dimensions of the computational domain for a 2 bladed turbine.

The computational mesh is an all-quad mapped structure-shaped mesh that utilises a combination of H-mesh and O-mesh topologies. An extremely coarse mesh is used to illustrate the mesh topology in Figure 4.3. This coarse mesh is constructed for illustration purpose only and has not been used in the simulations. The 2D baseline mesh includes 920600 elements across the entire computational domain with 1000 nodes around each blade profile. The baseline mesh is shown in Figure 4.4 and is

clustered near the turbine rotor region in addition to the wake region. Figure 4.5 shows the O-mesh topology around the blade in addition to the clustered mesh near the leading edge of the blade. Further discussion about the selection of the baseline mesh and its attributes is available in 4.2.6. This baseline mesh is utilised for all further 2D tests unless otherwise stated.

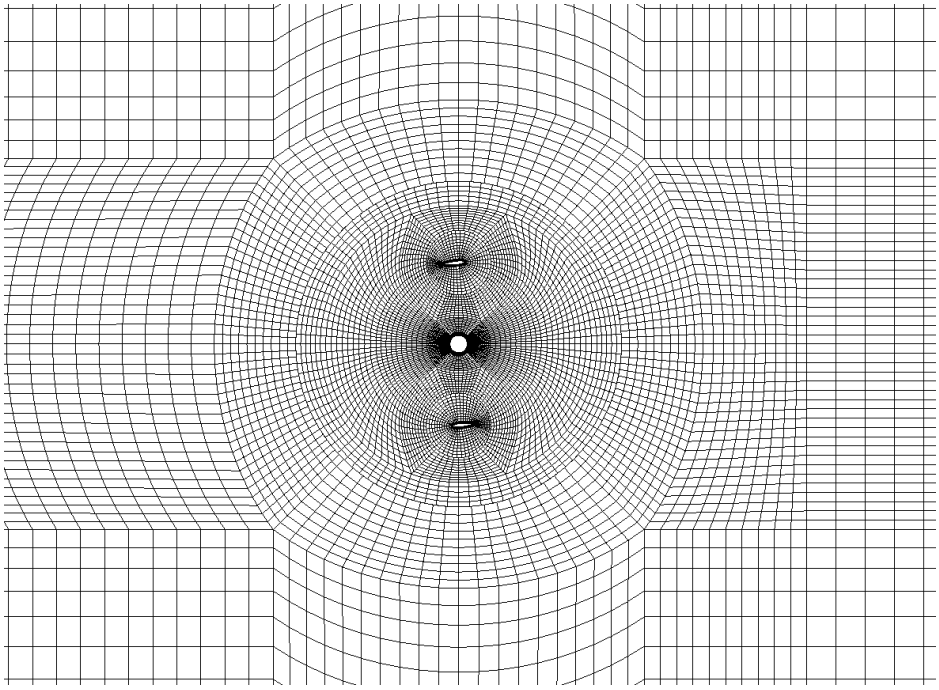

Figure 4.3 The structured mesh topology in an extremely coarse mesh, for illustration only.

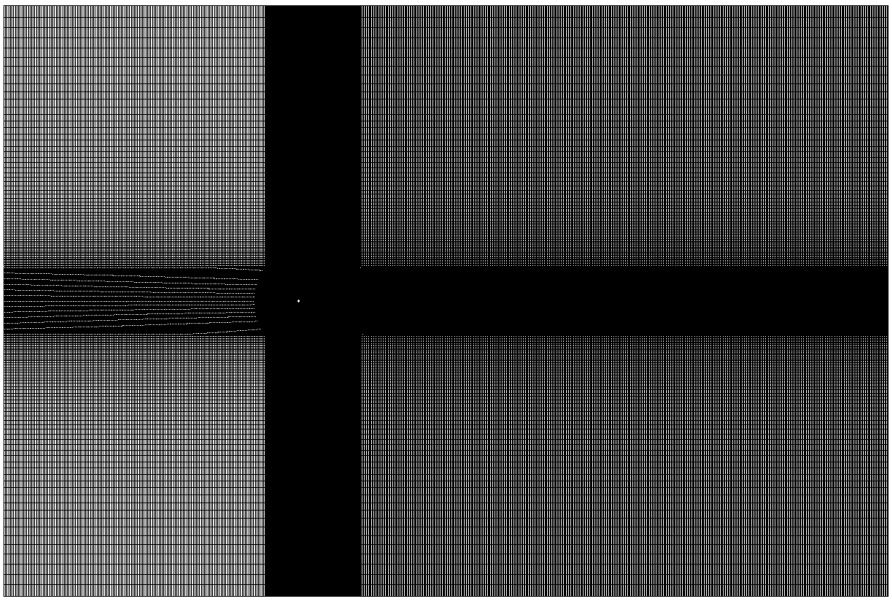

Figure 4.4 The mesh baseline across the entire computational domain shows the mesh clustering in the wake region and in the region near the rotor.

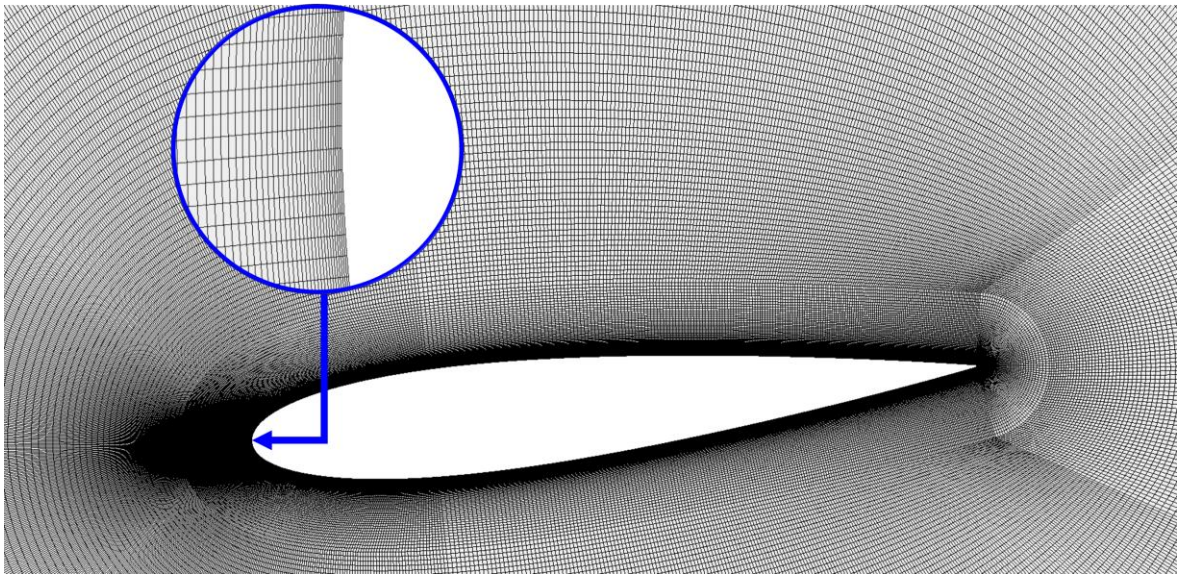

Figure 4.5 The baseline mesh around the blade with a magnified view of the clustered mesh near the leading edge of a blade with a pitch angle of 6°.

4.2.3 Solution periodicity

Due to the periodic motion of VAWTs, the simulations are expected to encounter a time-periodic solution except for the established unsteadiness in the first few cycles of the simulations. In order to ensure that a periodic solution is achieved the instantaneous torque coefficient is monitored over the first ten cycles based on both the SST k-ω and SST k-ω with the γ transition turbulence model as shown in Figure 4.6. Despite the starting unsteadiness in the first few cycles, it could be noticed that the torque coefficient data show that the solutions are fairly periodic in the upstream-parts of the cycles. However, there is some inconsistency in the downstream-parts of the cycles and this is due to the effects of the turbine shaft wake interactions as discussed later in this subsection.

In order to have a clear criterion for the selection of the minimum number of cycles required to obtain converged periodical solutions, the sensitivity of the time-averaged torque coefficient in the upstream part to the number of cycles is monitored. The aim is to achieve differences less than 1% in the time-averaged torque coefficient in the upstream part of the cycle between the successive cycles. This criterion is expressed as follows:

$$100 * \frac{\overline{C_m}_{N+1} - \overline{C_m}_N}{\overline{C_m}_N}\Big|_{upstream} < 1\% \qquad (4.2)$$

where $\overline{C_m}$ is the time-averaged torque coefficient and N is the selected number of cycles for a converged periodical solution.

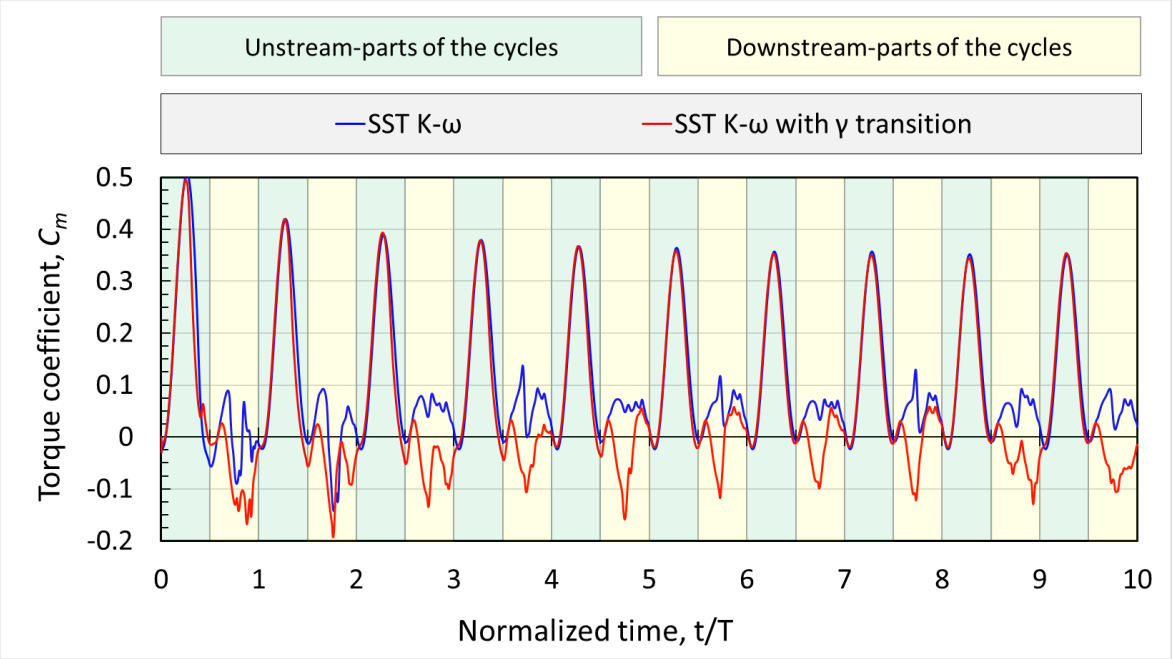

Figure 4.6 The instantaneous torque coefficient over the first 10 cycles.

The sensitivity of the time-averaged torque coefficient in the upstream part to the number of cycles drops below 1% at the 5th cycle in the case of the SST k-ω turbulence model while 6 cycles are required to achieve the same level for the transition model. Hence, for all further analyses and post-processing, the results are considered at the 5^{th} and 6^{th} cycles for the SST k-ω and SST k-ω with γ transition, respectively.

In this chapter and in order to make the visual comparison easy, all the Figures that show the instantaneous torque coefficient share the same vertical axis range. Figure 4.7 (a) shows the differences of the single blade instantaneous torque coefficient obtained at the 5^{th} and 6^{th} cycles angles for the SST k-ω turbulence model while Figure 4.8 (a) shows the differences of the single blade instantaneous torque coefficient obtained at the 6^{th} and 7^{th} cycles angles for the SST k-ω with the γ transition turbulence model. It could be noticed that there are some small insignificant differences on the profile of instantaneous torque coefficient curve in the upstream part of the cycle between the successive cycles, especially in the case of SST k-ω with γ transition. However, these differences are diminishing each other's and the net differences in average data of the upstream part of the cycle is within 1%. These diminishing differences are found also in the other sensitivity studies in Sections 4.1.4, 4.1.5,

and 4.1.6. On the other hand, there are some notable differences in the downstream part of the cycle, especially around ϕ= 270° where the vortices released from the shaft interact with the blade.

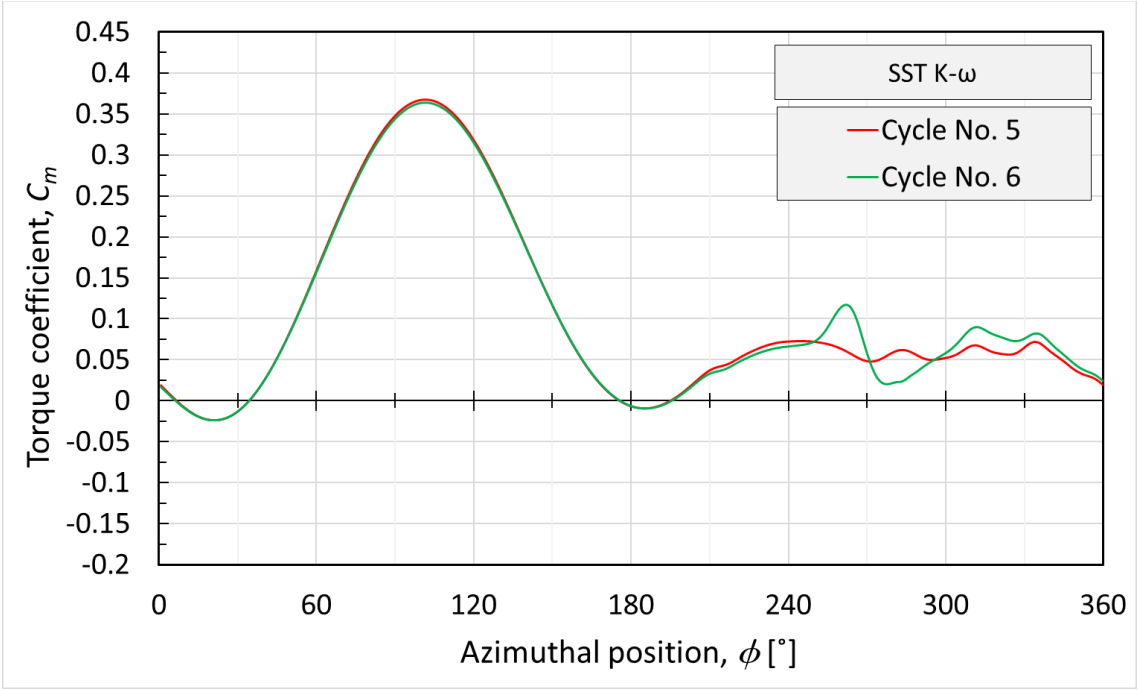

(a)

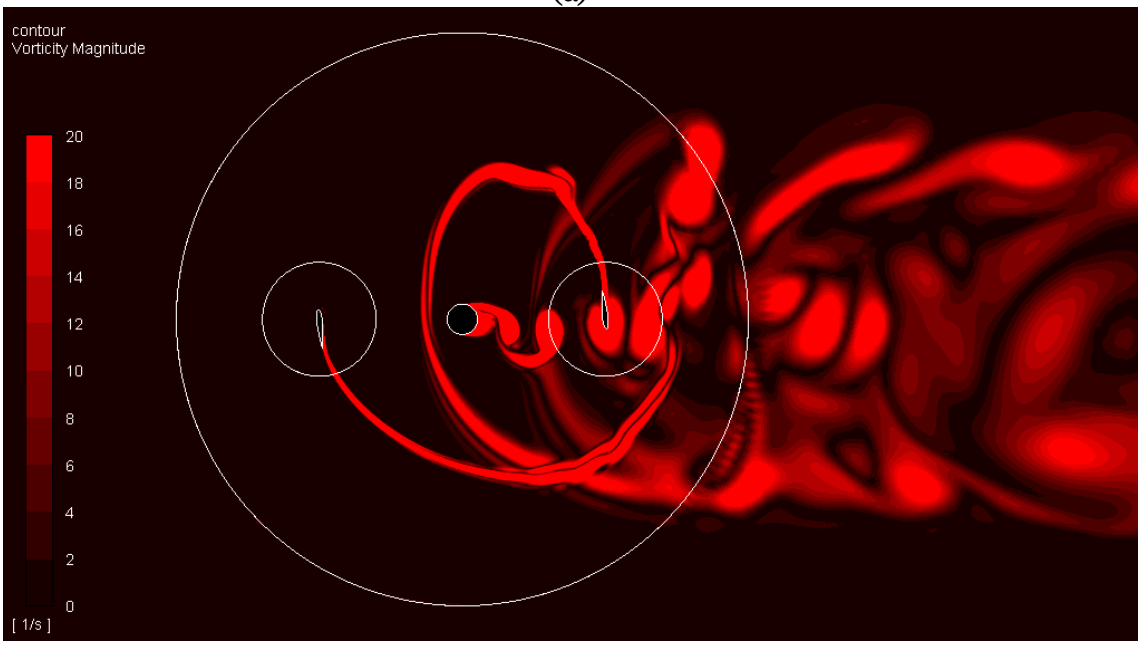

(b)

Figure 4.7 (a) The single blade instantaneous torque coefficient, C_m at the 5th and 6th cycles over 360° of azimuthal angles using the SST k-ω turbulence model. (b) The contour of the vorticity magnitude that visualises the vortex shedding from the blades and the shaft at 270° azimuthal position in the 5th cycle.

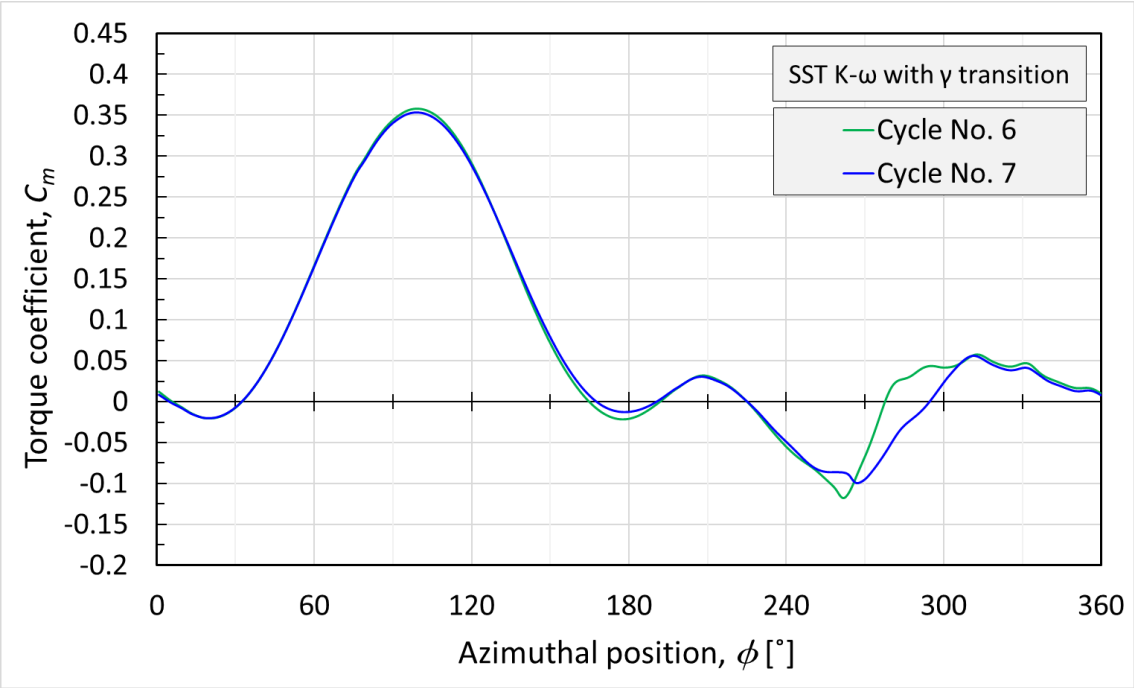

(a)

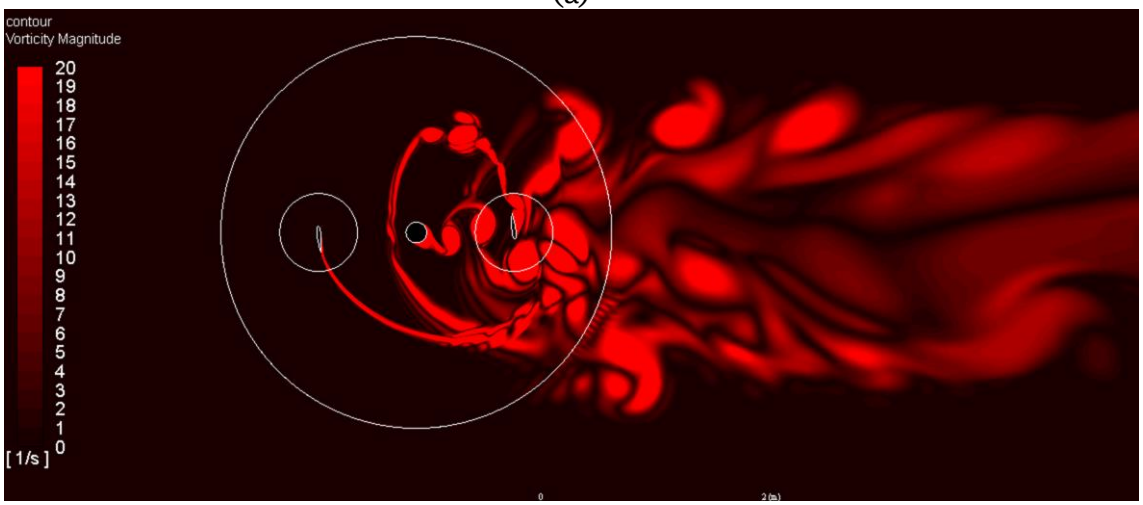

(b)

Figure 4.8 (a) The single blade instantaneous torque coefficient, C_m at the 6th and 7th cycles over 360° of azimuthal angles based on the SST k-ω with the γ transition turbulence model. (b) The contour of the vorticity magnitude that visualises the vortex shedding from the blades and the shaft at 270° azimuthal position in the 6th cycle.

Figures 4.7 (b) and 4.8(b) illustrate the vortex shedding from the turbine blades and shaft and this shows how these vortices interfere. By comparing Figures 4.7 (a) and (b) against Figures 4.8 (a & b), it may be noticed that the torque coefficient data obtained by the SST k-ω with the γ transition turbulence model is more sensitive to the vortices interaction behind the turbine shaft. This appears to be due to the overestimation of the separation vortices in the 2D results obtained by the transition

model as discussed further in Section 5.3.1. It could be concluded that the discrepancy in the solution periodicity in the downstream part of the cycle is due to the interaction between the vortices released from the shaft and the blade. These vortices are released with a different frequency than that of the turbine rotation and this makes the solution to be not fully periodic. In order to justify this conclusion, the domain and the baseline mesh are reconstructed without modelling the shaft. The simulations are carried out without the shaft consideration and Figures 4.9 (a) and 4.10 (a) show the differences in the single blade instantaneous torque coefficient between the successive cycles based on the SST k-ω and the SST k-ω with γ transition, respectively. By omitting the shaft from the consideration, a time-periodic solution is obtained over the whole cycles for the two turbulence models. Figures 4.9 (b) and 4.10 (b) illustrate the vortex shedding from the turbine blades by omitting the shaft from the consideration based on the SST k-ω and the SST k-ω with γ transition, respectively. The vortex shedding from the blades is synchronised with the turbine rotation and hence do not affect the solution periodicity. Based on this conclusion, the sensitivity of the results is calculated based on the upstream part of the cycle to exclude the effect of the discrepancy of shaft interactions in the downstream part of the cycle for all further sensitivity analyses and model verifications.

4.2.4 **Effect of the size of the computational domain**

In order to eliminate the effect of the computational domain boundaries on the obtained solution, a sufficiently large computational domain is required. This ensures that the blockage effect is negligible. However, the extension of the domain dimension is associated with increasing the number of elements and hence the computational cost. Several trials are carried out to select an adequate domain size with reasonable accuracy and computational cost. The computational domain is parameterised using the two parameters ℓ_a and ℓ_b as illustrated in Figure 4.11. Three different domain sizes, namely small, baseline, and extended domains, are selected to study the sensitivity of the results to domain size. To ensure consistency, the computational meshes of the small and extended domains are constructed to have the same attributes as the baseline mesh.

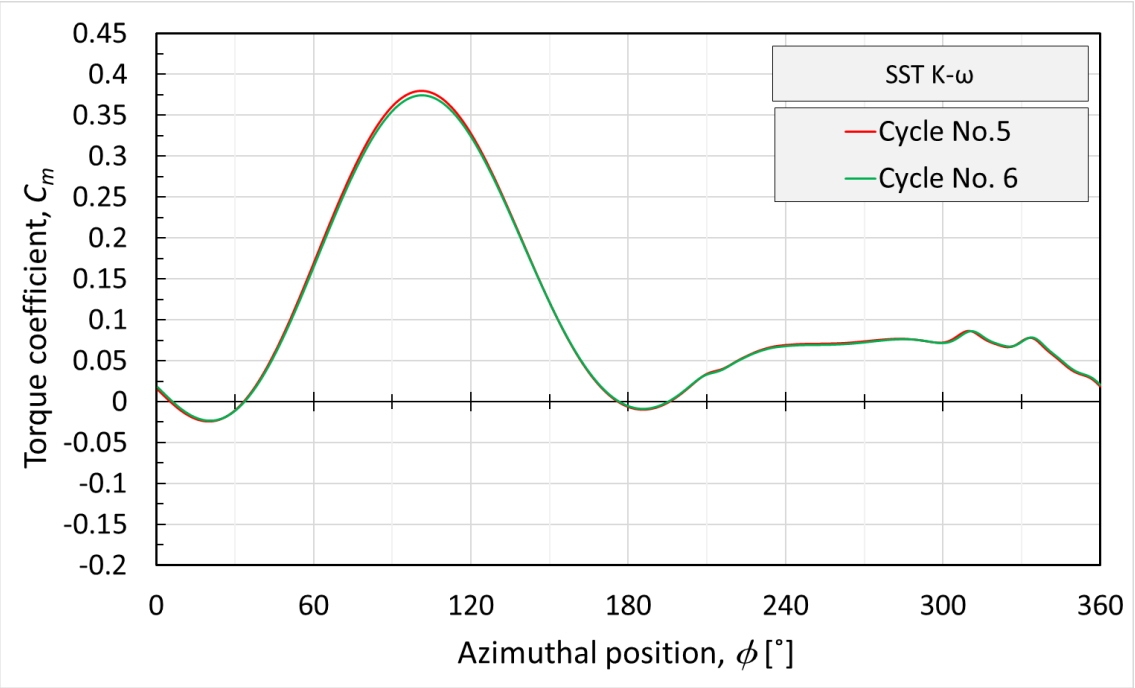

(a)

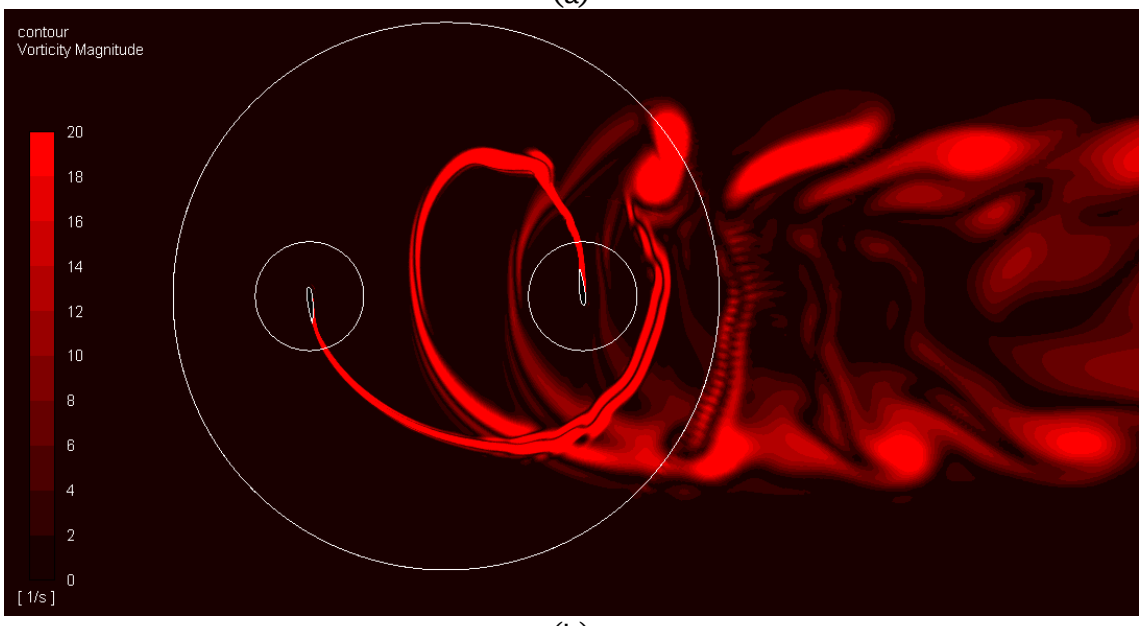

(b)

Figure 4.9 (a) The single blade instantaneous torque coefficient, C_m at the 5th and 6th cycles over 360° of azimuthal angles using the SST k-ω turbulence model without modelling the shaft. (b) The contour of the vorticity magnitude that visualises the vortex shedding from the blades and the shaft at 270° azimuthal position in the 5th cycle.

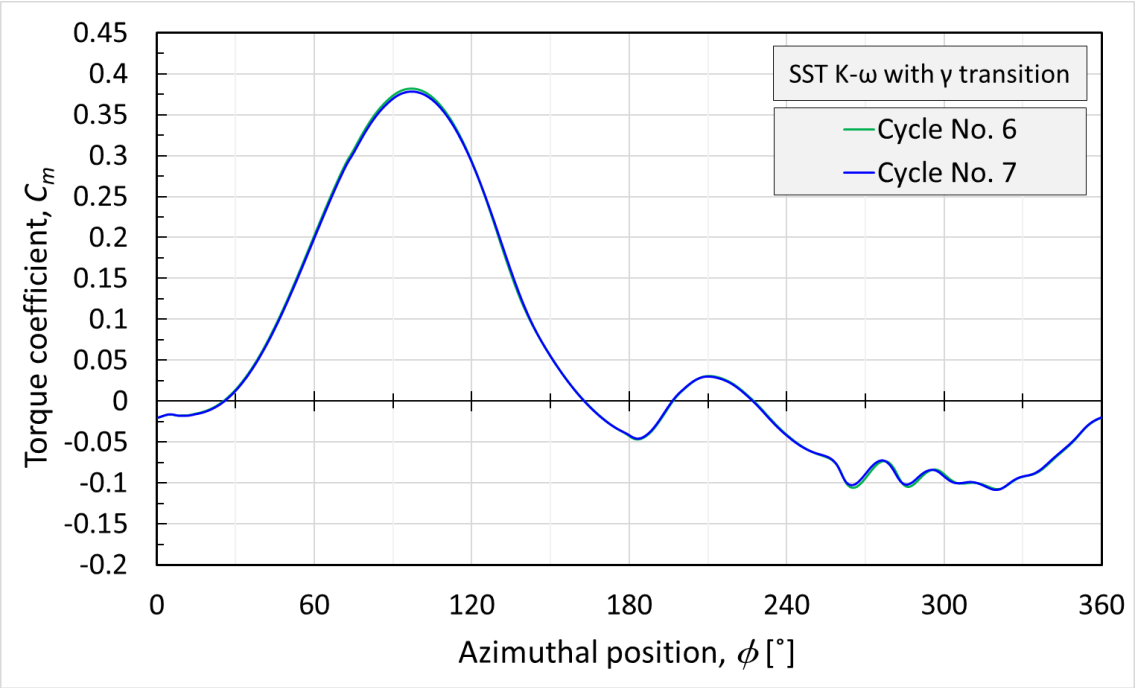

(a)

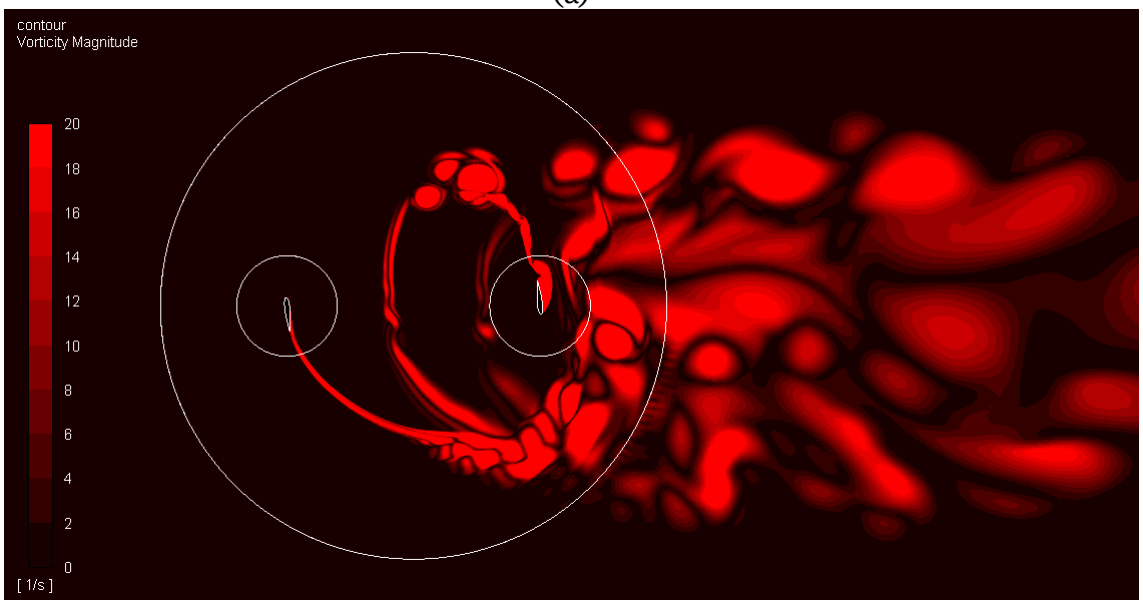

(b)

Figure 4.10 (a) The single blade instantaneous torque coefficient, C_m at the 6th and 7th cycles over 360° of azimuthal angles based on the SST k-ω with the γ transition turbulence model without modelling the shaft. (b) The contour of the vorticity magnitude that visualises the vortex shedding from the blades and the shaft at 270° azimuthal position in the 6th cycle.

Table 4.1 shows the details of the sizes of these three domains along with the sensitivity of the time-averaged torque coefficient in the upstream part of the cycle to the change in the domain size relative to the baseline domain for both the SST k-ω and SST k-ω with the γ transition models. It is noticed from Table 4.1 that the sensitivity of the results to increasing the domain size is around 1 % relative to the baseline domain for the two

turbulence models and hence the baseline domain is selected for the further analyses. The selected domain size agrees to some extent with the sizes that have been selected in several recent studies [200]–[202].

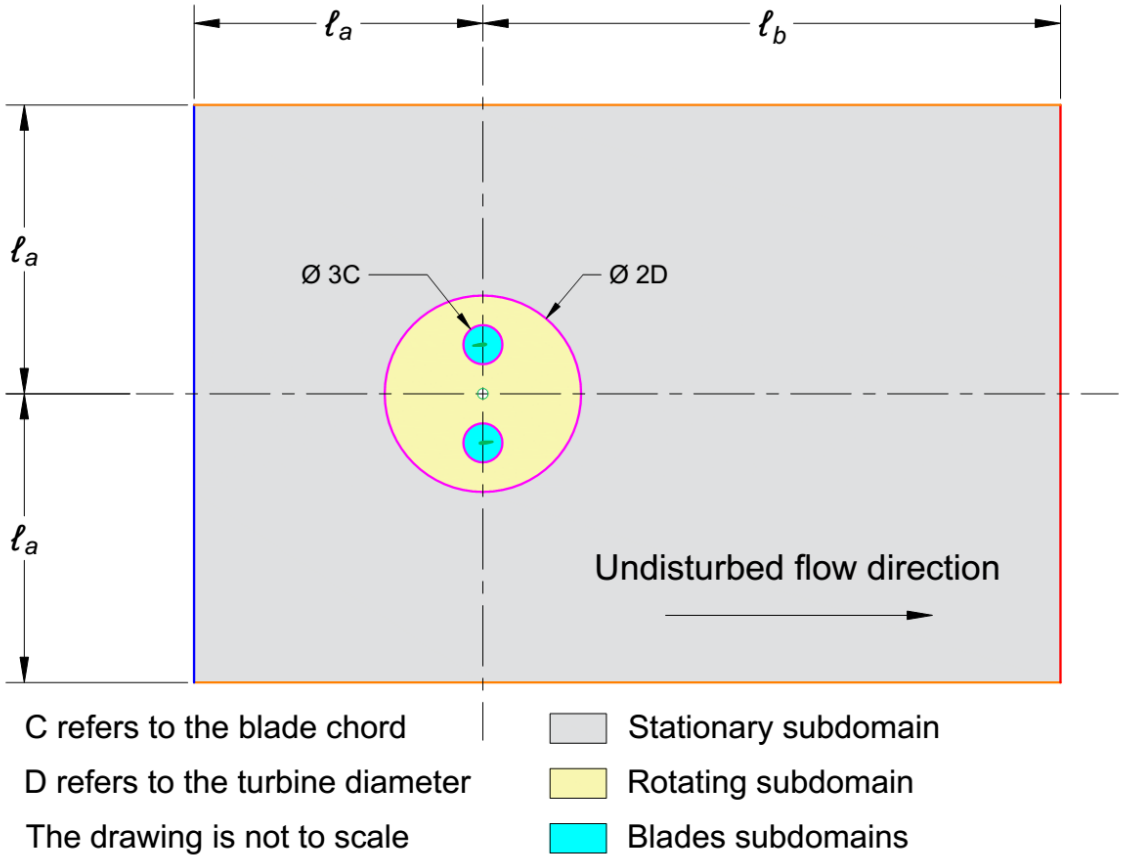

Figure 4.11 The parameterised computational domain used for study the effect of domain size based on ℓ_a and ℓ_b.

Table 4.1 The specifications of the size of three selected domains and the sensitivity of the time-averaged torque coefficient to the domain size where D refers to the diameter of the turbine.

	ℓ_a	ℓ_b	Sensitivity of the $\overline{C_m}$ in the upstream part of the cycle	
			SST k-ω	SST k-ω with γ transition
Small Domain	5D	10D	3.33%	3.27%
Baseline Domain	10D	20D	---	---
Extended Domain	20D	40D	-0.79%	1.02%

Figures 4.12 (a) and (b) shows the effects of the different domain sizes on the instantaneous torque coefficient for both the SST k-ω and SST k-ω with the γ transition models, respectively. It is noticed that the results obtained by the SST k-ω with the γ transition are more sensitive to the change in the domain size. There are noticeable

differences between the CFD predictions at the peak of the torque coefficient in the upstream part of the cycle where the AOA is relatively high.

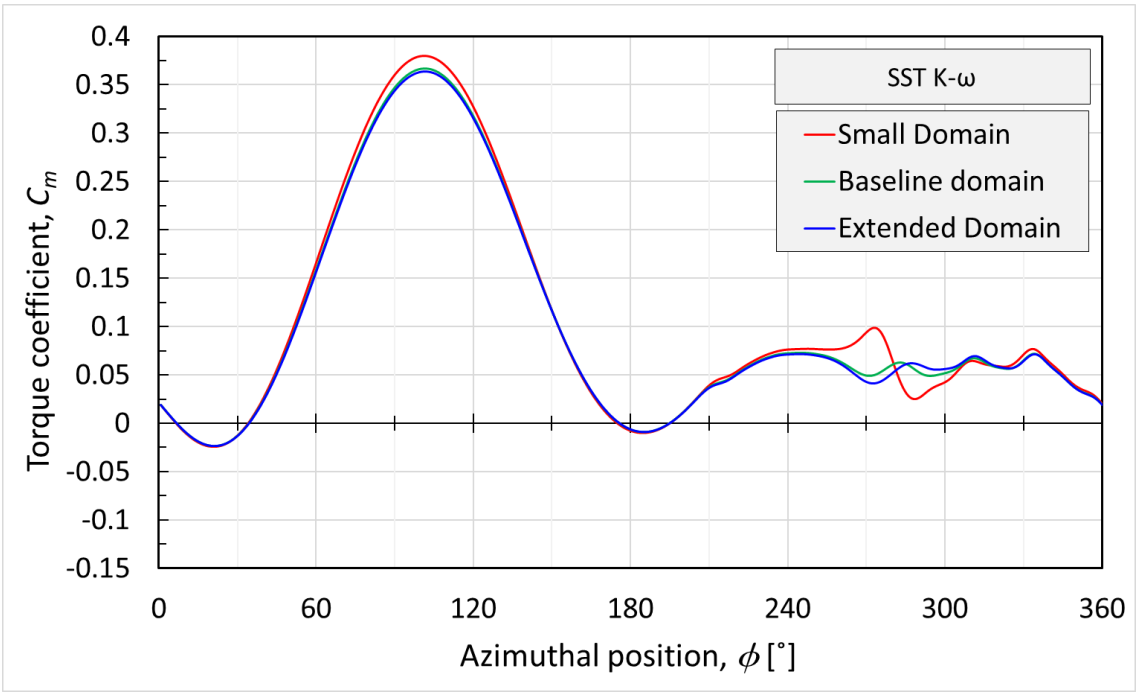

(a)

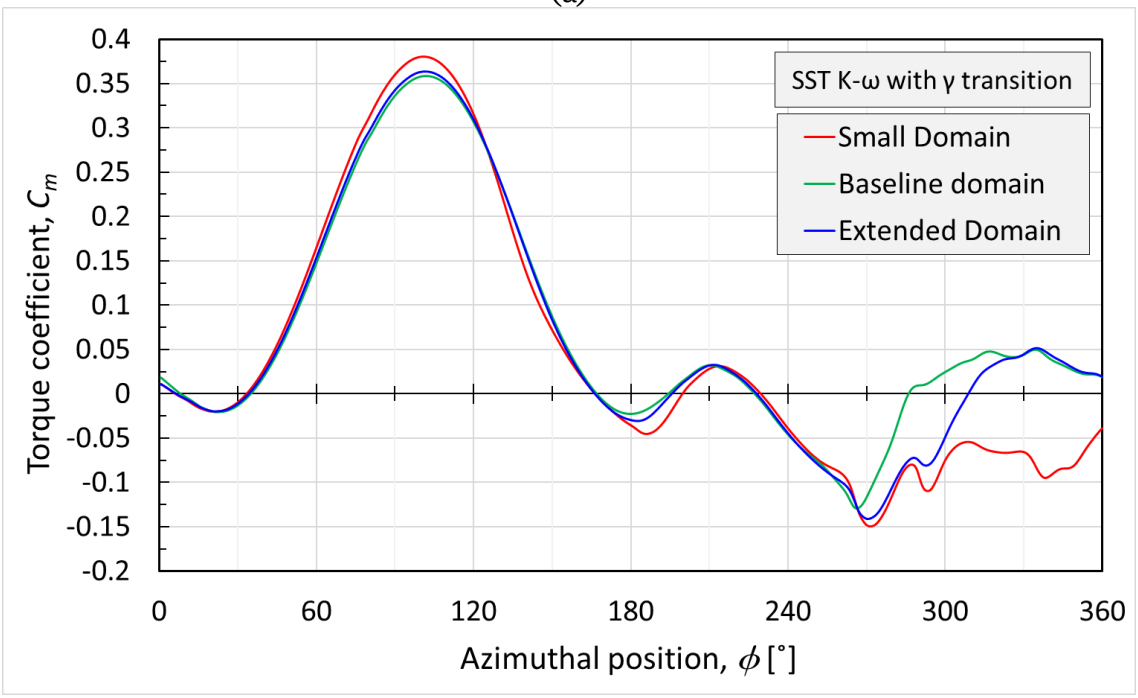

(b)

Figure 4.12 The effects of the domain size on the single blade instantaneous torque coefficient, C_m for (a) the SST k-ω and (b) the SST k-ω with the γ transition turbulence models.

4.2.5 **Time-step independency**

For such transient simulations, the time step size has a great influence on the convergence and the accuracy of the results, the time step size should be fine enough to capture the details of the rapid changes of the flow around the turbine in addition to obtaining a time step independent solution. For this purpose, a set of four different time step sizes have been selected to obtain a variety of fine temporal resolution over the cycle. Table 4.2 shows the selected time step sizes along with the equivalent temporal resolution per cycle and per each degree of the azimuthal angle. In addition, Table 4.2 shows the sensitivity of the time-averaged torque coefficient in the upstream part of the cycle to the change in the temporal resolutions relative to the baseline temporal resolution of 540 [time steps/cycle] for both the SST k-ω and SST k-ω with the γ transition models.

It is noticed from Table 4.2 that the sensitivity of the results to change in temporal resolutions is minimal and almost less than 0.5 % for the all tested cases. The reason for the low sensitivity to the time step size is due to the use of the coupled solver algorithm that enables the use of a large time-step size [192]. Figures 4.13 (a) and (b) shows the effects of the different temporal resolution on the instantaneous torque coefficient for both the SST k-ω and SST k-ω with the γ transition models, respectively.

Table 4.2 The implemented time step sizes with the corresponding temporal resolution.

No. of time steps per cycles [time steps/cycle]	The physical time step size [s]	No. of time steps per each degree of azimuthal angles [time step/°]	Sensitivity of the $\overline{C_m}$ in the upstream part of the cycle	
			SST k-ω	SST k-ω with γ transition
360	9.26×10^{-4}	1	0.44%	0.26%
540 (baseline)	6.17×10^{-4}	1.5	---	---
720	4.63×10^{-4}	2	-0.12%	-0.24%
1080	3.09×10^{-4}	3	+0.16%	0.49%

It is noticed from Figure 4.13 (b) that the instantaneous torque coefficient obtained by SST k-ω with the γ transition is more sensitive to the change in the temporal resolution, especially in the downstream part of the cycle. However, in terms of trends, the low resolution of 360 time-steps per cycle appears to have different behaviour, especially at ϕ= 270° and ϕ= 330°. In addition, in the case of the lowest temporal resolution of 360

time-steps per cycle using the SST k-ω with the γ transition, the results do not appear to be fully periodic and hence this low temporal resolution is not considered to be sufficient under the current operating conditions. In general, the temporal resolution of 540 time-steps per cycle is considered to have reasonable accuracy and computational cost. Therefore, it is selected for the further analyses. This temporal resolution corresponds to 1.5 time-steps per each azimuthal angle degree and a time step size of 6.17×10^{-4} seconds.

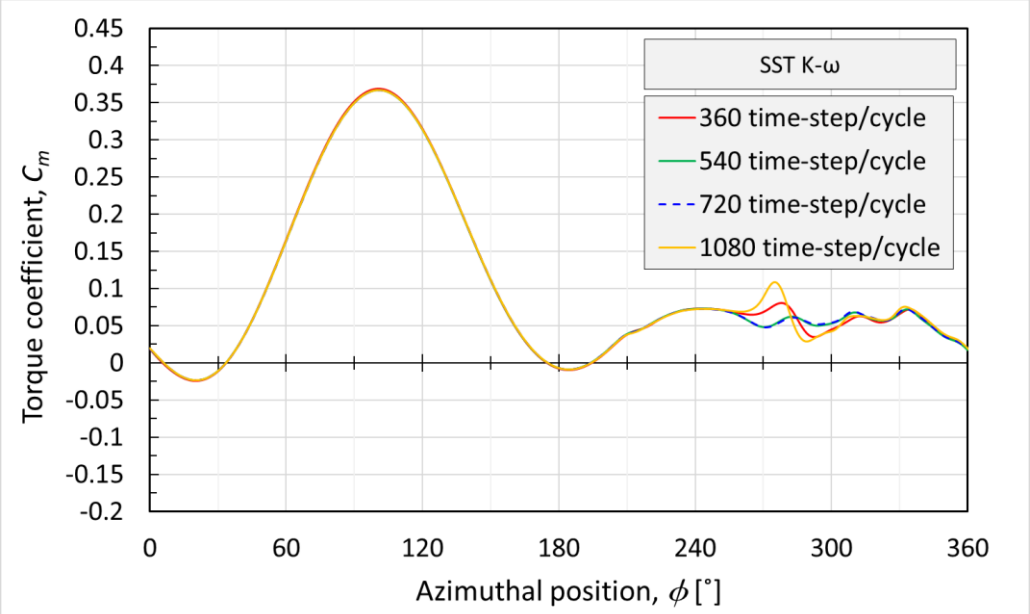

(a)

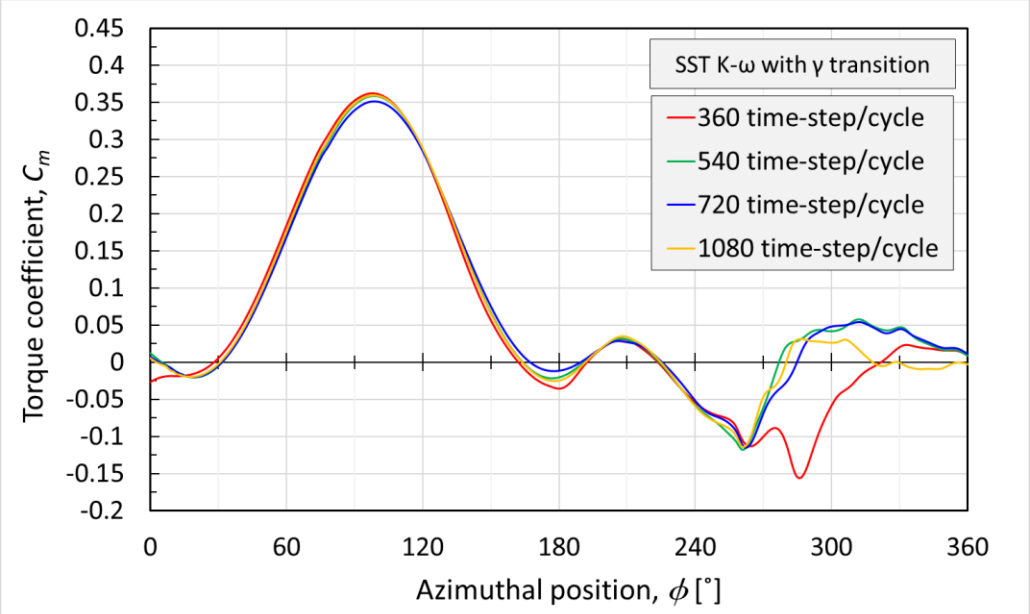

(b)

Figure 4.13 The effects of the temporal resolution on the single blade instantaneous torque coefficient, C_m for (a) the SST k-ω and (b) the SST k-ω with the γ transition turbulence models.

4.2.6 **Mesh independency study**

The computational mesh directly affects both the computational cost and the accuracy of the results. Therefore, the mesh should be optimised to accurately capture the details of the flow with a minimum element count to minimise the computational cost. In the 2D case, the optimisation of the number of elements is not prioritised as it is still affordable to perform the simulation with an extra-dense mesh in the High-Performance Computing (HPC) facilities. However, the 3D case introduces more challenges in the computational cost and hence it is crucial to minimise the number of elements while maintaining reasonable accuracy. This could be achieved by understanding the effect of the different selected mesh attributes on the obtained results and clustering the mesh efficiently in the significant regions. The aim of this section is to study the effects of the different mesh attributes on the results of the 2D simulations for both the SST k-ω and the SST k-ω with the γ transition models. These mesh attributes includes the number of nodes around the blade profile, the Growth Rate (GR) perpendicular to the blade profile, the maximum dimensionless wall distance, y+, at the maximum theoretical relative velocity point, i.e., ϕ= 0°, in addition to the global Refinement Factor (RF) which represents the mesh refinement, based on edge sizing, everywhere in the whole domain except the thin region around the blades in which the baseline GR and y+ is imposed to exclude their effect on the results.

Table 4.3 shows the features and the attributes of the eleven meshes that have been selected for the mesh independency study in addition to the sensitivity of the torque in the upstream part of the cycle to the change in the mesh attributes. Mesh 2D-A1 represents the baseline for the further comparisons with 1000 nodes clustered along the aerofoil profile, a GR of 1.05, a maximum y+ of 1, and a total number of elements of 920600. From the sensitivity data, it is clear that SST k-ω with the γ transition model is more sensitive to the changes in the mesh attributes. It is noticed that the results are highly sensitive to the change in the y+ and hence a fine y+ should always be used regardless of the increase in the computational cost. For the SST k-ω cases with a y+ <1, it could be concluded that solution is fairly independent of the other mesh attributes and good predictions could be obtained using coarse mesh attributes. The sensitivity results for RF, GR, and the node clustering around the blade profile are summarised in Figure 4.14. It is clear that the sensitivities to the increase in RF, the increase of the node

around the blade profile, and the reduction in the GR are less than or almost around 1%. Therefore, the baseline mesh is considered adequate for the further analyses.

Table 4.3 The implemented meshes and their attributes in addition to the sensitivity of the predicted results.

Name	Features and the total number of elements	No. of nodes around the aerofoil	Maximum y+ at the maximum theoretical relative velocity point	Sensitivity of the $\overline{C_m}$ in the upstream part of the cycle	
				SST k-ω	SST k-ω with γ transition
Mesh 2D-A1	Baseline mesh (920600 elements)	1000	≈ 1	---	---
Mesh 2D-A2	Refined chordwise (1105600 elements)	1500	≈ 1	-0.18%	-0.67%
Mesh 2D-A3	Coarsened chordwise (735600 elements)	500	≈ 1	0.62%	1.9%
Mesh 2D-A4	Coarsened chordwise (624600 elements)	200	≈ 1	0.66%	8.28%
Mesh 2D-A5	Lower growth rate (GR=1.03) (1030600 elements)	1000	≈ 1	-0.21%	-0.995%
Mesh 2D-A6	Higher growth rate (GR=1.1) (828600 elements)	1000	≈ 1	0.41%	4.04%
Mesh 2D-A7	Higher growth rate (GR=1.2) (774600 elements)	1000	≈ 1	0.55%	2.66%
Mesh 2D-A8	Higher y+ (764600 elements)	1000	≈ 25	-6.19%	-2.18%
Mesh 2D-A9	Extra higher y+ (732600 elements)	1000	≈ 60	-22.97%	-11.28%
Mesh 2D-A10	Coarse mesh (RF=0.5) (292300 elements)	500	≈ 1	-0.13%	2.97%
Mesh 2D-A11	Fine mesh (RF=2.0) (2854400 elements)	2000	≈ 1	1.07%	0.19%

Figure 4.15 (a) shows the effects of the number of nodes around the blade on the instantaneous torque coefficient based on the SST k-ω. It is clear that the effects of the number of nodes around the blade are not significant and there are some small discrepancies around ϕ= 270° due to the complexity of the interaction between the blade and the wake from the turbine shaft. However, the results based on the SST k-ω with the γ transition turbulence model are more sensitive to the change of the node resolution around the blade, especially in the downstream part of the cycle. In addition,

for several mesh resolutions using the SST k-ω with the γ transition, the results do not appear to be fully periodic. Figures 4.16 (a) and (b) show the effect of changing the growth rate on the instantaneous torque coefficient based on the SST k-ω and the SST k-ω with the γ transition turbulence model, respectively. While the growth rate has not any significant effect on the predictions based on the SST k-ω, there are some notable effects on the predictions based on the SST k-ω with the γ transition especially in the downstream part of the cycle. However, Figures 4.17 (a) and (b) shows that the dimensionless wall distance, y+, has significant effects on the trend and the peak value of the instantaneous torque coefficient for both the SST k-ω and the SST k-ω with γ transition.

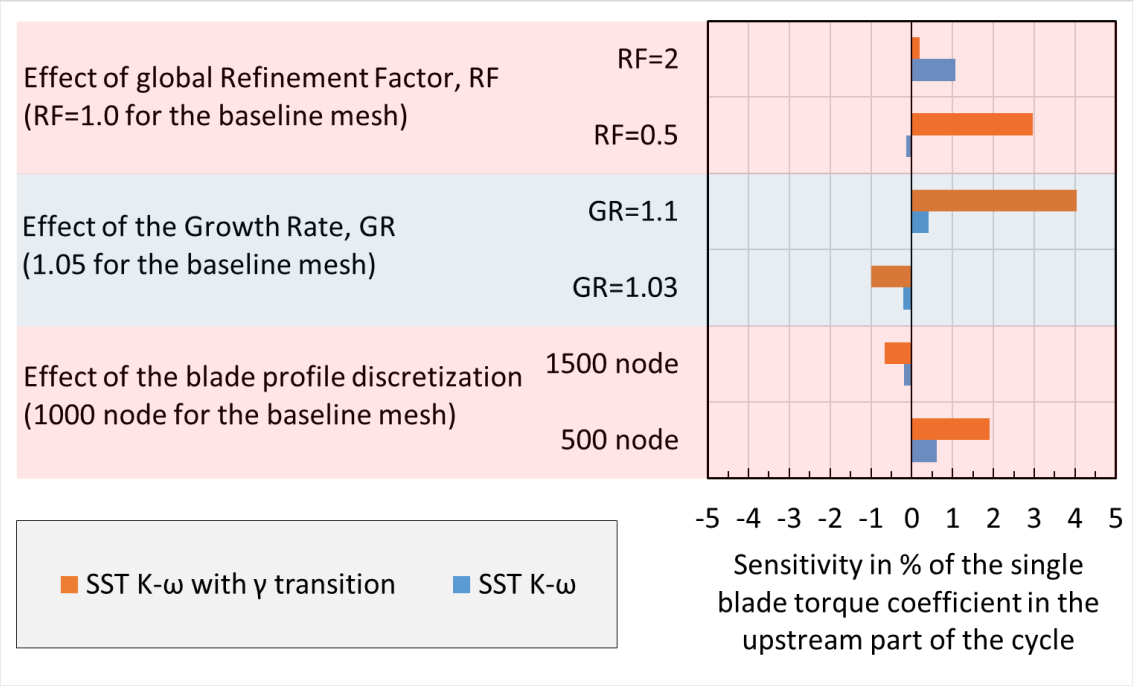

Figure 4.14 Summary of the sensitivity of the torque coefficient to the global refinement factor, growth rate, and the node clustering around the blade.

Both the SST k-ω and the SST k-ω with the γ transition use the enhanced wall treatment which is developed to give good predictions for a wide range of y+ without excessive error [192]. However, it is clear from Figures 4.17 (a) and (b) that the simulation of the VAWT requires a fine near-wall mesh that resolves the viscous sublayer rather than relying on the wall function approach. Figures 4.18 (a) and (b) show the effect of the global refinement on the predictions of the SST k-ω and the SST k-ω with the γ transition turbulence model, respectively. Despite the discrepancies in

the predictions of the transition model, the differences between the baseline and the fine meshes are considered acceptable. In addition, it is clear that a good prediction could be achieved with a coarse mesh, especially in the case of the SST k-ω model.

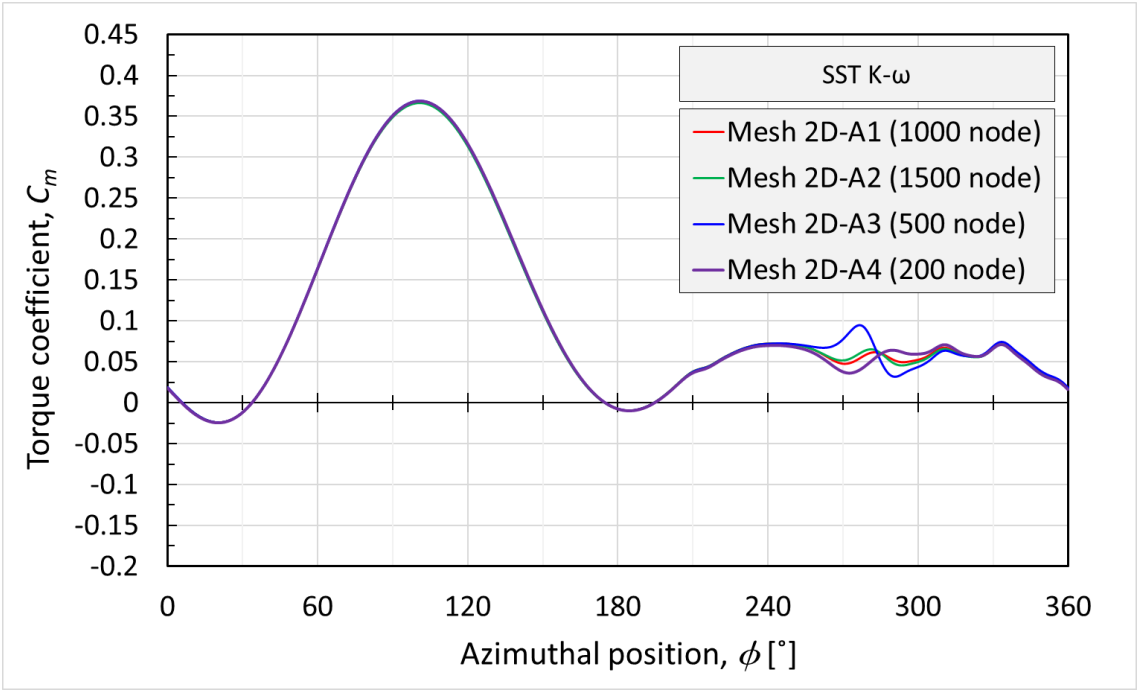

(a)

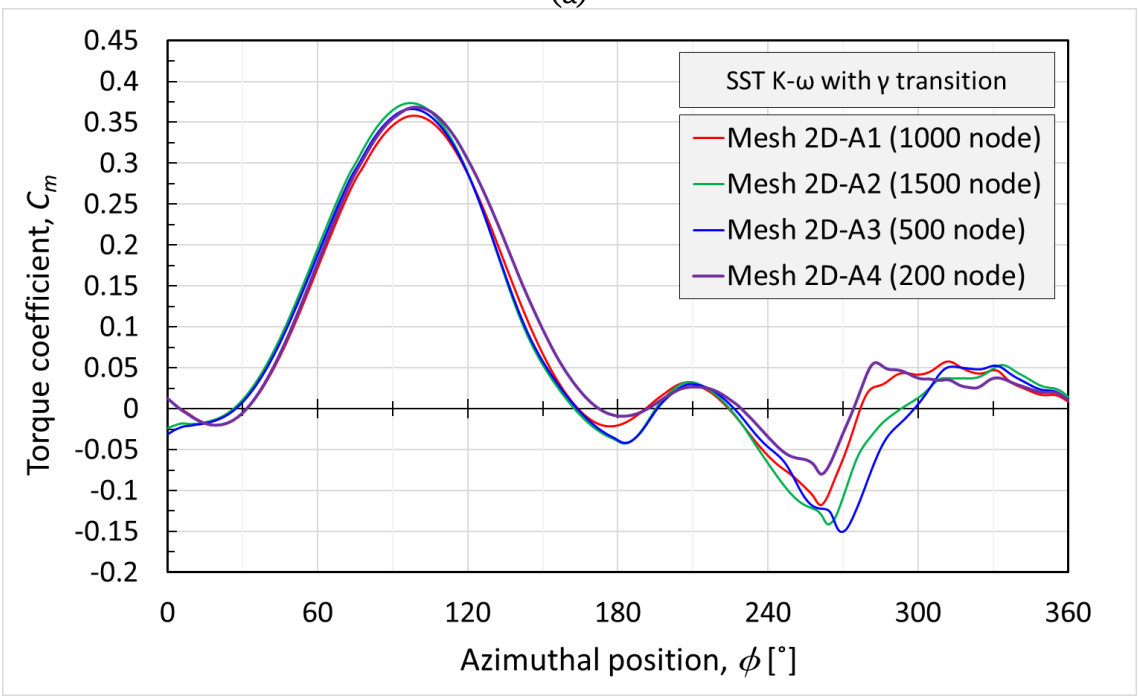

(b)

Figure 4.15 The effects of the number of nodes around the blade profile on the single blade instantaneous torque coefficient, C_m for (a) the SST k-ω and (b) the SST k-ω with the γ transition turbulence models.

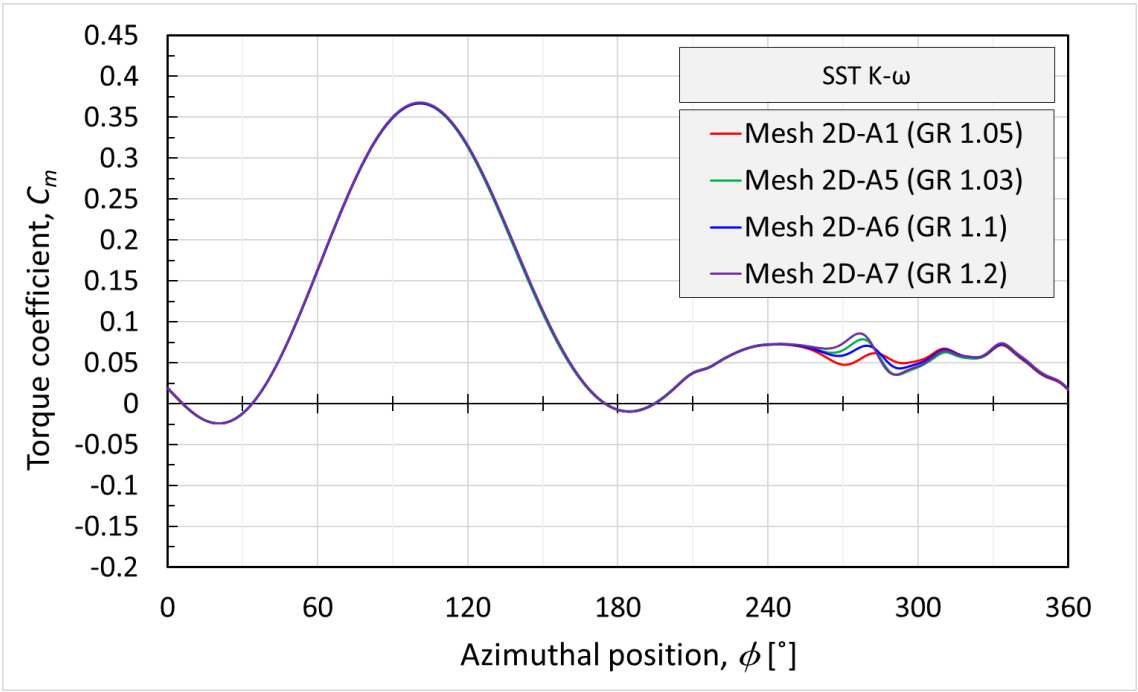

(a)

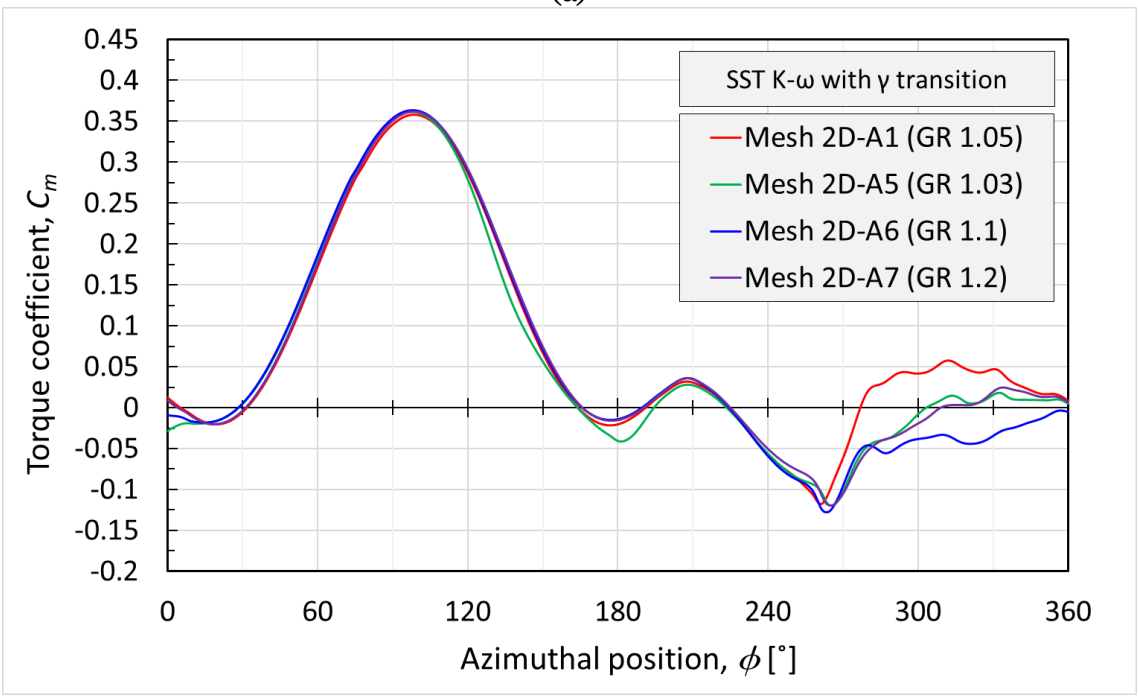

(b)

Figure 4.16 The effects of the Growth Rate, GR, on the single blade instantaneous torque coefficient, C_m for (a) the SST k-ω and (b) the SST k-ω with the γ transition turbulence models.

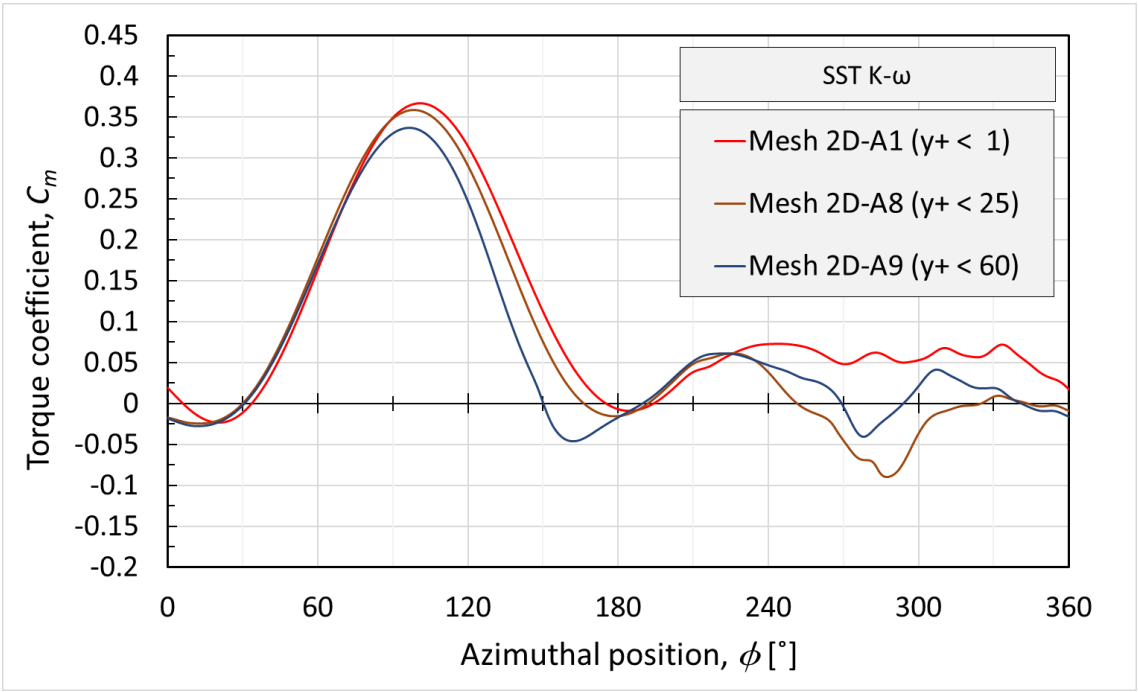

(a)

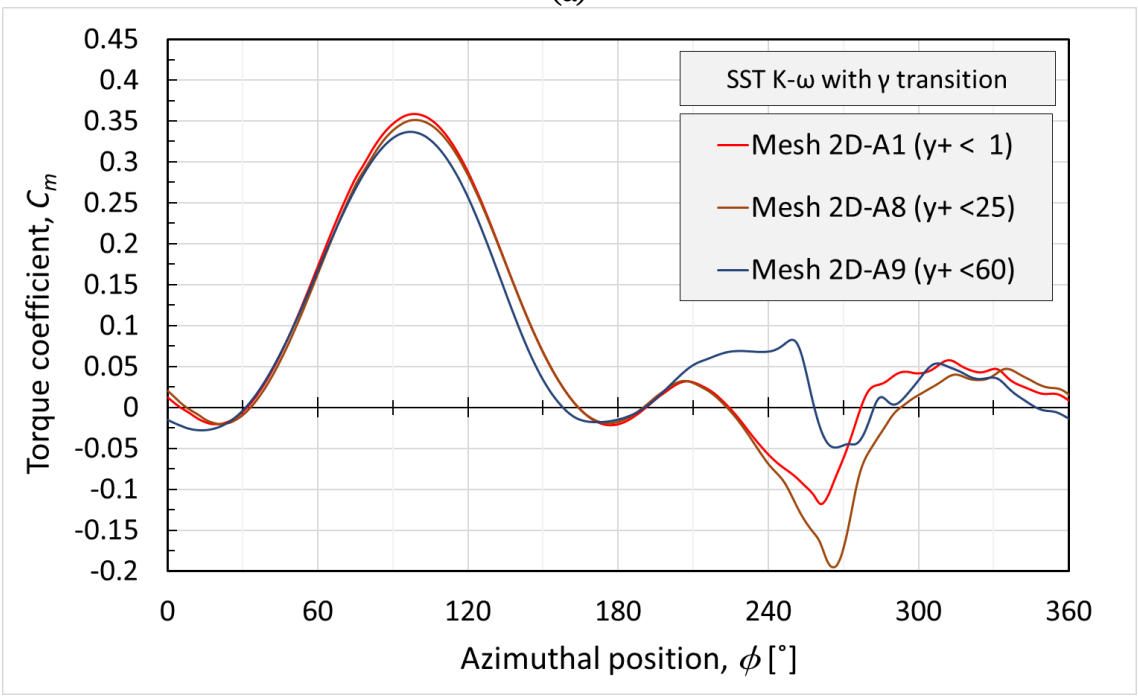

(b)

Figure 4.17 The effects of the maximum dimensionless wall distance, y+, on the single blade instantaneous torque coefficient, C_m for (a) the SST k-ω and (b) the SST k-ω with the γ transition turbulence models.

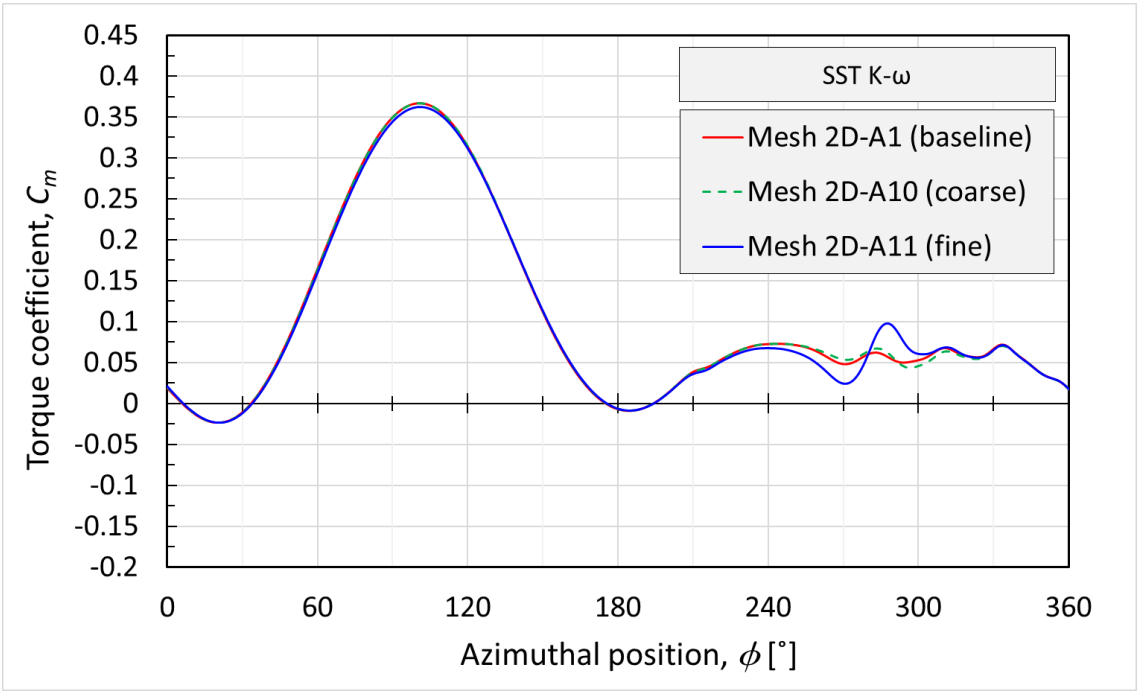

(a)

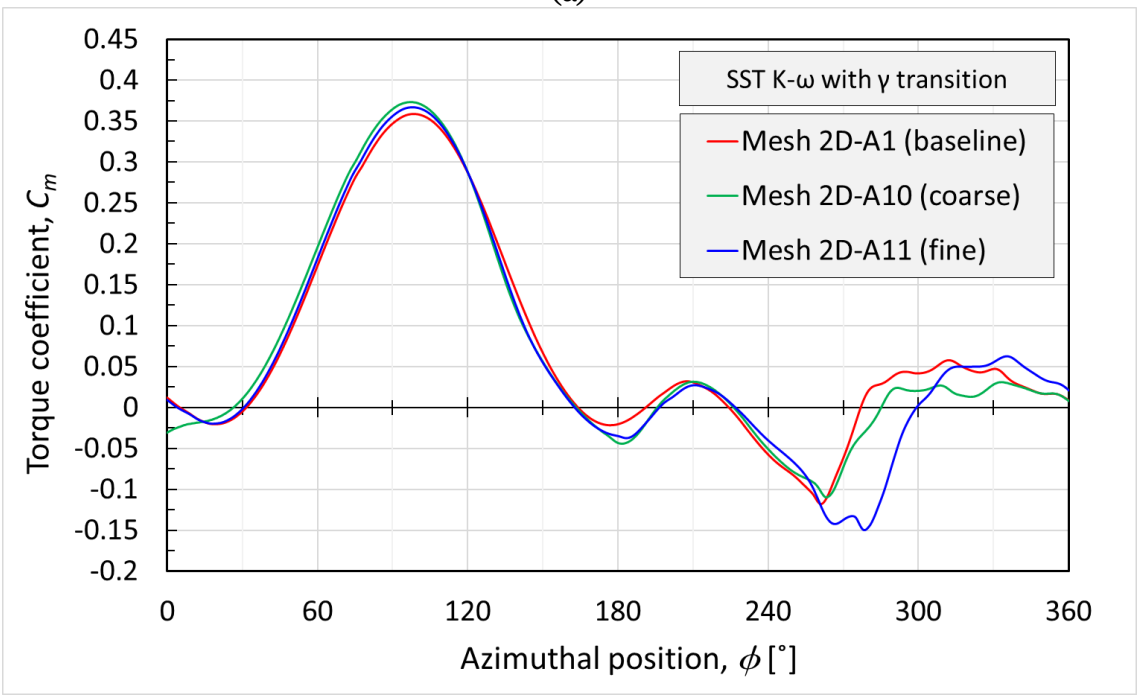

(b)

Figure 4.18 The effects of the global Refinement Factor, RF, on the single blade instantaneous torque coefficient, C_m for (a) the SST k-ω and (b) the SST k-ω with the γ transition turbulence models.

4.2.7 **Effect of the order of the spatial and temporal discretisation**

As mentioned in Section 4.2.1, the second-order schemes are used as the baseline schemes for the spatial and temporal discretisation in the present study. In order to assess the solution sensitivity to the order of the spatial discretisation for the momentum and turbulence model equations, three different discretisation schemes are considered, namely the First-Order Upwind, the Second-Order Upwind, and the Third-Order Quadratic Upwind Interpolation for Convective Kinematics (QUICK) schemes. Figures 4.19 (a) and (b) show the effect of the spatial discretisation order on the predicated instantaneous torque coefficient for both the SST k-ω and the SST k-ω with the γ transition models, respectively. It is clear that the differences between the second and the third-order schemes are almost negligible for the SST k-ω case. However, the results obtained from the SST k-ω with the γ transition model is more sensitive to the order of the discretisation scheme. The differences in the time-averaged torque coefficient in the upstream part between the second and the third-order scheme are less than 0.1% for both the SST k-ω and the SST k-ω with the γ transition model and hence the Second-Order Upwind scheme is considered adequate for the further analyses.

In terms of the transient formulations, both the First-Order and Second-Order Implicit schemes are investigated. Figures 4.20 (a) and (b) show the effect of the temporal discretisation order on the predicated instantaneous torque coefficient for both the SST k-ω and the SST k-ω with the γ transition models, respectively. It is clear that the results obtained based on the SST k-ω with the γ transition model are more sensitive to the order of the discretisation scheme. The differences in the time-averaged torque coefficient in the upstream part between the First and the Second-Order scheme are about 1.3% and 4.8% for the SST k-ω and the SST k-ω with the γ transition model, respectively. Due to the considerable differences between the predictions of the First and Second-Order schemes, the Second-Order Implicit scheme is selected for the further analyses.

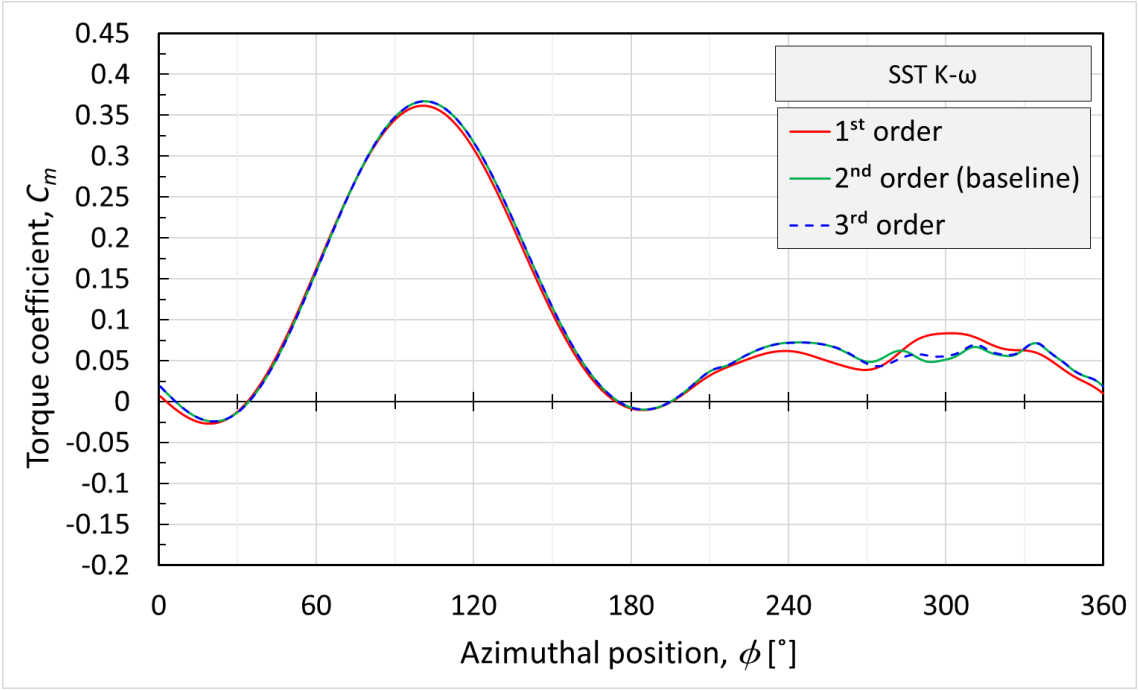

(a)

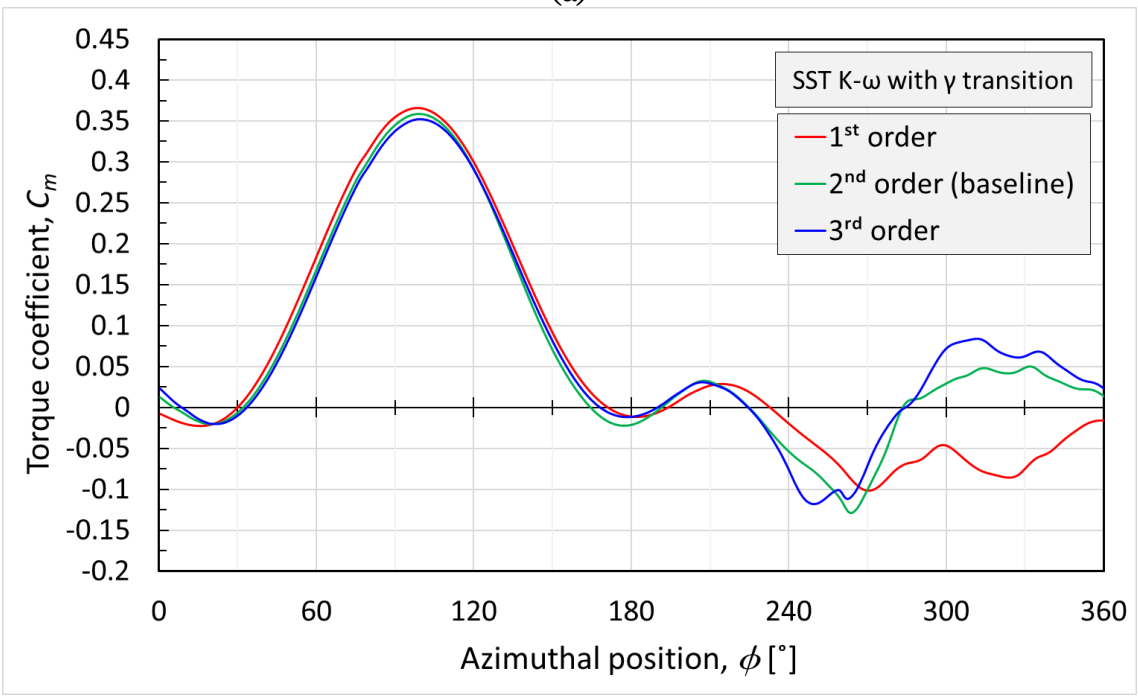

(b)

Figure 4.19 The effects of the order of spatial discretisation on the single blade instantaneous torque coefficient, C_m for (a) the SST k-ω and (b) the SST k-ω with the γ transition turbulence models.

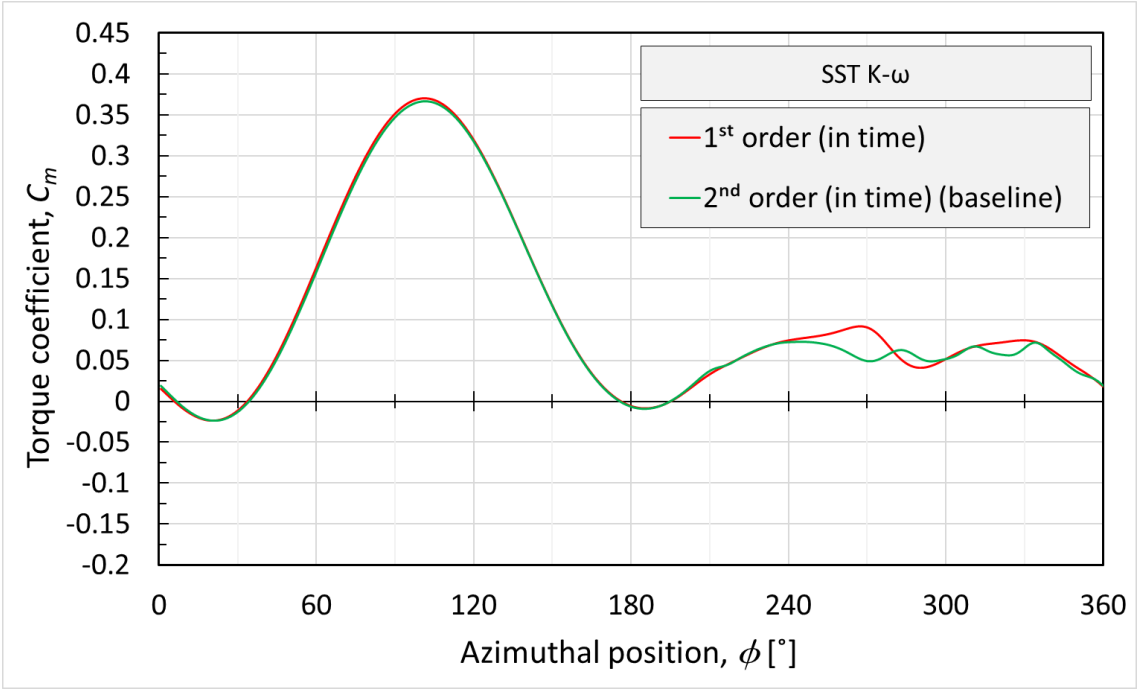

(a)

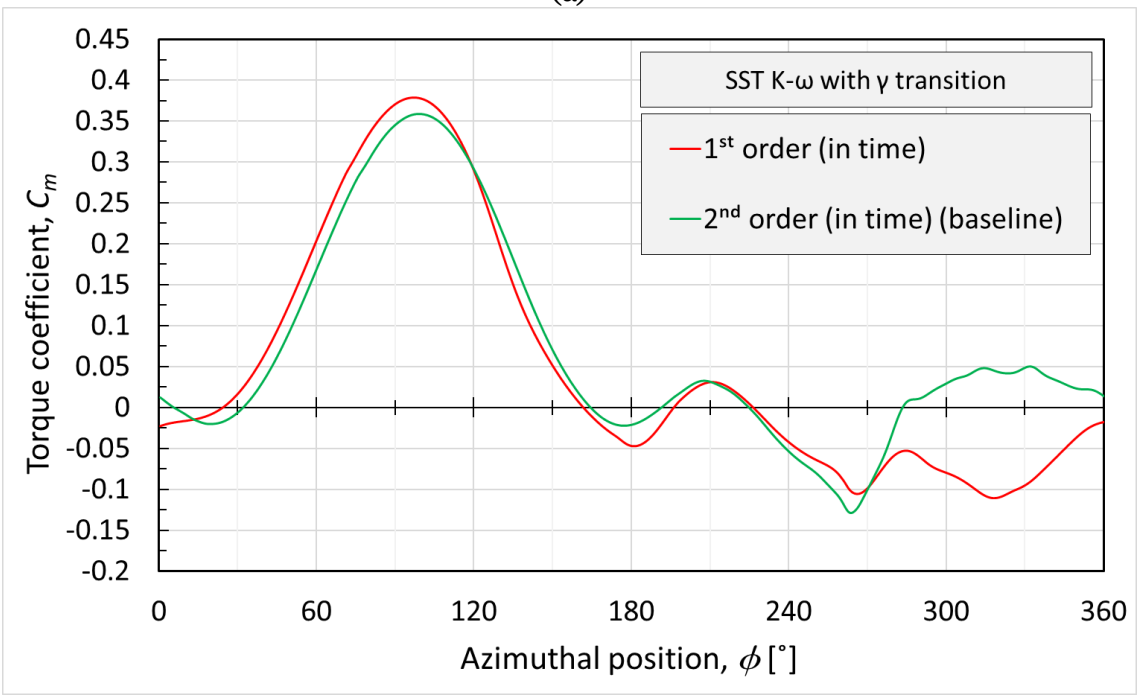

(b)

Figure 4.20 The effects of the order of temporal discretisation on the single blade instantaneous torque coefficient, C_m for (a) the SST k-ω and (b) the SST k-ω with the γ transition turbulence models.

4.2.8 **Conclusions**

Several sensitivity studies are carried out for the verification of the 2D model. In general, the results obtained using the SST k-ω with the γ transition turbulence model are more sensitive to any change in the model attributes. However, the baseline model is found to be adequate for the simulation of the 2D VAWT with a sensitivity of less than about 1% to any refinement of the model attributes for both the SST k-ω and the SST k-ω with γ transition. Despite the discrepancy in the downstream part of the cycles, the solution at the 5th and 6th cycles are considered to be almost periodic for the SST k-ω and the SST k-ω with γ transition, respectively. The size of the baseline domain is verified to have an insignificant effect on the predicted results. A temporal resolution of 540 time-steps per cycle is selected. The second-order scheme is found to be more suitable for the spatial and temporal discretisation. The baseline mesh with 920600 elements, a GR of 1.05, a maximum y+ of 1, and 1000 nodes around the blade profile are verified to be adequate for the VAWT simulations. However, this baseline 2D mesh is not optimised to minimise the computational cost, as it is affordable to carry out the simulations on the HPC facilities even with extra fine 2D mesh. The sensitivity analysis of the different mesh attributes, based on the SST k-ω model, suggests that by maintaining a good value for y+ then a relatively accurate solution could be obtained using a coarse mesh.

4.3 **3D CFD modelling**

4.3.1 **Model description**

The numerical specifications of the 2D CFD model, as clarified in Section 4.2.1, are adopted for the 3D case. The 3D double precision version of ANSYS FLUENT is utilised. Since the VAWT geometry is symmetrical about its mid-span section, only the upper half of the rotor is modelled and the turbine mid-span plane is subjected to the symmetric boundary condition. This assists to reduce computational cost [139]. Figure 4.21 illustrates the shape and dimensions of the 3D domain. The dimensions of the mid-span plane are the same as the baseline 2D domain size. The height of the domain is select to be 10 turbine diameters that is around 17 turbine heights. This is considered large enough as only half of the turbine height is modelled. The boundary conditions

and frame motions settings, clarified in Sections 4.2.1 and 4.2.2, are adopted for the 3D case. Figure 4.21 shows the location of the inlet, outlet, and symmetric boundary conditions. The domain is divided into four subdomains, as shown in Figure 4.22, which represent the region around each blade, the region around the rotor and the surrounding region. Non-conformal mesh interfaces are used to connect the relevant subdomains. It is found that a temporal resolution of 540 time-steps per cycle is sufficient and the results are reasonably periodic at the 5^{th} cycle for the SST k-ω and the 6^{th} cycle for the SST k-ω with the γ transition model. It should be noted that in some cases it may take around 20 cycles to get a periodic solution, but for our cases 5-6 cycles have been enough. In addition, 30 iterations per time step are found to be sufficient to obtain a converged solution. This is found to be consistent with the detailed 2D sensitivity studies in Sections 4.2.54.2.3 and 4.2.5.

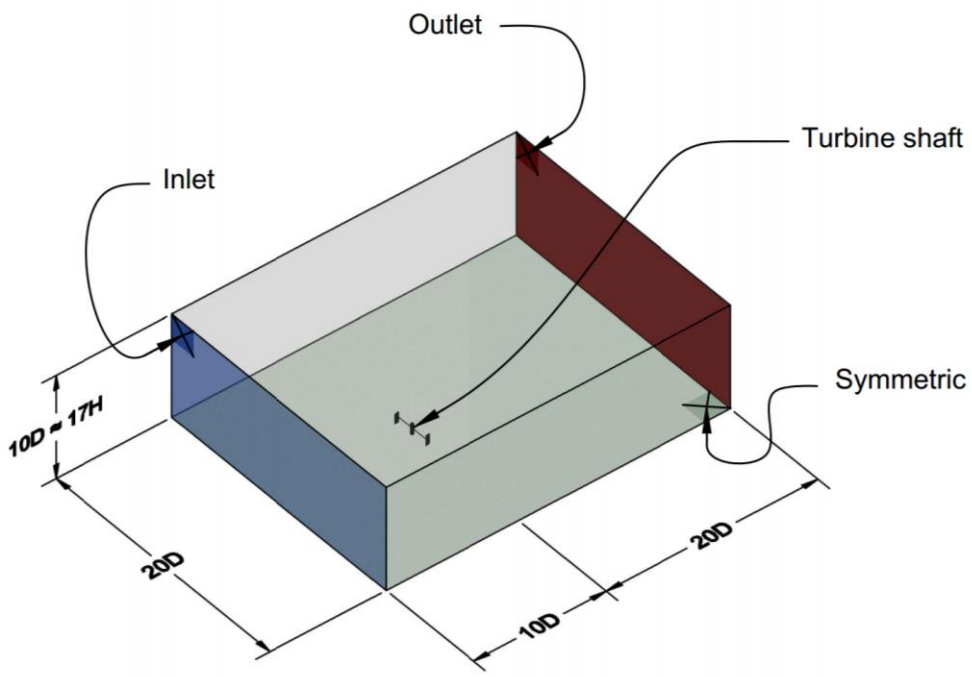

Figure 4.21 Main boundary conditions and dimensions of the 3D computational domain for a 2 bladed turbine (the drawing is not to scale).

4.3.2 3D mesh topology and mesh independency study

As mentioned in Section 4.2.8, based on the sensitivity analysis of the different mesh attributes on the 2D predictions using the SST k-ω model, relatively good predictions could be obtained by maintaining y+ <1 even with a relatively coarse mesh. Due to the high computational cost of the 3D model, the use of a space-efficient mesh is essential

to have a computationally affordable 3D model without sacrificing the accuracy. In order to achieve this, multi-block structured mesh topologies are mainly used for the blades and rotor subdomains, except in a very small region near the tips of blades. For these subdomains, 1125 structured meshing blocks have been constructed. In contrast with unstructured mesh, the structured mesh features a higher degree of control on how the nodes are distributed and this enables to use fine mesh distribution in the sensitive region while gradually transform to a coarse distribution where the solution gradients are expected to be minimal. In addition, the structured mesh enables the freely controlling of the mesh distributions in the blade-spanwise direction regardless of the fine mesh distributions perpendicular to the blade surface.

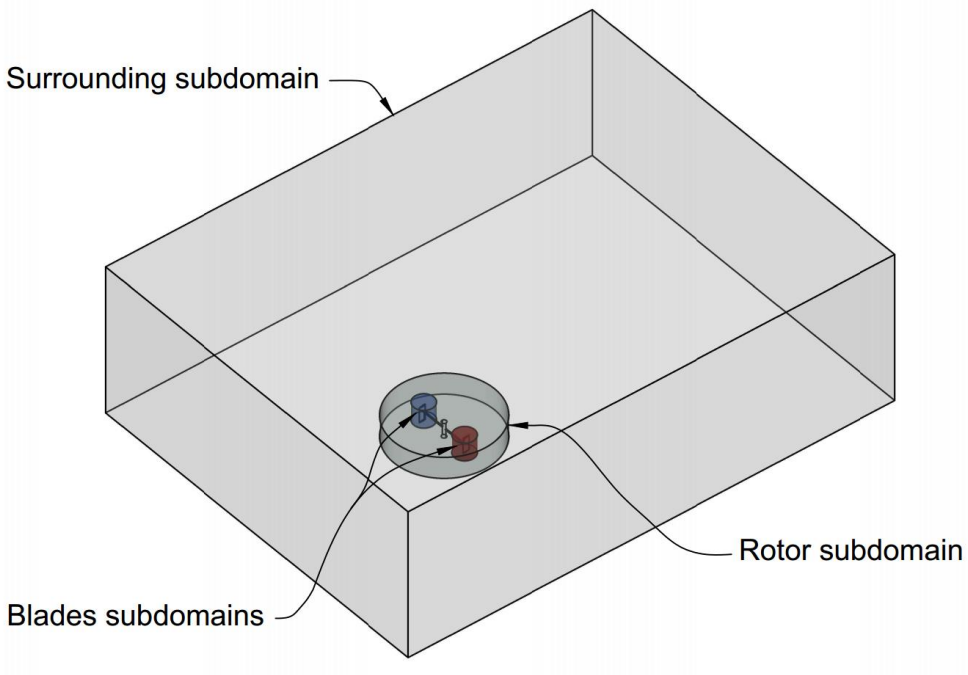

Figure 4.22 Schematic of the 3D computational domain and its subdomains (the drawing is not to scale).

The baseline mesh has 180 nodes around the blade cross-section with 50 divisions in the spanwise direction along the half blade height. The boundary layer mesh around the blade has 60 mesh layers with a GR of 1.1 and y+ <1 at the maximum theoretical relative velocity point. The mesh clustering around the blade is shown in Figure 4.23 on the symmetric plane that represents the blade mid-span. Figure 4.24 shows the structured mesh topology on the symmetric plane through the blades and rotor subdomains. An illustration of the mesh clustering around the blade and its adjacent

arm is shown in the sectional views in Figure 4.25 while the mesh clustering near the blade tip is shown in Figure 4.26.

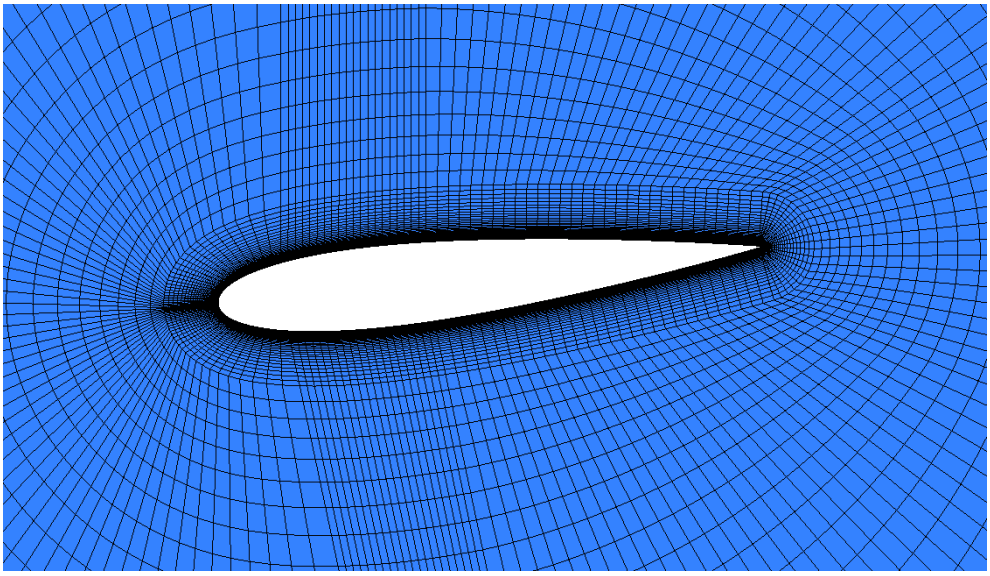

Figure 4.23 The baseline mesh on the symmetric plane around the blade with a pitch angle of 6°.

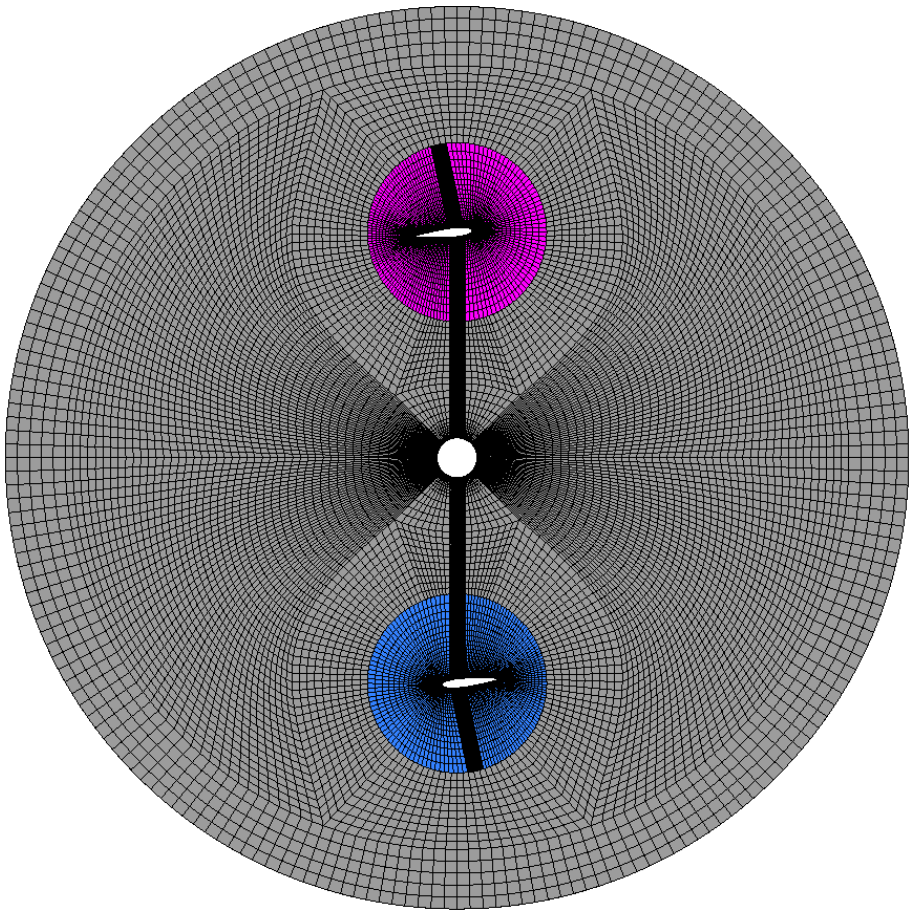

Figure 4.24 The baseline mesh on the symmetric plane for the blades and rotor subdomains.

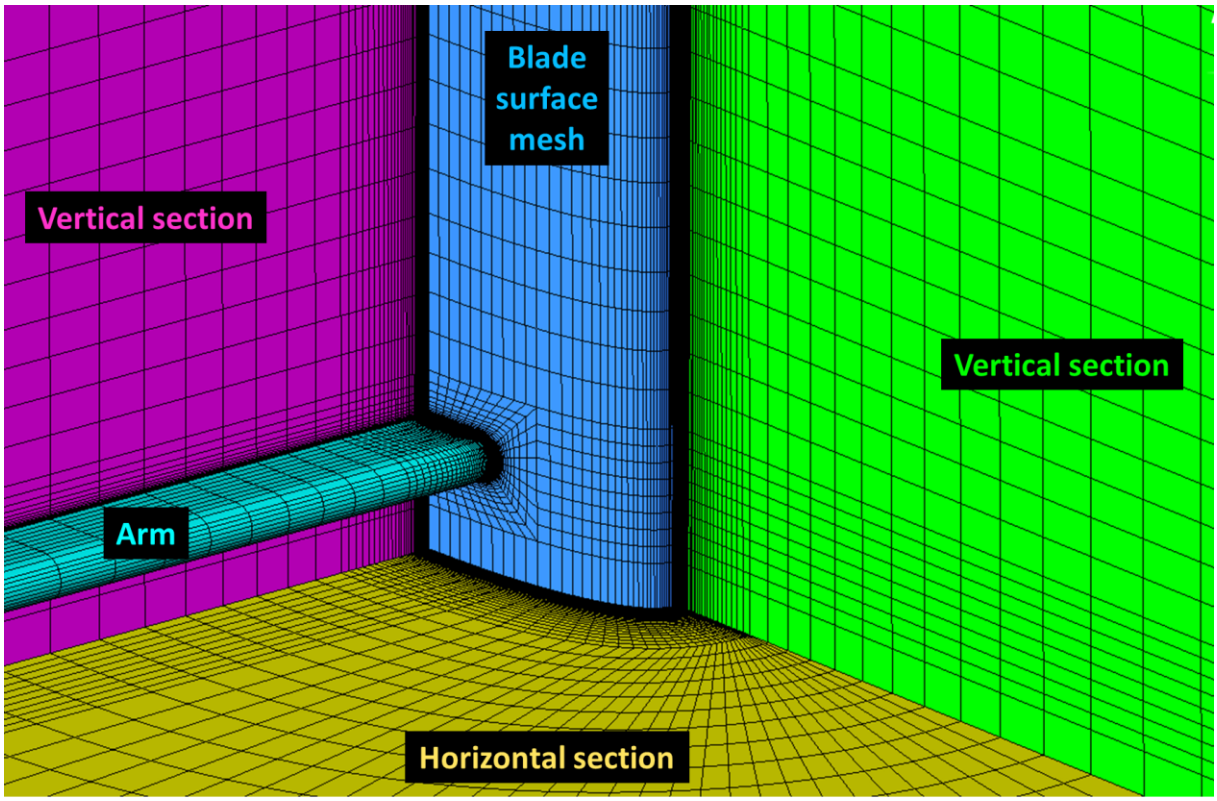

Figure 4.25 An illustration of the sectional views of the 3D baseline mesh showing the mesh clustering around the blade and adjacent arm.

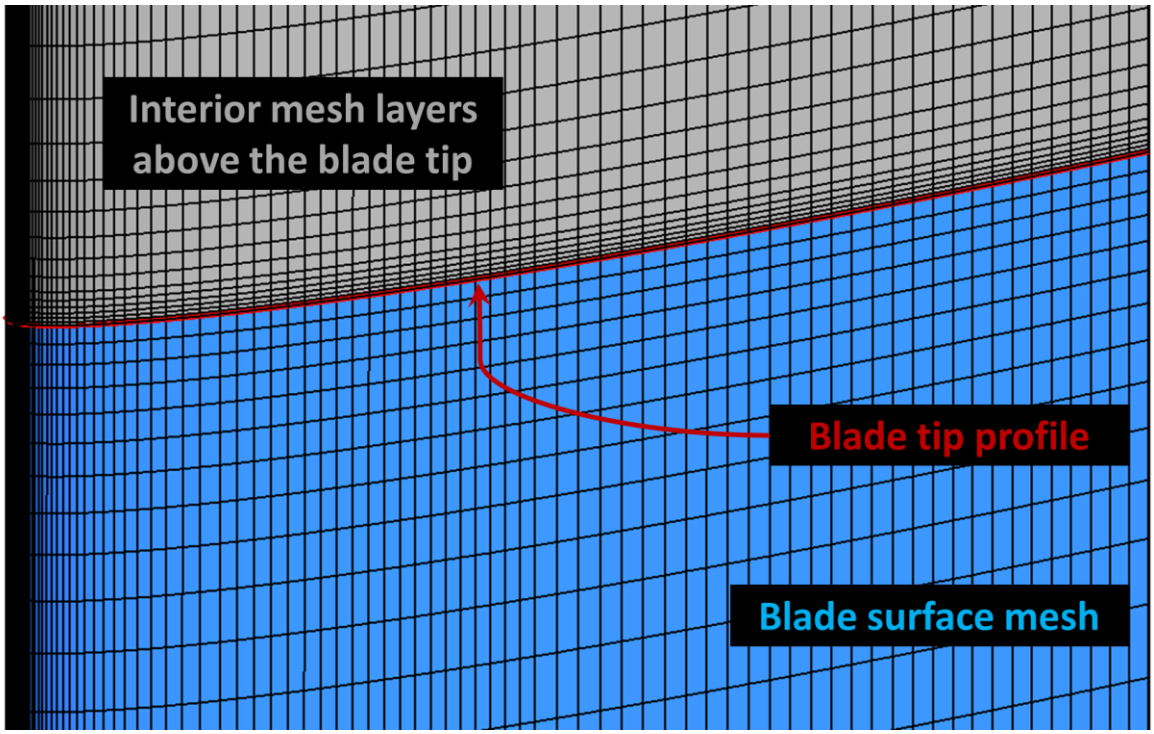

Figure 4.26 Mesh clustering near the blade tip.

Due to the chosen large domain-size, deep attention is given to the meshing of the surrounding subdomain. It is required to have a relatively fine mesh around the rotor zone and along the turbine wake zone. However, the mesh sizes elsewhere need to be relatively large in order to reduce the number of elements and hence the computational cost. In order to meet these requirements, the CutCell meshing technique [203] is used in the mesh of the surrounding subdomain. This technique helps to build predominantly a Cartesian mesh which is mainly consisted of hexahedral elements with good aspect ratio everywhere. In addition, it could sustain a high growth rate without building any high skewed cells. Different sizing controls are imposed to generate a relatively fine mesh near the rotor and in the wake region as shown in Figure 4.27. It is noticed that the CutCell meshing technique assists to efficiently distribute the elements with different sizes in a more flexible way in contrast with the structured meshing techniques. However, the structured meshing still offers a higher degree of control that is more valuable in meshing the regions near the turbine blades.

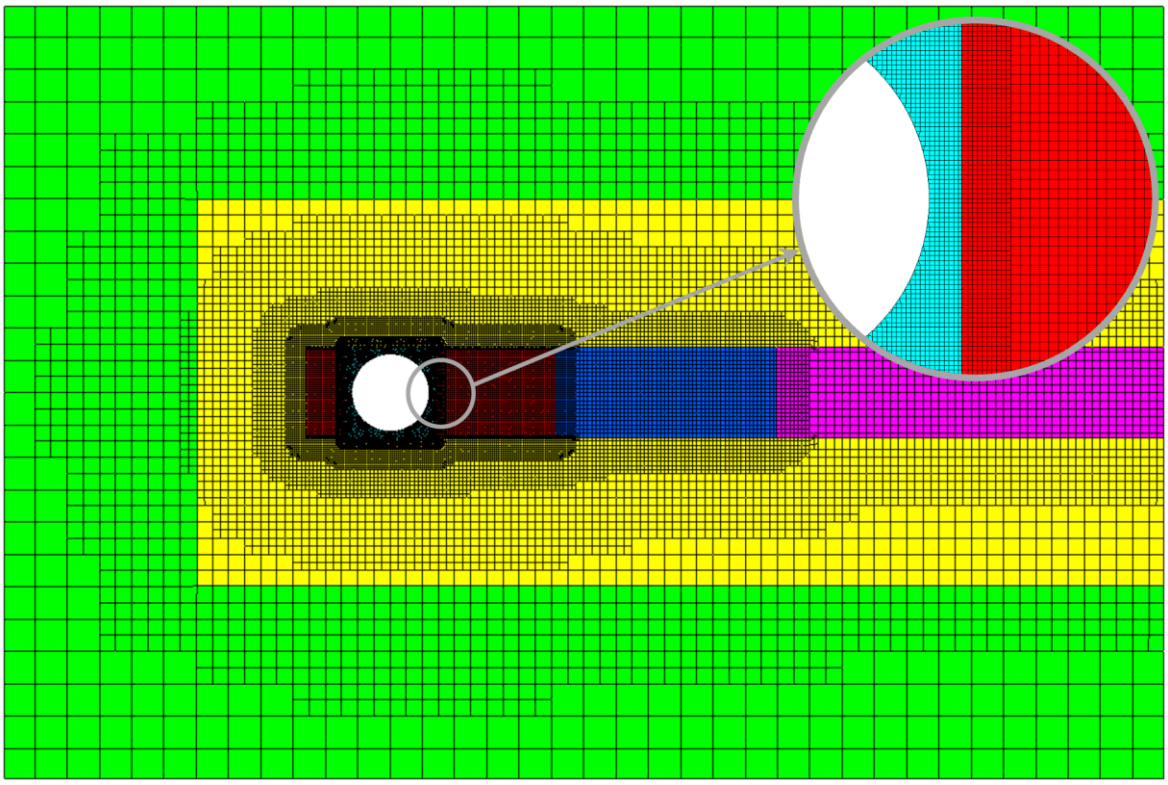

Figure 4.27 An illustration of the baseline 3D mesh on the symmetric plane of the surrounding subdomain showing the CutCell mesh with a magnified view of the region near the rotor interface. The regions with different colours represent different targeted element sizes, namely 0.2C, 0.4C, 0.8C, 1.6C, 5C, and 20C where C is the blade chord.

The baseline mesh has 3,838,303 elements in total. In order to verify the mesh independence, two other meshes are constructed and used to check the effect of the mesh refinement on the predicted results. The three meshes have the same near-wall resolution in order to eliminate the effect of the near-wall modelling on the mesh independency. The boundary layer mesh around the blade has 60 mesh layers with a GR of 1.1 and y+ <1 at the maximum theoretical relative velocity point. This includes the coarse 3D mesh with an RF of 0.8 and the fine 3D mesh with an RF of 1.3. The values of the RF are selected using the cubic root of the targeted number of elements, particularly 0.5 for the coarse mesh and 2.0 for the fine mesh. Table 4.4 shows the specifications of the coarse, fine, and baseline meshes in addition to the effect of the mesh refinement on the time-averaged torque coefficient in the upstream part of the cycle. For the coarse and fine meshes, the number of elements ratios are 0.66 and 2.05 for the targeted number of elements ratios of 0.5 and 2.0, respectively. This suggests that the use of the cubic root of the targeted number of element ratio assists to achieve a good estimation of the RF.

Table 4.4 The implemented 3D meshes and their attributes in addition to the sensitivity of the predicted results.

Name	Number of nodes around the blade cross-section and the total number of elements	Refinement factor	The ratio between the number of elements relative to the baseline mesh	Sensitivity of the $\overline{C_m}$ in the upstream part of the cycle	
				SST k-ω	SST k-ω with γ transition
Mesh 3D-A1 (Baseline mesh)	180 nodes (3,838,303 elements)	1	1	---	---
Mesh 3D-A2 (Coarse mesh)	180×0.8= 144 nodes (2,540,426 elements)	$\sqrt[3]{0.5} \approx 0.8$	0.66	-0.2 %	-1.8 %
Mesh 3D-A3 (Fine mesh)	180×1.3= 234 nodes (7,872,013 elements)	$\sqrt[3]{2.0} \approx 1.3$	2.05	-0.9 %	-0.6 %

Figures 4.28 (a) and (b) show the effect of the 3D mesh refinement on the instantaneous torque coefficient. Based on the SST k-ω with the γ transition turbulence model, it is observed that that the 3D model is less sensitive to the mesh refinement in contrast with the 2D model. This is clear in the comparison between the effects of the global mesh refinement in the 2D case in Figure 4.18 (b) against the 3D

case in Figure 4.28 (b). However, it is observed that the solution periodicity and the time-step independence of the 3D model are in line with the conclusions of the 2D verification studies in Section 4.2.

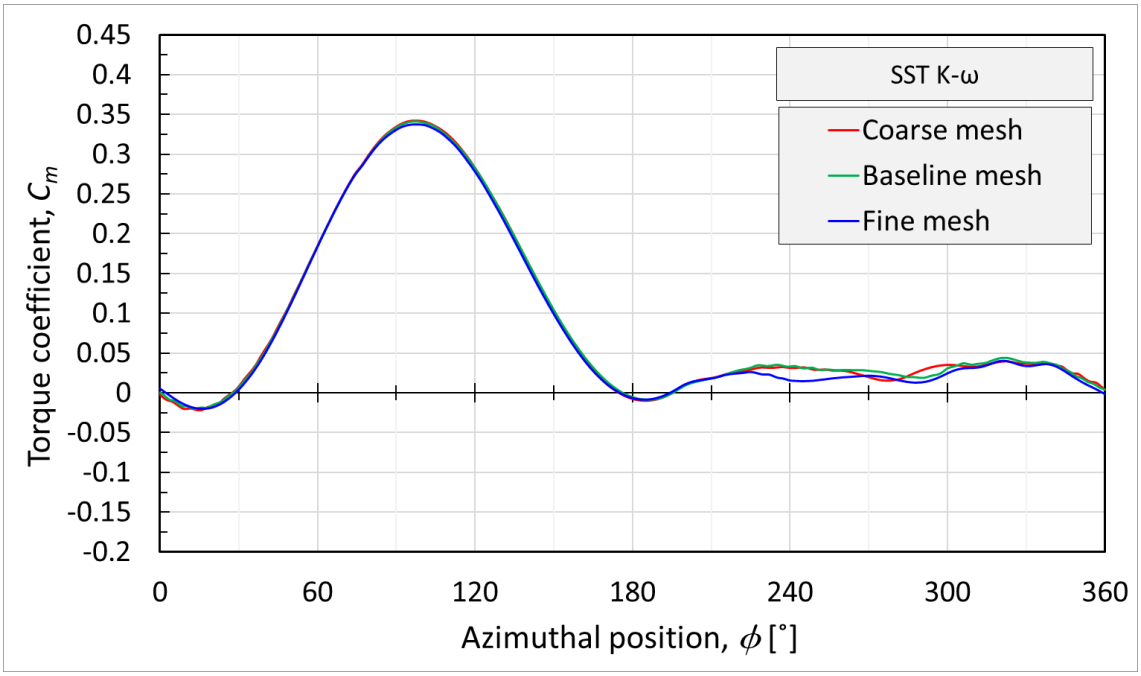

(a)

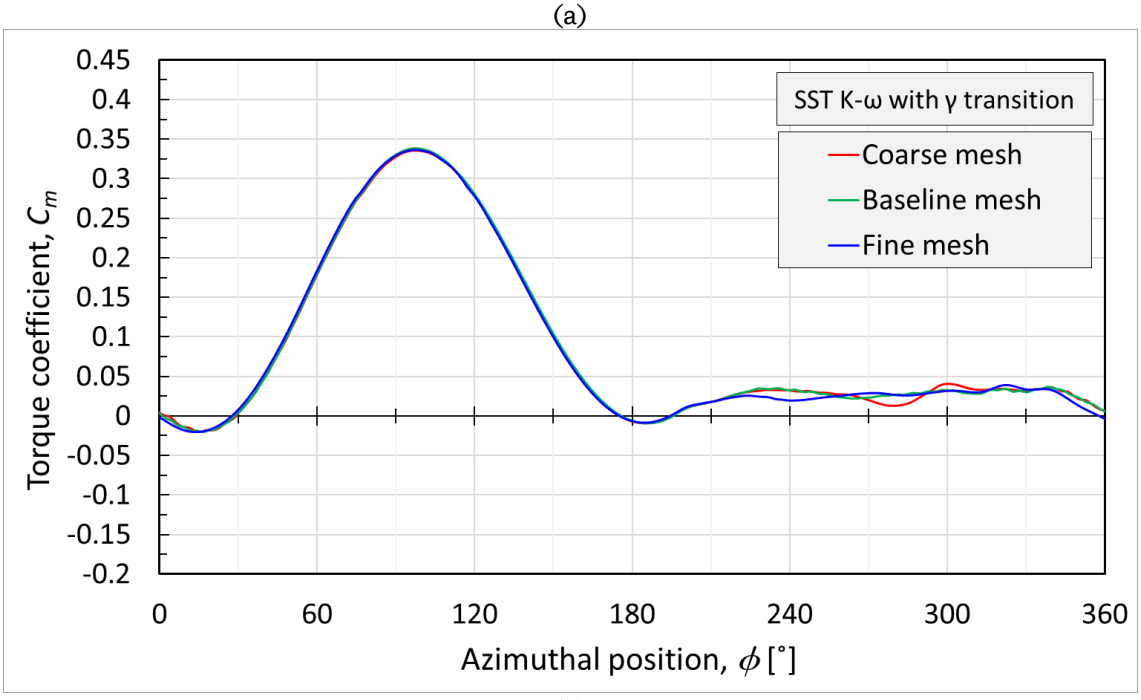

(b)

Figure 4.28 The effects of the 3D mesh refinement on the single blade instantaneous torque coefficient, C_m for (a) the SST k-ω and (b) the SST k-ω with the γ transition turbulence models.

4.3.3 **Conclusions**

In contrast with the 2D case, the 3D results based on the SST k-ω with the γ transition are found to be less sensitive to the change in the mesh refinements. A computationally affordable 3D model is constructed based on a space-efficient mesh. This mesh maintains a fine mesh resolution perpendicular to the blade surface where the strong gradients exist due to the boundary layer effects while maintaining a relatively coarse distribution where the changes in the flow variables are minimal. This coarse distribution is implemented in the spanwise direction away from the blade tip and in the regions far from the rotor and its wake. In order to build such space-efficient mesh, the use of multi-block structured mesh topologies is found to be essential in the regions near the rotor. In addition, the CutCell meshing technique is found to be useful in the discretisation of the large extended domain around the rotor due to its high growth rate and excellent orthogonal quality.

In summary, both the 2D and 3D models have been verified numerically. The baseline 2D mesh with 920,600 elements and the baseline 3D mesh with 3,838,303 elements are selected for the further analyses.

5 THE EFFECT OF DIMENSIONALITY AND TURBULENCE MODEL ON THE CFD PREDICTIONS OF VAWTS

5.1 Overview

The aim of this chapter is to validate both the 2D and 3D results against the experimental data in addition to study the effects of the model dimensionality on the behaviour of the SST k-ω and the SST k-ω with the γ transition turbulence models. The 3D flow patterns around the blade are visualised in order to better understand the separation flow structure. Furthermore, the 3D results are compared to the experimental data at different spanwise locations in order to examine the capability of the 3D model in the prediction of the 3D flow characteristics around the turbine. In order to differentiate between the effects of the 3D flow behaviour and the influence of the supporting arms, the 3D results are compared both with and without the modelling of the arms.

The validations of the CFD results are based on the comparisons with the experimental data obtained by Li et al. [180] for a two-bladed configuration with the NACA 0015 aerofoil and 6° of fixed pitch. The experimental model has a diameter of 1.7 m, a chord length of 0.225 m and a blade height of 1.02 m. Their experiments were carried out on an open test section of a closed-circuit wind tunnel with a diameter of 3.6 m and a low turbulence intensity of 0.5%. The selected test case has a wind tunnel velocity of 7 m/s and a TSR of 2.29 and this equates to a rotational speed of 18.85 rad/s, i.e. around 180 rpm.

These experimental data include the detailed pressure coefficient distributions around the blade at different azimuthal angles obtained using a high-speed multiport pressure sensor [97], mainly located at the mid-span section of the blade. In addition, the experimental data include the instantaneous torque coefficient contribution at the mid-span section and some other spanwise locations based on the integration of the pressure data around the blade at these sections. The availability of the detailed data at the mid-span section, where the 3D effect is minimal, enables fair comparisons with both the 2D CFD data that neglect the 3D effect and the 3D data at the mid-span section.

The aerodynamic forces acting on a body are the shear forces and the pressure forces. Since the chosen experimental data are based on the pressure measurements, all the torque coefficient results, presented in this chapter, are extracted based on the pressure contribution only. More details about the pressure and shear contribution calculations and comparisons are available in Appendix C.

Although the available studies in the literature rely on some integral data, the novelty of this investigation is based on the assessment of the CFD predictions against detailed instantaneous pressure data captured by a high-frequency pressure scanner. This provides a much better judgment on the behaviour of the CFD predictions of the selected turbulence models.

5.2 Model validations against the experimental data

5.2.1 Instantaneous single-blade torque coefficient at the blade mid-span section

Based on both the SST k-ω and the SST k-ω with the γ transition turbulence models, Figure 5.1 (a) shows a comparison between the 2D CFD predictions of the instantaneous torque coefficient against the experimental data at the mid-span section of the blade. It is observed that the torque coefficient is underestimated in the region between ϕ=20° and ϕ=70° based on the predictions of the two turbulence models. The results obtained using the SST k-ω turbulence model are overestimated over the rest of the cycle. However, the results obtained using the SST k-ω with the γ transition model have some underestimation in the regions between ϕ=135° and ϕ=180° and there is a noticeable unexpected underestimation in the downstream region, particularly where 210°< ϕ <280°. In general, there are considerable differences between the results obtained from the two turbulence models while the results based on the SST k-ω turbulence model appear to be more consistent in the 2D case.

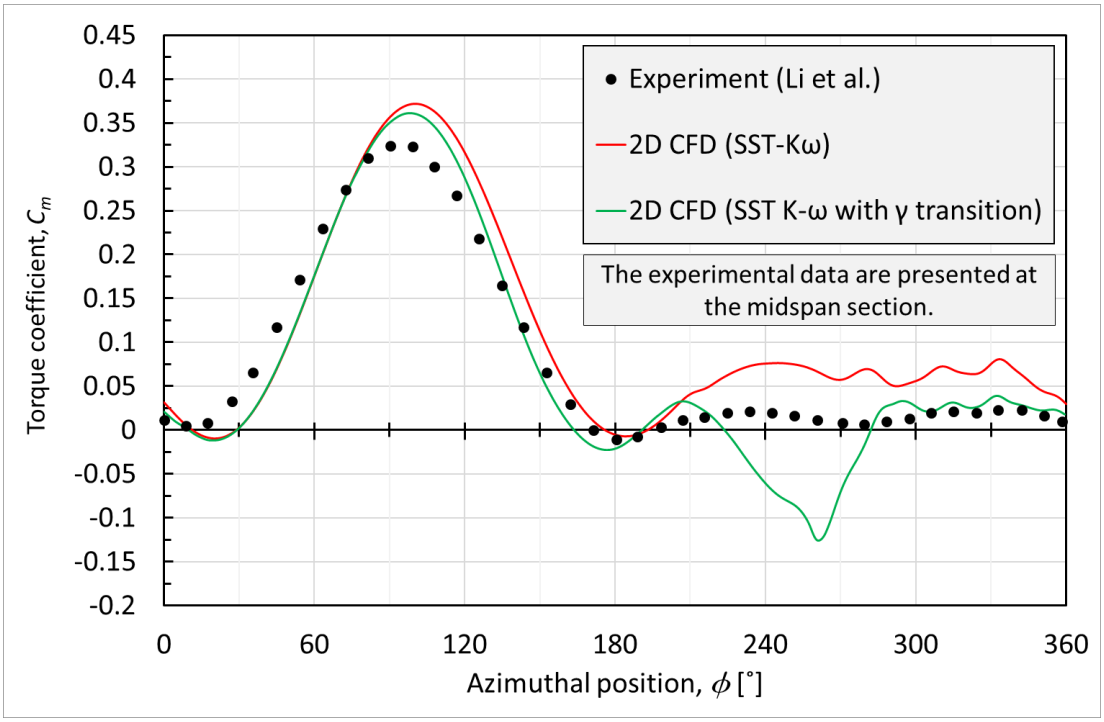

(a)

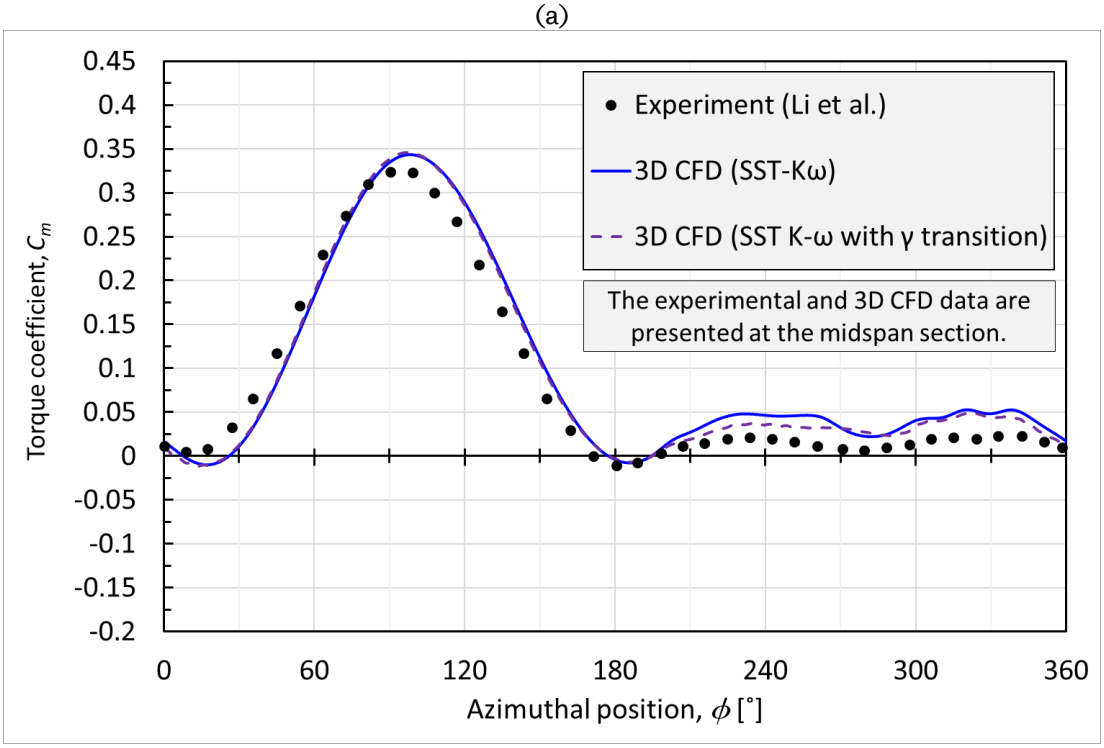

(b)

Figure 5.1 A comparison of (a) the 2D and (b) the 3D CFD results obtained using the SST k-ω and the SST k-ω with the γ transition turbulence models against the experimental data for the single blade instantaneous torque coefficient at the blade mid-span section over 360° of azimuthal angles.

Figure 5.1 (b) compares the 3D CFD predictions of the instantaneous torque coefficient against the experimental data where both the 3D and the experimental data are

considered at the mid-span section. In general, the differences in the predictions of the two turbulence models are relatively small. It is observed that the results, based on the SST k-ω with the γ transition model, are closer to the experimental data in the downstream part of the cycle and this is in contrast with the results based on the SST k-ω model. It is clear that the 3D results have a better agreement with the experimental data in contrast with the 2D results.

5.2.2 Pressure coefficient around the blade mid-span section at different azimuthal positions

In order to obtain a better assessment of the differences between the 2D and 3D predictions based on the selected turbulence models, the CFD predictions are compared against the pressure coefficient data at different azimuthal positions with an increment of 30°. These comparisons are shown in Figure 5.2 for the upstream part of the cycle and in Figure 5.3 for the downstream part of the cycle.

The CFD predictions are expected to overestimate the suction peak near the leading edge of the aerofoil. However, it is observed that the 2D results, based on the SST k-ω model, have higher suction peaks in contrast with the 3D results and this is clearly observed in Figures 5.2 (a) and 5.3 (b-f). Further, it is observed that the suction peaks are less overestimated in the results of the SST k-ω with the γ transition turbulence model in both the 2D and 3D cases when compared to the SST k-ω results at the same azimuthal location, as shown in Figures 5.2 (a) and 5.3 (e-f).

Figures 5.2 and 5.3 show that the 3D CFD predictions based on the two turbulence models and the 2D CFD predictions based on the SST k-ω model have a fair agreement with the experimental data. However, the 3D CFD predictions have a better agreement in contrast with the 2D CFD predictions. On the other hand, the 2D CFD predictions of the pressure coefficient based on the SST k-ω with the γ transition turbulence model have a strange behaviour for the azimuthal angles between ϕ=150° and ϕ=270°and this clarifies the deviation between the experimental data and the prediction of the torque coefficient in Figure 5.1 (a) in the SST k-ω with the γ transition case.

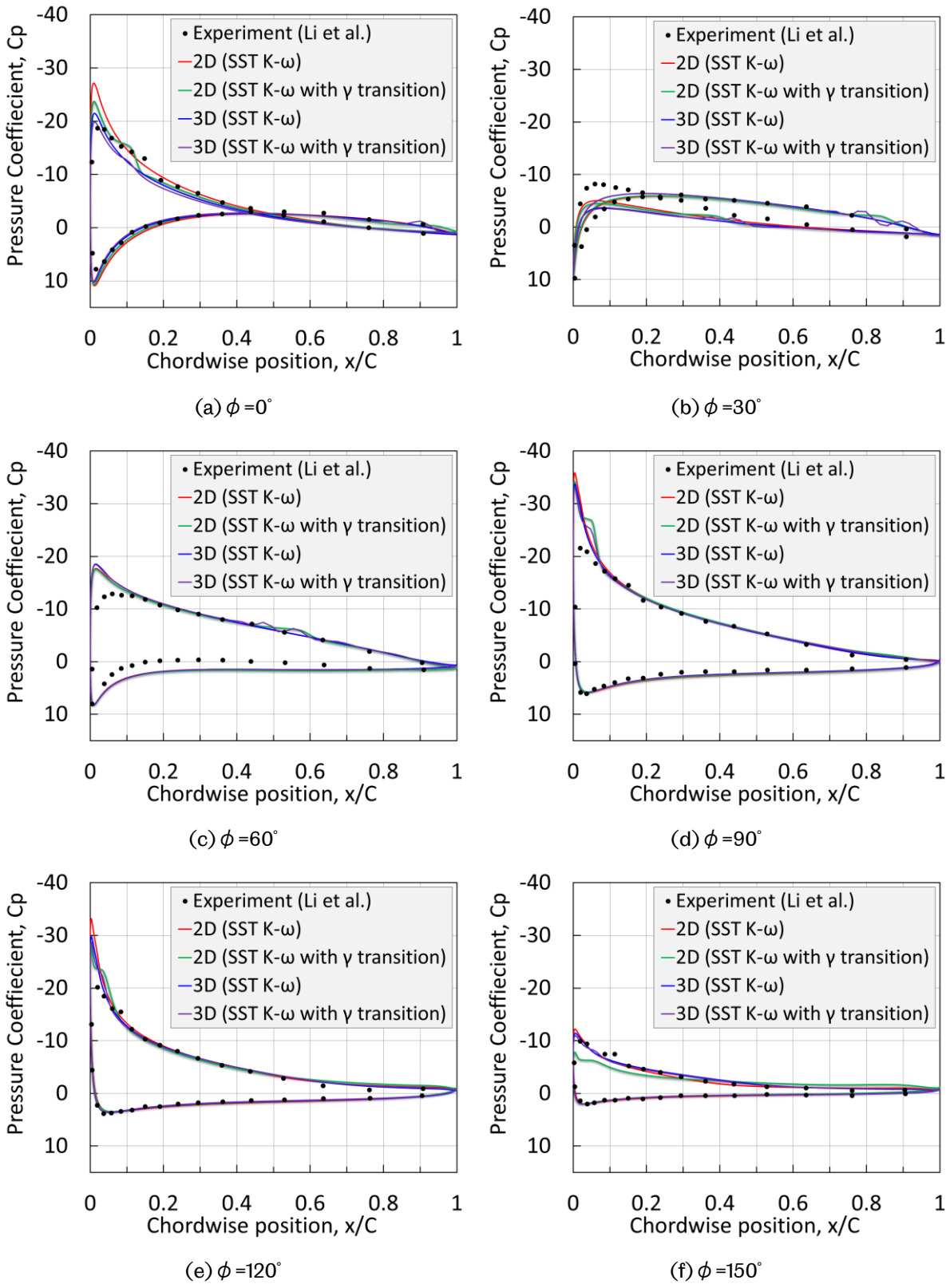

Figure 5.2 A comparison between the experimental and the numerical pressure coefficient around the blade at different azimuthal angles on the upstream part of the cycle.

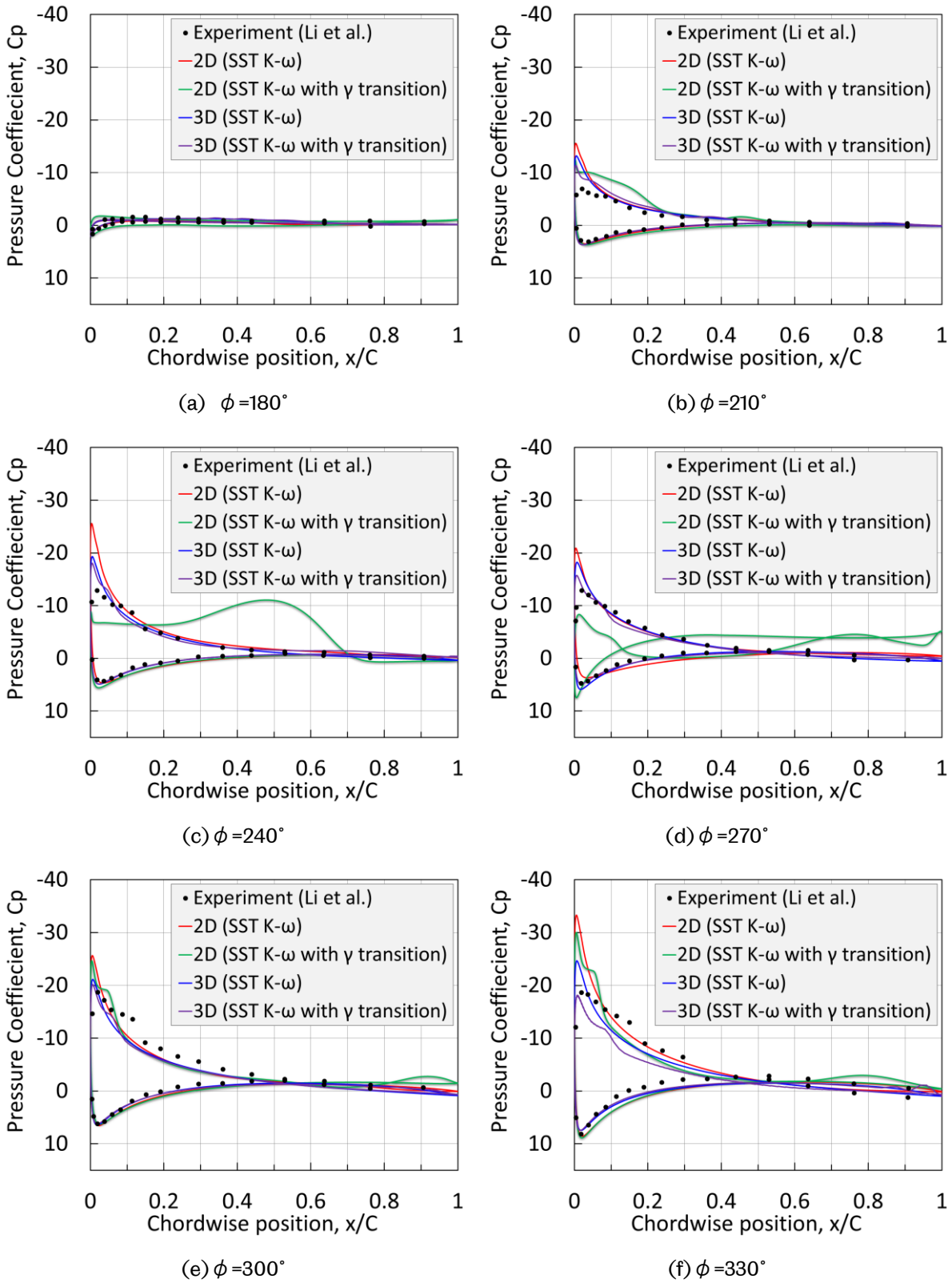

Figure 5.3 A comparison between the experimental and the numerical pressure coefficient around the blade at different azimuthal angles on the downstream part of the cycle.

5.2.3 **Aerodynamics and 3D flow pattern on the blade suction-side**

Most of the noticeable differences between the experimental data and the CFD predictions of the pressure coefficient occur at the suction side, which is associated with a complex flow pattern and a possible separation. The aim of this section is to inspect the flow pattern on the suction side and to visualise the reverse flow region in order to understand the differences between the prediction of the two selected turbulence models in both the 2D and 3D cases. The reverse flow region is a main part of the separation and hence the visualisation of the reverse flow regions assist in the assessing as to which model is more capable of predicting a realistic aerodynamic flow pattern. This assessment is based on the understanding of the differences between the CFD predictions and the experimental data of the pressure coefficient around the blade mid-span.

Three different azimuthal positions are selected for this analysis and these include ϕ=90° and ϕ=150° in the upstream part of the cycle and ϕ=270 in the downstream part of the cycle. In order to facilitate the visual comparison between the 2D and 3D results, ANSYS CFD-Post [204] has been used to visualise the 2D data in a 2.5D representation with a depth equal to the blade-span where the flow variables are kept constant in the spanwise direction. For simplicity, the 2.5D representation of the 2D data will be referred to as the 2.5D data or results. Despite the fact that the 3D analysis only includes a half of the blade-span, ANSYS CFD-Post has been used to visualise the full blade by mirroring the 3D data.

Figure 5.4 shows comparisons between the 2D and 3D predictions based on the two selected turbulence models at ϕ=90°. These comparisons include visualisations of the flow pattern near the suction side of the blade in the Subfigures 5.4 (a, b, d, e). These Subfigures show the relative velocity vectors on a defined offset surface at a distance of 0.001 m from the suction side of the blade and these vectors illustrate the flow pattern and the reverse flow regions that are associated with the existence of the separation.

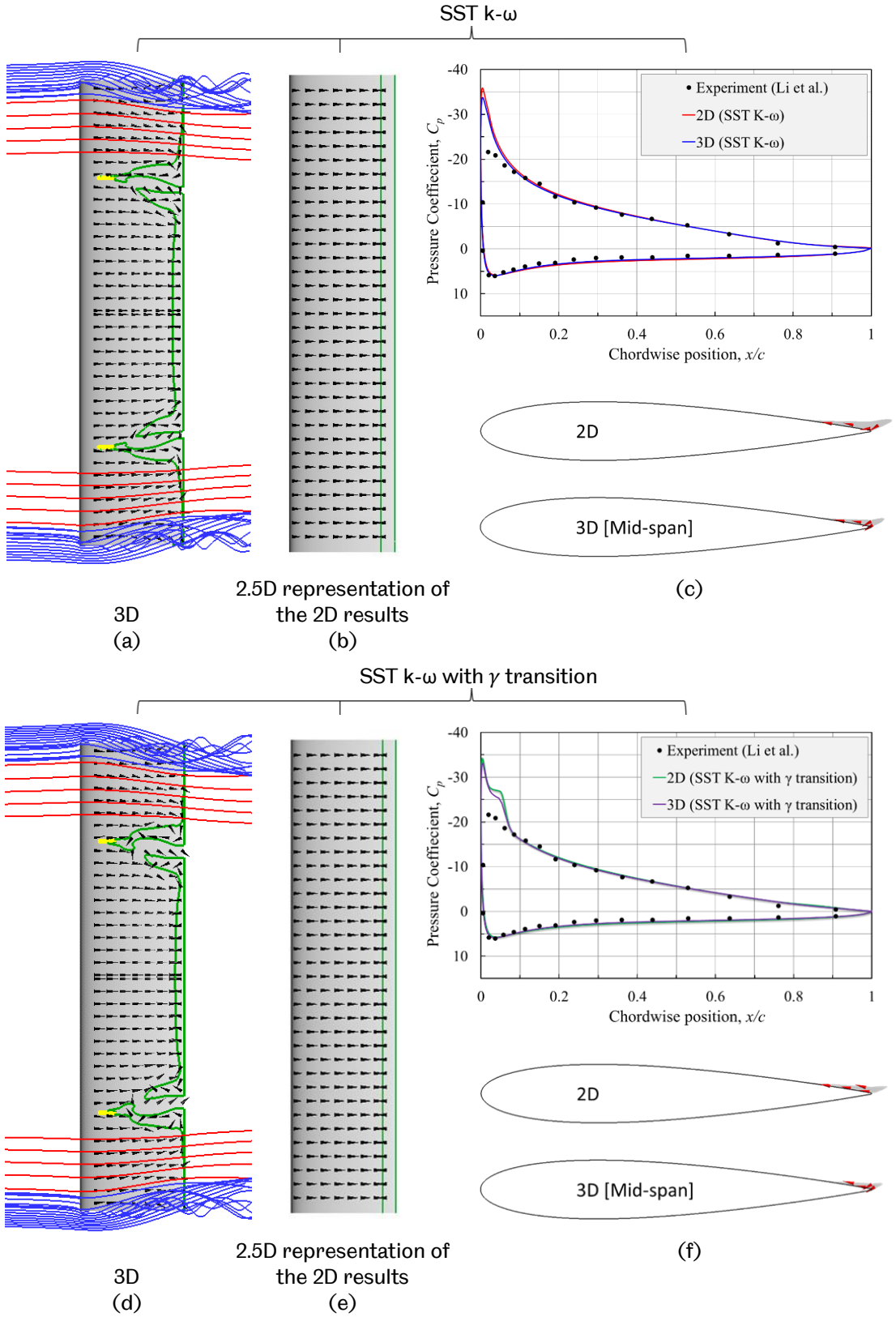

Figure 5.4 Comparisons between the 2D and 3D predictions based on the selected turbulence models at ϕ=90° and this includes: (a, b, d, e) visualisations of the flow pattern over the suction side of the blade, and (c, f) comparisons between the pressure coefficient data in addition to visualisations of the reverse flow region.

The reverse flow regions are bounded by the green lines in Subfigures 5.4 (a, b, d, e) and are defined by a zero chordwise relative velocity iso-clip of the defined offset surface. The yellow regions represent the locations of the arms while the red and blue relative velocity streamlines are released in the vicinity of the blade tip to visualise the tip flow pattern. Subfigures 5.4 (c, f) shows the pressure distribution in addition to visualising the reverse flow regions around the blade in the 2D case and around the blade mid-span section in the 3D case while the red vectors represent the direction of the relative velocity. While investigating the skin friction coefficient may be employed for a quantitative assessment of the reverse flow region, the use of the chordwise relative velocity has been reported to provide a good qualitative assessment of the size of the reverse flow region [205].

Based on the SST k-ω turbulence model at ϕ=90°, the comparison between the 3D and 2.5D results in Subfigures 5.4 (a, b) shows that the 3D flow patterns are similar to the 2D predictions at the mid-span section. However, there are clear differences near the blade tip and the arm and this is similar to the case of the SST k-ω with the γ transition turbulence model in Subfigures 5.4 (d, e). For the two turbulence models, the differences between the 3D and 2D predictions are minimal. However, the Subfigures 5.4 (c, f) shows that the reverse flow zones in the 2D cases are slightly larger in contrast with the 3D results based on the two turbulence models.

In Figure 5.4, the blade at ϕ=90° is close to the maximum torque azimuthal position and it operates at a favourable flow condition. Hence, the separation is minimal and both turbulence models give similar results. On the other hand, Figure 5.5 shows the results at ϕ=150° that is associated with a lower torque coefficient and less favourable flow conditions. Based on the SST k-ω turbulence model at ϕ=150°, Subfigures 5.5 (a, b) show that both the 3D and 2.5D data show some separated regions. In contrast with the 2.5D data, the 3D results appear to have a smaller separation region near the blade mid-span section while encountering large separation regions near the supporting arms. In addition, the separation is eliminated near the blade tip. It is observed that the tip flow that escapes from the pressure side to the suction side near the blade tip assists to reduce the separation.

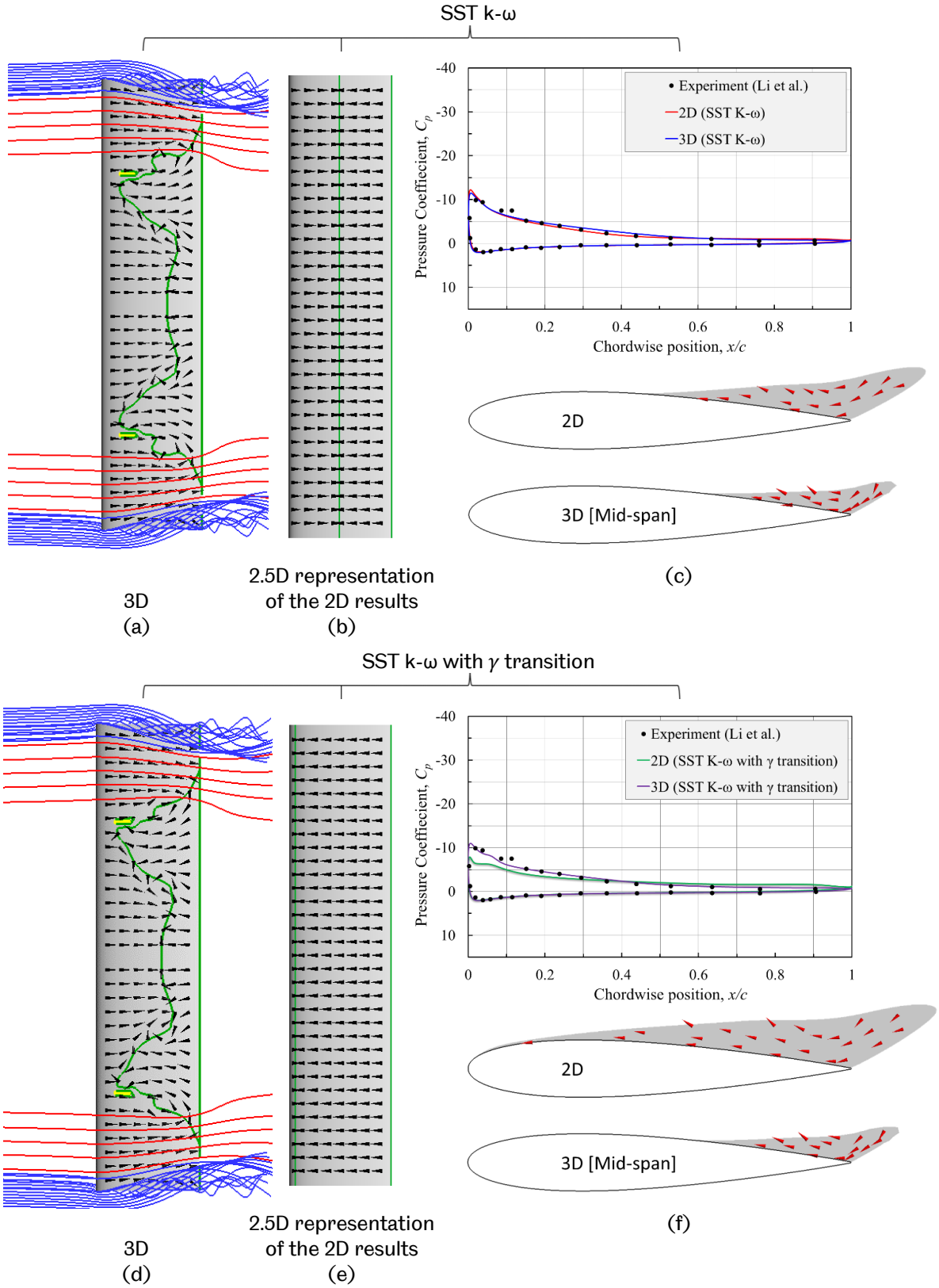

Figure 5.5 Comparisons between the 2D and 3D predictions based on the selected turbulence models at ϕ=150° and this includes: (a, b, d, e) visualisations of the flow pattern over the suction side of the blade (c, f) comparisons between the pressure coefficient data in addition to visualisations of the reverse flow region.

In the case of the SST k-ω with the γ transition turbulence model in Subfigures 5.5 (d, e), the 2.5D representation of the 2D data shows a large separation region over the majority of the suction side of the blade and this large separation appears to be unphysical, especially based on the deviation between the 2D-SST k-ω with the γ transition results and both of the 3D results and the experimental data that appears on the pressure coefficient around the blade in Subfigure 5.5 (f). In addition, Subfigure 5.5 (d) illustrates the large reverse flow zone over the suction side in the 2D predictions based on the SST k-ω with the γ transition and this is relatively overestimated in contrast with the SST k-ω case in Subfigure 5.5 (c).

Figure 5.6 shows the results at ϕ=240° where the blade passes through the turbine wake in the downstream part of the cycle. Subfigures 5.6 (a, b, d, e) show that the 3D-SST k-ω results have a minimal separation which may be considered to be most accurate when comparing the different CFD predictions of the pressure coefficient against the experimental data in Subfigures 5.6 (c, f) in the chordwise locations between x/c= 0.5 and x/c= 1.0. It is clear from Subfigure 5.6 and 5.5 (c) that the 2D-SST k-ω with the γ transition results have some strange predictions of the pressure coefficient and this is associated with the extremely overestimated leading-edge separation. In contrast with the 3D-SST k-ω results, it is observed from Subfigure 5.6 (d) that the 3D-SST k-ω with the γ transition results are associated with a stronger tip flow structure which consists of two tip vortices: the first is propagated downstream and is visualised by the blue streamlines while the second is shifted in the spanwise direction and is visualised by the red streamlines

Based on the comparison of the CFD predictions of the pressure around the mid-span section against the experimental data in addition to the visual comparison of the 2D and 3D predictions, it is concluded that the 2D CFD predictions of flow pattern based on the SST k-ω with the γ transition is not trustworthy.

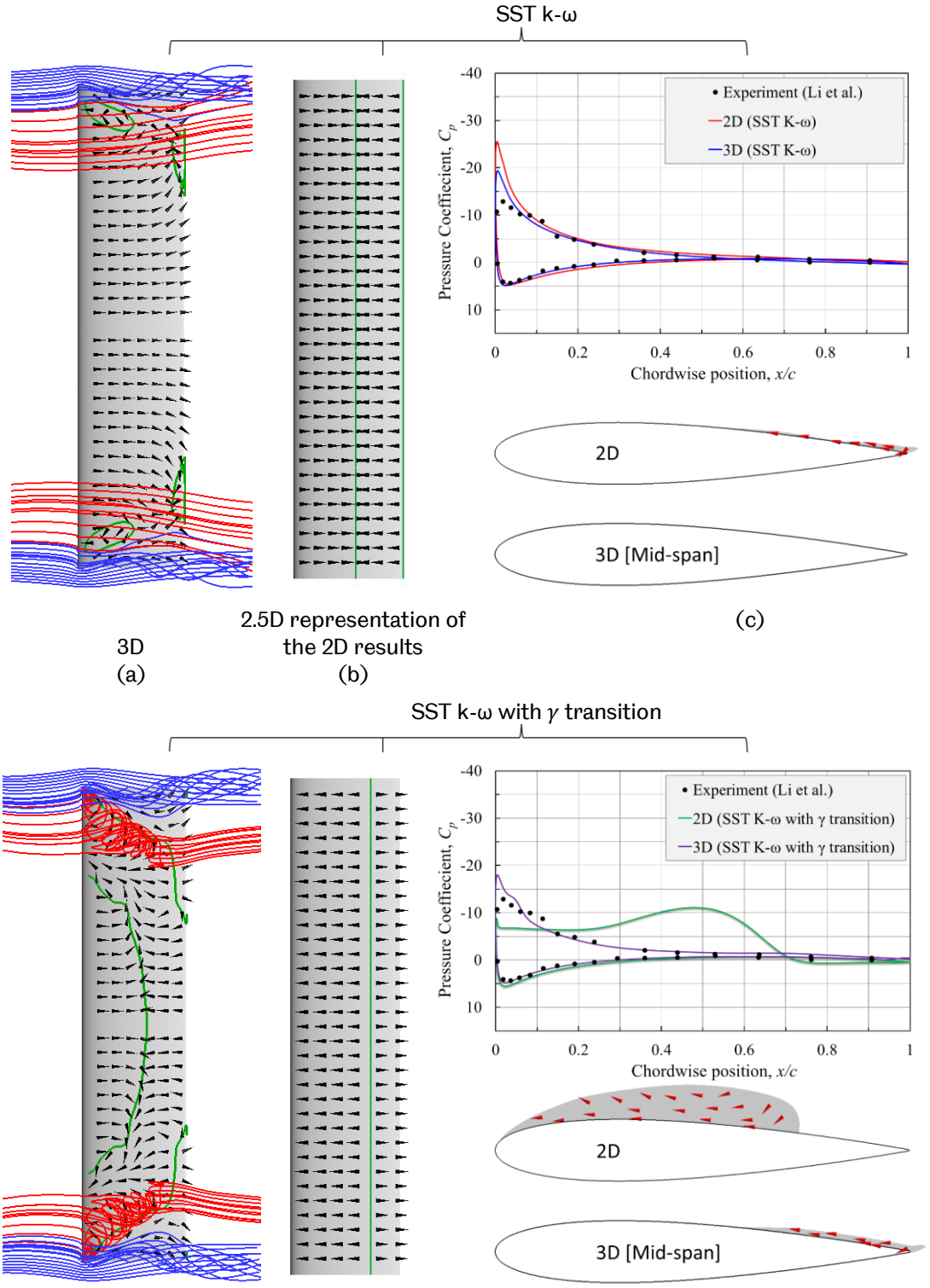

3D (a) | 2.5D representation of the 2D results (b) | (c)

3D (d) | 2.5D representation of the 2D results (e) | (f)

Figure 5.6 Comparisons between the 2D and 3D predictions based on the selected turbulence models at ϕ=240° and this includes: (a, b, d, e) visualisations of the flow pattern over the suction side of the blade (c, f) comparisons between the pressure coefficient data in addition to visualisations of the reverse flow region.

5.2.4 The instantaneous torque contribution at different spanwise locations

In order to investigate the ability of the 3D CFD model in the prediction of the turbine performance along the blade span, the predicted torque coefficient contributions at different spanwise locations are compared against the experimental data as shown in Figure 5.7. These spanwise locations include 70% and 80% of the blade half span, also referred to as z=0.7*h/2 and z=0.8*h/2, in addition to the mid-span section, where z is the spanwise coordinate of the selected location and h/2 is the blade half span. It is observed that the differences between the results of the two turbulence models are minimal in the upstream part of the cycle. However, the differences are relatively larger at the downstream part of the cycle, especially between ϕ=210° and ϕ=300° at z=0.7*h/2 and z=0.8*h/2 where the trend of the SST k-ω with the γ transition results deviate from that of the experimental data and the SST k-ω results. This deviation appears to be related to the previously discussed tip vortex that is visualised by the red streamlines in Subfigure 5.6 (d). It may be observed from Figure 5.7 that the results based on the SST k-ω turbulence model have a more consistent trend in the downstream part of the cycle while the SST k-ω with the γ transition results are slightly closer to the experimental data at the upstream part of the cycle.

In contrast with the experimental data, the CFD results have a better agreement at the mid-span section and the differences between the CFD and the experimental data are relatively higher at z=0.7*h/2 and z=0.8*h/2. However, the trends of the SST k-ω results, at z=0.7*h/2 and z=0.8*h/2, show a fair agreement with the trend of the experimental data at the corresponding locations. While the current 3D model includes a simplified geometry of the supporting arms, the measurement tubes that were connecting between the blade and the multiport pressure sensor near z=0.55*h/2 were not modelled as their details were not reported by Li et al. [180]. The simplified connections between the arms and the blade, in addition to the absence of the measurement tubes in the CFD model, could be a source for the differences between the CFD results and the experimental data at z=0.7*h/2 and z=0.8*h/2. More details about the effect of the modelling of the supporting arms on the predicted results are available in Section 5.3.

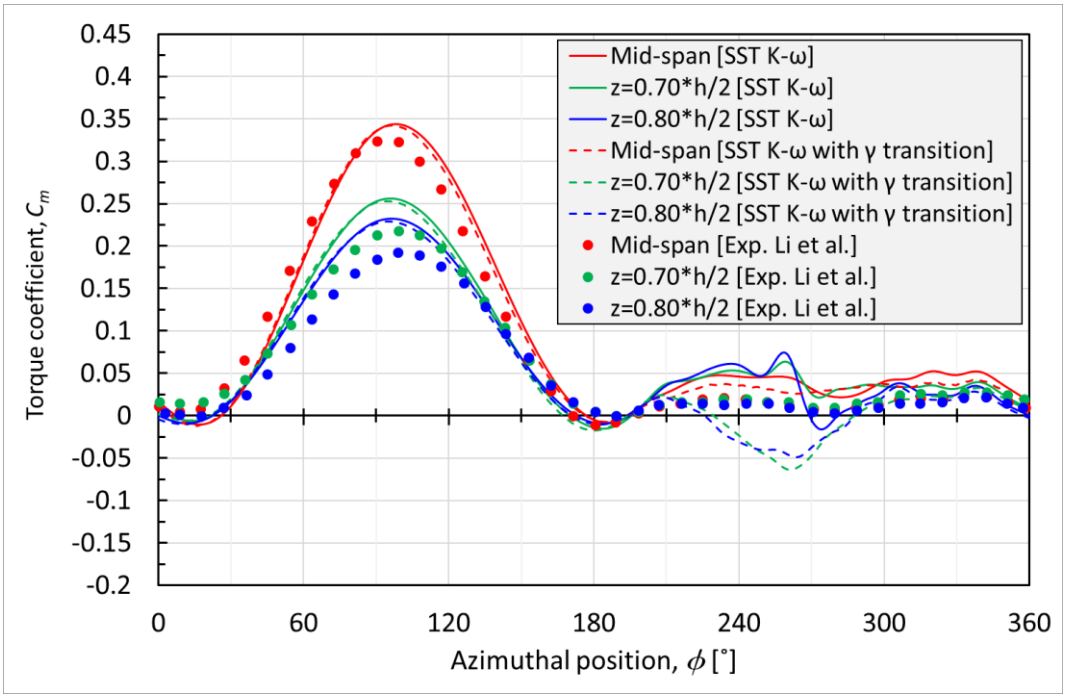

Figure 5.7 A comparison of the 2D and 3D CFD results obtained using the SST k-ω and the SST k-ω with the γ transition turbulence models against the experimental data of single blade instantaneous torque coefficient at the different spanwise locations over 360° of azimuthal angles.

5.2.5 Quantitative assessment of the CFD predictions

While the comparisons of the instantaneous torque coefficient, as shown previously in Figures 5.1 and 5.7, are found to be useful in the qualitative assessment of the different CFD predictions, it is essential to quantify these differences. The quantitative assessment is carried out based on the single blade values of the average torque coefficient, $\bar{C}_m$, the maximum torque coefficient, $\hat{C}_m$, and the azimuthal location of maximum torque coefficient, ϕ at $\hat{C}_m$, as shown in Table 5.1. Three values of the average torque coefficient, $\bar{C}_m$, are reported based on the upstream part of the cycle, the downstream part, and the whole cycle. It is observed that both the 2D and 3D predictions of the average torque coefficient based on the upstream part are in a good agreement with the experimental data at the mid-span section, with a maximum relative deviation of 6% in the 2D cases and 3% in the 3D cases.

Table 5.1 A comparison between the predicted and experimental single blade values of the average torque coefficient, $\bar{C}_m$, the maximum torque coefficient, $\hat{C}_m$, and the azimuthal location of the maximum torque coefficient, ϕ at $\hat{C}_m$ at the mid-span, z=0.70*h/2, and z=0.80*h/2 sections.

			$\bar{C}_m$			$\hat{C}_m$	ϕ at $\hat{C}_m$
			Upstream part	Downstream part	Cycle-average		
Mid-span	Exp. (Li et al.)		0.151	0.013	0.082	0.325	93°
	2D CFD	SST k-ω	0.154	0.05	0.102	0.367	101.3°
		SST k-ω with γ transition	0.142	-0.004	0.069	0.358	99.3°
	3D CFD	SST k-ω	0.155	0.033	0.094	0.344	98.7°
		SST k-ω with γ transition	0.153	0.029	0.091	0.343	96°
z=0.70*h/2	Exp. (Li et al.)		0.108	0.018	0.063	0.218	99.3°
	3D CFD	SST k-ω	0.114	0.032	0.073	0.257	95.3°
		SST k-ω with γ transition	0.112	-0.0007	0.056	0.253	94.7°
z=0.80*h/2	Exp. (Li et al.)		0.091	0.013	0.052	0.192	99°
	3D CFD	SST k-ω	0.105	0.027	0.066	0.232	96.7°
		SST k-ω with γ transition	0.103	-0.001	0.051	0.229	94.7°

The deviations from the experimental values are large in the case of the cycle-average values of the torque coefficient and this is clearly because of the significantly larger differences in the downstream part of the cycle. The downstream part of the cycle is associated with strong wake interaction effects and due to the limited experimental data; the reasons for the differences in the downstream part could not be completely defined. Regarding the maximum torque coefficient, $\hat{C}_m$, it is observed that both the 2D and 3D predictions are in a fair agreement with the experimental data at the mid-span section, with a maximum absolute relative deviation of 13% in the 2D cases and 6% in the 3D cases and with a maximum phase shift of 8.3° in the 2D cases and 6.3° in

the 3D cases in contrast with the experimental data. At z=0.70*h/2 and z=0.80*h/2 spanwise locations, the deviations between the 3D CFD predictions and the experimental data are relatively larger in terms of the average and maximum torque coefficient. However, the azimuthal locations of the maximum torque coefficient are shifted upstream in the CFD predictions.

5.2.6 **Conclusions**

The 2D and 3D predictions based on both the SST k-ω model and SST k-ω with the γ transition model are compared against the experimental data. In terms of the cycle-averaged torque coefficient, it is noticed that the 2D CFD predictions based on the SST k-ω with the γ transition are unexpectedly underestimated, even in the upstream part of the cycle. In addition, the comparisons in Sections 5.1.1 and 5.1.2 show that the predictions of the SST k-ω with the γ transition have some unphysical behaviour, especially in the downstream part of the cycle. In addition, the 2D CFD predictions of the pressure coefficient at certain azimuthal positions appear to overestimate the separation. Hence, the SST k-ω with the γ transition model is excluded and the SST k-ω model is selected for the further 2D analyses.

Although the 3D CFD predictions of the cycle-averaged and maximum torque coefficient based on SST k-ω with the γ transition shows a better quantitative agreement with the experimental data, in contrast with the SST k-ω predictions, it has been found that the trends of the SST k-ω with the γ transition predictions in the downstream part of the cycles are unexpected at some spanwise locations as discussed in Section 5.2.4. Hence, the SST k-ω model is selected for the further 3D analyses.

It is observed that the 2D and 3D CFD results are generally over-predicted in the downstream part of the cycle where strong wake interactions exist. However, more experimental data, including the velocity distribution in the wake region, are needed in order to be able to obtain a better assessment for the source of these over-predictions.

5.3 **The 3D behaviour of the VAWT**

While the 2D analysis represents a VAWT with an infinite blade length without considering the supporting arms, the 3D analysis enables the modelling of the

supporting arms and the finite blade length of the turbine. This also accounts for the complex flow structure near the tip and the variation of the torque coefficient along the spanwise direction. The 2D analysis is usually associated with higher performance by eliminating the losses due to these 3D features. Hence, the understanding of the reasons of the differences between the 2D and 3D predictions will assist in the design of a VAWT with higher performance.

In order to investigate the effect of modelling the supporting arms of the VAWT, a new 3D mesh is constructed for the turbine geometry without the supporting arms. This mesh has the same meshing attributes as the baseline 3D mesh that is discussed in Section 4.3.2. Figure 5.8 shows a comparison between the 2D prediction of the instantaneous torque coefficient and the 3D prediction of instantaneous torque coefficient contributions at different spanwise locations both with and without the supporting arms. These spanwise locations include z=0.7*h/2 and z=0.8*h/2, in addition to the mid-span section. In the upstream part of the cycle, it is clear that the 3D instantaneous torque coefficient contribution of the mid-span is relatively close to the 2D predictions. However, there are considerable differences between the coefficient contribution of the mid-span and that of z=0.7*h/2 and z=0.8*h/2. These differences are considered as losses due to the three-dimensional characteristics of the turbine. In order to analyse the sources of these losses, further analyses are performed for the streamtube expansion around the turbine, the upstream velocity magnitude profiles, and the pressure distribution over both the suction and pressure sides of the blade at the 90° azimuthal position, which is close to the location of the maximum torque coefficient.

Figure 5.9 shows the 3D streamtube expansion around the rotor. The selected streamtube is released from an area equal to the turbine swept area and at a distance of 0.75 turbine diameters upstream from the rotation axis. It is visualised using two sets of streamlines. The red streamlines are released from the black vertical lines and this shows how the streamtube expands in the horizontal direction around the rotor. However, the blue streamlines are released from the green horizontal lines and this shows how the streamtube expands in the vertical direction over the rotor. While the 3D simulations enable the modelling of the expansion, both of the horizontal and

vertical direction, the 2D analysis could not account for the vertical expansion as the flow only is allowed to expand in the 2D plane of rotation.

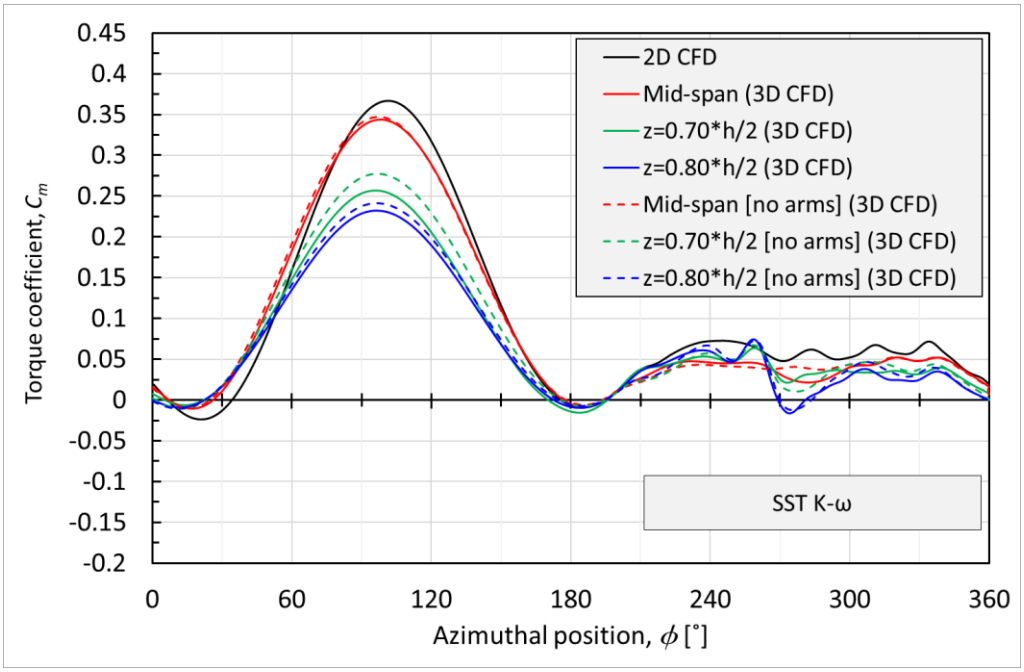

Figure 5.8 A comparison between the 3D CFD predictions of the single blade instantaneous torque coefficient at the different spanwise locations with and without the modelling of supporting arms against the 2D predictions.

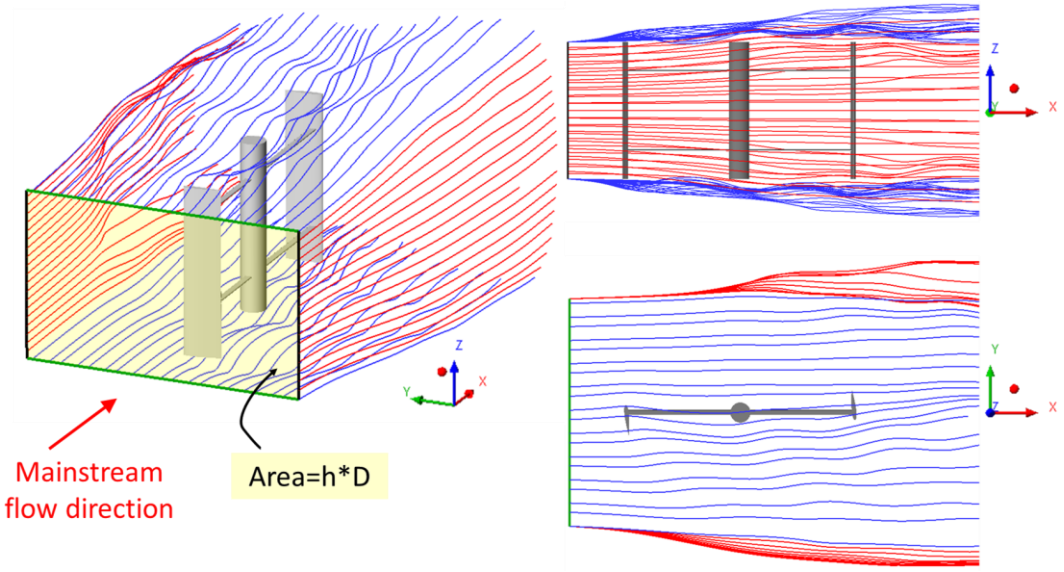

Figure 5.9 Two sets of streamlines that represent the streamtube expansion around the 3D rotor at the 90° azimuthal position; the blue streamlines are released from the green horizontal lines and the red streamlines are released from the black vertical lines. These green and black lines are located at 0.75 of turbine diameters distance upstream from the rotation axis.

In order to analysis velocity magnitude profiles upstream from the rotor, three different lines are selected at a distance of 0.75 turbine diameters upstream from the rotation axis. These lines are located at a spanwise distance z=0.0*h/2, z=0.7*h/2 and z=0.8*h/2 from the mid-span plane. Figure 5.10 illustrates the locations of these lines in addition to the gauge pressure contours of the high-pressure region near the pressure side of the upstream blade at the selected spanwise levels. It is clear from Figure 5.10 that a larger high-pressure region is associated with the mid-span section. In addition, the size of the high-pressure region is reduced when moving further in the spanwise direction.

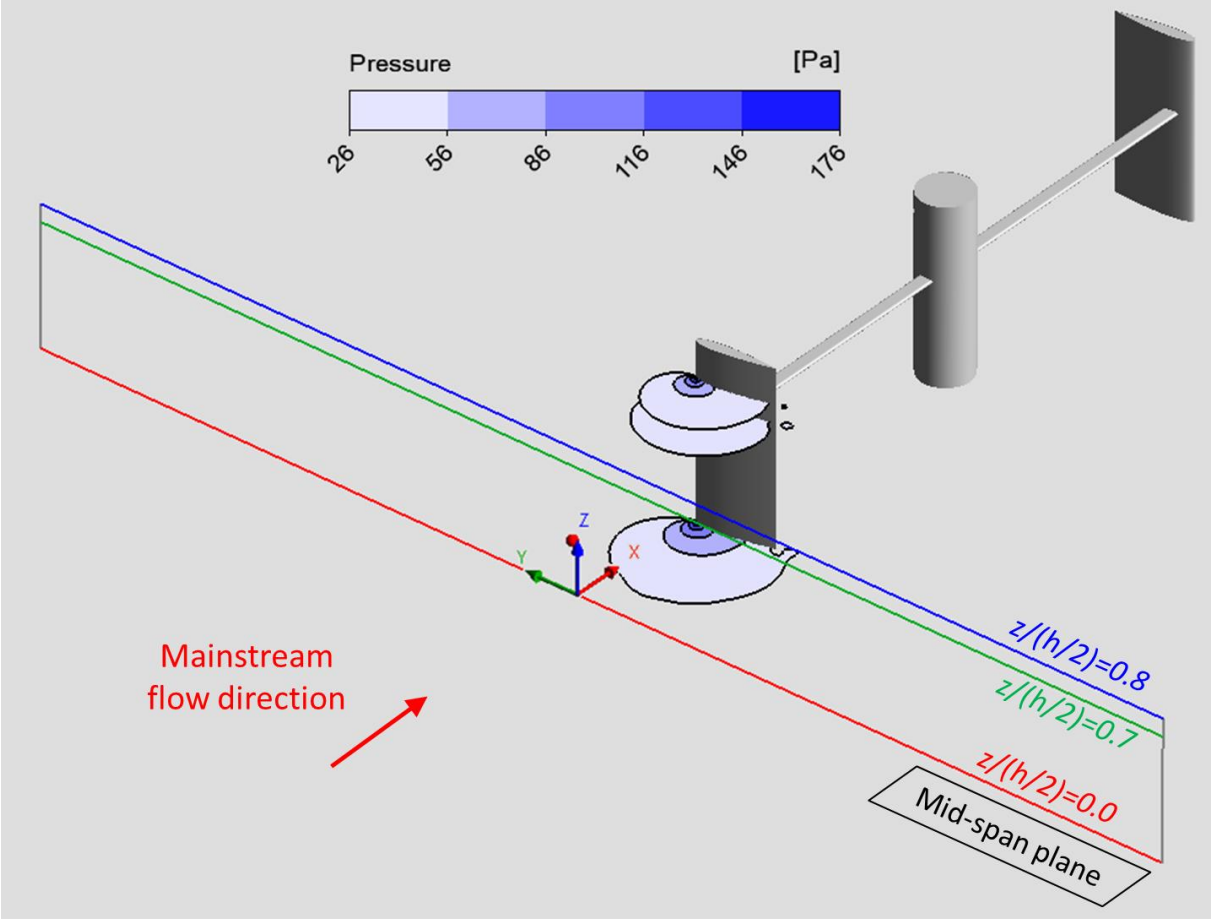

Figure 5.10 A 3D schematic of the upper half of the rotor at the 90° azimuthal position showing the locations of the measuring lines of the velocity magnitude at z/(h/2)= 0.0 (mid-span), 0.7, and 0.8. In addition, the gauge pressure contours limited to the high-pressure region are illustrated at z/(h/2)= 0.0 (mid-span), 0.7, and 0.8.

Figure 5.11 shows the velocity magnitude profiles, with and without the consideration of the supporting arms, at the selected lines, in addition to the undisturbed flow

velocity and corresponding 2D velocity profile at the same distance upstream from the rotor. It is observed that the corresponding 3D velocity magnitude profiles are almost identical with and without the consideration of the supporting arms and this appears to be due to the fact that the arms are located completely downstream of the blade at the selected azimuthal position of 90°. The velocity magnitude profiles are observed to be non-symmetric in shape due to the effect of the turbine rotation in the clockwise direction. It is clear that the largest velocity deficit is associated with the 2D data where the lowest values of velocity magnitude are found. Regarding the 3D data, the velocity deficit at the mid-span is lower than the 2D case. However, the velocity deficit is reduced when moving further in the spanwise direction and this is due to the reduction in the size of the high-pressure regions near the blade along the spanwise direction as shown in Figure 5.10.

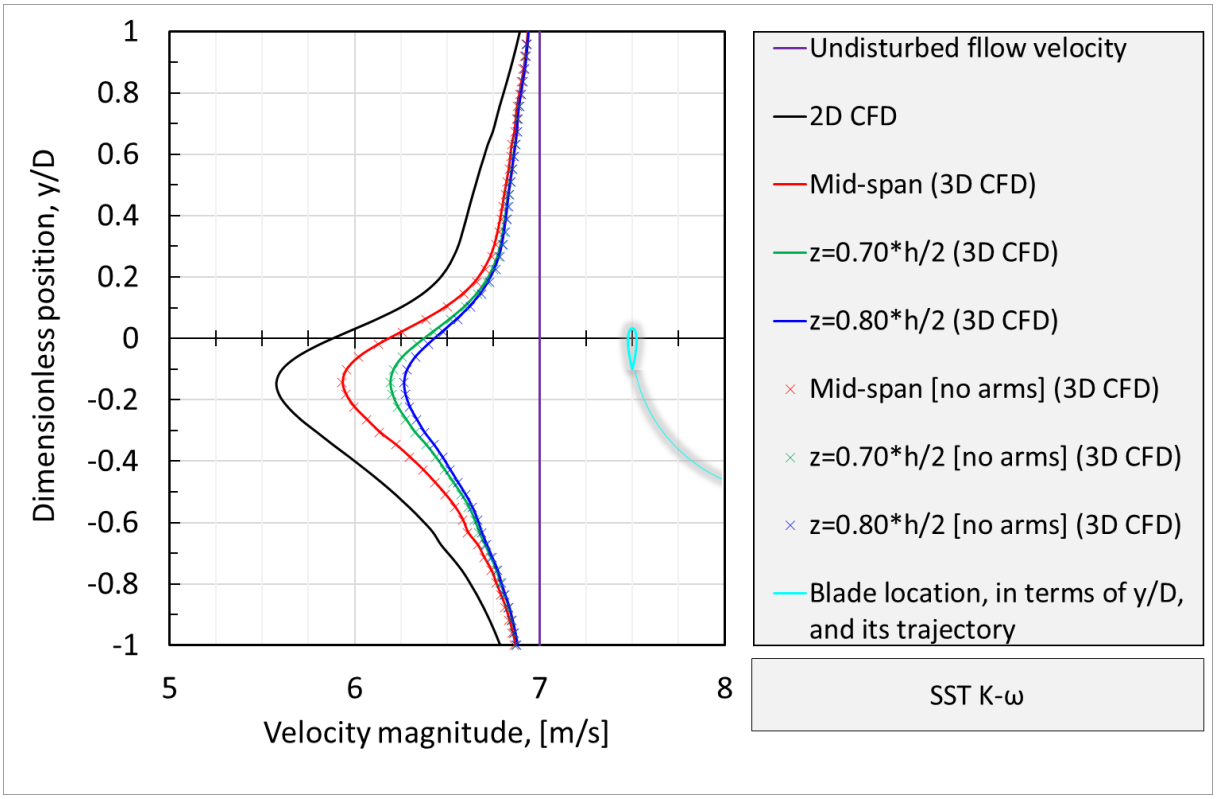

Figure 5.11 A comparison of the 3D CFD prediction of the velocity magnitude at z/(h/2)= 0.0 (mid-span), 0.7, and 0.8 with and without the modelling of supporting arms against the 2D predictions and the undisturbed flow velocity. The velocity magnitude profiles and the shown blade location correspond to the 90° azimuthal position.

Although the blade is subjected to a lower velocity magnitude near the mid-span section in contrast with the other spanwise locations as shown in Figure 5.11, the torque

contribution at the mid-span section is higher. This suggests that the changes in the turbine performance in the spanwise direction are not related to the incident velocity magnitude and it appears that it is associated with the pressure distributions in the vicinity of the blade. In order to analyse how the pressure distributions could affect the turbine performance in the spanwise direction, pressure contours on both the pressure and suction sides of the blade are shown in Figure 5.12 at the 90° azimuthal position for the 3D cases with and without the consideration of the arms, in addition to the 2.5D visualisation of the 2D data. As discussed before in the current section, the 2D analysis neglects the 3D losses and hence could be considered here as the reference case. Over the pressure sides, the difference in the pressure contours between the three cases are relatively small from the mid-span at z/(h/2)=0.0 and up to z/(h/2)=0.5. Then, the high-pressure region appears to be significantly reduced in the 3D cases. Over the suction sides, the difference in the pressure contours between the three selected cases are relatively small near the mid-span section and these differences are slightly increased in the spanwise direction, especially near the blade tips. In addition, it is observed that there are some considerable differences between the two 3D cases near the arm mounting location. This explains why the instantaneous torque coefficient contributions with and without the arms at the mid-span section are relatively similar as shown in Figure 5.8, while there are relatively larger differences between these contributions at z/(h/2)=0.7 and z/(h/2)=0.8. It is observed that there is a rapid change in the colour of the pressure contours between the pressure side and suction side near the leading edge in Figure 5.12 and this is due to the very rapid change in the pressure in a very small region near the leading edge rather than a discontinuity in the pressure. This rapid change can not be shown clearly in the Figure.

The pressure distribution around the blades directly affects the blade loading and hence the torque production. Figure 5.13 shows the CFD predictions of the blade loading (per centimetre of span) at the 90° azimuthal position for the 2.5D representation of the 2D data in addition to the 3D cases with and without the modelling of the blade arms. It could be noticed that the influence of the modelling of the arms is minimal except the region near the arm mounting location. However, both the 3D tangential and radial loading are reduced in the spanwise direction towards the blade tip and are generally lower than the 2D loading.

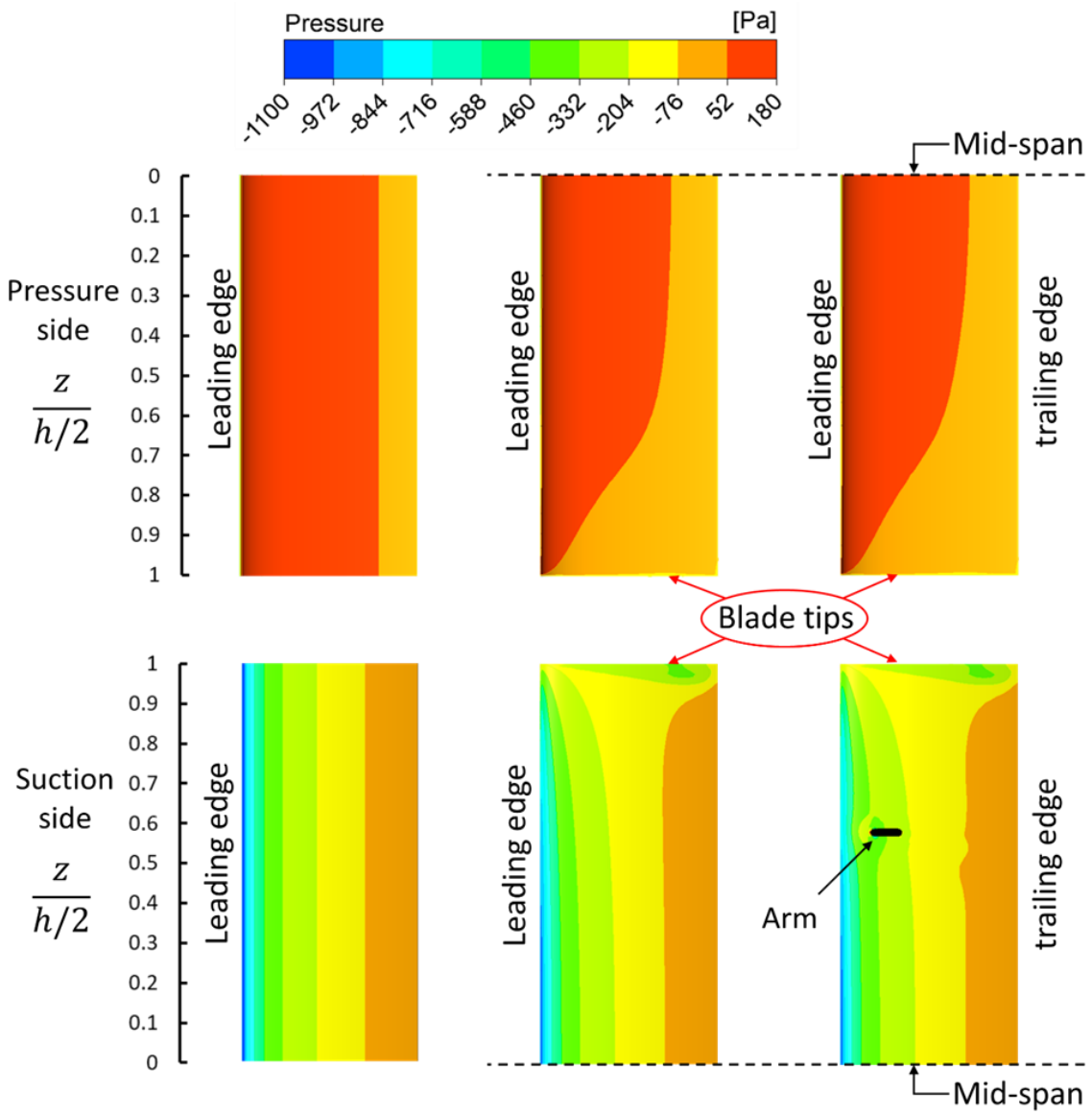

(a) 2.5D representation of the 2D results

(b) 3D without arms

(c) 3D with arms

Figure 5.12 A comparison of the pressure contours on both the suction and pressure sides between the 2.5D representation of the 2D results and the 3D results with and without the supporting arms.

In order to visualise the effects of the pressure difference between the suction and pressure sides on the flow pattern around the blade, a set of relative velocity streamlines are released from selected points, which are located at a distance of 1 cm over the blade surface over the tip, in addition to the suction and pressure sides near z/(h/2)=0.8 as shown in Figure 5.14. It may be observed that the streamlines over the

suction side are inclined towards the mid-span while the streamlines over the pressure side are inclined towards the blade tip. In addition, the green streamlines illustrate the flow motion over the tip. It may be concluded that due to the pressure difference between the suction and pressure sides of the blade in the 3D case, a secondary flow will be generated and it is leaked over the blade tip. This flow pattern is in agreement with the finding of Amato et al. [78]. This secondary flow attempts to mitigate the differences between the suction and pressure sides and this leads to a considerable loss in the generated lift force near the tip and hence this affects the torque coefficient. This suggests that overall turbine performance could be improved by means of tip devices, such as endplates or winglets, which could assist in the preserving of the pressure differences between the blade sides and reduce the secondary flow vortices near the tip.

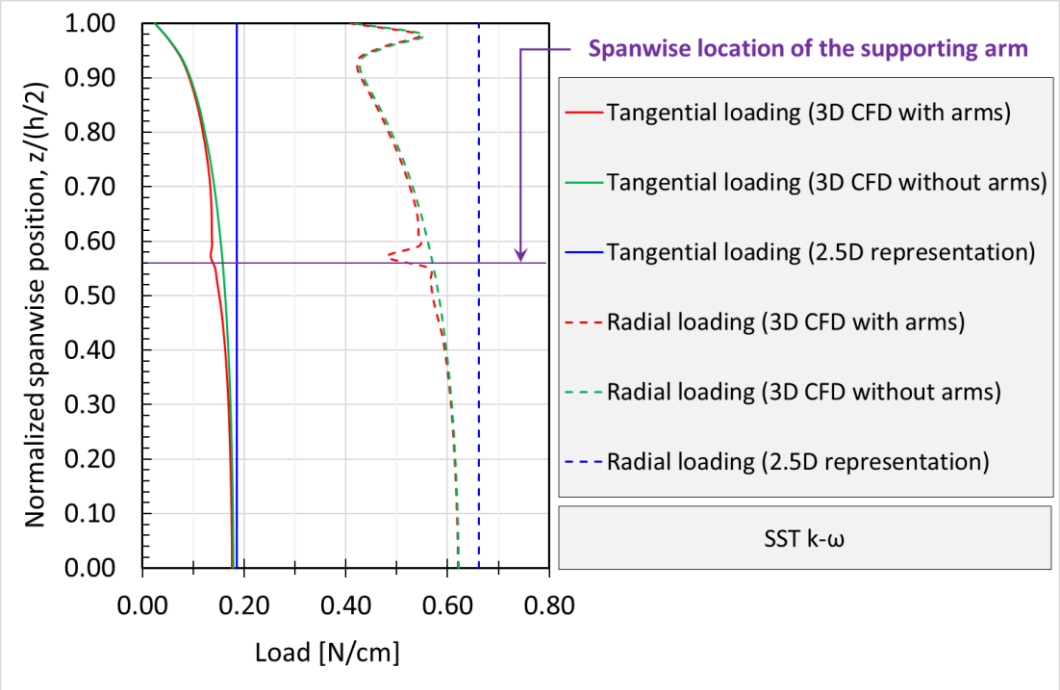

Figure 5.13 A comparisons between the tangential and radial loading for the 2.5D representation of the 2D data and the 3D cases with and without the modelling of the arms at the 90° azimuthal position.

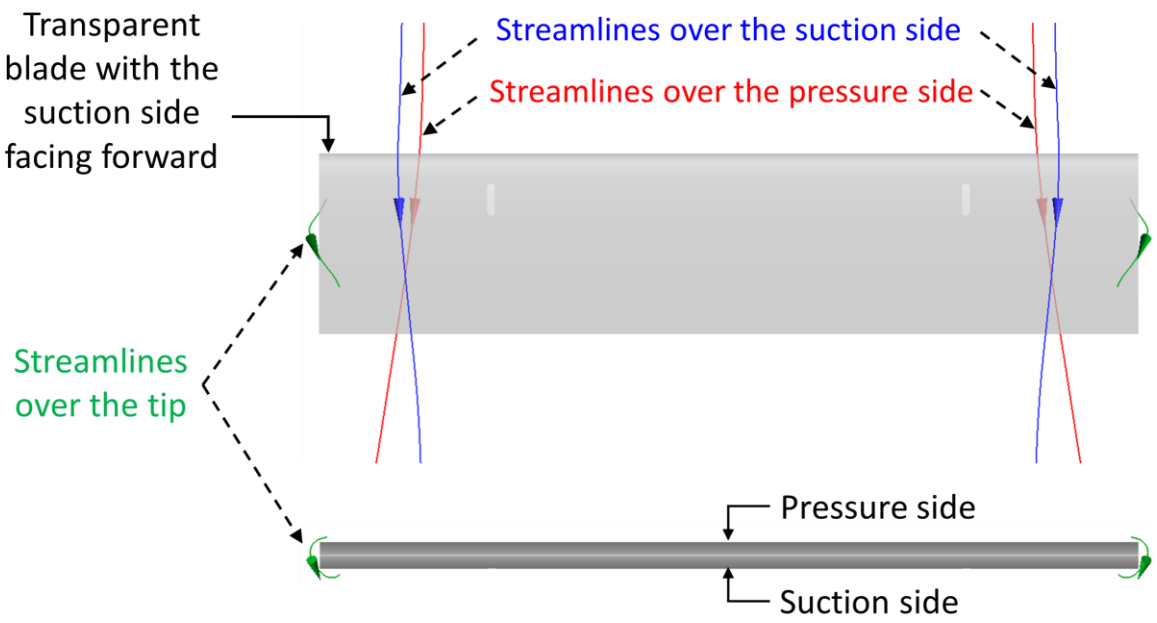

Figure 5.14 Selected relative velocity streamlines near the blade at the 90° azimuthal position. The streamlines are released from points at a distance of 1 cm from the blade surface.

5.4 Conclusions

The following conclusions are drawn:

- Although the available studies in the literature rely on some integral data, the novelty of this investigation is based on the assessment of the CFD predictions against detailed instantaneous pressure data captured by a high-frequency pressure scanner. This provides a much better judgment on the behaviour of the CFD predictions of the selected turbulence models.
- Considering both the quantitative and qualitative assessment of the CFD predictions against the experimental data, the SST k-ω with the γ transition model is excluded and the SST k-ω model is selected for the further 2D and 3D analyses.
- In terms of the average torque coefficient in the upstream part of the cycle at the mid-span section, both the 2D and 3D CFD predictions based on the SST k-ω model shows a good agreement against the experimental data with a deviation less than 2% and 3%, respectively.

- In the downstream part of the cycle, both the 2D and 3D CFD results are generally over-predict the experimental data. However, more experimental data are needed in order to fully assess the source of these over-predictions.
- Based on the SST k-ω model, the trend of the 3D CFD predictions matches better with the experimental data in contrast with the 2D predictions. However, the 2D predictions still have a fair comparison with the experimental data and hence is considered to be more suitable for optimisation producers and extensive parametric studies when the 3D simulations are not suitable due to the high computational cost. On the other hand, the 3D simulations would assist in the testing of the final designs before prototyping is undertaken, in addition to the investigation of the 3D features that could not be tested in 2D, i.e. the supporting structure, blade tip devices, and non-straight blades.
- The turbine performance is generally reduced from the mid-span section towards the tip in the spanwise direction and this is partially due to the tip losses. This is associated with the secondary flow vortices that tend to reduce the pressure difference between the suction and pressure sides near the tip.
- It is expected that the tip losses could be reduced by introducing an appropriate tip device such as endplates or winglets.

6 NOVEL PROCEDURE FOR THE ESTIMATION OF THE AOA AND THE ANALYSIS OF TURBINE PERFORMANCE BASED ON THE CFD DATA

6.1 Overview

The majority of the VAWT research consider the power coefficient over TSR curve to investigate the effect of the various design variables, i.e. both geometric and dynamic parameters, on the performance of VAWT. Moreover, an increasing amount of the research focuses on the effect of the design variables on the instantaneous single blade power coefficient in order to get some insight on the effect of the design variables on the performance over the different parts of the cycle. While the above-mentioned analyses could describe the effect of the design variables on the turbine performance and could assist in identifying the best configuration, these analyses cannot assist in identifying why a certain configuration is better than another.

Darrieus VAWTs are lift-type turbines that are driven by aerofoil-profiled blades. In order to obtain a better understanding of the complex aerodynamic performance of VAWT, it is useful to decompose its performance in terms of the simpler aerofoil aerodynamic characteristics, i.e. the lift and drag coefficients and their relation to the associated AOA. While the theoretical AOA is based on the trigonometry of the theoretical velocity triangles and ignores the flow behaviour, especially on the downstream part of the cycle, it is crucial to have a much better estimation of the AOA based on the CFD flow-field data.

In this chapter, a novel method for the estimation of the AOA based on the CFD flow-field data is presented in Section 6.2. This method provides a straightforward estimation of the AOA with minimal post-processing while having a reasonable accuracy. In addition, a novel procedure for the analysis of VAWT based on CFD data is proposed in Section 6.3. Finally, the proposed procedure is applied to analyse the differences in performance between two fixed pitch VAWT configurations. It is found that the proposed procedure assists in obtaining a better understanding of how a certain turbine configuration performs better than another.

The novelty of this work is that it provides an accurate estimation method of the AOA with minimal post-processing based on the CFD flow-field data. Also, this work provides a powerful analysis tool for the investigation of the performance of VAWTs based on the simpler aerodynamic characteristics of its aerofoil-shaped blades.

6.2 The estimation of the AOA based on CFD flow-field data

6.2.1 The proposed methodology for AOA estimation

It is noted that most of the estimation methods of the AOA that are available in the literature have two common drawbacks, namely (i) the lack of a reference for comparison and validation of the methods and thus can lead to relatively large errors, and (ii) the need for extensive post-processing. This section presents a new method for the estimation of the AOA which uses the CFD flow-field data at two well-selected reference points around the blade. Since the relative approaching flow velocity and direction to the blade are very complex and constantly changing, it is critical to select appropriate reference points where a representative incident flow direction can be obtained in order to obtain an accurate estimation of the blade AOA. In order to find these reference points around the blade that can result in an accurate and easy calculation of the AOA for VAWTs, the fluid flow around a static aerofoil with a range of AOAs has been used as a reference case. The use of a static aerofoil with a set of prescribed AOA facilitate a good reference for the comparisons and the validation of the ability of the proposed method in the estimation of an accurate AOA based on the flow-field data.

CFD simulations have been performed to obtain the flow-field data around the aerofoil at a set of several reference-points, and these data are used to calculate the AOAs around this static aerofoil. Then, the calculated AOAs are compared with the prescribed AOAs. The normalised Root Mean Square Error (RMSE), based on the differences between the calculated and the prescribed AOAs, is calculated and used to select the most appropriate reference-point locations with a minimal error, as discussed in Section 6.2.4. The well-selected reference-point locations are then utilised in the VAWT simulations where a UDF is used to access the flow-field data at these locations. Then, the estimated AOA of the flow past the VAWT blade is calculated

based on the relative velocity vector. This proposed method for the estimation of the AOA is illustrated in Figure 6.1.

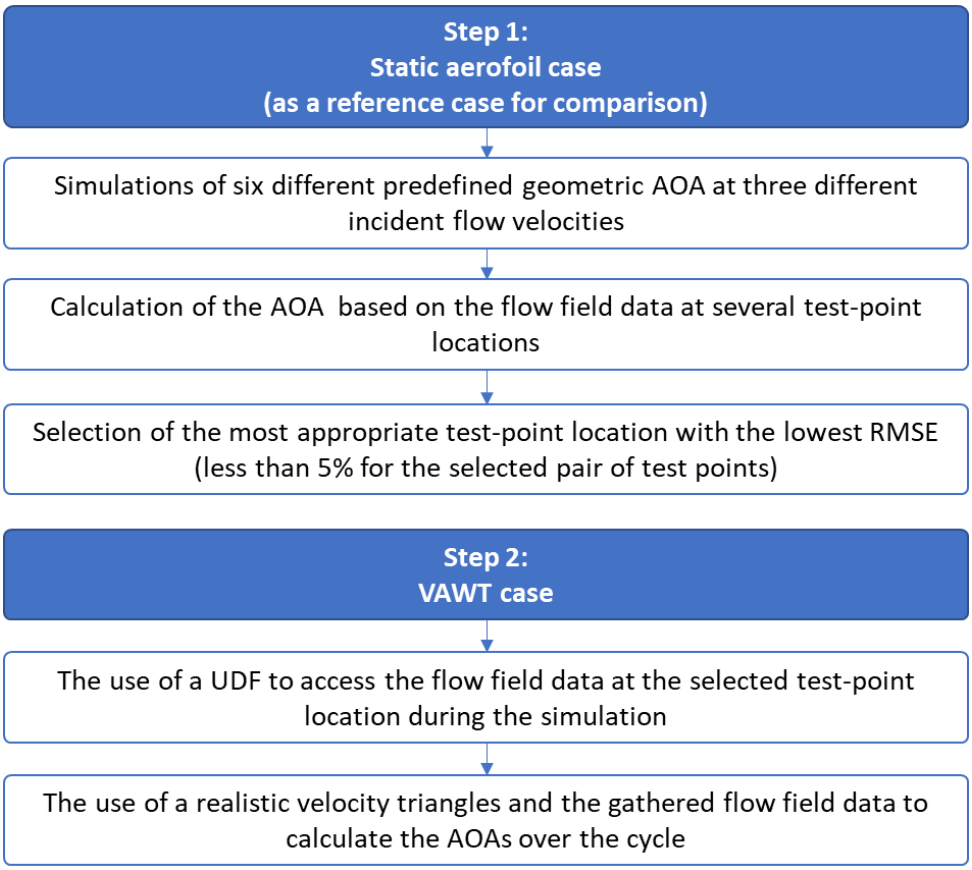

Figure 6.1 A flow diagram for the proposed method for the estimation of AOA.

6.2.2 The reference case

The flow around a static aerofoil is considered as a reference case with a prescribed geometric AOA as shown in Figure 6.2 (a) where the NACA0015 aerofoil with a chord length of 0.225 m is used. A range of AOAs is considered including the angles between 0° to 25° with a 5° increment. The flow conditions and aerofoil geometry are chosen according to the reference two-bladed VAWT case that is used in Chapters 4 and 5. The static aerofoil simulations are performed at different incident flow velocities of 7, 14, and 21 [m/s] and these correspond to the average relative velocities around a VAWT blade that operates at TSRs of 1, 2, and 3, respectively, when rotating across a mainstream flow with a velocity of 7 m/s. This range of TSRs is chosen to cover the optimum operating range of moderate solidity VAWTs.

In order to impose the prescribed AOA, the whole computational domain is inclined with the prescribed AOA as shown in Figure 6.2 (b). The computational domain is extended to 40 chord lengths in the downstream direction and 20 chord lengths elsewhere in order to eliminate any effects of the domain boundaries on the flow around the aerofoil. The computational domain is divided into a circular subdomain around the aerofoil and a rectangular extended domain while a circular non-conformal interface is used to connect these subdomains. This configuration, two subdomains, assists in maintaining the same mesh structure and quality regardless of the changes in the imposed AOA.

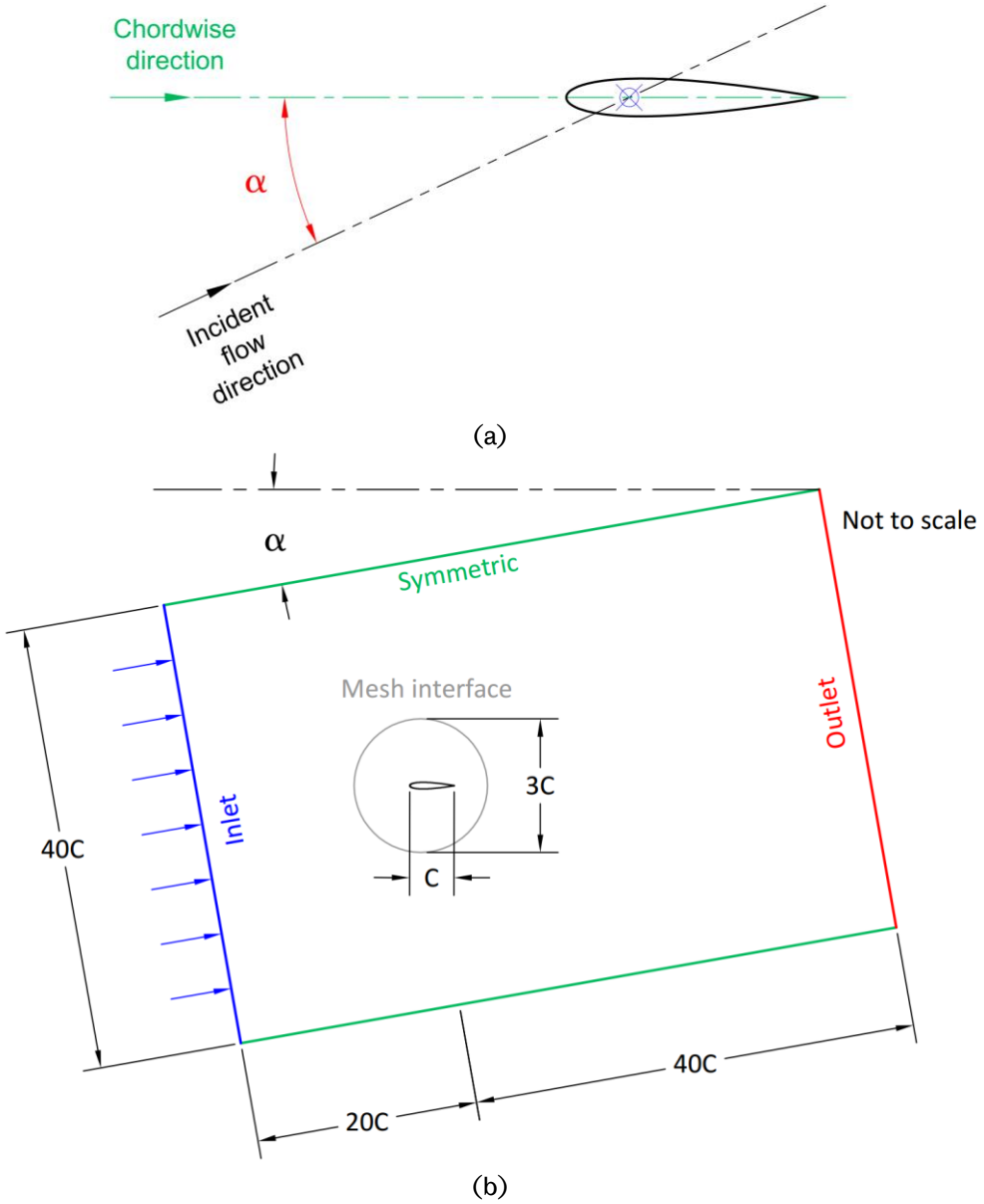

Figure 6.2 Schematics of (a) the incident flow around a static aerofoil and (b) the computational domain for the static aerofoil case (not to scale). The AOA is arbitrarily chosen for illustration.

The static aerofoil computational model utilises the same numerical aspects of the proposed VAWT model as in Chapter 4 except that the solver is utilised in the steady mode. In addition, the mesh near the aerofoil has the same meshing attributes of the verified mesh as in Chapter 4. Hence, this static aerofoil computational model is assumed to be accurate enough for the simulation of the flow around the static aerofoil. However, a dedicated verification and validation of the static aerofoil computational model are presented in Appendix D.

6.2.3 Selection of the initial set of reference-points

The proposed estimation of the AOA using CFD is based on the calculation of the inclination of the relative velocity vector in one or multiple reference-points. Both the single reference-point and pair of reference-points criteria are considered, and two groups of reference-points are selected. The first group is distributed around the chordwise direction, regardless of the incident flow direction, as shown in Figure 6.3 (a), and in the second group, the points are distributed around the incident flow direction as shown in Figure 6.3 (b). Figure 6.4 shows the typical streamlines released from the first group of reference-points that are clustered around the aerofoil chordwise direction at AOA=10° and these streamlines show how the flow around the aerofoil is distorted, especially in the vicinity of the leading edge. The degree of distortion depends on the location of the chosen test point and hence the appropriate selection of the reference-point locations is essential for the accurate estimation of the AOA. Several aspects are considered in the selection of the locations of the reference-points. The points should not be located in the wake of the aerofoil and the distance between each point and the aerofoil profile should not be too small to be affected by the flow distortion around the leading edge of the blade. In addition, this distance should not be too large to miss-represent the incident velocity vector.

6.2.4 Validation of the proposed method

In order to examine the accuracy of the AOA estimation using the flow-field data at the specific reference-point locations, the normalised RMSE is calculated based on the differences between the calculated values from the flow-field data and the exact values of the six prescribed geometric AOAs. The test point locations are considered appropriate with acceptable accuracy if the corresponding normalised RMSE is less

than 5%. Figure 6.5 shows a comparison of the normalised RMSE of the estimated value based on the single reference-points in addition to the normalised RMSE of the pairs of reference-points at the three selected incident flow velocities. It is clear that the pairs (i_1&j_1) and (i_2&j_2) have the lowest normalised RMSE, being less than about 5.0% and this illustrates how the pair of reference-points criterion could achieve a better estimation of the AOA in contrast with the single point criterion. From a practical perspective, the pair (i_1&j_1) is considered to be more suitable than the pair (i_2&j_2) for the VAWT case due to the simpler extraction of the data around the predefined chordwise direction.

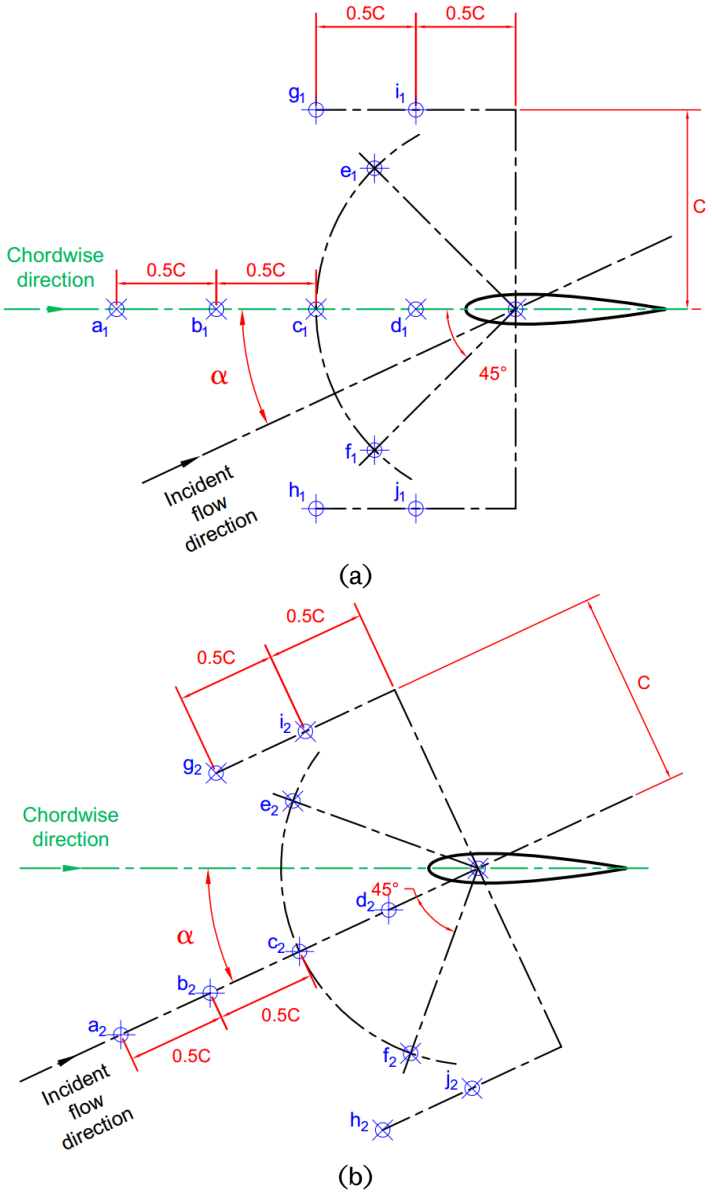

Figure 6.3 Locations of the reference-points. The AOA is arbitrarily chosen for illustration.

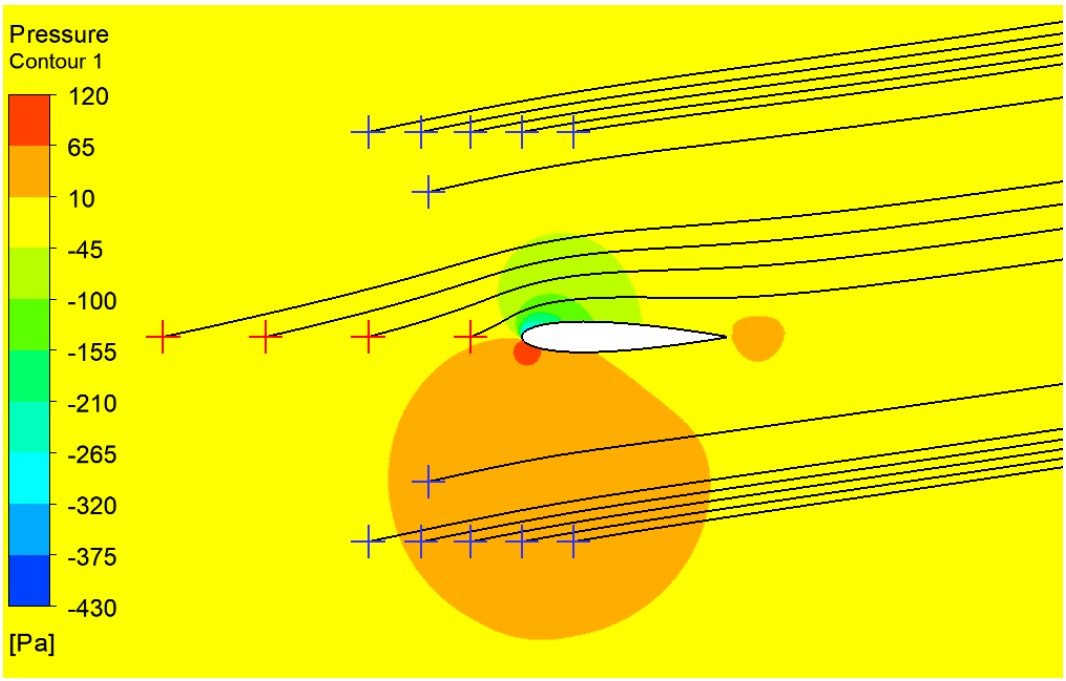

Figure 6.4 Streamlines released from the reference-points overlaid on the pressure contours around the aerofoil at AOA=10°.

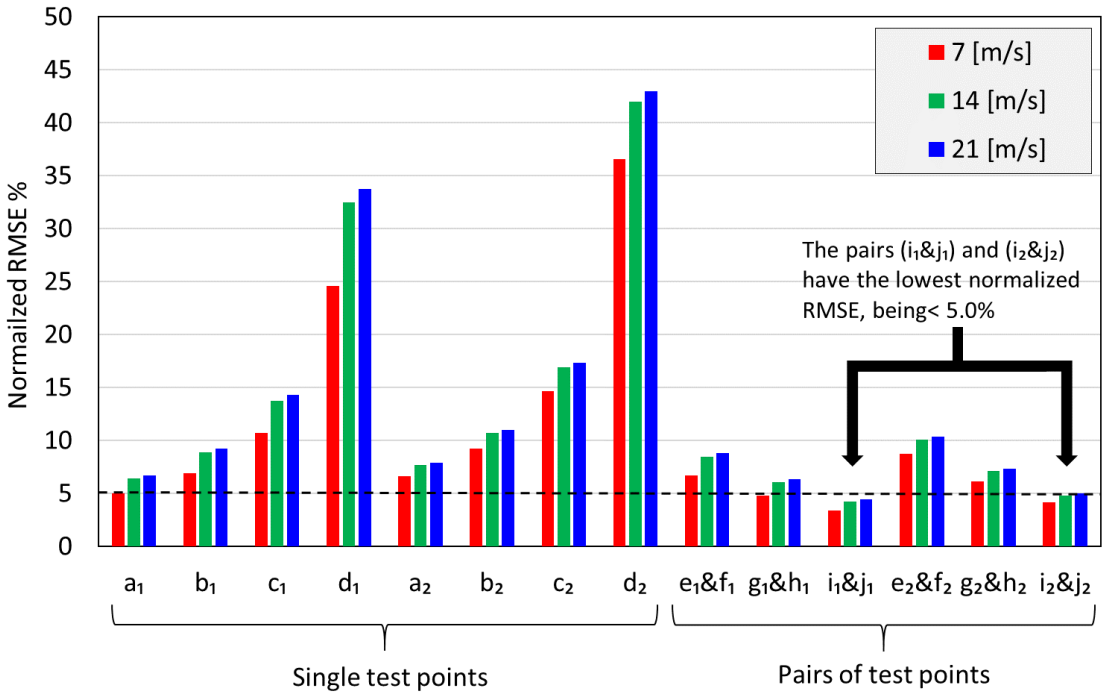

Figure 6.5 The normalised RMSE for the selected reference-points and pairs of reference-points against the permissible limit of 5%.

One of the well-cited methods of estimating the AOA in the literature is proposed by Gosselin et al. [28] using the flow-field data at 2-chord lengths from the aerofoil mount point and this corresponds to employing the single reference-point (a_1) in the current study, see Figure 6.3. In comparison, the proposed method, based on the selected pair of reference-points (i_1&j_1) as shown in Figure 6.3 (a), reduces the RMSE from 6.7% down to 4.4% for the incident flow velocities of 21 [m/s] and this represents a relative reduction of 34% in the normalised RMSE at 21 [m/s] and an average reduction of 33.8% for the three tested flow velocities in contrast with the method employed by Gosselin et al. [28]. In addition, the locations of the selected pair of reference-points (i_1&j_1) are much closer to the aerofoil in contrast with the point employed by Gosselin et al. [28] and hence are expected to provide a better estimation of the AOA in the VAWT case where a stronger flow curvature effect exists. Furthermore, most of the other AOA estimation methods [87]–[89] in the literature require many intermediate and time-consuming steps which make them very difficult to be applied to the current test case under the current operating conditions for the purpose of comparisons. Therefore the location of the pair (i_1&j_1), as shown in Figure 6.6, is selected for the estimation of the AOA based on the velocity field around the VAWT blade as introduced in Section 6.2.5.

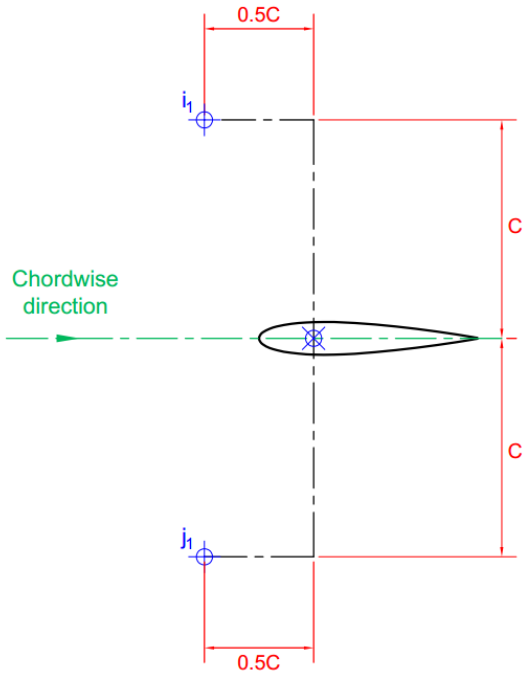

Figure 6.6 Locations of the selected pair of reference-points (i_1&j_1).

6.2.5 **FP-VAWT case**

The simple analytical analysis of the AOA, α, is based on the assumption that the magnitude and direction of the approaching wind velocity, V, are constants and equal to that of the undisturbed flow velocity, V_∞. Figure 6.7 (a) illustrates the theoretical velocity triangle at the blade mount point for a zero fixed pitch turbine in an arbitrary azimuthal position, ϕ, and the rigid body velocity of the blade is represented by TSR* V_∞. Therefore, the local incident relative velocity, V_r, and the AOA are simply defined as follows:

$$V_r = V\sqrt{sin^2\,\phi + (TSR + cos\,\phi)^2} \tag{6.1}$$

$$AOA = \alpha = tan^{-1}\frac{sin\,\phi}{TSR + cos\,\phi} \tag{6.2}$$

In the present study, the outward pitch angles, as illustrated in Figure 6.7 (a), are considered positive. Therefore, the theoretical AOA for a VAWT with a pitch angle, β, can be expressed as follows:

$$\text{AOA} = \alpha = tan^{-1}\frac{sin\,\phi}{TSR + cos\,\phi} - \beta \tag{6.3}$$

where β is the pitch angle.

This calculation of the AOA is referred to as the theoretical AOA. However, in the real flow conditions, there are several phenomena that result in some distortion in both the magnitude and direction of the approaching wind velocity vector. These include the streamtube expansion, the flow deceleration upstream of the turbine, and the blades wake interactions. A more realistic relative velocity triangle could be obtained by considering the variation of the magnitude and direction of the approaching wind velocity as shown in Figure 6.7 (b). A simple aerodynamic analysis could not achieve an accurate prediction of the AOA and the relative velocity magnitude. However, detailed CFD data could provide a good estimation of these quantities that could facilitate a better understanding of the turbine performance.

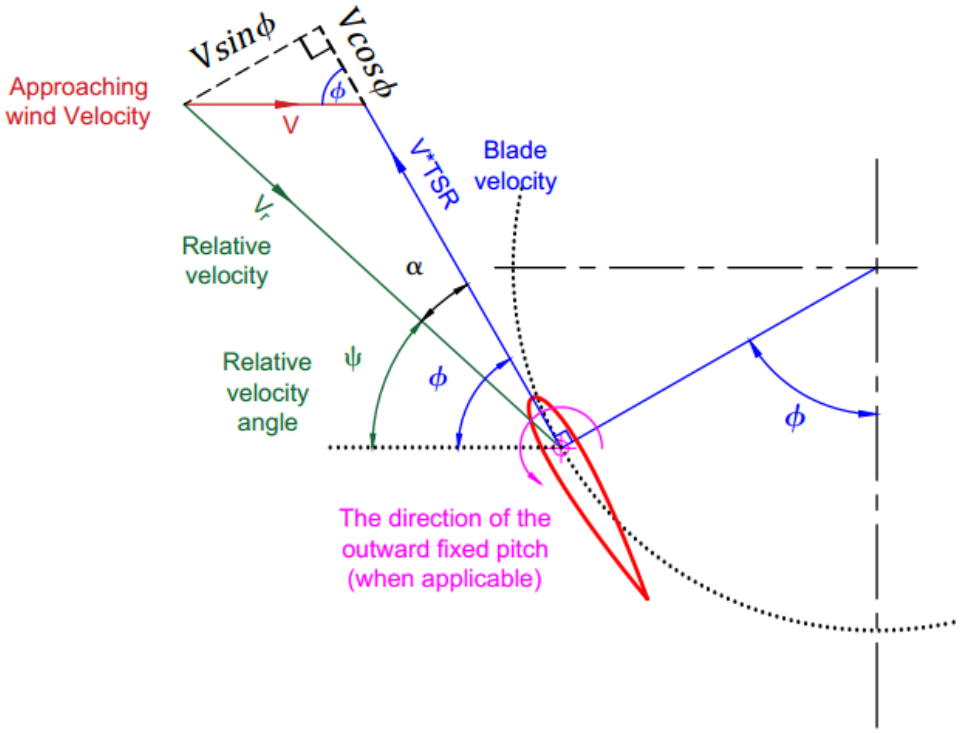

(a)

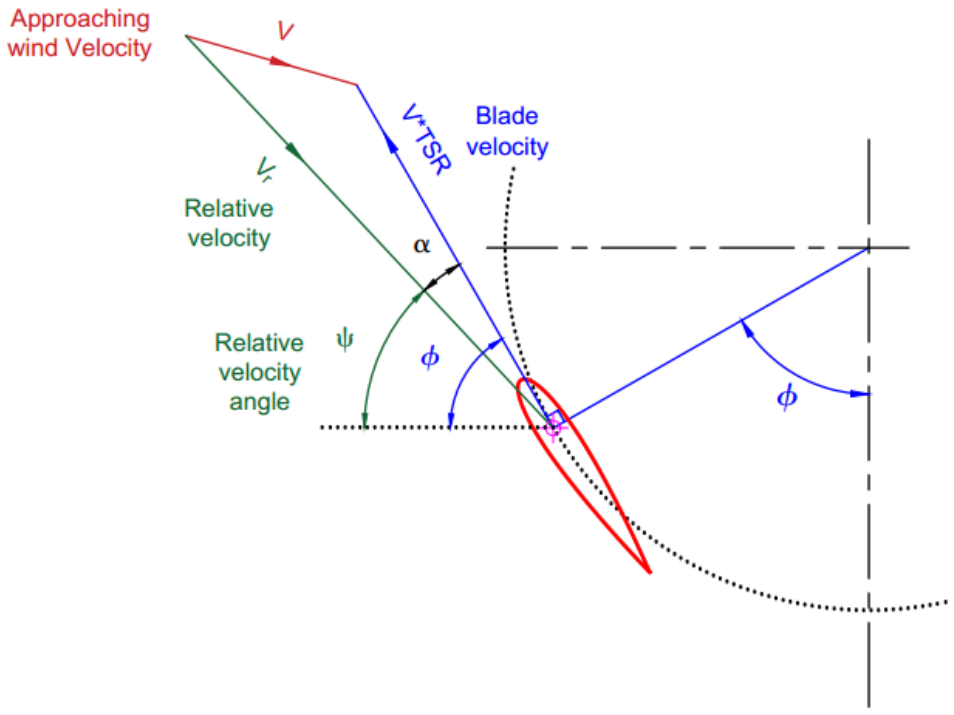

(b)

Figure 6.7 (a) A theoretical velocity triangle and (b) a realistic velocity triangle at an arbitrary azimuthal position for a zero fixed pitch blade. The drawing is not to scale and the angle of the approaching wind velocity in the realistic velocity triangle is arbitrarily chosen for illustration.

For the VAWT simulations, an interpreted UDF is hooked to the solver for the estimation of the AOA and the relative velocity magnitude. A typical example of the used

UDF is provided in Appendix A. Firstly, the absolute velocity component is calculated at the suggested reference-points. Then, the AOA and the relative velocity magnitude are calculated and averaged between the pair of reference-points. Figure 6.8 shows a comparison between the theoretical AOA obtained using equation (6.3) and the estimated AOA based on the proposed method, over one cycle, for both 0° fixed pitch (0° FP) and 6° fixed pitch (6° FP) configurations operating under the same condition as the validated test case. It is clear that the differences between the theoretical AOA and the estimated AOA are relatively smaller in the upstream part of the cycle, i.e. from 0° to 180° of azimuthal angle. These differences are expected to be due to the streamtube expansion phenomenon in addition to the flow deceleration upstream of the turbine. However, the differences in the downstream part of the cycle are dramatically higher due to the complexity of the turbine wake where the velocity magnitude has a significant drop.

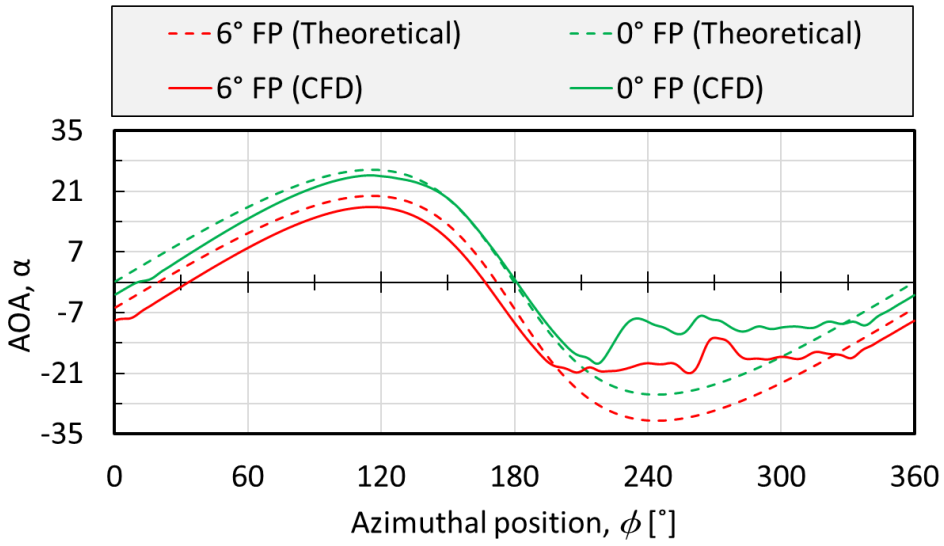

Figure 6.8 A comparison between the theoretical AOA and the estimated AOA based on the CFD data using the pair of reference-points for both of ZFP and 6° FP.

6.3 The proposed procedure for the analysis of the VAWT performance

The proposed procedure relies on the interpretation of the single-blade instantaneous power coefficient of a VAWT through the simpler performance of the aerofoil-profiled blade. This includes the analysis of the instantaneous lift and drag coefficient along with the local AOA and velocity magnitude. The strength of this analysis comes from the

utilisation of the data from high-fidelity CFD simulations rather than the trigonometry of theoretical velocity triangles or other simplified aerodynamic models.

The directions of the lift and drag, also referred to as L and D, respectively, directly depend on the time-variant AOA and hence the direction of the relative velocity vector. This makes it challenging to estimate the lift and drag. For simplicity, the CFD solver is used to report the forces in the principal Cartesian directions, namely F_x and F_y, at each time step. Then, the Cartesian forces and the relative velocity angle are used to calculate the lift and drag. Figure 6.9 illustrates the relationship between the direction of the lift and drag and the direction of the Cartesian forces in terms of the relative velocity angle, ψ. Hence, the lift and drag forces can be calculated as follows:

$$L = F_x * \sin(\psi) + F_y * \cos(\psi) \tag{6.4}$$

$$D = F_x * \cos(\psi) - F_y * \sin(\psi) \tag{6.5}$$

In addition, the dimensionless lift and drag coefficient, also referred to as C_L and C_D, are defined as follows:

$$C_L = \frac{L}{0.5\ \rho\ A_c\ V_r^2} \tag{6.6}$$

$$C_D = \frac{D}{0.5\ \rho\ A_c\ V_r^2} \tag{6.7}$$

where ρ is the air density, V_r is the average relative velocity based on the CFD data on the selected reference-points, and A_c=C*H is the blade area based on the chord, C and the blade span height. For a 2D simulation, the results are extracted per unit height, i.e. H=1 m.

Figure 6.10 illustrates the workflow of the proposed procedure. Firstly, the flow-field data is extracted using the UDF to calculate the velocity vectors and the AOA, as discussed in Section 6.2.5. Then, the lift and drag coefficients are evaluated. Finally, the instantaneous power coefficient is interpreted by analysing the AOA and the local velocity magnitude and their effect on the lift and drag coefficients.

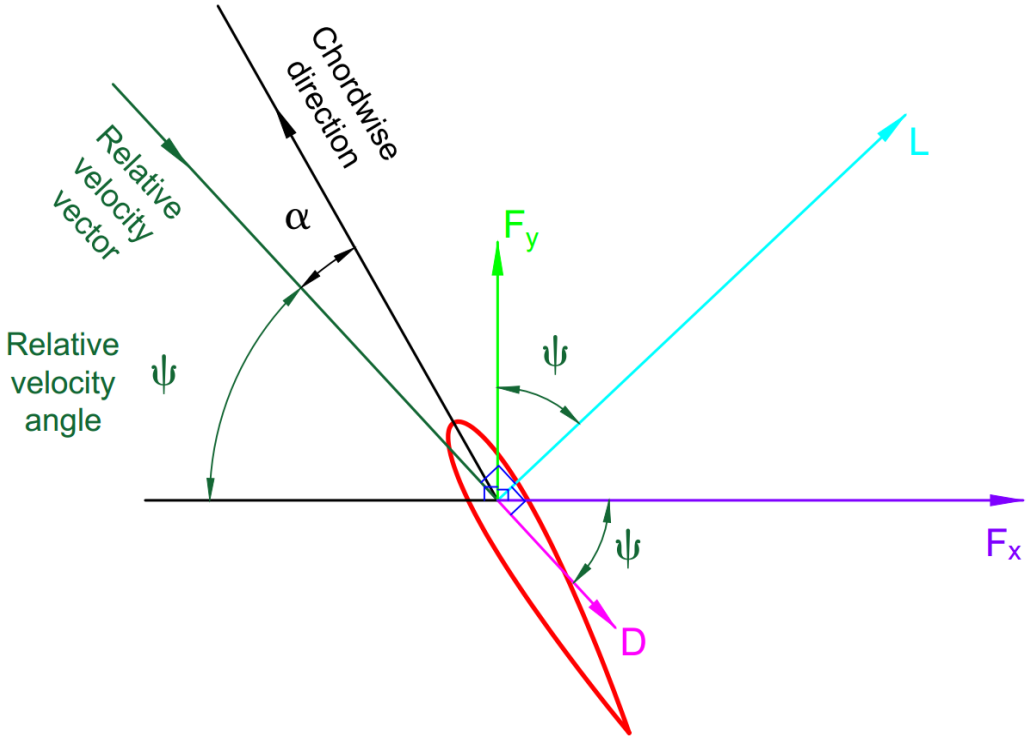

Figure 6.9 A schematic for the relations between the directions of the lift and drag forces and the direction of the Cartesian forces. The angle of the chordwise direction and the angle of the relative velocity vector are arbitrarily chosen for illustration.

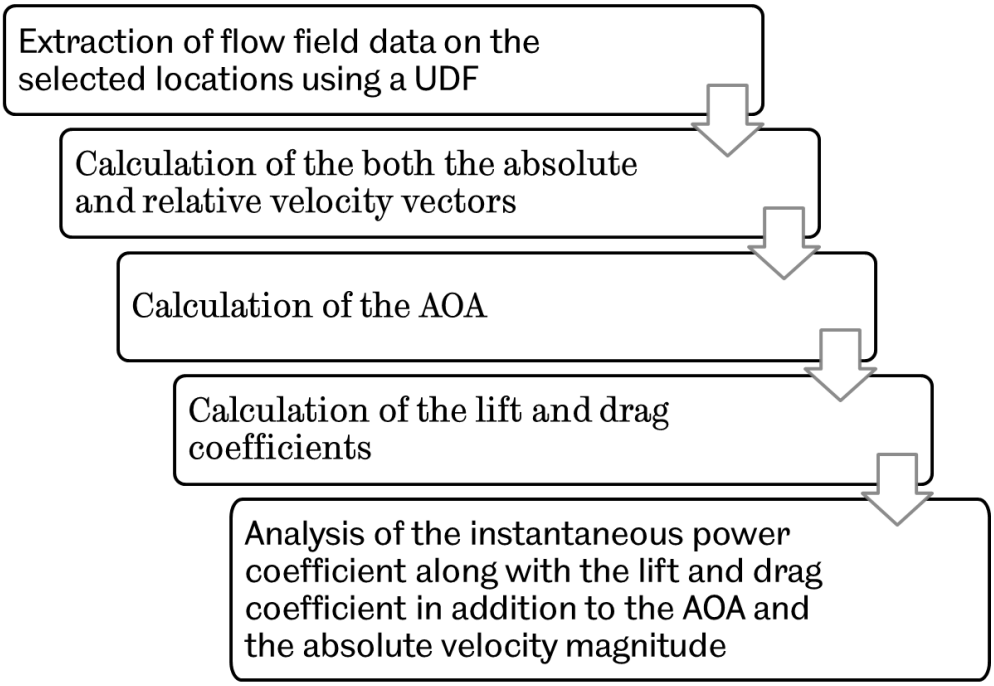

Figure 6.10 An illustration of the proposed procedure for the analysis of the VAWT performance.

6.4 Application of the proposed procedure on the fixed pitch configurations

The proposed procedure is applied to analyze the differences in the performance for two fixed pitch configurations, particularly with 6° and 0° of fixed pitch that are referred to as 6° FP and 0° FP, respectively. These pitch-configurations are simulated under the same geometrical and dynamical specifications as the 2D test model that is described and validated in Sections 4.2 and 5.2. The rotor spins at a TSR of 2.29 which have a maximum theoretical AOA of about 25.9° and 19.9°, according to equation (6.2), for the 6° FP and 0° FP configurations, respectively. These values of the AOA are relatively high for the NACA0015 aerofoil which have been reported to have a static stall angle of 14° at a relevant Reynolds number of about 3.6×10^5 [15].

The proposed five key parameters have been considered and these include the instantaneous single blade power coefficient, the AOA, the absolute velocity magnitude, lift coefficient, and drag coefficient. Figure 6.11 illustrates the variations of these characteristics over a complete cycle, from 0° to 360° of azimuthal angle, ϕ, for both the 6° FP and 0° FP configurations. The quantities, based on equations (6.1) and (6.3), are plotted with the dashed lines and marked as theoretical values and these are only plotted in the subfigures 6.11 (b) and (c). Due to the complex aerodynamics and the dynamic behaviour of the flow around the VAWT, it is not possible to calculate the power coefficient theoretically. Also, the calculation of the dynamic lift and drag coefficients based on the incoming flow conditions will need a complex dynamic stall modelling and this is not included in the scope of this thesis. The single-blade instantaneous power coefficient represents the generated power from a certain blade regardless of any other turbine component and hence gives more information on the performance of the blade in contrast with the instantaneous power coefficient of the whole turbine. The variations of the single-blade power coefficient for both of the 6° FP and 0° FP are shown in Figure 6.11 (a). It is clear that the single-blade power coefficient of the 6° FP configuration is significantly higher in the region between ϕ=110° and ϕ=180°. In addition, the 6° FP configuration has a higher single-blade power in the downstream part of the cycle, i.e. between ϕ=180° and ϕ=360°. The cycle-averaged single blade power coefficient is found to be 0.233 and 0.143 for the 6° FP and 0° FP, respectively. Hence, the 6° FP configuration is able to improve the overall performance

of the turbine by about 63% compared with the 0° FP configuration under the current setup.

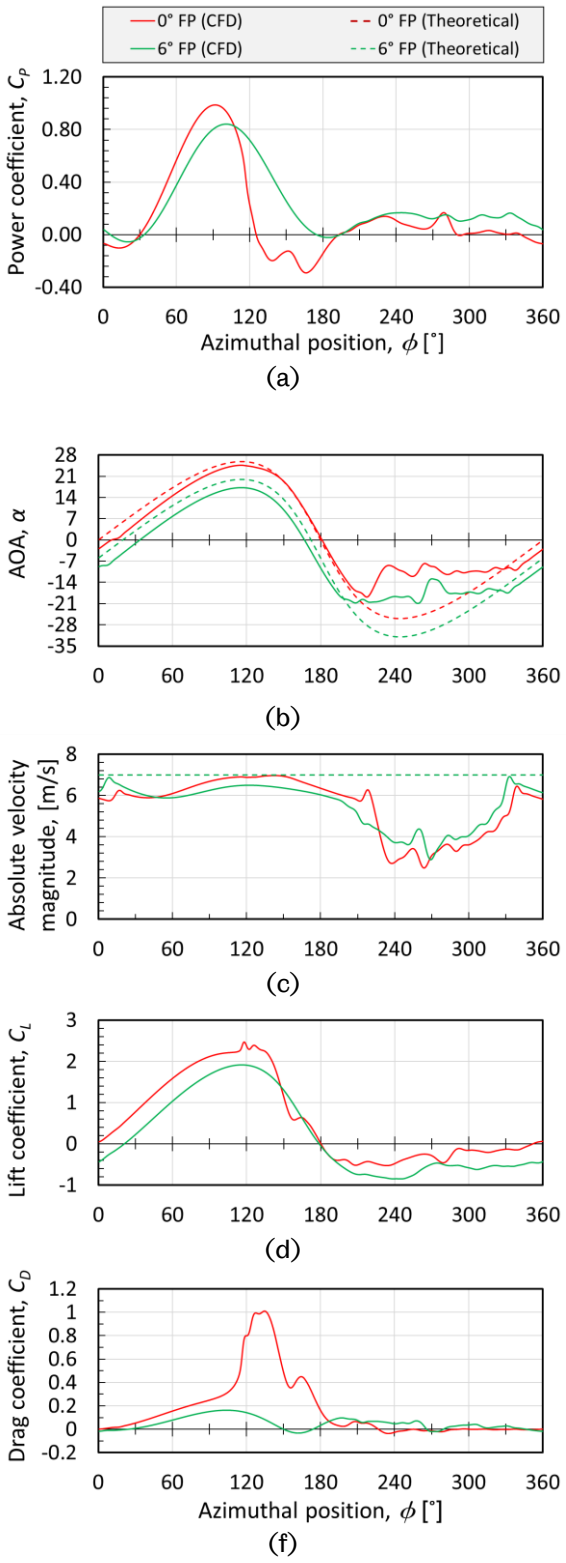

Figure 6.11 A comparison between the 6° FP and 0° FP according to (a) the instantaneous power coefficient, (b) AOA, (c) relative velocity magnitude, (d) lift coefficient, and (f) drag coefficient (the horizontal axis of all the subfigures represent the azimuthal position).

Figure 6.11 (b) shows the variation of both of the theoretical AOA and the estimated AOA based on the CFD data for both the 6° FP and 0° FP. In the downstream part of the cycle, it is found that the theoretical AOA, that reaches about -32° for the 6° FP configuration, could not describe how the 6° FP has a better power coefficient in contrast with the 0° FP configuration because the NACA 0015 is not expected to perform well at such high AOA magnitude. However, based on the CFD data between ϕ=240° and ϕ=360°, it is found that the average estimated AOA is about 16.1° and 9.4° for the 6° FP and 0° FP, respectively. Hence, the estimated AOA based on the CFD data illustrates that the blade with 6° FP has a better AOA potential, in contrast with the 0° FP configuration, which illustrates why the 6° FP configuration outperforms the 0° FP configuration between ϕ=240° and ϕ=360°. The theoretical velocity magnitude and its estimated values based on CFD data are compared in Figure 6.11 (c) for both the 6° FP and 0° FP. The differences between the theoretical and the CFD based values in the upstream part of the cycle represents the deceleration of the flow due to the turbine blockage. While these differences in the upstream part of the cycle are minimal, there are considerable differences in the downstream part due to the distortion of the flow in the wake region.

Figures 6.11 (d) and (f) show the variation of the lift and drag coefficients, respectively, for both the 6° FP and 0° FP configurations. Due to the aerodynamic characteristics of the VAWT, both the favourable AOA and lift coefficient are negative in the downstream part of the cycle. In addition, the aerodynamic definition of the drag forces illustrates that it is always positive. Therefore, any negative value in the estimated drag coefficient is considered as an error. The reason for these negative values is that any slight misrepresentation of the AOA may result in adding a fraction of the relatively higher negative lift component into the drag coefficient. Considering the variations of the lift and drag coefficients along with the AOA, it is clear that the 0° FP blade encounters a severe stall condition between ϕ=90° and ϕ=140° and this is characterised by a high AOA followed by a sudden reduction in the lift and drag coefficients. Although the 0° FP blade has a higher lift coefficient in the period between ϕ=90° and ϕ=140°, its power coefficient is dramatically lower. The reason is that the large drag forces in this period act to significantly reduce the tangential force and hence reduce both the driving torque and the power coefficient. On the other hand, the 6° FP blade operates at a

more favourable AOA and produces a lower lift coefficient while maintaining a significantly lower drag coefficient and this is in contrast with that of the 0° FP blade in the upstream part of the cycle. This enables the 6° FP blade to achieve a better power coefficient distribution over the upstream part of the cycle.

In the downstream part of the cycle, the 6° FP blade operates at a higher AOA in contrast with the 0° FP blade. However, as mentioned before, this higher AOA is still more favourable than the relatively low AOA encountered by the 0° FP blade. This enables the 6° FP blade to obtains a higher lift coefficient with a negligible drag due to its favourable AOA potential. These favourable lift and drag coefficients illustrate how the 6° FP configuration obtains a higher power coefficient over the downstream part of the cycle, in contrast with the 6° FP configuration.

6.5 **Conclusions**

The following conclusions are drawn:

- The distribution of the AOA over the entire cycle has significant effects on the overall power coefficient of the VAWT and this makes an accurate estimation of the AOA essential. Hence, a new method for the estimation of the AOA is proposed and is compared against a set of prescribed AOAs in static aerofoil simulations.
- In comparison with an existing method in the literature, the proposed AOA estimation method can reduce the RMSE by as much as an average of 33.8% for the three tested flow velocities. In addition, the new method could be used to calculate and store the AOA data during the CFD simulations without the need for extensive post-processing.
- In order to gain a better understanding of the performance of the VAWT, a new procedure for the VAWT performance analysis is proposed based on the CFD data. This relies on the interpretation of the VAWT power coefficient with the aid of the understanding of the AOA and velocity magnitude and their effect on the lift and drag coefficient of the turbine blade.
- It is found that the proposed procedure provides a better understanding of how a certain VAWT configuration performs better than another. This is achieved by

interpreting the VAWT performance based on the estimation of the lift, drag, and AOA encountered by the blade.

7 AERODYNAMIC DESIGN AND OPTIMISATION OF A SMALL SCALE FP-VAWT

7.1 Overview

The aim of this chapter is to clarify the details of the design optimisation of the baseline fixed pitch VAWT based on the Response Surface Optimisation and the 2D CFD simulations. The 2D simulations are selected for the optimisation study due to its reasonable accuracy and computational cost. In addition to assisting the selection of the optimal design, the Response Surface provides a valuable insight into how the different input parameters affect the VAWTs performance over the entire design space. After identifying the optimal design configuration, the final design is adjusted for possible manufacture. In addition, 3D CFD simulations are carried out in order to assess the effect of the turbine aspect ratio and the blade tip shape on the 3D performance of the final design.

The majority of the design and performance investigations of the VAWT are based on parametric studies in which the effect of each design parameter is investigated while keeping the other parameters constants. The novelty of the investigation in this chapter is based on the utilisation of the Response Surface Optimisation methodology combined with the detailed CFD simulations of the VAWT. Together, they provide a very powerful tool in exploring the entire design space based on the whole range of the selected design parameters. While this combination has not been utilised before in the VAWT literature, it is found to be a viable tool for both the optimal design of the VAWT and for the exploration of the effect of the different design parameters on the performance of the VAWT with reasonable computational costs.

While the model verifications and validations in Chapters 4 and 5 are based on a two-bladed VAWT, the design of the baseline fixed pitch VAWT is based on a three-bladed VAWT. In contrast with two-bladed VAWTs, the three-bladed rotor has less torque ripple [33] and better start-up characteristics [208]. Despite the change in the number of blades, the selected range of solidity is considered to be moderate and hence the blade interactions are still similar. Therefore, the CFD model is assumed to be valid even for the three-bladed configuration with in the selected range of turbine solidity. The turbine diameter in the optimisation study is slightly increased to 1.8 m in contrast

with 1.7 m in the model verifications and validations. This slight increase in the turbine diameter has a small effect on the Reynolds number based on the cycle averaged relative velocity and it is expected to have an insignificant effect on the flow regime and the aerodynamic behaviour. Hence, the current numerical model is considered valid for the analysis of the VAWT based on the new diameter. However, the new diameter is favourable for its suitability for future one-third scale down studies in the available wind tunnel at the University of Sheffield. In order to reduce the computational cost, the design optimisation study is carried out based on the data from 2D CFD simulations. These simulations utilise the same numerical aspects of the proposed model in Chapter 4.

7.2 The workflow of the optimisation

Figure 7.1 (a) illustrates the workflow of the Goal-Driven Optimisation based on the Response Surface, and this optimisation method is also referred to as Response Surface Optimisation (RSO) or Response Surface Methodology (RSM). Firstly, the design problem is parameterised into a set of input and output parameters. Then, the Design of Experiments (DoE) technique is used to select the initial set of design points in the form of an initial DoE table that contains the values of the input parameters. Furthermore, the DoE table is updated with the values of the output parameters from detailed CFD simulations. The updated DoE table is used to construct the Response Surface that represents the relation between the input and output parameters. The Goal-Driven Optimisation is used to select the optimised design candidates that satisfy both the objective function and the design constraints. The performance of the selected optimised design candidates is validated with detailed CFD simulations.

Upon the validation of the optimised design candidates, it is observed that some of the optimised design candidates have a slightly lower performance in contrast with the best design point in the initial DoE table. This indicates that the Response Surface requires further refinements and hence the modified workflow is proposed as shown in Figure 7.1 (b). This allows for the refinement of the Response Surface until the optimised design outperforms the best design point in the initial DoE table. More details about the optimisation steps and the implemented techniques are discussed in the following sections.

ANSYS DesignXplorer [175] offers a wide range of DoE, Response Surface and optimisation methods. The design exploration is not only limited to the selection of the optimised design but also is extended to explore the relations between the different design parameters and the performance of the investigated system and/or components. In the current study, ANSYS DesignXplorer [175] is used to carry out the different tasks of the proposed optimisation workflow.

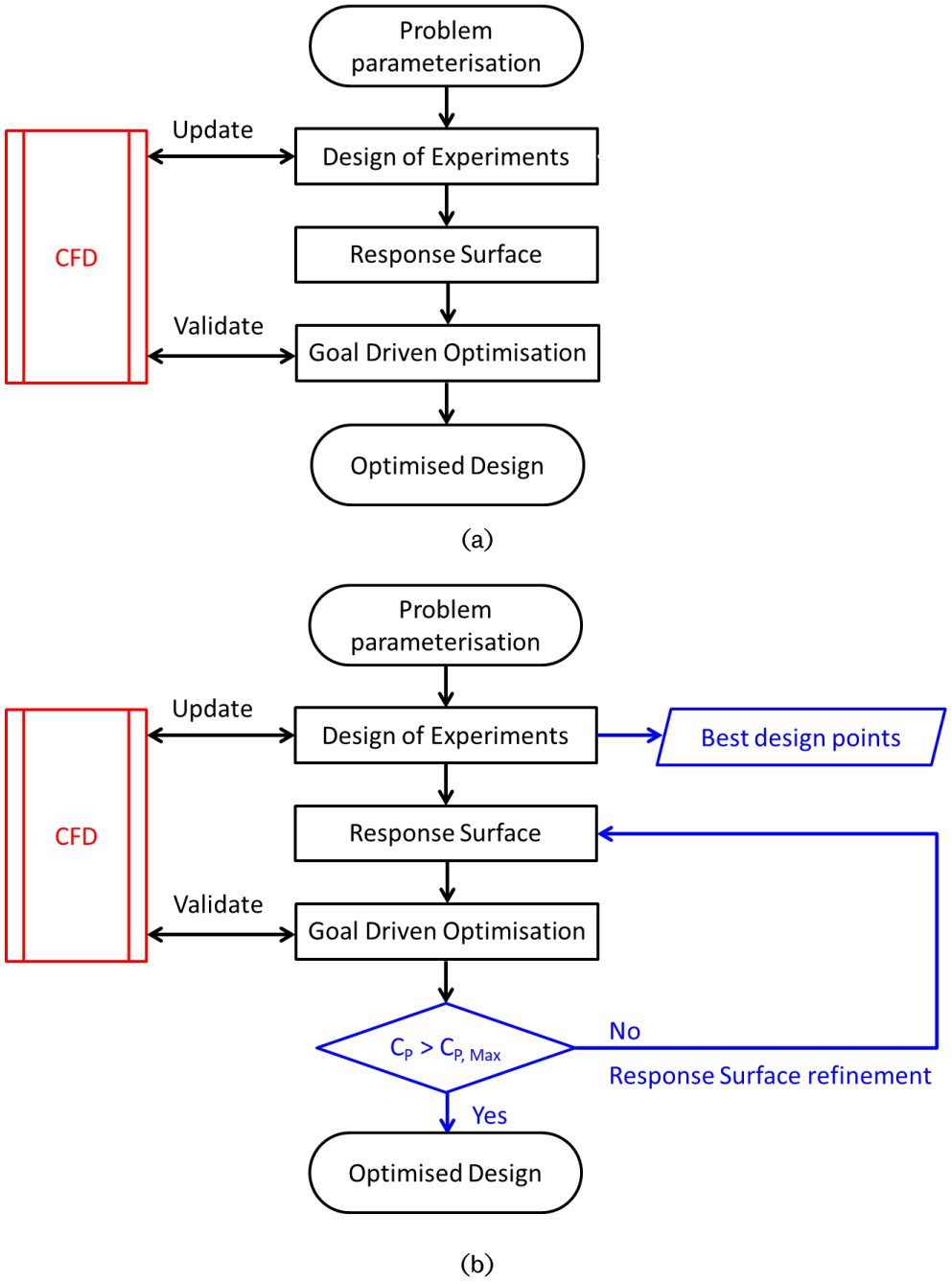

Figure 7.1 Flow chart of (a) the original optimisation workflow and (b) the modified optimisation workflow.

7.3 Problem parameterisation

The 2D design of a FP-VAWT, based on three blades with a NACA0015 profile, is simplified/reduced into the selection of three significant input parameters. These include the design TSR, the turbine solidity, σ, and the pitch angle, β. An extended range of each input parameter is chosen in order to gain a good insight into how these input parameters affect the performance of the VAWT. The selected range of TSR includes $1.5 < TSR < 4.5$, which correspond to a rotational speed between about 111 and 334 rpm. For a predefined number of blades, the turbine solidity, σ, is directly related to the blade chord. The current optimisation study covers a wide range of turbine solidity including $0.2 < \sigma < 0.6$, which corresponds to a blade chord between 0.12 and 0.36 m. Only the outward pitch is investigated since it has been found to enhance the VAWT performance [38], [41], [209]. A wide range of pitch angles is selected and this includes $0° < \beta < 10°$. While the CFD model has been validated for a single TSR, the change of the TSR in this investigation does not have a significant effect on the Reynolds Number or the dynamic behaviour of the flow around the turbine and hence the current CFD model is considered to be valid for the test in the selected TSR range.

The optimised design is intended to work with high performance at low wind velocities. Therefore, the selected output parameters are chosen as the cycle-averaged power coefficients at wind velocities of 7 m/s and 5 m/s, also referred to as $C_{P,7}$ and $C_{P,5}$, respectively. Table 7.1 summarises the selected input parameters and their ranges in addition to the selected output parameters.

Table 7.1 Summary of the selected input and output parameters.

	Name	Symbol	Lower Bound	Upper Bound
Input parameters	Tip speed ratio	TSR	1.5	4.5
	Solidity	σ	0.2	0.6
	Pitch angle	β	0°	10°
Output parameters	Power coefficient at a wind velocity of 7 m/s	$C_{P,7}$	-	-
	Power coefficient at a wind velocity of 5 m/s	$C_{P,5}$	-	-

7.4 **Design of Experiments**

The DoE aims to efficiently cover the design space using the minimal number of combinations of the values of input parameters. These combinations are referred to as experiments or design points. The DoE assist in the well-selection of the design points that are efficiently distributed over the whole ranges of input parameters. While there is a variety of DoE techniques, the Central Composite Design (CCD) is commonly used to build the initial DoE data for the Response Surface Method. The CCD distribute the design points in a structured manner around the central point of the design space. In the current study, the enhanced rotatable CCD is implemented and this consists of 29 design points. In addition to the enhanced rotatable CCD points, eight extra design points are added to cover the corners of the design space. Figure 7.2 shows the distribution of the enhanced rotatable CCD points and the corner points in a 3D design space. In addition, Figure 7.2 illustrates the projections of the design points into the main 3D planes. These projections illustrate how the enhanced rotatable CCD points well cover the central part of the design space while the corner points make sure that even the extreme ends of the design space are covered. Figure 7.3 shows the Parameters Parallel plot for the selected design points that illustrates the variety of the combinations of the input parameters values in the selected design points. In addition, Figure 7.3 shows who the ranges of the input parameters are coved into nine levels.

Figure 7.4 shows a conventional alternative that implements the Brute Force Method and this requires 125 design points to cover the three input parameters in five levels. In contrast with the Brute Force Method, the proposed DoE is observed to cover the design space in an efficient manner, especially the central part while minimising the number of the required design points to 37 points. This assists in reducing the computational cost significantly.

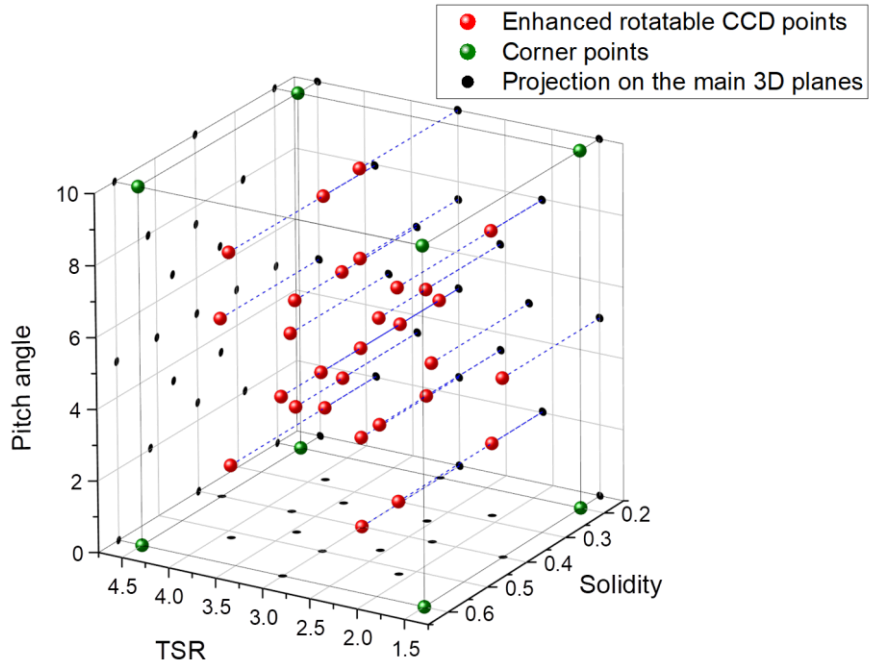

Figure 7.2 A 3D illustration of the selected design points and their projections on the main 3D planes.

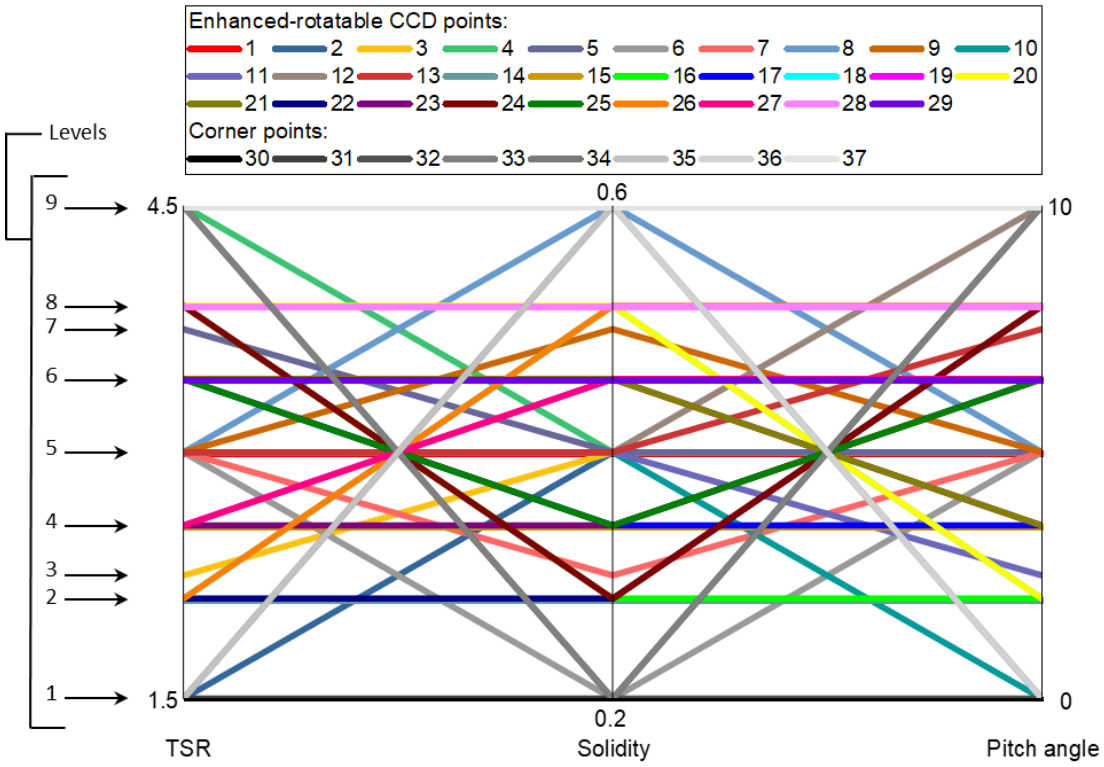

Figure 7.3 A Parameters Parallel plot for the selected design points that illustrate the selected combinations between the nine levels of each input parameter.

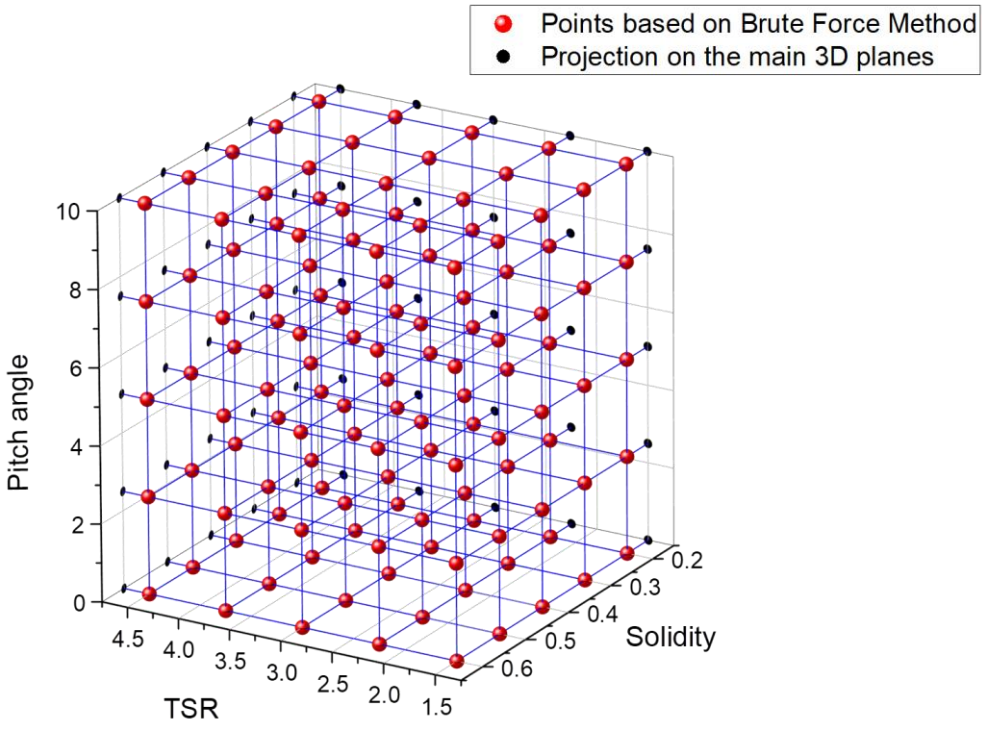

Figure 7.4 A 3D illustration of the design points required to cover the three input parameters in five levels based on the Brute Force Method.

After the selection of the design points and the associated values of the input parameters, detailed 2D CFD simulations are carried out in order to update the initial DoE with the corresponding values of the output parameters. A set of 2D structured mesh is constructed for each design point following the same meshing attributes as the baseline 2D model that is discussed in Chapter 4. An example of the implemented mesh topology is discussed in Appendix E. In addition, the 2D CFD simulations adapt the same numerical specifications of the selected 2D model based on the SST k-ω model as clarified in Chapter 4. Figure 7.5 shows the Parameters Parallel plot for the selected design points including the values of both input and output parameters. It is observed that the predictions of both the $C_{P,7}$ and $C_{P,5}$ are relatively very similar. This means that the change on the undisturbed wind speed from 7 m/s to 5 m/s does not have a significant influence in the turbine power coefficient.

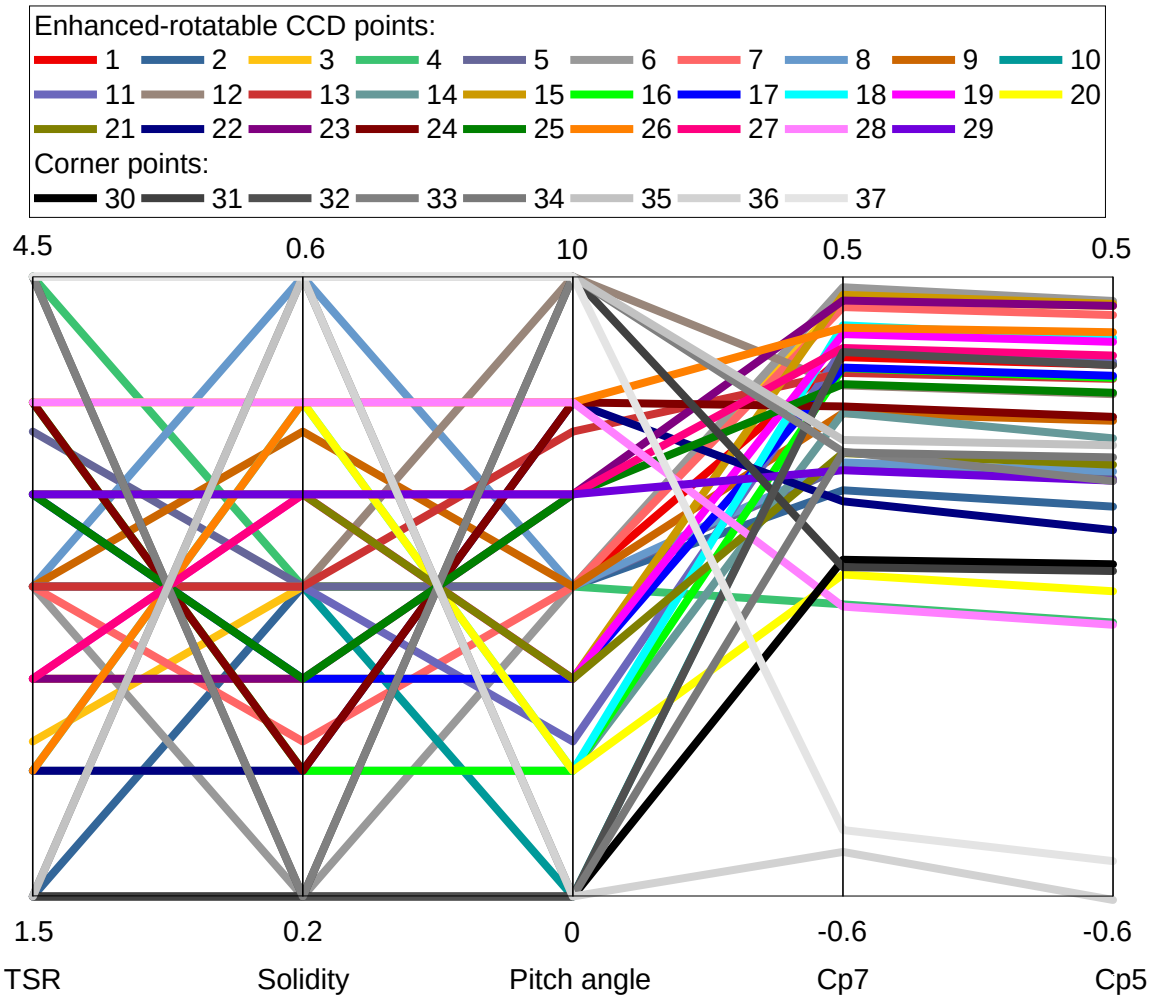

Figure 7.5 A Parameters Parallel plot for the selected design points including the values of both input and output parameters.

7.5 Response Surface

In the optimisation process, the importance of Response Surface is that it acts as a metamodel which represents the DoE data in the form of fast running surrogate model. Instead of performing a detailed CFD simulation, the surrogate model enables a fast evaluation of the output parameters values for any combinations of the input parameters when requested by the optimiser. In the current study, the Kriging method is implemented as a metamodelling algorithm. In contrast with alternative regression-based models, The Kriging is based on multidimensional interpolation that fits all the points in the DoE table with 100% goodness of fit.

Figure 7.6 (a) shows an example of the response chart at the optimal pitch angle, β=3.6228°, based on the initial Response Surface. The response chart illustrates the

effects of the TSR and the solidity on the power coefficients at a wind velocity of 7 m/s. It is observed that the response chart has two peaks and one of them is the low solidity region. Figure 7.6 (b) shows a contour map of the power coefficient at a wind velocity of 7 m/s, which highlights the regions of peak power coefficient. Due to the fact that low solidity VAWT suffers from start-up difficulties [208], it is decided to exclude the low solidity region, $\sigma < 0.3$, from the optimisation scope. Therefore, the optimisation objective is not to find the global optimal. However, it is focused on finding the local optimal design in the moderate solidity range that is associated with better start-up characteristics.

7.6 **Optimisation**

The present optimisation of the FP-VAWT is based on the Multi-Objective Genetic Algorithm (MOGA) [175], which supports multiple objective-functions and provides a fast convergence [210]. In addition, it relies on the evolutionary search of the genetic algorithm that provides strong searching capabilities. The objective functions of the present optimisation include the maximisation of both the power coefficients at a wind velocity of 7 m/s and at 5 m/s. However, a higher priority is associated with the maximisation of the power coefficient at a wind velocity of 7 m/s as the design wind velocity. Further as discussed in Section 7.5, the optimisation constraint is imposed so that the solidity of the turbine is greater than 0.3.

After each converged optimisation loop, the MOGA suggests a set of three optimal design candidates which are associated with the optimal values of the output parameters. These optimal values are based on the metadata of the Response Surface. Hence, they need to be validated with full CFD simulations. In the current optimisation study, there is a considerable difference between the expected values from the Response Surface and the validated values from the CFD simulations. In addition, the best design point in the initial DoE table is found to outperform the three optimal design candidates based on the validated CFD values. This indicates that the Response Surface needs to be refined near these initial optimal design candidates. Therefore, the three initial optimal design candidates are considered as the first refinement design points. These refinement points are added to the DoE table to reconstructed the Response surface. Table 7.2 includes the specifications of the first refinement

points that represents the initial optimal design candidates after the first optimisation loop. Similarly, the design candidates of the second optimisation loop are considered as the second refinement design points.

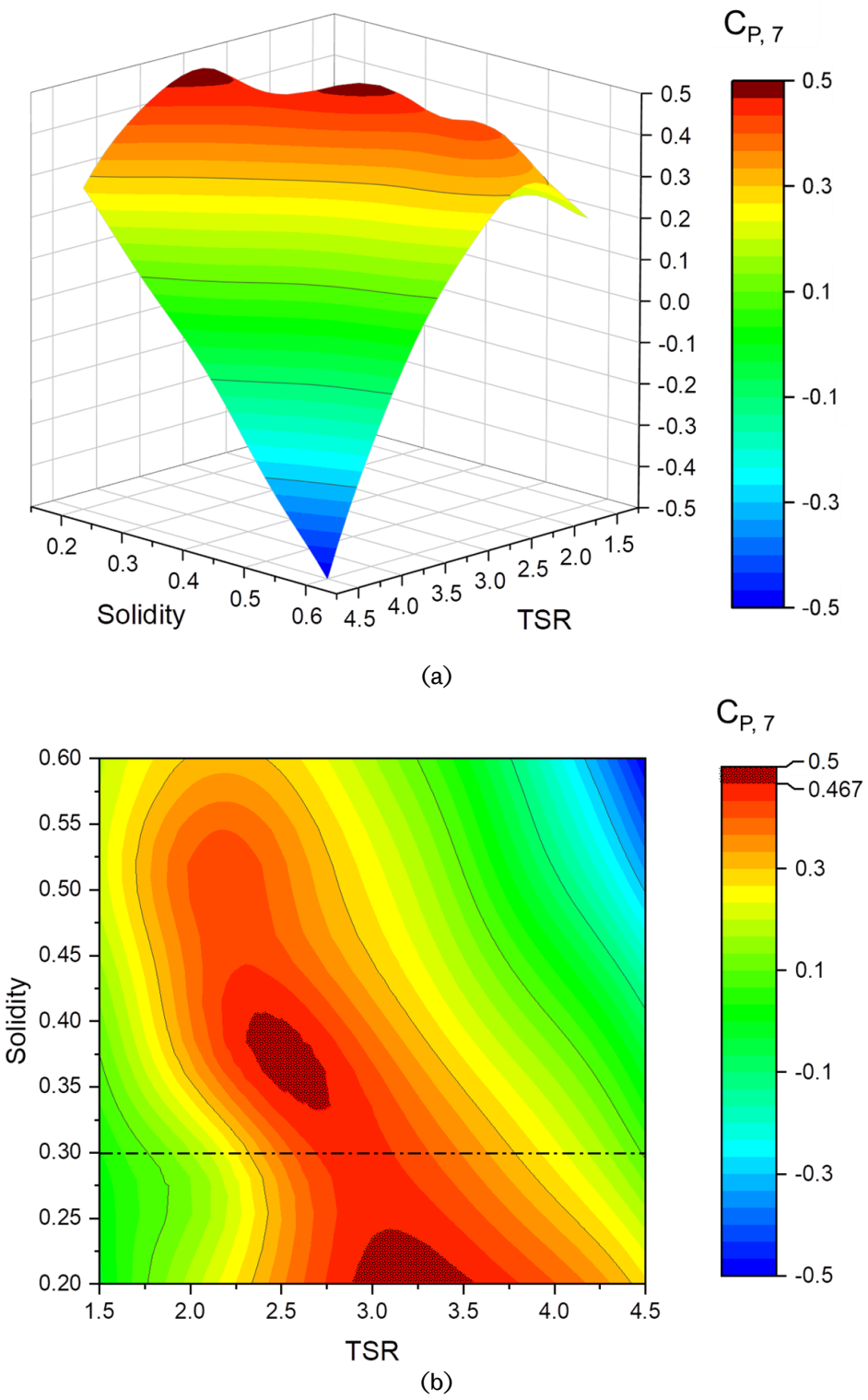

Figure 7.6 (a) 3D response chart and (b) contour map of power coefficient at a wind velocity of 7 m/s for the optimal pitch angle based on initial Response Surface. These represent the metamodel data at the optimal pitch angle, β=3.6228°.

In the present optimisation, two Response Surface refinements and three optimisation loops have been carried out in order to obtain the final design candidates that outperform the best design point in the initial DoE table. The specifications of the refinement points and the final optimal design candidates are identified in Table 7.2. The best optimal design candidate is selected based on the value of the power coefficients at 7 m/s and at 5 m/s and this corresponds to a TSR of 2.5998, a solidity of 0.3153, and a pitch angle of 3.6228°. Figures 7.7 (a) and (b) show the contour maps of the power coefficient at a wind velocity of 7 m/s based on the initial Response Surface and the refined Response Surface, respectively, at the optimal pitch angle of 3.6228°. In addition, the location of the best optimal design candidate in the design space is highlighted in Figure 7.7 (b). It is observed from the visual comparisons between Figures 7.7 (a) and (b) that the successive refinements of the Response Surface assists in improving the Response Surface in the region around the best optimal design candidate. It is noticed from the data in Table 7.2 that the difference between the CFD values and the expected values from the metamodel is reduced after the successive refinements of the response surface. This indicates the improvement in the accuracy of the Response Surface after the successive refinements.

Table 7.2 The specifications of the refinement points and the final design candidates including both the CFD values of the power coefficient and the expected value from the metamodel. The best optimal design candidate is marked in red.

	TSR	Solidity	Pitch angle [°]	$C_{P,7}$		$C_{P,5}$	
				Expected	CFD	Expected	CFD
Best initial design point	2.554	0.3405	3.5134	---	0.4677	---	0.4519
First refinement points	2.5757	0.3672	5.0034	0.4845	0.4474	0.4714	0.4359
	2.5951	0.3658	4.7923	0.4839	0.4466	0.4702	0.4335
	2.595	0.3657	4.5332	0.4841	0.4473	0.4698	0.4338
Second refinement points	2.3123	0.4385	2.6681	0.5132	0.4343	0.4599	0.42
	2.3545	0.4062	4.2958	0.4968	0.4497	0.475	0.4358
	2.3615	0.4268	3.6556	0.5005	0.4375	0.4701	0.4264
Final design candidates	2.5998	0.3153	3.6228	0.4651	0.4777	0.4464	0.4626
	2.627	0.308	2.6306	0.4645	0.4773	0.4431	0.457
	2.6414	0.3081	2.4223	0.4464	0.4755	0.4607	0.4554

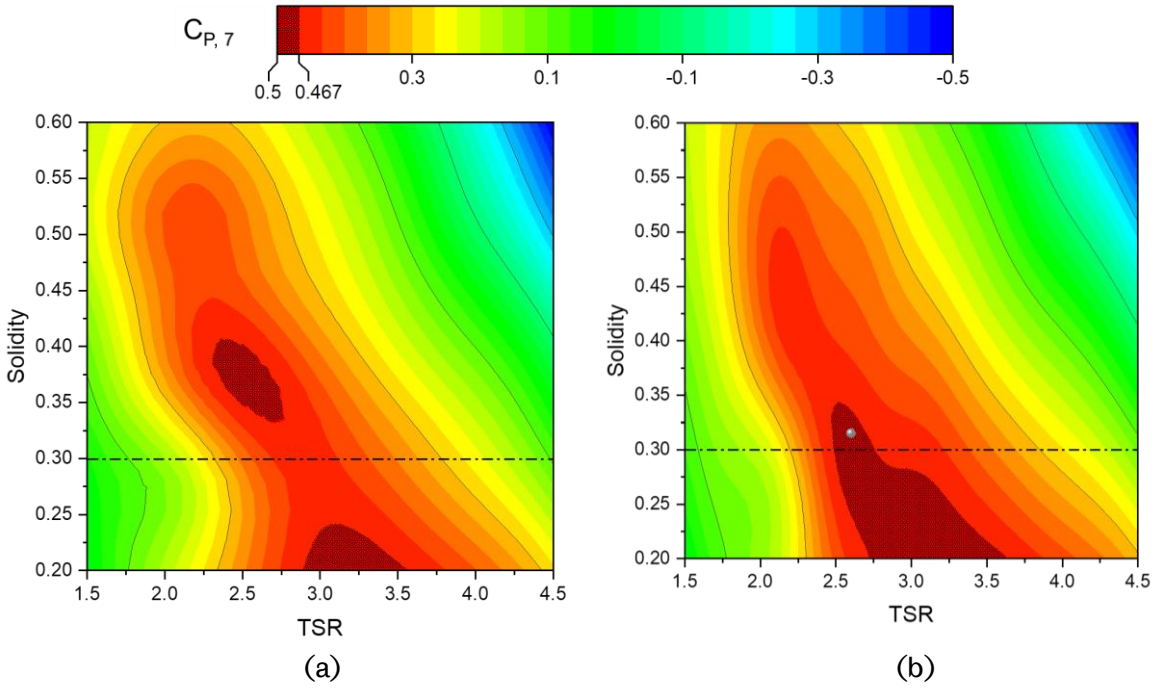

Figure 7.7 The contour maps of power coefficient at a wind velocity of 7 m/s based on (a) initial Response Surface, and (b) refined Response Surface. These represent the metamodel data at the optimal pitch angle, β=3.6228°. In addition, the best optimal design candidate is illustrated with the grey circular symbol.

The use of the Response Surface enables one to have insight into the behaviour of the output parameters over the whole range of the input parameters. In addition, the sensitivity of the output parameters to the changes in the different input parameters can be easily assessed. Considering the best optimal design candidate as a reference point, Figure 7.8 illustrates the sensitivity of the power coefficient at 7 m/s to the change in (a) TSR, (b) solidity, and (c) pitch angle. It is observed that the power coefficient is very sensitive to the change TSR. The solidity is ranked the second most influenced parameter, while the pitch angle has a relatively lower influence.

7.7 Design for possible manufacture

In the current optimisation, the input parameters are considered as continuous parameters without any manufacturing constraints. Therefore, the values of solidity and pitch angle for the optimal design candidate needs to be adjusted for better manufacture. Two manufacture designs, i.e. manufacturing-friendly designs, are proposed as shown in Table 7.3. In these manufacture designs, the solidity is changed from 0.3153 in the optimal design candidate to 0.315, which corresponds to a chord

length of 189 mm. While the optimal design candidate has a pitch angle of 3.6228°, the pitch angle is changed to 3.5° and 4° in the proposed manufacture designs. The corresponding values of the power coefficient for the proposed manufacture designs are shown in Table 7.3 based on the CFD simulations.

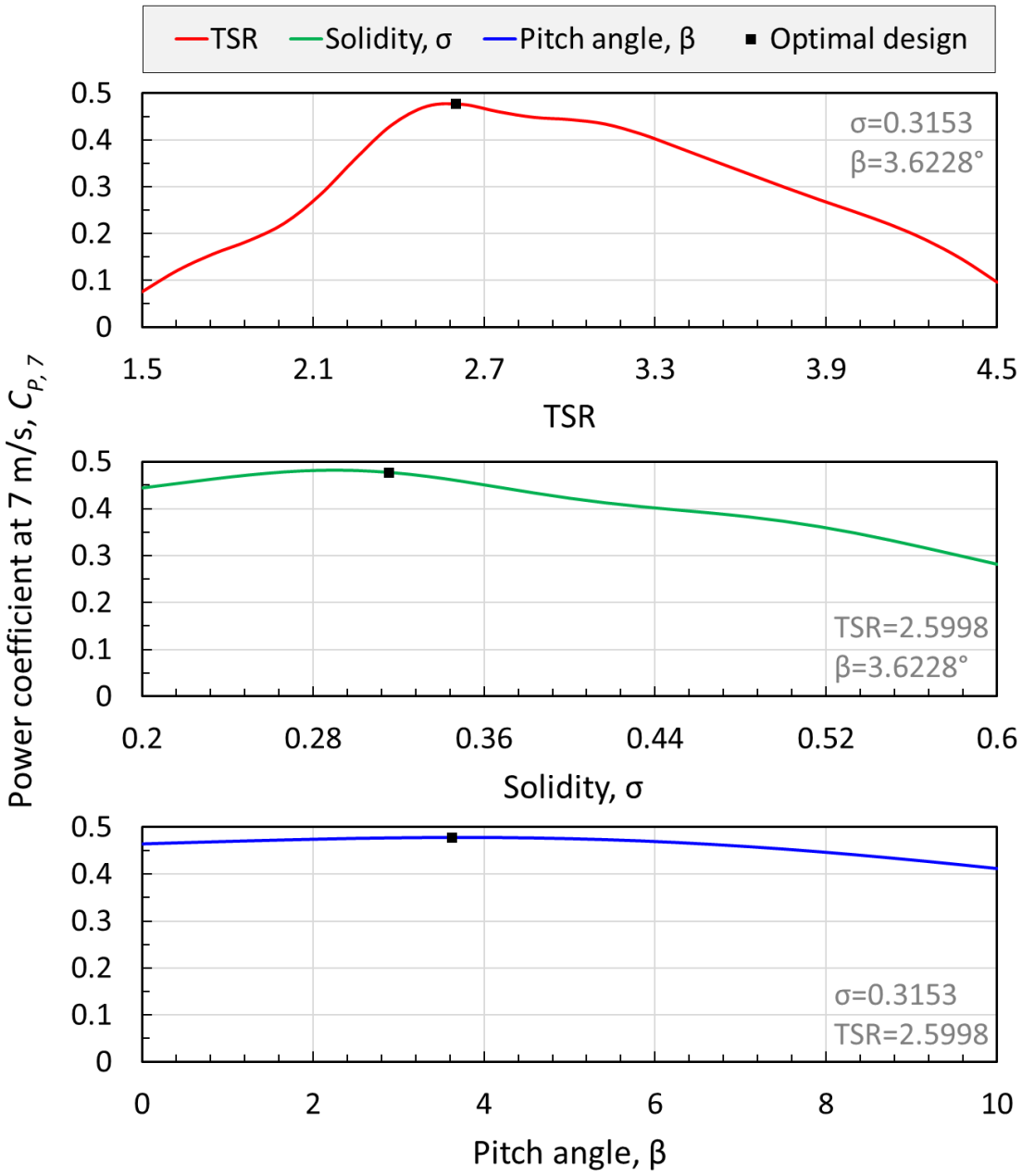

Figure 7.8 The effect of the different input parameters on the power coefficient at 7 m/s. For simplicity, the data is presented considering the best optimal design candidate as a reference point where TSR=2.5998, σ=0.3153, and β=3.6228°.

The first manufacture design is selected as the final optimal design based on the values of the power coefficients at wind velocities of 7 m/s and 5 m/s. It is observed that the

slight adjustments in the input parameters in the manufacture designs have a minimal influence on the output parameters. This is due to the fact that the optimal design candidate, as well as the manufacture designs, are within the optimal region of the design space despite the small manufacture adjustments. The manufacture design with a solidity of 0.315, a pitch angle of 4° and an optimal TSR of 2.6 is selected as the optimal design for a FP-VAWT under the current setup due to its higher power coefficients.

Table 7.3 The specifications of the best optimal design candidate and the two proposed manufacture designs including the CFD values of the power coefficient.

	TSR	Solidity	Pitch angle [°]	$C_{P,7}$	$C_{P,5}$
Best optimal design candidate	2.5998	0.3153	3.6228	0.4777	0.4626
Manufacture design No.1 (Final optimal design)	2.6	0.315	4	0.4778	0.4632
Manufacture design No.2	2.6	0.315	3.5	0.4777	0.4623

7.8 The 3D aspects of the VAWT

In order to reduce both the preprocessing time and the computation cost, the optimisation study in this chapter is based on 2D CFD simulations. A 2D model represents a VAWT with an infinite turbine height, also referred to as blade height, span or length, where there is no change in flowfield variables in the spanwise direction. However, a physical VAWT has its own finite height, h, that affects its 3D behaviour. The concept of the Aspect Ratio, AR, assists in identifying how large is the turbine blade height. In this study, unless otherwise specified, the turbine AR is based on the diameter, D, and is defined as $AR_{h/D}=h/D$. While the turbine support structures, i.e the supporting arms or struts, have their own 3D effects on the turbine performance, the design of these supporting elements depends on both the aerodynamic and structural aspects. This includes a trade-off between the structural design, aerodynamic shape, materials and cost. Therefore, the design of the supporting structure and its effects on the turbine performance are considered to be out of the scope of this study. Hence, the 3D modelling in this section includes the blades and the shaft while excluding the supporting arms.

The 3D CFD simulations are carried out in order to shed more light on the effect of the $AR_{h/D}$ on the performance of the VAWT by considering the $AR_{h/D}$ in the range between

1 and 5 in increments of 1. These 3D simulations are based on the geometric and dynamic specifications of the final optimal design that is clarified in Section 0 while utilising the same numerical aspects and meshing attributes of the proposed 3D CFD model in Section 4.3. Figure 7.9 illustrates how the AR affects the 3D power coefficient and it is observed that the 3D power coefficient is enhanced by increasing the AR. However, the 3D power coefficient is considerably lower than the corresponding 2D value even for the $AR_{h/D}$=5, which is considered to be a high AR and is larger than that of most of the available VAWT designs. As discussed in Section 5.3, the reduced performance in the 3D case is partially associated to the tip losses. Therefore, the 3D performance could be enhanced by the use of tip devices such as the winglets or end-plates. The use of a winglet is discussed further in this section.

In order to enhance the 3D performance of the proposed design, a well-selected winglet is attached to each blade tip. The winglet design is based on the outcome of a dedicated optimisation study [79] in which the six design parameters of the winglet shape are optimised for maximising the 3D power coefficient of the two-bladed turbine that is described in Section 4.1. This optimised winglet design is scaled down to match with the chord length of the final optimal design that has been proposed in Section 7.7.

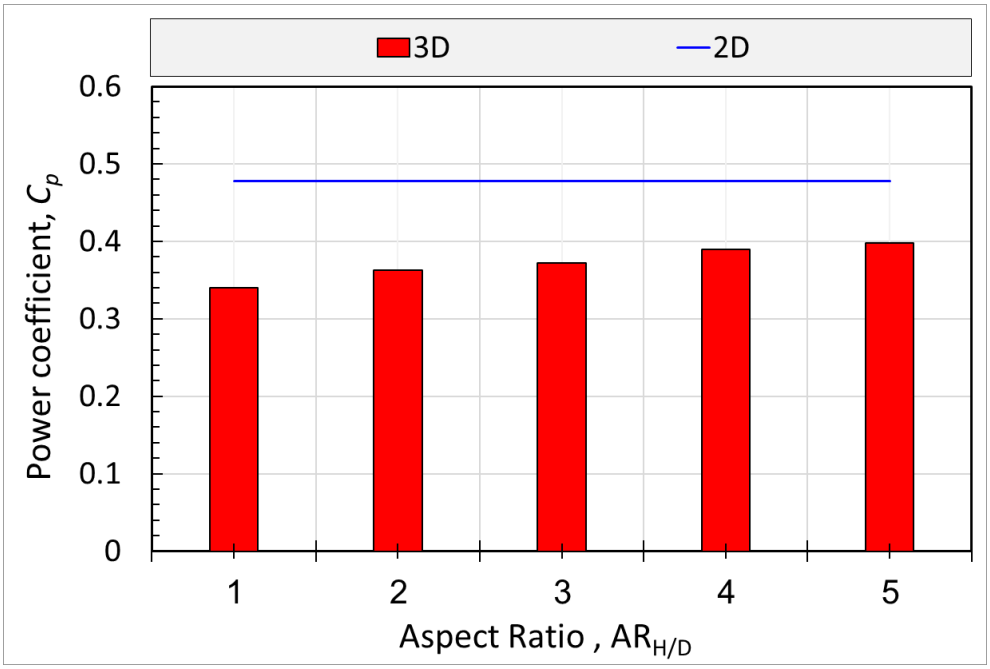

Figure 7.9 The effect of the $AR_{h/D}$ on the 3D power coefficient in contrast with the 2D power coefficient.

Figure 7.10 illustrates the shape of the optimised winglet and the parameters that have been used in the optimisations. These parameters include; the sweep angle about the blade mount axis, θ_{sweep}, the radius of the cant, R_{cant}, the angle of the cant, Ω_{cant}, the twist angle, σ_t, the tip straight extension, L_{tip}, and the ratio between the tip chord and the blade chord, $\gamma_{tip}=c_{tip}/c$. Table 7.4 shows the optimised values of the winglet parameters according to the optimisation study. These parameters are expressed as a function of the blade chord, c, when applicable. More details about the winglet optimisation procedure are available in [79]. Together, Figure 7.10 and Table 7.4 provide the full details of the winglet geometry and this enables the others to reconstruct the winglet geometry using ANSYS DesignModeler or any similar CAD software.

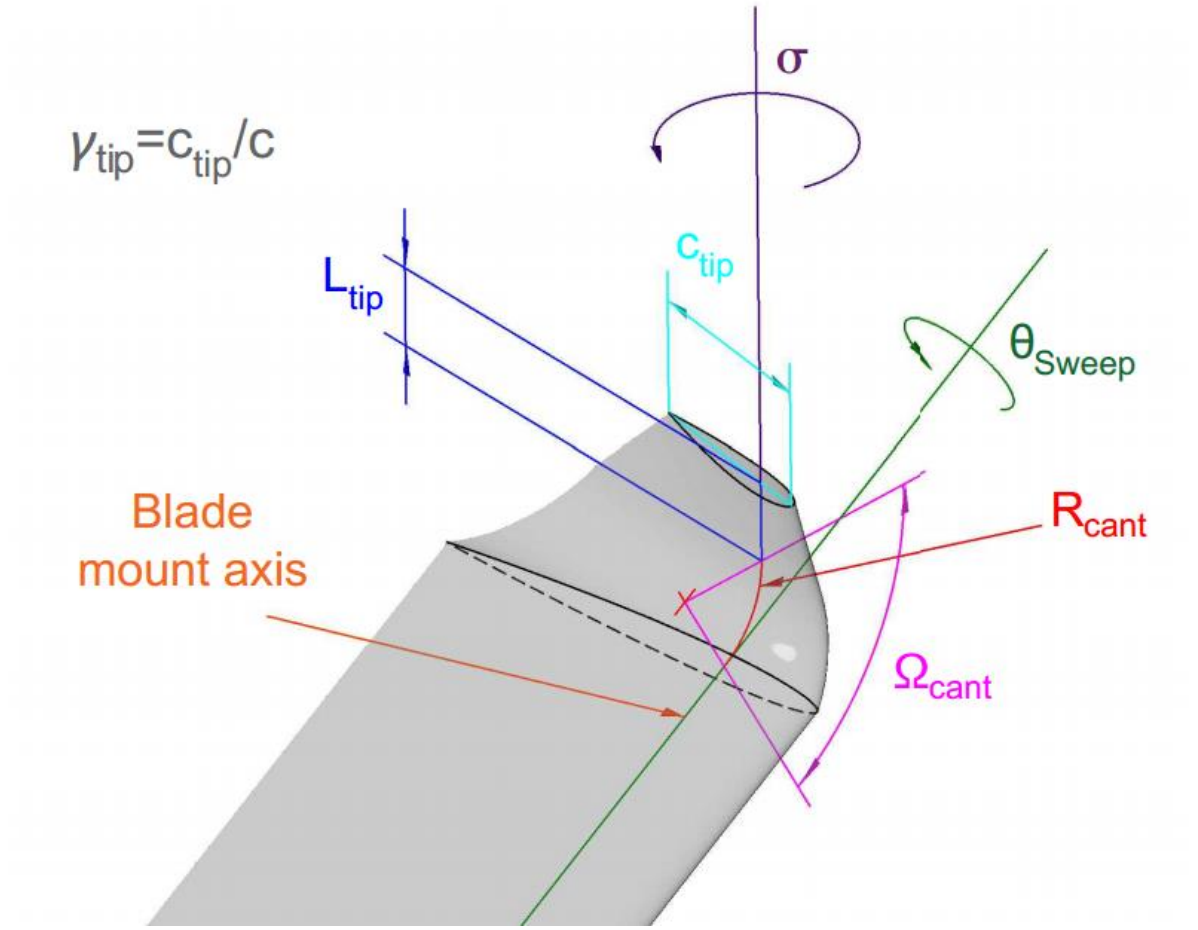

Figure 7.10 Illustration of the winglet and its geometric parameters.

Attaching the winglets to the end of the blades increases the total blade length and hence increases the swept area of the rotor. It is required to accurately calculate the modified swept area since this directly affects the power coefficient of the turbine. In

this study, the modified swept area is calculated based on the centreline of the blade profile and Figure 7.11 illustrates an example for the modified swept area for the case with $AR_{h/D}$=1.

Table 7.4 The specifications of the parameters of the optimised winglet according to the optimisation study [79]**. The parameters are expressed as a function of the blade chord, c, when applicable.**

θ_{sweep}	R_{cant}	Ω_{cant}	σ	L_{tip}	c_{tip}
0°	0.222*c	60°	−14.4°	0.178*c	0.45*c

The 3D CFD simulations are carried out in order to evaluate the effect of the implementation of the winglet on the power coefficient for $AR_{h/D}$ in the range between 1 and 5 in increments of 1. A hybrid mesh strategy is implemented in the region near the winglet in order to accommodate the complex shape of the winglet while maintaining the structured mesh topology around the winglet surface. The details of the mesh topology for the winglet case are available in Appendix E. Figure 7.12 (a) shows the effect of the implementation of the winglet on the 3D power coefficient for $AR_{h/D}$ between 1 and 5. In contrast with the cases without the winglet, the 3D power coefficient with the winglet is higher for all the tested $AR_{h/D}$.

Moreover, it is observed that the relative improvement in the power coefficient due to the implementation of the winglet is reduced by increasing the $AR_{h/D}$ as illustrated in Figure 7.12 (b). This is due to the fact that the significance of the 3D effects is reduced with the increase in the $AR_{h/D}$. Despite this improvement, there is a considerable difference between the 2D and 3D power coefficients even at the high $AR_{h/D}$.

By considering the 2D power coefficient as the best value where the 3D losses are eliminated, the ratio between the 3D and 2D power coefficients, $C_{P,3D}/C_{P,2D}$, is used to quantify the significance of the 3D effects. Figure 7.13 shows the $C_{P,3D}/C_{P,2D}$ ratio with and without the winglet in addition to the corresponding trendlines. These trendlines are based on the power functions clarified in Figure 7.13 that provide a good fit with the data of $AR_{h/D}$ up to 5. For $AR_{h/D}$ of 5, it is found that the $C_{P,3D}/C_{P,2D}$ ratio is about 85.5% and 83.1% for the cases with and without the winglets, respectively. In addition, the trendlines are extrapolated based on the power functions up to an $AR_{h/D}$ of 15 and it is predicted that the $C_{P,3D}/C_{P,2D}$ ratio would reach 90% for an $AR_{h/D}$ of about 11 and 12 for the cases with and without the winglets, respectively.

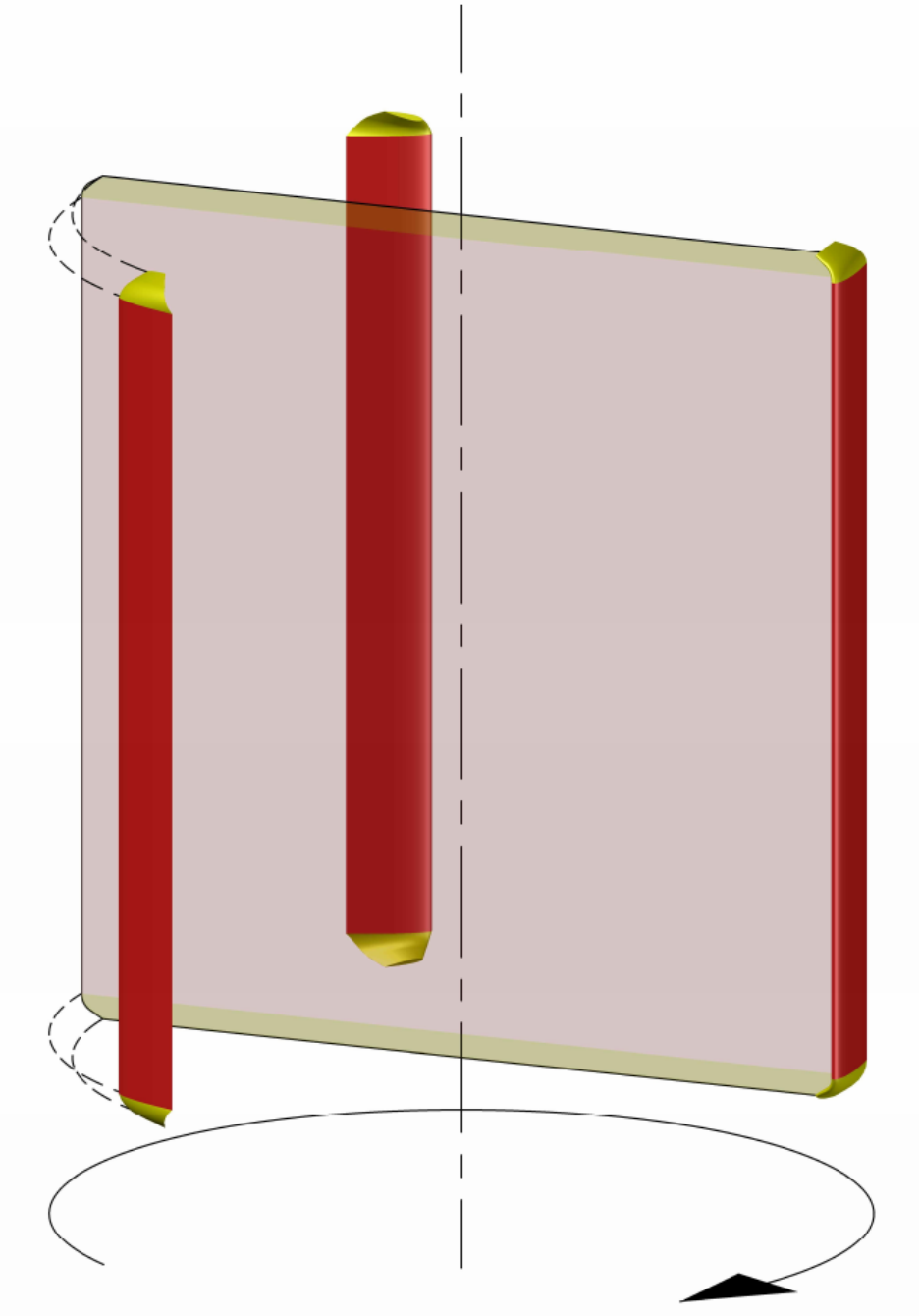

Figure 7.11 A schematic of the turbine blades for $AR_{h/D}$=1 with the winglets where the shaded area represents the modified swept area.

These results illustrate how it is difficult to eliminate the 3D losses even with an appropriate tip device and relatively high $AR_{h/D}$. However, it is clear how the implementation of an appropriate winglet could reduce the 3D losses and enhance the 3D power coefficient, especially at low $AR_{h/D}$. It is concluded that the selection of the turbine blade height or aspect ratio based on a parametric study is not achievable as the larger the turbine blade height, the better the 3D performance. However, several

factors may influence the selection of the turbine blade height or aspect ratio. This includes the available space for the installation, the required nominal power, the structural preference, and the design for manufacture. In the current study, the turbine blade height of 5.4 m is proposed and this corresponds to an $AR_{h/D}$ of 3. The aim of this selection is to maximise the 3D performance while being easy to manufacture and transport. For an $AR_{h/D}$ of 3, it is found that the $C_{P,3D}/C_{P,2D}$ ratio is about 81.5% and 77.7% for the cases with and without the winglets, respectively, neglecting the effects of the supporting arms. Due to the high computational cost of the 3D CFD simulations that account for the winglet geometry, the effect of the winglet on the performance at different TSR is not included in the scope of this thesis.

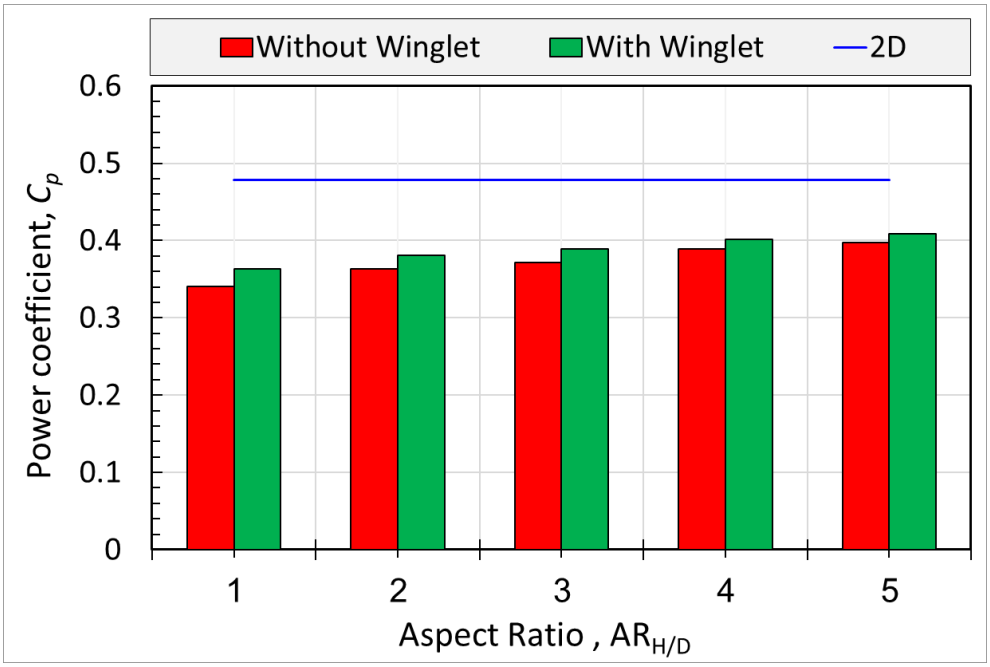

(a)

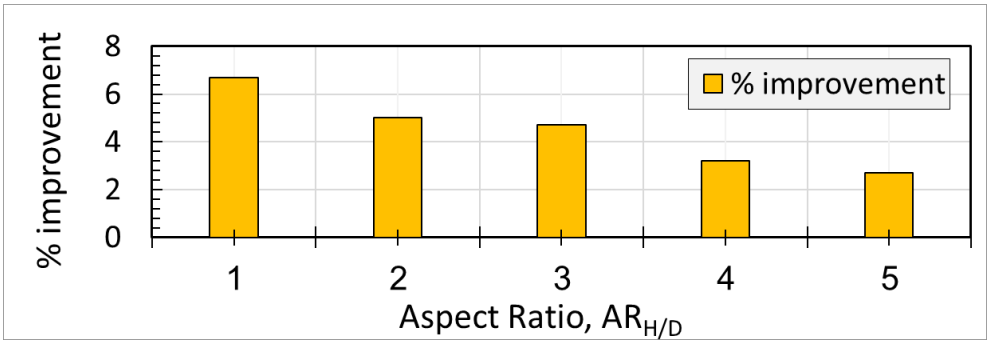

(b)

Figure 7.12 (a) The effect of the $AR_{h/D}$ on the 3D power coefficient with and without the winglet and (b) the percentage improvement in the power coefficient due to the implementation of the winglet.

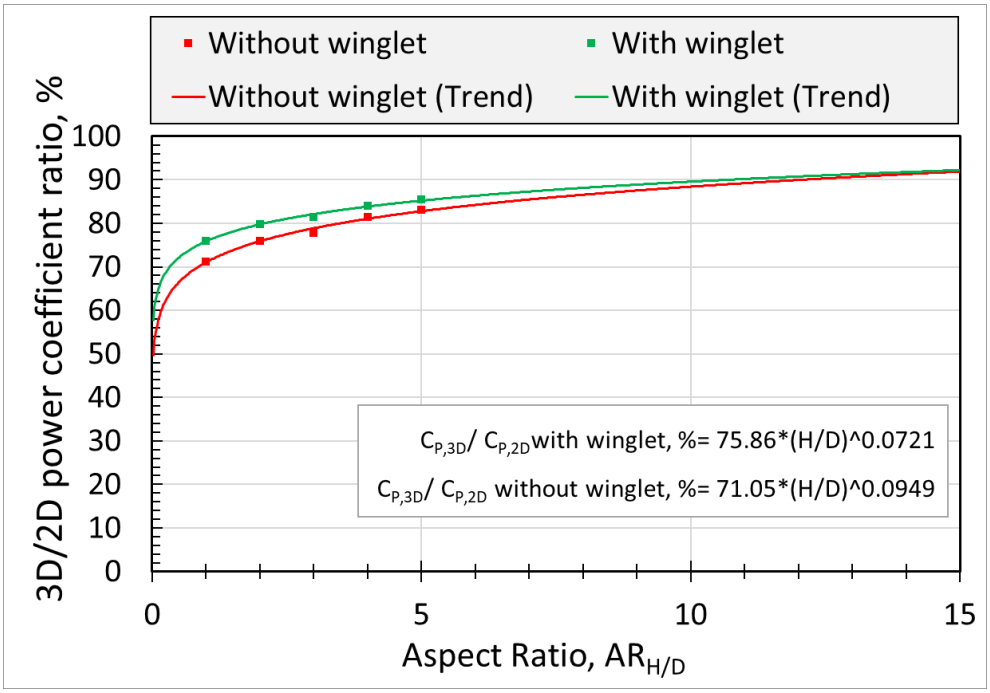

Figure 7.13 The power function trendline for the ratio between the 2D and 3D power coefficient with and without the winglet for the data of $AR_{h/D}$ up to 5 with extrapolation until $AR_{h/D}$ of 15.

7.9 Conclusions

The following conclusions are drawn:

- The use of the Goal-Driven Optimisation based on the 2D CFD simulations assists in the selection of the optimal design of a fixed pitch VAWT within the specified range of input parameters.
- The optimisation based on the Response Surface enables the exploration of the relations between the selected input parameters and the performance of the VAWT.
- The combination of the enhanced rotatable Central Composite Design (CCD), with the additional corner design points to build the DoE table, is observed to provide a good coverage of the design space, especially in the central part.
- Due to the complex non-linear relations between the input parameters and the performance of the VAWT, several Response Surface refinements are required to minimise the differences between the metamodel data and the CFD data in the optimal region of the design space.

- After the successive refinements, the constructed Response Surface has a very good agreement with the CFD validation data points.
- Without predefined manufacture constraints, the optimal design candidate could be slightly adjusted to be a manufacturing-friendly design without any significant change in the performance.
- Under the current setup and constraints, the optimal 2D design of a fixed pitch VAWT after the manufacture adjustments has a solidity of 0.315, a pitch angle of 4° and an optimal TSR of 2.6.
- The implementation of an appropriate winglet reduces the 3D losses and enhance the 3D power coefficient, especially in low aspect ratio VAWTs.
- The aspect ratio of the turbine has a significant effect on the 3D performance of the VAWT. It is concluded that the selection of the turbine blade height or aspect ratio based on a parametric study is not achievable as the larger the turbine blade height, the better the 3D performance.
- The turbine with an aspect ratio of 3 and a blade height of 5.4 m is proposed in order to maximise the 3D performance while being easy to manufacture and transport.

8 AERODYNAMIC ANALYSIS OF VP-VAWT CONFIGURATIONS

8.1 Overview

This chapter aims to investigate the effects of both the fixed pitch and variable pitch on the performance of the VAWT. The optimised three-bladed turbine in Chapter 7 is considered for this investigation. Four different VPPs are considered and the characteristics of a good VPP are identified. The effects of the targeted maximum AOA on the upstream and downstream contributions to the power coefficient as well as the cycle-averaged power coefficient are analysed. In addition, the effect of both the inward and outward preset fixed pitch on the turbine performance is discussed. Furthermore, the power required to overcome the aerodynamic torque due to the pitch motion is quantified for the different variable pitch profiles and targeted maximum AOAs. Under the current operating condition, the best fixed pitch and variable pitch configurations are identified.

The novelty in this chapter is not about the design of the best fixed pitch and variable pitch configurations, but about providing a better understanding of how a certain configuration is better than another and how the different design parameters affect the turbine performance in both the upstream and downstream part of the cycle. This includes applying the proposed novel procedure in Chapter 6 to analysis the turbine performance. In addition, this chapter sheds much light on both the effect of the targeted maximum AOA and the quantification of the pitch power which have not been addressed before in the literature. In this investigation, the targeted maximum AOA is found to have a significant influence on the performance of the VP-VAWT.

8.2 The effect of FP angle on the VAWT performance

While the optimisation study in Chapter 7 showed that the optimal pitch angle for the optimised three-bladed rotor is 4°, this subsection aims to get more insight on the effect of the FP angle on the performance of the FP-VAWT. The effect of the outward FP angle within the range between $0° < \beta < 10°$ with a 1° increment on the single blade instantaneous power coefficient is investigated as shown in Figure 8.1. It is noticed that by increasing the FP angle between $0° < \beta < 9°$, the peak power coefficient is reduced

in the upstream part of the cycle. However, the value of the peak power coefficient is increased in the downstream part of the cycle. In addition, when the FP angle is increased from 9° to 10°, the peak power in the downstream part of the cycle is significantly reduced. In order to quantify the effect of the trend of the instantaneous power coefficient on the performance of the turbine at different FP angles, the average power coefficient over the cycle and its upstream and downstream contributions are calculated.

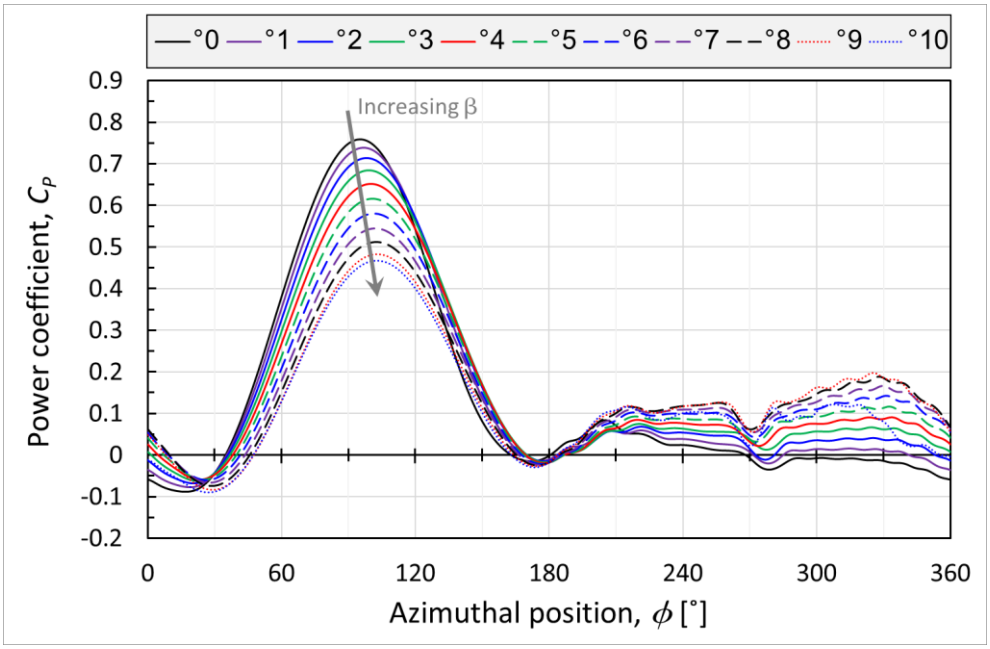

Figure 8.1 The effect of the FP angle, β, on the instantaneous power coefficient.

Figure 8.2 represents the upstream and downstream contributions to the power coefficient in a stacked form that also illustrates the total cycle-averaged power coefficient over the selected range of the FP angles. As expected from the optimisation results, the maximum cycle average power coefficient is associated with 4° FP with about 11.7 % improvement in contrast with the 0° FP configuration. It is observed that the downstream contribution to the power coefficient is increased with the FP angles up β=9°, then it gets reduced.

It is noticed from Figure 8.2 that the increase in the downstream contribution to the power coefficient, does not necessarily lead to an increase in the cycle-averaged power coefficient. The same applies to the upstream contribution. In addition, it is noticed from Figure 8.1 that the peak power coefficient is not associated with the best FP

configuration. Therefore, the objective of the design and optimisation of VAWT should focus on maximising the cycle-averaged power rather than maximising the upstream or downstream contributions to the power coefficients or even the peak power coefficient. Furthermore, this conclusion is supported by the data shown later in the following sections, particularly Figures 8.9 , 8.10 , 8.11 , and 8.12 .

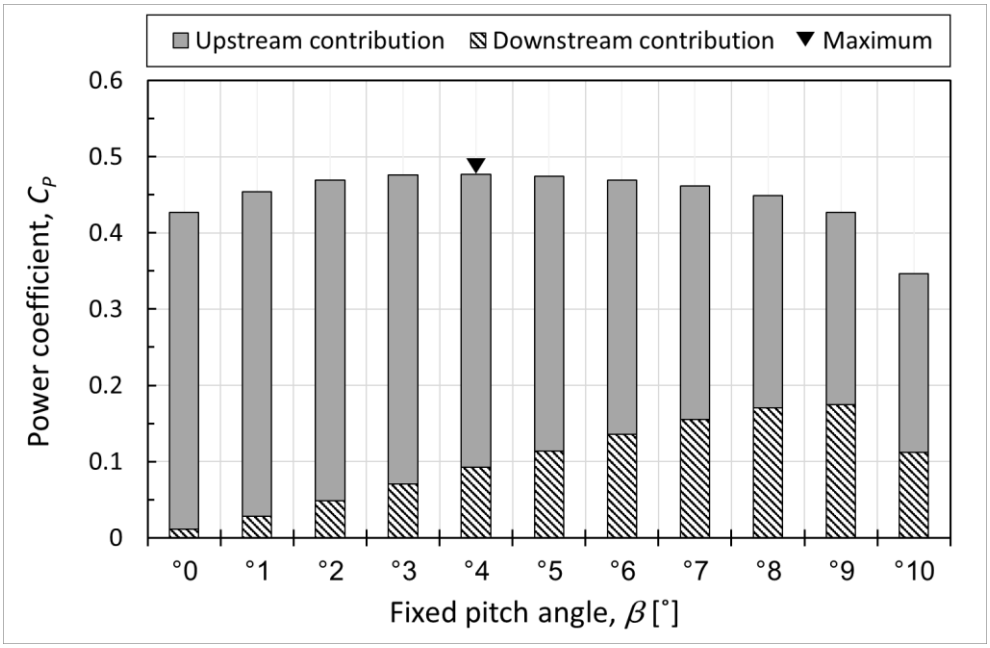

Figure 8.2 The effect of the FP angle, β, on the upstream and downstream contributions to the power coefficient in a stacked form that represents the total cycle-averaged power coefficient.

In order to have more insight on the effect of the FP angle on the performance of VAWT, the proposed procedure in Chapter 6 is implemented for the analysis of the performance of two off-design FP configurations, particularly β=0° and β=10° against the best FP configuration, β=4°. Figure 8.3 shows the effect of the selected FP angles on five different parameters that include the instantaneous single blade power coefficient, the AOA, local velocity magnitude, and the lift and drag coefficient over the cycle. In contrast with 4° FP, the 0° FP configuration has a significantly higher power coefficient where 30° <ϕ< 120°. However, the 4° FP configuration has a better power coefficient of the majority of the cycle as shown in Figure 8.3 (a). While the 4° FP configuration significantly outperforms the 10° FP configuration in the upstream part of the cycle as shown in Figure 8.3 (b), the 10° FP configuration has a slightly higher power coefficient in the downstream part of the cycle.

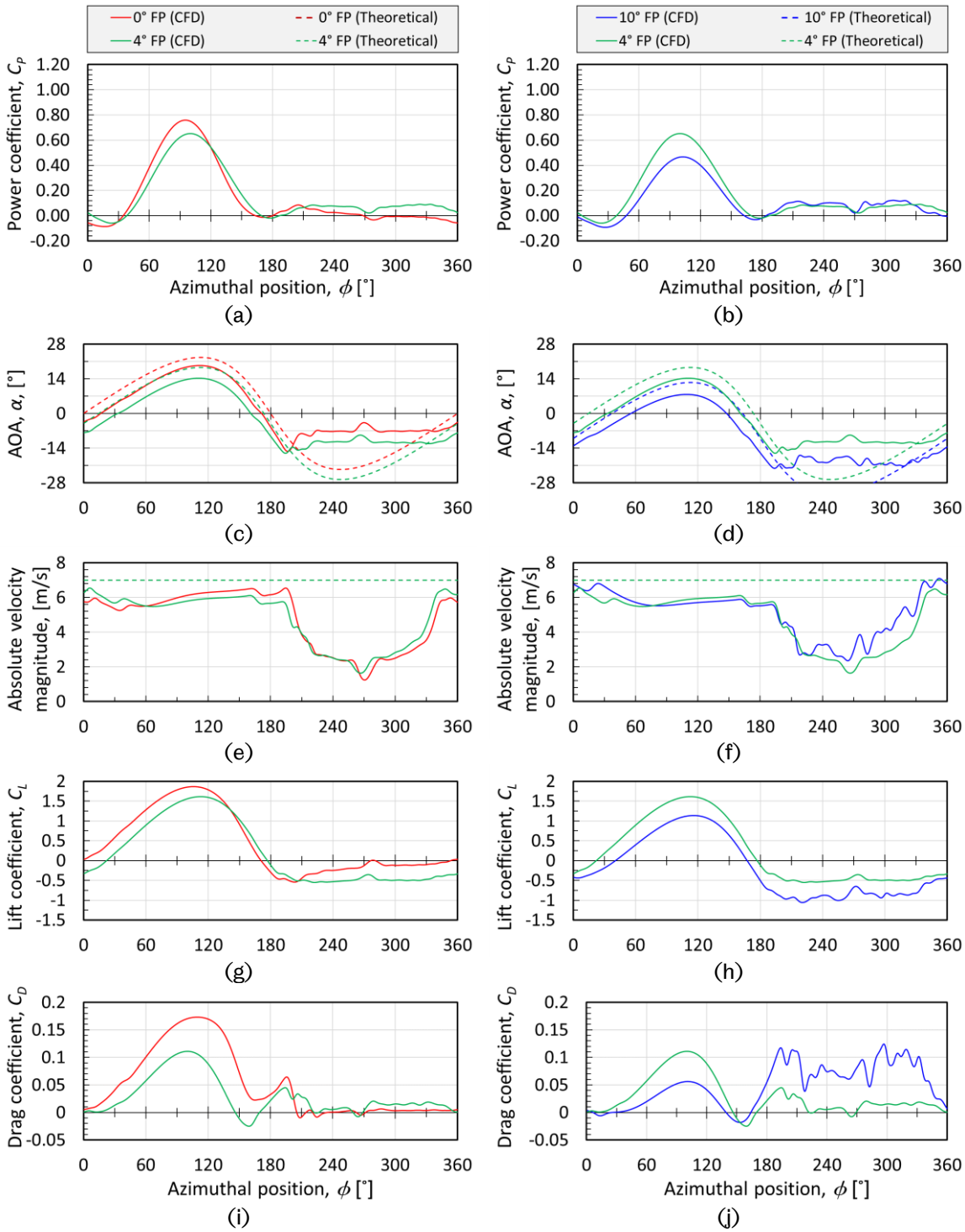

Figure 8.3 A comparison between the 0°FP and 10°FP configurations against the 4°FP configuration in terms of the instantaneous power coefficient, AOA, the local velocity magnitude, the lift coefficient and the drag coefficient.

Figures 8.3 (c) and (d) show both the theoretical and the predicted AOA for the selected FP configurations. In contrast with the theoretical AOA, it is noticed that the predicted AOA based on the CFD results is lower in magnitude in the upstream part of the cycle and significantly lower in magnitude over the majority of the upstream part.

It is noticed, under the current FP configurations, that the AOA profile has a noticeable peak in the upstream part of the cycle and a fluctuating behaviour about an average value in the downstream part of the cycle. Therefore, the peak AOA in the upstream part of the cycle and the average AOA in the downstream part of the cycle are used to judge which AOA profile is better than another based on the comparison with the static stall angle of the NACA0015 aerofoil that is reported to be 14° [206], [207]. More discussion about the favourable AOA is available in Section 8.4. The peak AOA in the upstream part of the cycle is about 19.3°, 14.3°, and 7.8° for the 0° FP, 4° FP, and 10° FP configurations, respectively. On the other hand, the average amplitude of the AOA in the downstream part of the cycle is about 7.4°, 11.7°, and 19° for the 0° FP, 4° FP, and 10° FP configurations, respectively. Taking into account that, it is clear that the 4° FP configuration has a better AOA profile over the entire cycle in contrast with the off-design 0° FP and 10° FP configurations.

Figures 8.3 (e) and (f) show the change in the predicted velocity magnitude over the cycle in contrast with the undisturbed flow velocity for the selected FP configurations. It is noticed that the higher the peak AOA in the upstream part of the cycle the lower the velocity magnitude in the downstream part of the cycle. In other words, by avoiding high AOA in the upstream part of the cycle, the strength of the wake effect is reduced and a higher velocity magnitude is obtained in the downstream part of the cycle.

Figures 8.3 (g) and (i) show comparisons of the lift and drag coefficients over the cycle for the 0° FP and 4° FP configurations. In contrast with 4° FP, the 0° FP configuration has a relatively higher peak AOA in the upstream part of the cycle and the blade seems to encounter dynamic stalls. While the higher AOA profile of the 0° FP configuration leads to a higher lift in the upstream part of the cycle, it leads to relatively higher drag. In the downstream part of the cycle, the 4° FP configuration has a higher and more favourable AOA amplitude that leads to higher lift production with minimal drag and thus a better power coefficient in the downstream part of the cycle in contrast with the 0° FP configuration.

Figures 8.3 (h) and (j) show comparisons of the lift and drag coefficients over the cycle for the 4° FP and 10° FP configurations. In contrast with 4° FP, the 10° FP configuration has very low AOA magnitudes in the upstream part of the cycle and this leads to lower

lift, drag, and power coefficients in the upstream part of the cycle. However, in the downstream part of the cycle, the 10° FP configurations have relatively higher but unfavourable AOA magnitudes. This leads to higher lift but with significantly higher drag and hence, despite the relatively high lift, the power coefficient has a slight improvement in the downstream part of the cycle in contrast with the 4° FP configuration.

8.3 The effect of the VPP on the VP-VAWT performance

In the previous Subsection 8.2, it is observed how the FP configuration can improve the turbine performance by introducing more favourable AOAs over certain parts of the cycle. Due to the turbine kinematics, the FP configuration has a limited effect on the AOA. The FP configuration can only reduce the AOA in the upstream part of the cycle while increasing its magnitude in the downstream part. However, the VP configurations give more control on the variation of the AOA over the different part of the cycle.

In this subsection, different VPPs are introduced and their effects on the turbine performance are discussed and these include both the continuous sinusoidal pitch and some other piecewise variable pitch profiles. In this subsection, the favourable AOA is assumed to be the static stall angle of the aerofoil as suggested by Staelens et al. [124] and this is reported to be 14° for NACA0015 [206], [207]. For the selected VPPs the maximum theoretical VP AOA is adjusted to be equal to the favourable AOA and is also referred to as the Targeted Maximum AOA, TMAOA, ζ. Figure 8.4 (a) shows the theoretical 0°FP AOA, the applied variable pitch, and the resultant theoretical VP AOA for the first VPP, also referred to as VPP1. Figure 8.4 (b) shows the corresponding values for the second VPP, also referred to as VPP2. In both the VPP1 and VPP2, the blade is pitched outward in the upstream part of the cycle and inward in the downstream part of the cycle. This reduces the magnitude of the AOA in both the upstream and downstream parts. The VPP1 is a sinusoidal VPP whose amplitude is adjusted so that the maximum theoretical VP AOA equals to the TMAOA. This amplitude of the sinusoidal motion is calculated based on a FORTRAN code for which an example is presented in Appendix F.

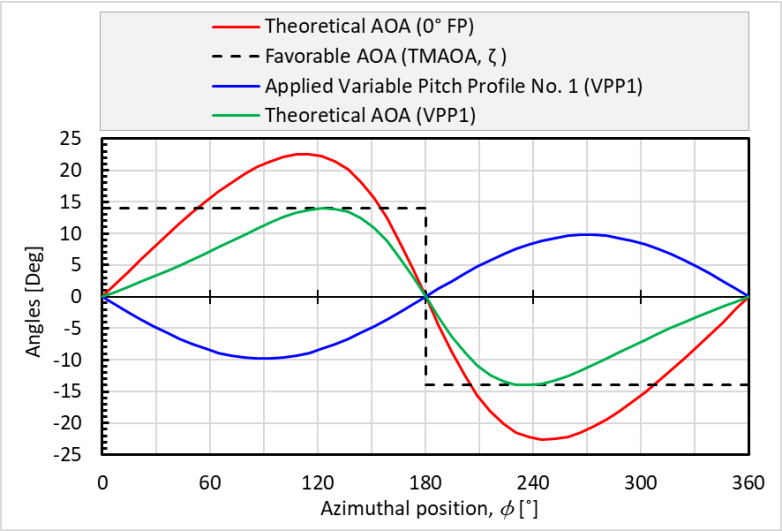

(a)

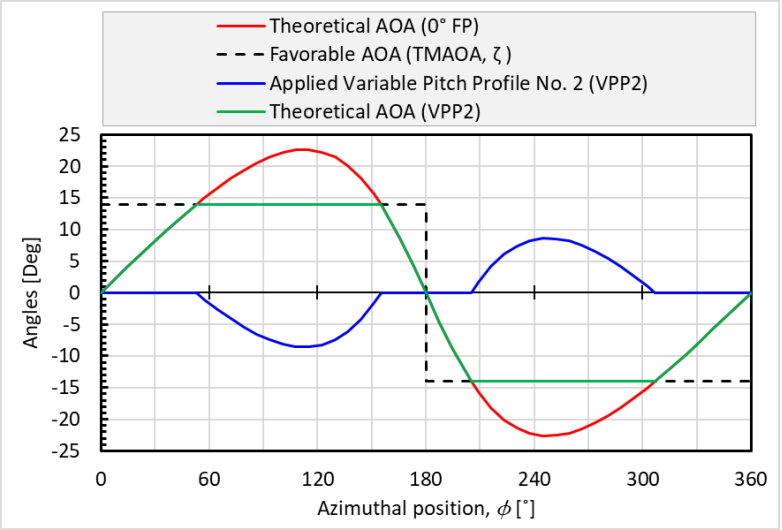

(b)

Figure 8.4 The theoretical 0°FP AOA, the applied variable pitch, and the resultant theoretical variable pitch AOA for (a) VPP1 and (b) VPP2.

The VPP2 is a piecewise VPP that is only applied where the amplitude of the theoretical 0°FP AOA exceeds the TMAOA. The VPP2 eliminates the peak regions from the resultant theoretical VP AOA and maintains the favourable AOA over considerable parts of the cycle. The bounds of the piecewise function intervals are calculated based on the theoretical AOA based on a FORTRAN code for which an example is presented in Appendix F. Figure 8.5 shows a comparison between the VPP1 and VPP2 configurations for ζ=14° against the 0°FP configuration in terms of the instantaneous power coefficient, AOA, the local velocity magnitude, the lift coefficient and the drag coefficient.

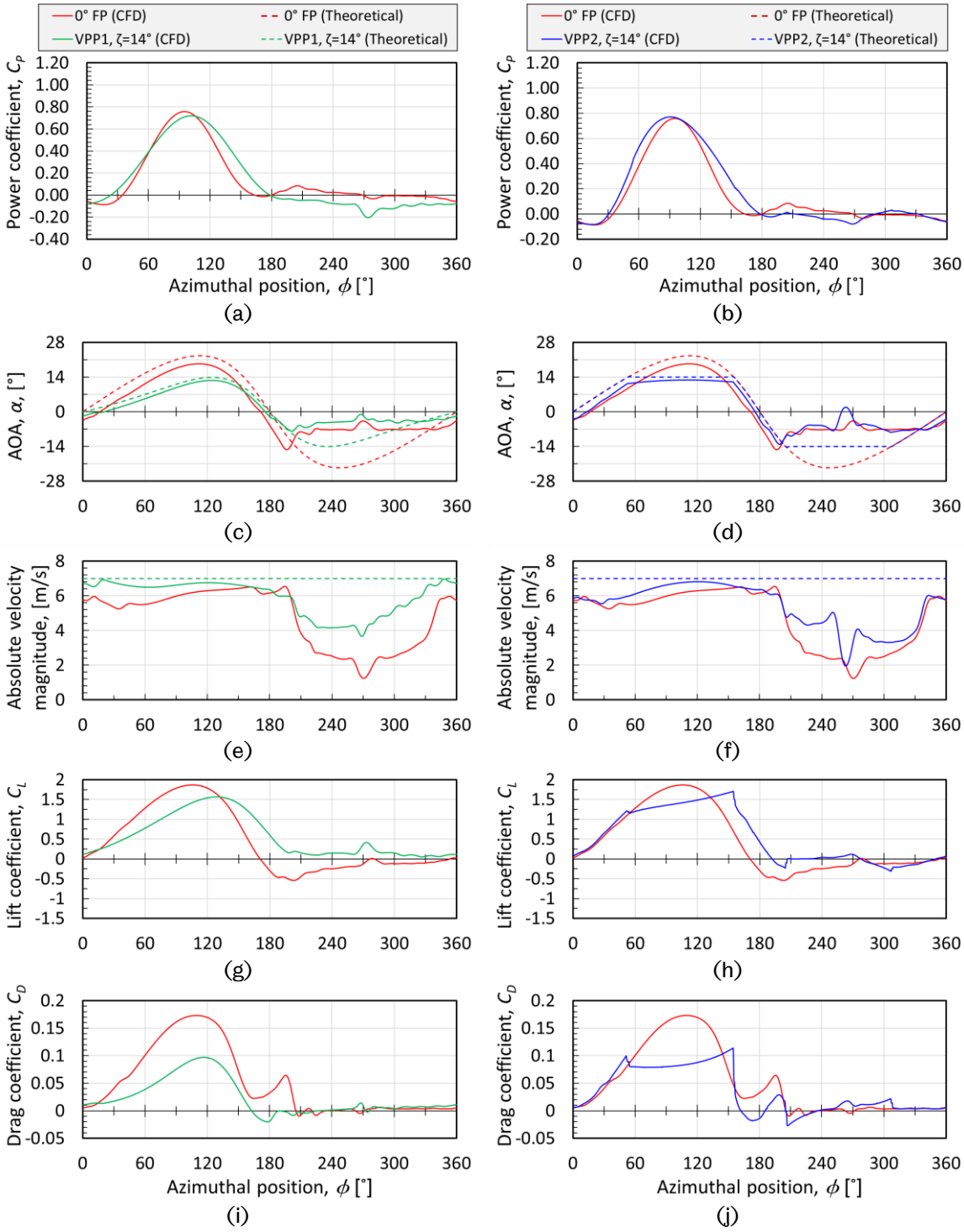

Figure 8.5 A comparison between the VPP1 and VPP2 configurations for ζ=14° against the 0°FP configuration in terms of the instantaneous power coefficient, AOA, the local velocity magnitude, the lift coefficient and the drag coefficient.

In contrast with the 0°FP configuration, both the VPP1 and VPP2 has a higher power coefficient in the majority of the upstream part of the cycle. This is due to the reduced AOA to a more favourable value. Although the reduced AOA leads to a relatively lower

lift in some region in the upstream part of the cycle, it significantly reduces the drag and hence enhances the power coefficient. In the downstream part of the cycle, both the VPP1 and VPP2 has a slightly lower AOA in contrast with the 0°FP configuration. However, due to the fact that the predicted AOA is relatively low in the downstream part of the cycle due to the reduction of the velocity magnitude in the wake region, the further reductions due to the VPPs are not favourable. This slight reduction of AOA in the downstream part of the cycle reduces the lift as well as the power coefficient. It could be concluded that the inward VP in the downstream part of the cycle is not favourable due to the kinematic of VAWT. Hence the VPP3 and VPP4 are introduced by eliminating the VP in the downstream part of the cycle as discussed below. The negative power coefficient that is observed in the downstream part of the cycle means that power expenditure is required in order for the blade to rotate.

Figures 8.6 (a) and (b) shows the theoretical 0°FP AOA, the applied variable pitch, and the resultant theoretical VP AOA for the third and fourth VPP, also referred to as VPP3 and VPP4, respectively. The VPP3 and VPP4 follow the same definitions of VPP1 and VPP2, respectively, in the upstream part of the cycle while applying no VP motion on the downstream part of the cycle. Figure 8.7 shows a comparison between the VPP3 and VPP4 configurations for ζ=14° against the 0° FP configuration in terms of the instantaneous power coefficient, AOA, the local velocity magnitude, the lift coefficient and the drag coefficient. In contrast with the 0° FP configuration, both the VPP3 and VPP4 has a higher power coefficient in the majority of both the upstream and downstream parts of the cycle. Despite the fact that the 0° FP configuration has a higher peak power coefficient, the VPP3 and VPP4 are found to have a better overall performance. In the upstream part of the cycle, both the VPP3 and VPP4 reduces the maximum AOA. While this reduces the peak lift coefficient in contrast with the 0° FP configuration, the drag is significantly reduced. Hence, both the VPP3 and VPP4 outperform the 0° FP configuration over the majority of the upstream part of the cycle. However, in contrast with the VPP3, the VPP4 maintains a favourable AOA over a wider region in the upstream part of the cycle and hence achieves a better lift and power coefficient.

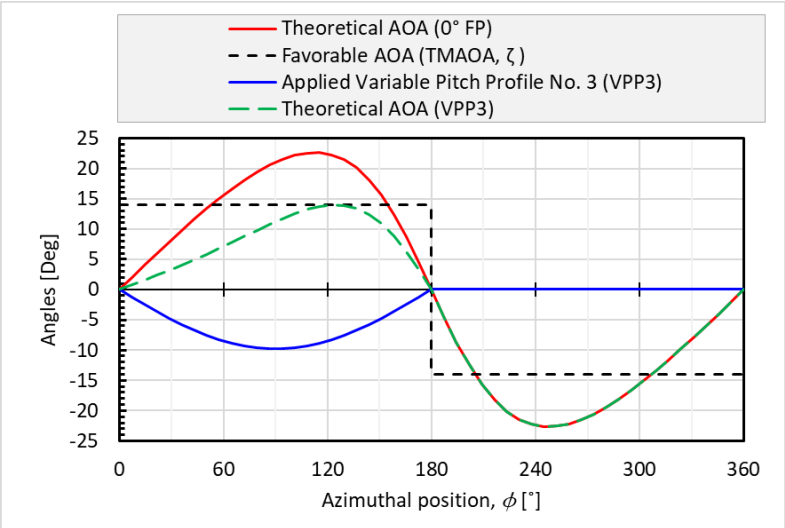

(a)

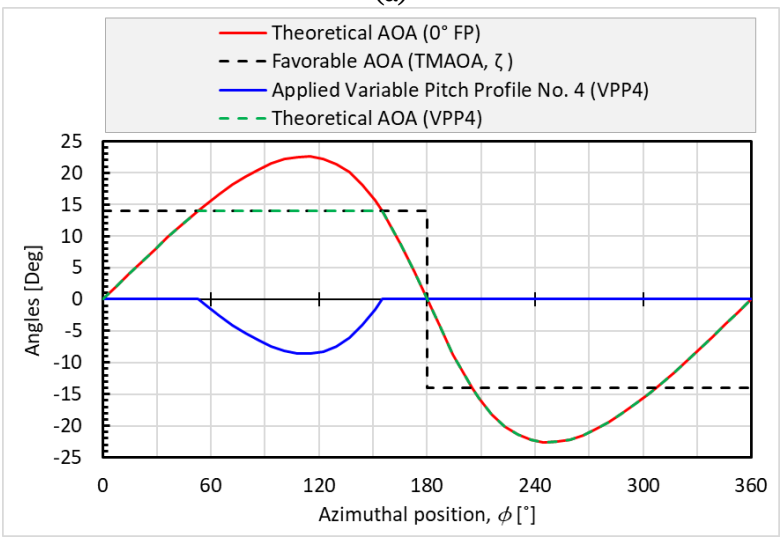

(b)

Figure 8.6 The theoretical 0°FP AOA, the applied variable pitch, and the resultant theoretical variable pitch AOA for (a) VPP3 and (b) VPP4.

Although the VPP3 and VPP4 have the same theoretical AOA as the 0° FP configuration in the downstream part of the cycle, the CFD predictions of the AOA show that VPP3 and VPP4 have a relatively higher and more favourable AOA in contrast with the 0° FP configuration. The reason is that both VPP3 and VPP4 reduce the AOA in the upstream part of the cycle and this reduces the strength of the wake effect and increase the flow induction through the rotor. Hence, a higher velocity magnitude is found over the majority of the cycle. In contrast with the 0° FP configuration, by reducing the wake interaction in the VPP3 and VPP4, the relatively higher velocity magnitude in the downstream part of the cycle leads to a relatively higher AOA. Hence, the VPP3 and

VPP4 have a relatively higher lift and power coefficients over the majority of the downstream part of the cycle, while producing a minimal drag.

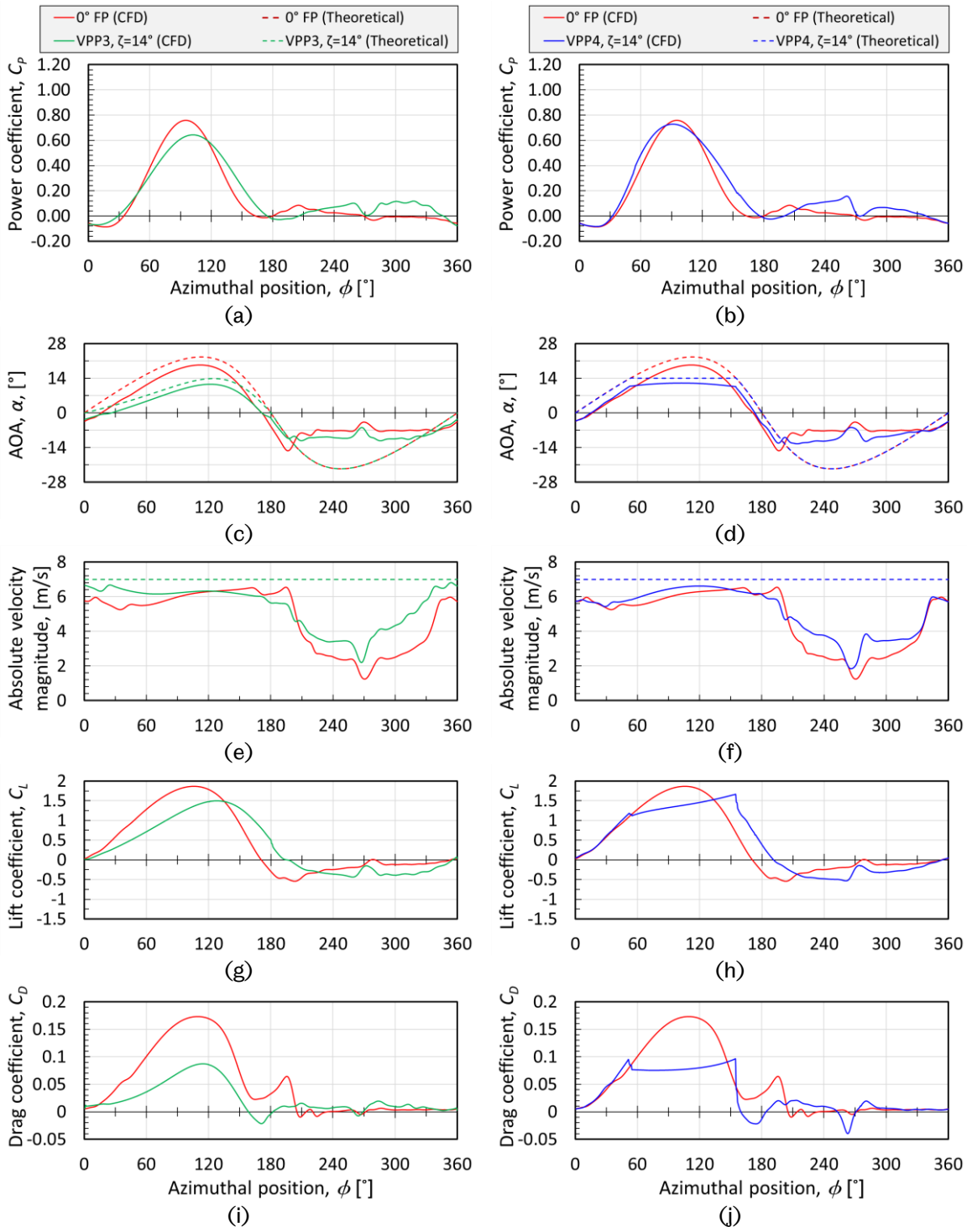

Figure 8.7 A comparison between the VPP3 and VPP4 configurations for ζ=14° against the 0°FP configuration in terms of the instantaneous power coefficient, AOA, the local velocity magnitude, the lift coefficient and the drag coefficient.

In order to assess the feasibility of the different VPPs, the cycle-averaged power coefficient is used. For all the VP configurations in the current chapter, the values of the cycle-averaged power coefficient represent the power coefficient by deducing the power required to overcome the aerodynamic moment against the pitch motion as discussed further in Section 8.6. Figure 8.8 shows a comparison of the cycle-averaged power coefficient for the different VPPs with TMAOA, ζ=14° against that of the 0° FP and 6° FP configurations. It is observed that all the implemented VPPs, except VPP1, outperform both the 0° FP and 4° FP configurations. However, VPP4 is found to have the best power coefficient with enhancements of about 30.1% and 16.5% in contrast with the 0° FP and 4° FP configurations, respectively. However, as clarified before, the TMAOA is chosen as the static stall angle and this raises the question of what is the best TMAOA and whether it depends on the VPP or not. These questions are discussed further in the next section.

It is concluded that a good VPP is characterised by maintaining a favourable angle of attack on a large region of the upstream part of the cycle and maintain a zero pitch angle in the downstream part of the cycle.

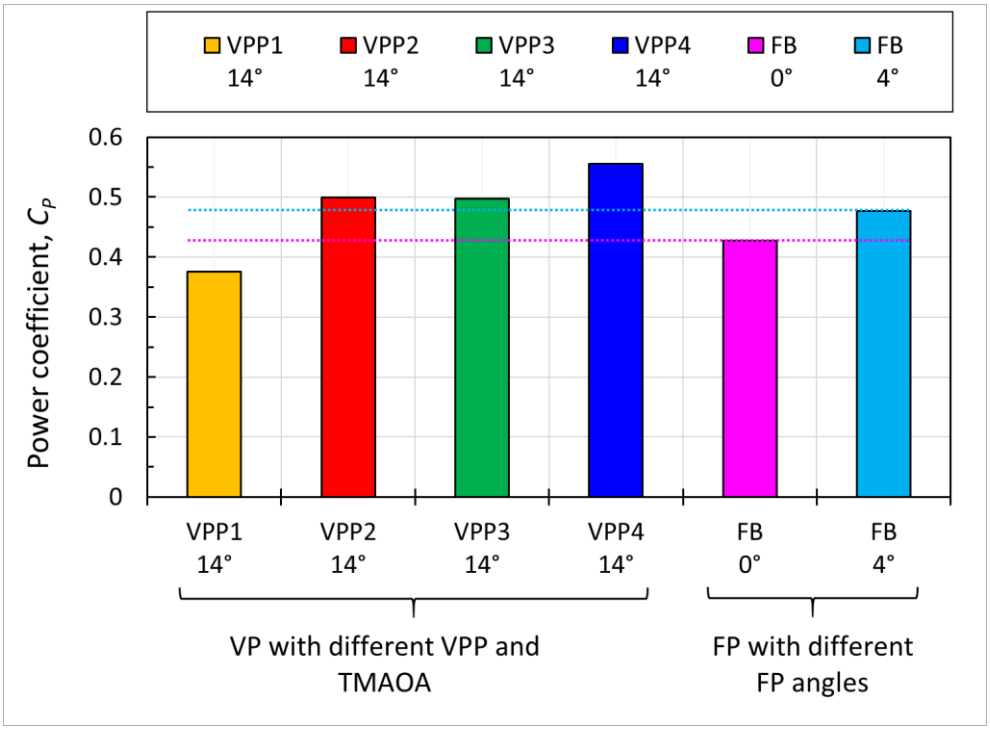

Figure 8.8 A comparison of the cycle-averaged power coefficient for different VPPs with ζ=14° against that of the 0° FP and 4° FP configurations.

8.4 The effect of TMAOA on the VP-VAWT performance

In this section, the effects of the TMAOA on VP-VAWT performance are investigated. While the cycle-averaged power coefficient is considered as the key performance measure, both the upstream and downstream contributions to the power coefficient are analysed. The TMAOA between 10° and 22° with a 1° increment are considered. The maximum TMAOA is selected just below the maximum theoretical AOA for a 0° FP turbine under the same operating condition that is about to 22.6°. The TMAOA has a big influence on the AOA profile over the cycle for the different VPPs as shown before on Figures 8.4 and 8.6. Figure 8.9 shows the effect of the TMAOA on the upstream, downstream, and the cycle-averaged power coefficient for VPP1. It is observed that the VPP1 has a poor downstream contribution to the power coefficient that has a negative effect on the cycle-averaged power coefficient up to TMAOA=21°. The TMAOA at the maximum power coefficient is referred to as the best TMAOA despite considering the TMAOA with 1° resolution. For VPP1, the best TMAOA is found to be 20° at which the VPP1 outperforms the 0° FP configuration. However, the 4° FP configuration provides relatively higher performance.

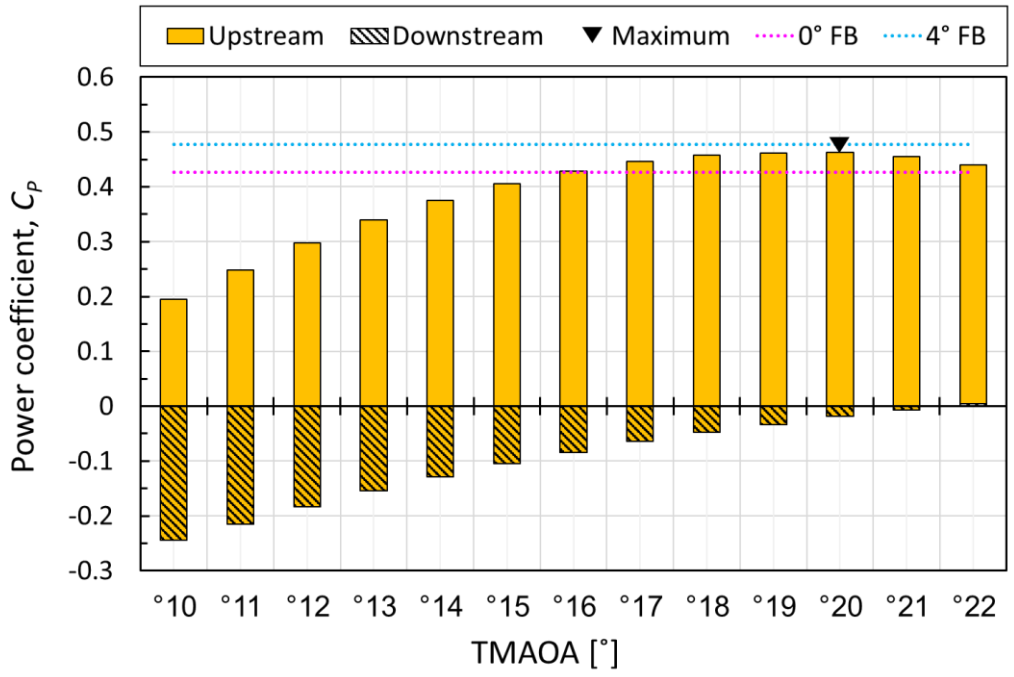

Figure 8.9 The effect of the TMAOA, ζ, with VPP1 on the upstream and downstream contributions to the power coefficient in a stacked form that represents the total cycle-averaged power coefficient.

Figure 8.10 shows the influence of the TMAOA on the performance of the VAWT using the VPP2. It is observed that the downstream contribution to the power coefficient is negative up to TMAOA=17°. However, the best TMAOA is found as 14° that has the maximum power coefficient despite having a negative downstream contribution. It is found that the VPP2 at the best TMAOA outperforms the best FP configuration, i.e. the 4° FP. In addition, the VPP2 is found to outperform the 4° FP over a wide range of TMAOA from 12° to 18°.

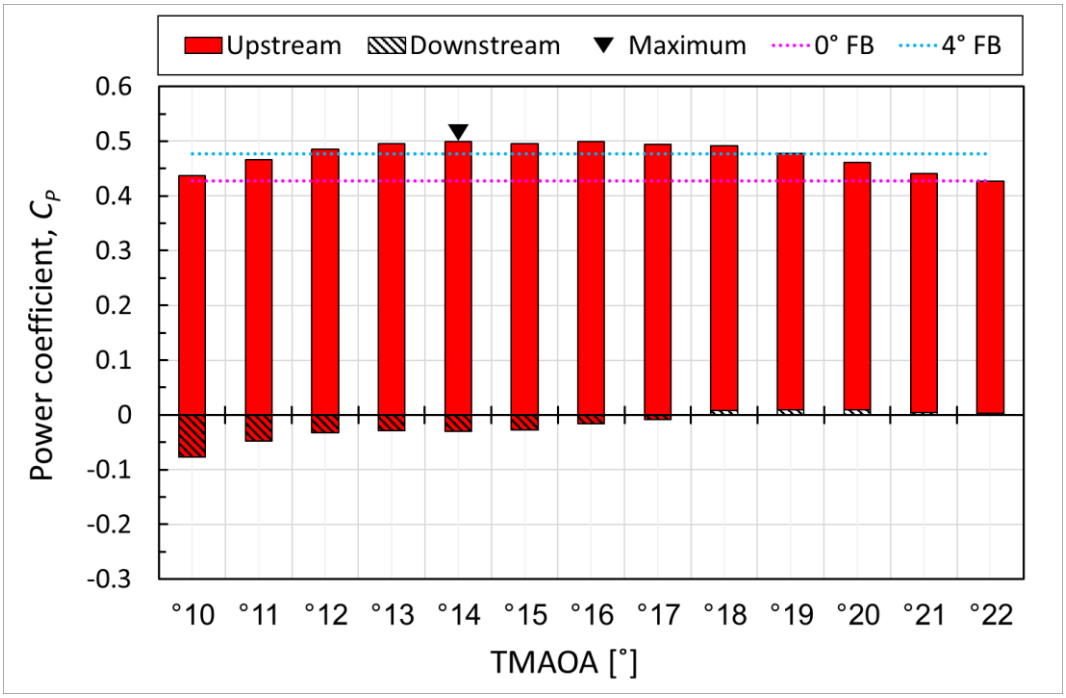

Figure 8.10 The effect of the TMAOA, ζ, with VPP2 on the upstream and downstream contributions to the power coefficient in a stacked form that represents the total cycle-averaged power coefficient.

Using VPP3, Figure 8.11 shows the effect of the TMAOA on the performance of the VAWT. The VPP3 achieves the best performance at TMAOA of 17°. In addition, VPP3 outperforms the best FP configuration for TMAOA between 12° to 19°. However, VPP4 outperforms the best FP configuration for TMAOA between 10° to 19° as shown in Figure 8.12 while achieving the best performance at TMAOA=12°. It is observed that both the VPP3 and VPP3 has positive downstream contributions over the entire range of tested TMAOA. This confirms that eliminating the VP over the downstream part of the cycle is more favourable than the outward VP that is implemented in VPP1 and VPP2.

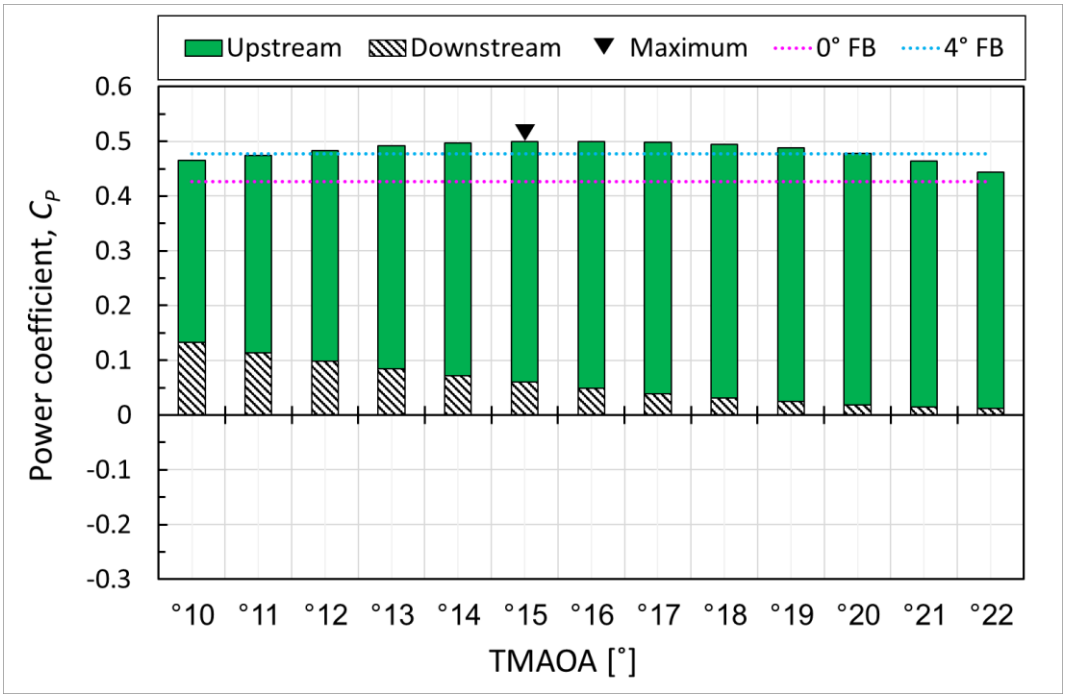

Figure 8.11 The effect of the TMAOA, ζ, with VPP3 on the upstream and downstream contributions to the power coefficient in a stacked form that represents the total cycle-averaged power coefficient.

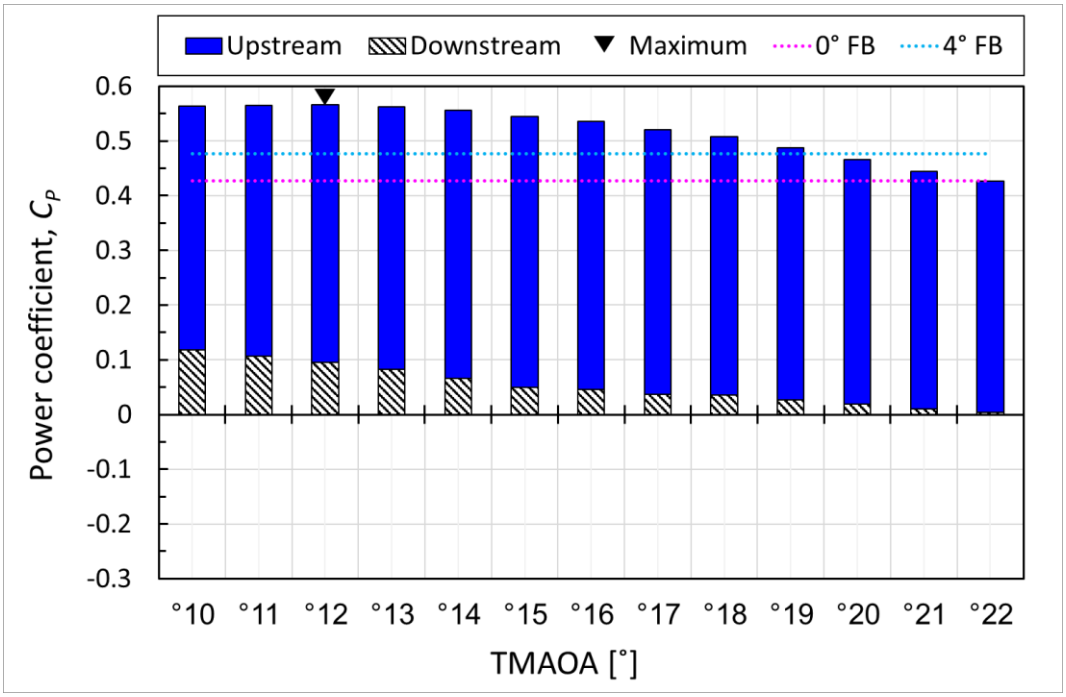

Figure 8.12 The effect of the TMAOA, ζ, with VPP4 on the upstream and downstream contributions to the power coefficient in a stacked form that represents the total cycle-averaged power coefficient.

Figure 8.13 shows a comparison of the cycle-averaged power coefficient between the different VPPs at the corresponding best TMAOA against the 0° FP and 6° FP configurations. All the VPPs at the corresponding best TMAOA outperform the best FP configurations except the VPP1. While the VPP1 at the best TMAOA outperform the 0° FP, its power coefficient is lower than that of the best FP design. It is clear how the VPP4 at TMAOA, ζ=12° has a considerable improvement in the power coefficient over all other VP and FP configurations which make it the best overall design. The VPP4 at TMAOA, ζ=12° is found to have an improvement in the power coefficient of about 32.5% and 18.6% in contrast with the 0° FP and 4° FP configurations, respectively.

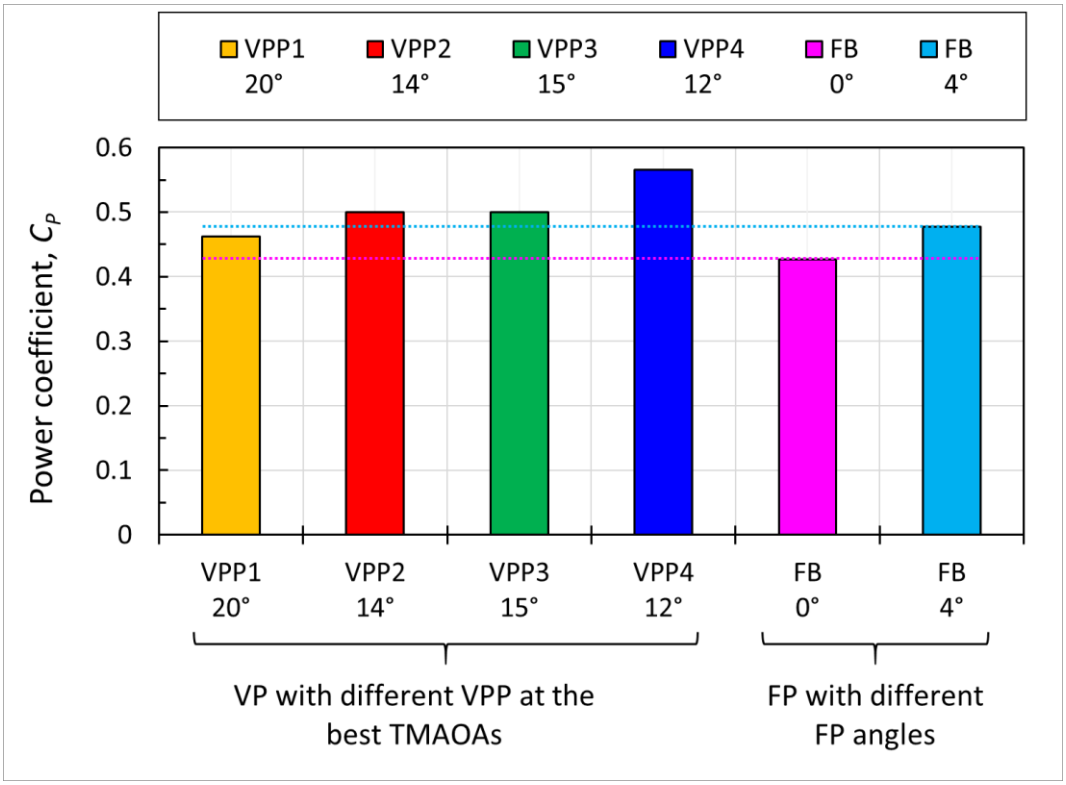

Figure 8.13 A comparison of the cycle-averaged power coefficient for different VPPs with the corresponding best TMAOA, ζ, against that of the 0° FP and 4° FP configurations.

In order to assess the importance of the selection of the TMAOA for each VPPs individually, the power coefficient of the VPPs at the best TMAOA are compared against the corresponding value at TMAOA=14° as shown in Figure 8.14. It is observed that the percentage improvement in the power coefficient varies between the VPPs. While VPP1 get an improvement of about 23% using the best TMAOA instead of TMAOA=14°, the VPP4 improved by 1.8% which is still a considerable improvement. It is concluded that

the selection of the TMAOA based on a parametric study is viable rather than considering it to be equal to the static stall angle. The maximum power coefficient found in this study is about 56.6% and this is very good in comparison with the Betz limit (59.3%). However, this high value is based on the 2D simulation that is expected to be overpredicted.

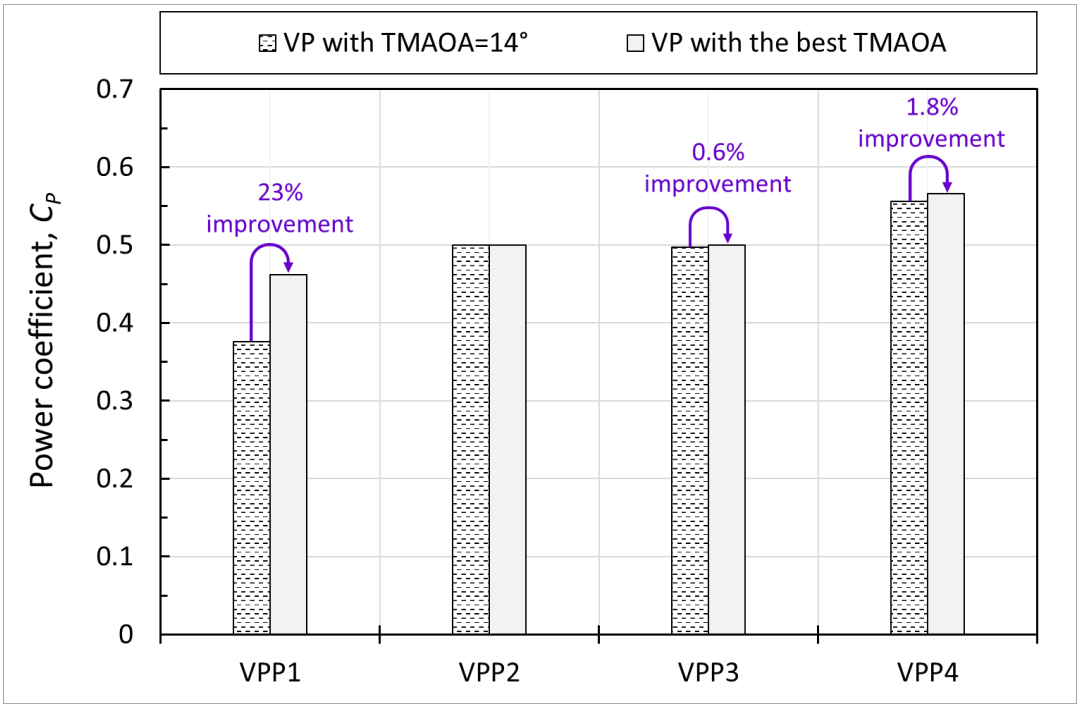

Figure 8.14 A comparison of the cycle-averaged power coefficient for different VPPs with TMAOA, ζ =14° against that with the corresponding best TMAOA.

In order to shed the light on how the performance of the turbine with VPP4 improves by changing the TMAOA from 14° to 12°, the performance of the two configurations are compared in terms of the instantaneous power coefficient, AOA, the local velocity magnitude, the lift coefficient and the drag coefficient as shown in Figure 8.15. The source of the improvement in the power coefficient for the TMAOA=12° is from the downstream part of the cycle. Although the lower TMAOA reduces the lift as well as the power coefficient in the upstream part of the cycle, the lower TMAOA appears to reduce the strength of the wake and achieve a slightly higher velocity magnitude in the downstream part of the cycle. This leads to a slightly higher AOA magnitude in the downstream part of the cycle in contrast with the TMAOA=14° case. Hence, a relatively higher lift and power coefficient are obtained in the downstream part of the cycle for the TMAOA=12° case.

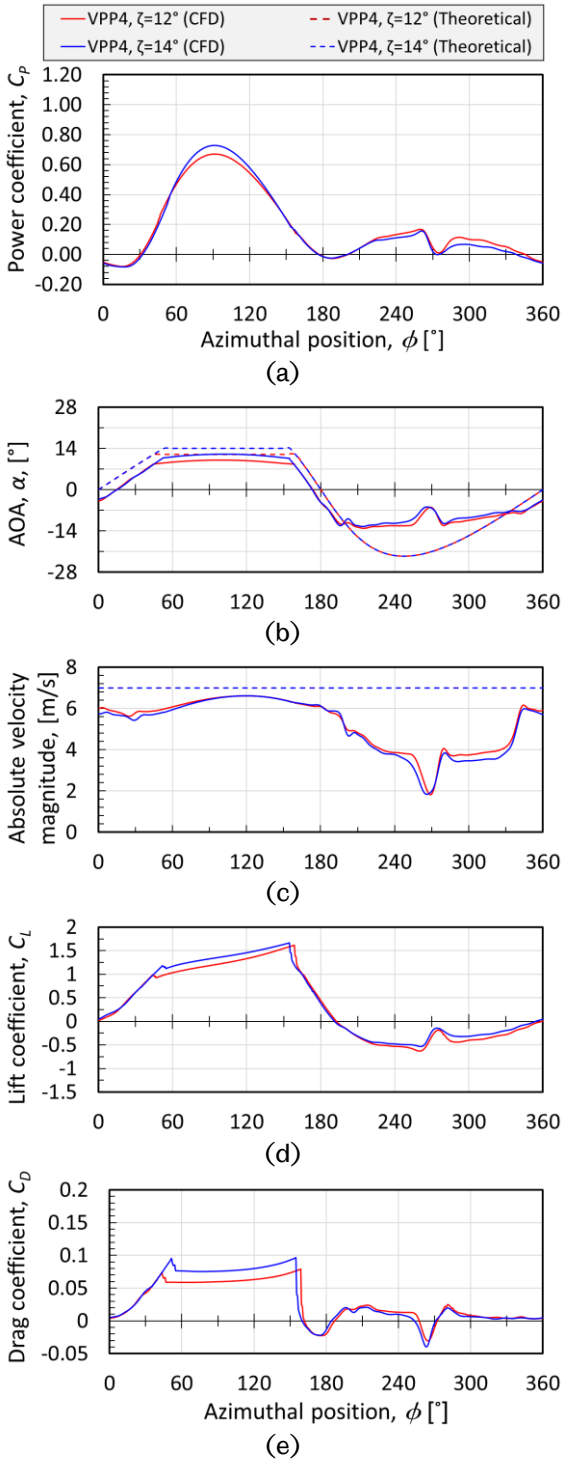

Figure 8.15 A comparison between VPP4 with ζ=14°and ζ=12° configurations in terms of the instantaneous power coefficient, AOA, the incident relative velocity, the lift coefficient and the drag coefficient using the SST k-ω turbulence model.

8.5 The effect of the preset FP angle on the VP-VAWT performance

This section aims to investigate the effect of the preset FP on the performance of a VAWT with the best VP configuration, i.e. the VPP4 and a TMAOA of 12°. Both the inwards and outward preset FP is considered with a maximum amplitude of 3°. Figure 8.16 shows the effect of both the inwards and outward preset FP angle on the theoretical AOA over the cycle. It is noticed that the inward FP increases the region the theoretical AOA is equal to the TMAOA, i.e the favourable AOA, in the upstream part of the cycle. This is expected to enhance the power coefficient in the upstream part of the cycle. However, the inward FP reduces the magnitude of the AOA in the downstream part of the cycle which is expected to have a negative effect on the power coefficient.

Figure 8.17 illustrates the upstream and downstream contributions to the power coefficient in addition to the total cycle-averaged power coefficient over the cycle for the different preset FP angles. The inward preset FP increases the upstream contribution to the power coefficient and reduces the downstream contribution while the preset outward FP has the opposite behaviour. However, the maximum cycle-averaged power coefficient is found to be associated with the case of 0° preset FP. Figure 8.18 shows the effect of the three preset FP angles on the instantaneous single blade power coefficient, the AOA, local velocity magnitude, and the lift and drag coefficient over the cycle.

As expected from the theoretical AOA, the CFD predictions of the AOA around the blade shows how the inward preset 3° FP extends the region that has a favourable AOA in the upstream part of the cycle. This leads to a relatively higher lift and power coefficients in the upstream part of the cycle while having a minimal effect on the drag. However, it observed that the outward preset 3° FP have a more favourable AOA in the downstream part of the cycle. Hence, it has a higher lift and power coefficient on the downstream part of the cycle.

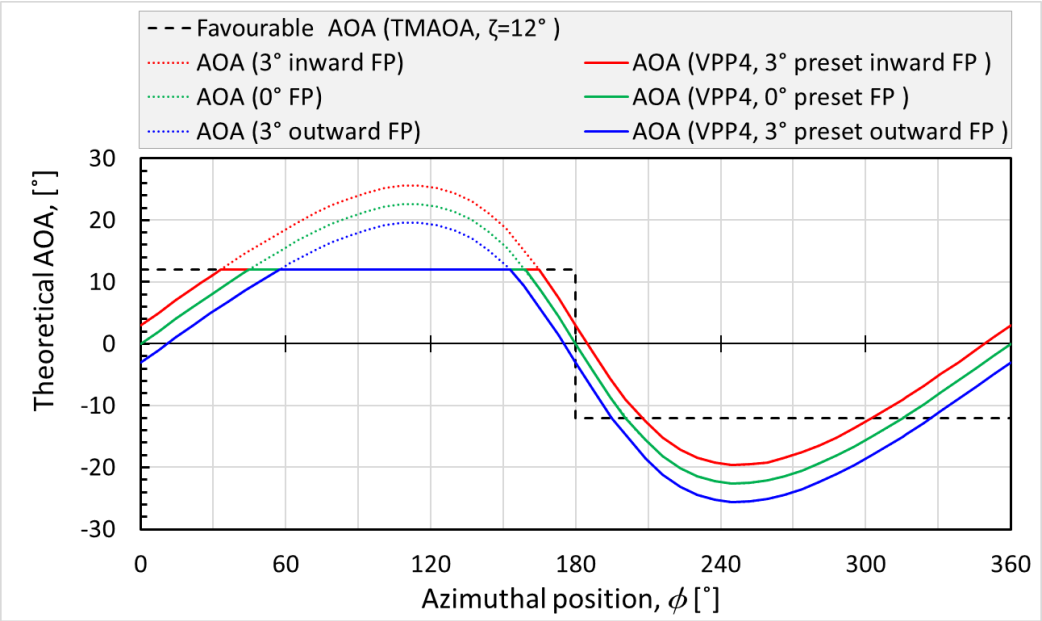

Figure 8.16 The theoretical FP AOA and the resultant theoretical variable pitch AOA for VPP4 with different preset FP angles that includes 3° inward FP, 0° FP, 3° outward for ζ=12°.

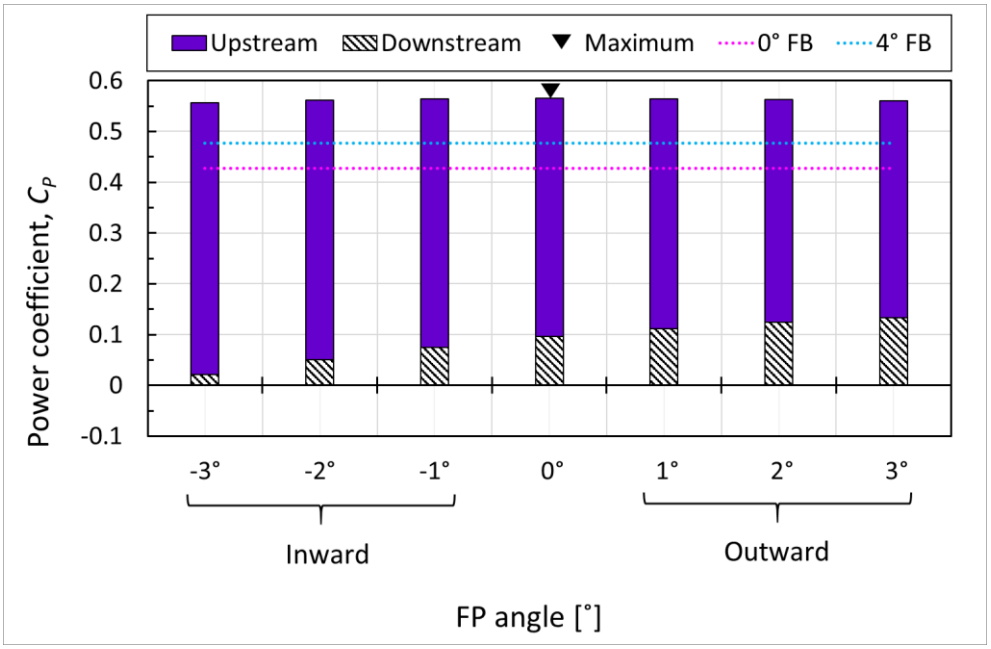

Figure 8.17 The effect of the preset FP angle on the upstream and downstream contributions to the power coefficient in a stacked form that represents the total cycle-averaged power coefficient for VPP4 with ζ=12°.

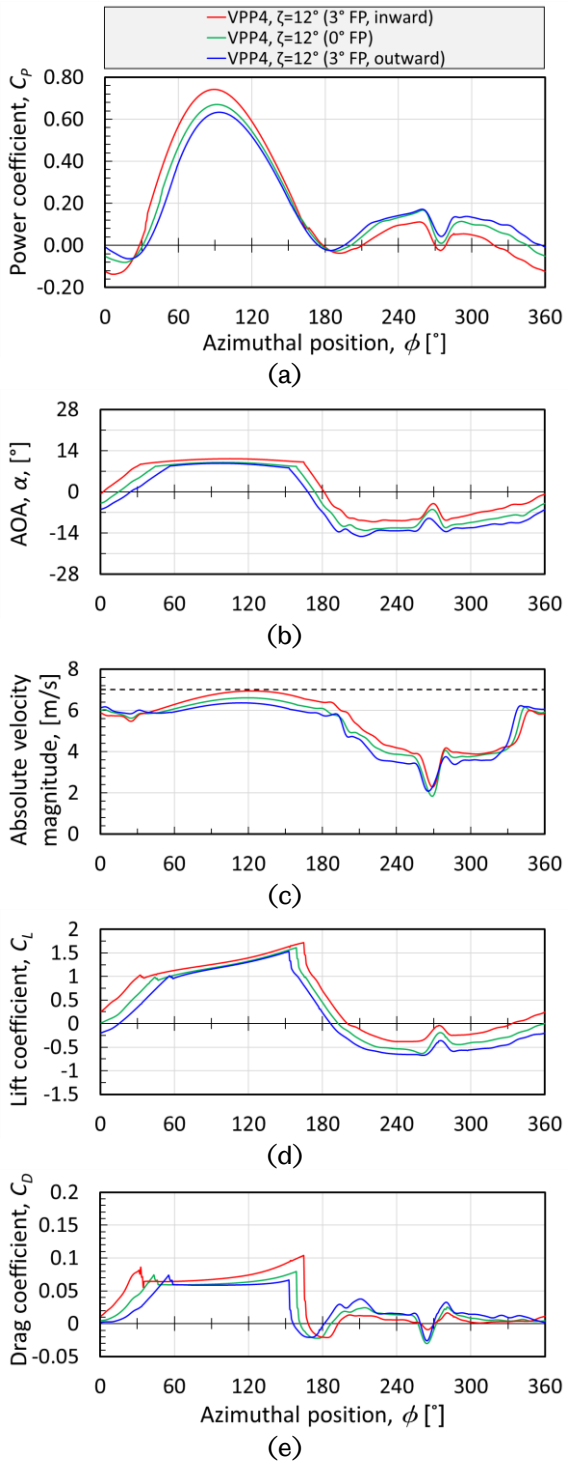

Figure 8.18 A comparison between VPP4 configuration with different preset FP angles that includes 3° inward FP, 0° FP, 3° outward FP for ζ=12° in terms of the instantaneous power coefficient, AOA, the local velocity magnitude, the lift coefficient and the drag coefficient.

8.6 Quantification of the power spent on the Variable Pitch

The aim of this section is to study the power required to apply the pitch motion. However, the inertial, damping, and friction losses in the pitching mechanism are excluded from this study as they depend on the structural design aspects. Hence, this study is reduced to quantify the power required to overcome the aerodynamic moment during the pitch motion. Firstly, the pressure and shear contributions to the aerodynamic torque around the blade mount point are calculated using a UDF for which an example is presented in Appendix A. Then the pitch power is calculated as follows:

$$Pitch\ power = Aerodynamic\ torque\ * Pitch\ rate \tag{8.1}$$

Figures 8.19 (a-c) show the variation of the pitch torque, pitch rate, and pitch power, for the pitching motion of VPP1 with for ζ=10°. This sinusoidal VP configuration is selected here for being the most power demanding VPP in the present study. The dimensionless pitch power is normalised by the turbine input power based on the rotor swept area as follows:

$$Dimensionless\ pitch\ power = Pitch\ power/(0.5\ \rho\ A\ V^3) \tag{8.2}$$

where ρ is the air density, A is the swept area, V is the undisturbed flow velocity.

Figure 8.19 (d) shows the variation of the dimensionless pitch power over the cycle. It could be noticed that there are small regions of the cycle in which the dimensionless pitch power is positive as the aerodynamic torque assists the pitch motion. However, the nature of the pitch mechanism based on a cam will not get benefit from this positive power. Therefore, the positive pitch power is excluded from the calculation of the cycle-averaged values. Figure 8.19 (e) shows the instantaneous power coefficient with and without the consideration of the pitch power for the pitching motion of VPP1 with for ζ=10°. It is noticed that the consideration of the pitch power does not have any significant effect on the trend or the magnitude of the instantaneous power coefficient. This conclusion is limited to the considerations of the pitch power due to the aerodynamic torque only and neglecting the inertial, damping, and friction losses in the pitching mechanism.

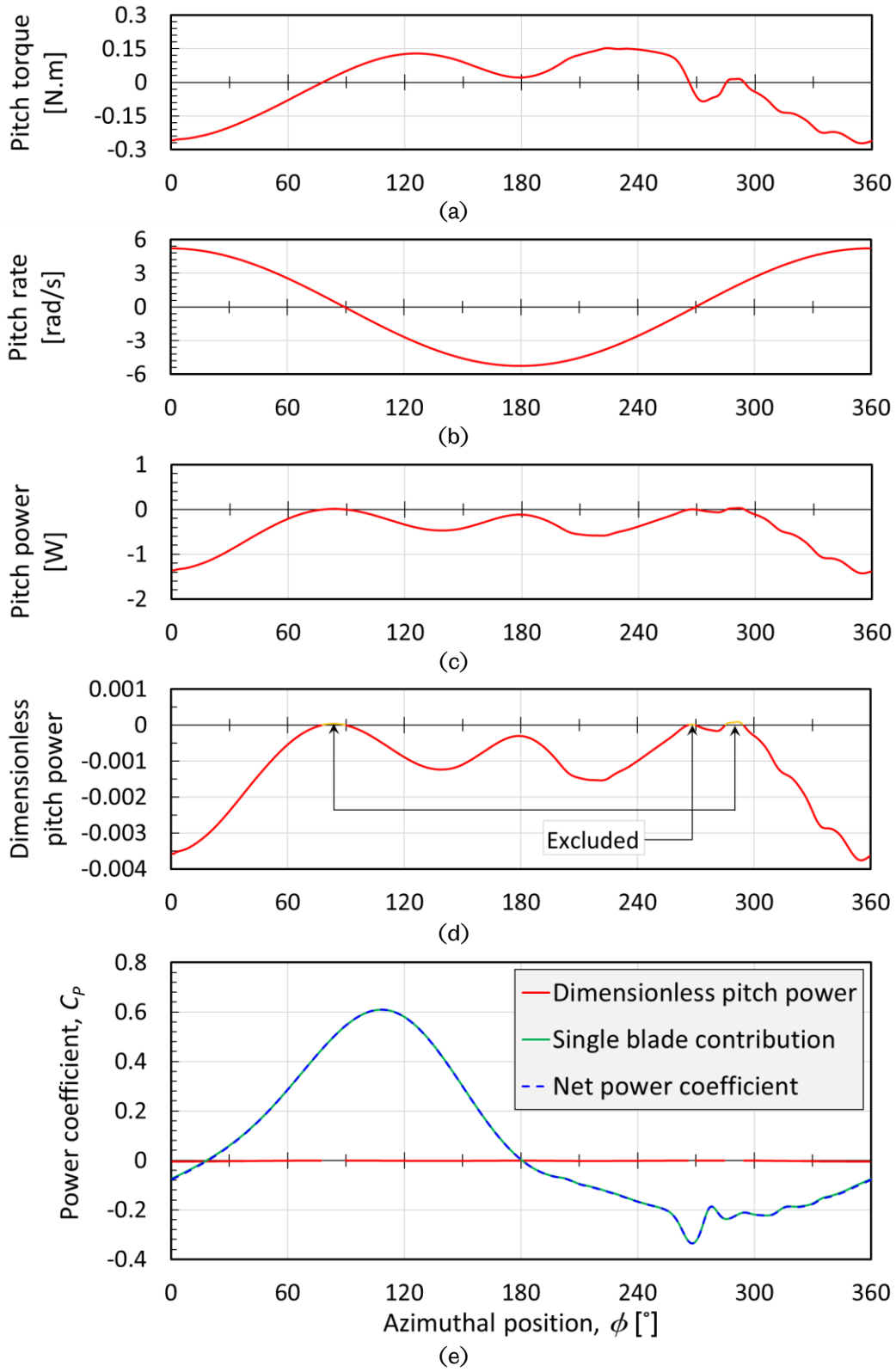

Figure 8.19 The variation of the (a) pitch torque, (b) pitch rate, (c) pitch power, and (d) dimensionless pitch power for the pitching motion of VPP1 with for ζ=10° in addition to (e) the instantaneous power coefficient with and without the consideration of the pitch power.

The ratio between the pitch power due to the aerodynamic forces and the output power gives an indication of how a certain VPP is a power demanding. Figure 8.20 shows this ratio the different VPPs over a range of TMAOA, ζ. In general VPP3 and VPP4 are less demanding than VPP1 and VPP2.

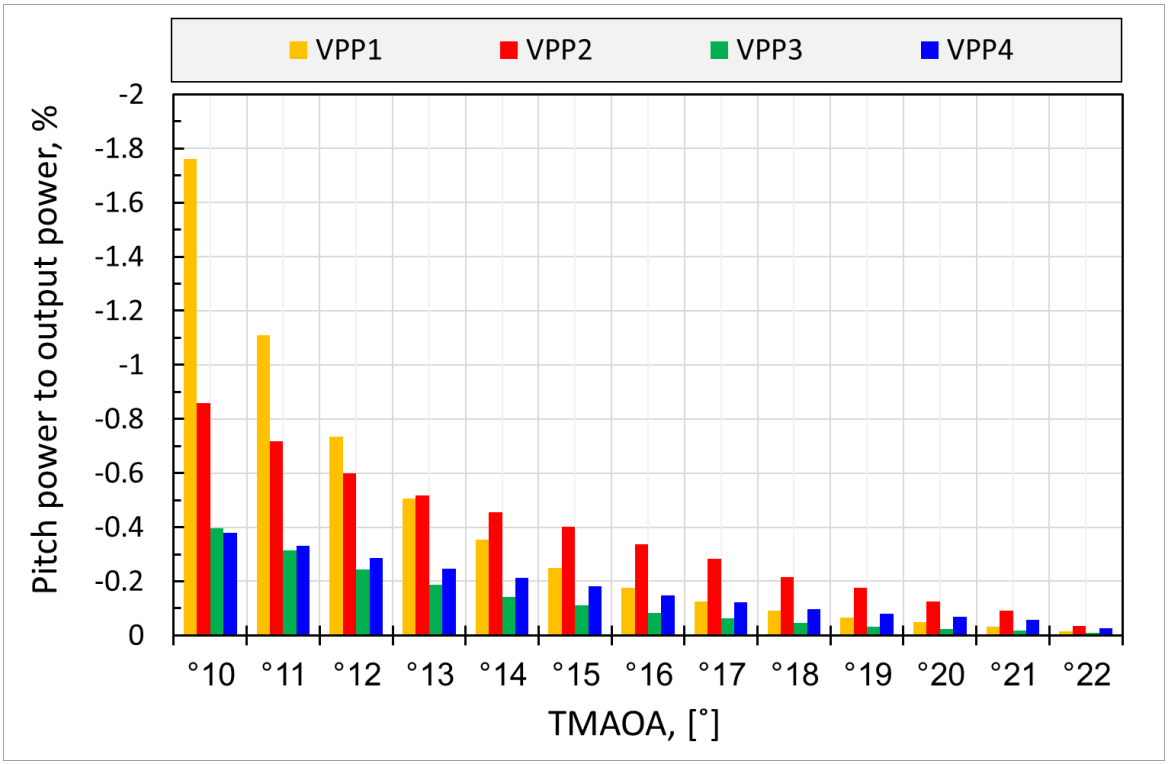

Figure 8.20 A comparison of the ratio between the pitch power due to the aerodynamic forces and the output power for different VPPs over a range of TMAOA, ζ.

While VPP1 with for ζ=10° required about 1.8% of the produced power to overcome the aerodynamic torque, both VPP3 and VPP4 requires less than 0.5%. It is found that the power required to overcome the aerodynamic forces reduced with the increase of the TMAOA, ζ. The reason why the power required to overcome the aerodynamic torque is relatively low is due to the fact that the blade mounted at the aerodynamic centre of the aerofoil. This is located at one-fourth of the chord length from the leading edge for NACA0015 as shown in Figure 8.21. From the static aerofoil data, it is reported that the aerodynamic torque about the aerodynamic centre of NACA0015 is minimal.

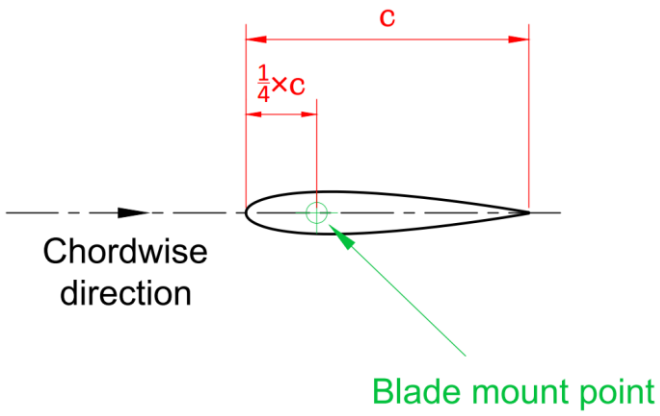

Figure 8.21 An illustration of the location of the blade mount point and the aerofoil aerodynamic centre.

8.7 The 3D CFD predictions for the best FP and VP configurations

The investigations of the FP and VP effects on the VAWT performance in this chapter are mainly based on 2D CFD simulations in order to reduce the computational cost. However, this section aims to evaluate the 3D performance of the best FP and VP configurations. The 3D simulations are carried out as discussed in Section 7.8 with and without the implementation of the winglet considering a turbine aspect ratio of 3. Figure 8.22 (a) shows a comparison between the CFD predictions of the 3D power coefficient with and without the winglet against the corresponding 2D power coefficient for both the two best configurations that include the 4° FP and VPP4 with a TMAOA of 12°. While the 3D power coefficient with and without the winglet lack behind the corresponding 2D values, it is observed that the implementation of the winglet leads to an improvement in the 3D power coefficient for both the tested FP and VP configurations as clarified in Figure 8.22 (b). Furthermore, the improvement due to the implementation of the winglet is much higher in the 4° FP case. It is concluded that the 4° FP configuration get more benefits from the winglet effects in reducing the tip losses due to the fact that the tip losses are more stronger in the FP case in contrast the VP configuration. The reason behind the stronger tip losses is that the FP design encounters a higher AOA and hence a larger pressure difference between the suction and pressure side. This motivates a larger pressure leak and tip vortices and hence a higher 3D tip losses. The stronger 3D effects are also clear when comparing the ratio between the 2D and 3D power coefficient for both the FP and VP configurations as shown in Figure 8.22 (c). In contrast with the FP configuration, it is observed that the

VP configuration have a higher 2D to 3D power coefficient ratio. Hence, it is concluded that, by reducing the AOA, the VP assists in reducing the 3D tip losses, which leads to a better overall 3D performance in contrast with the FP configuration.

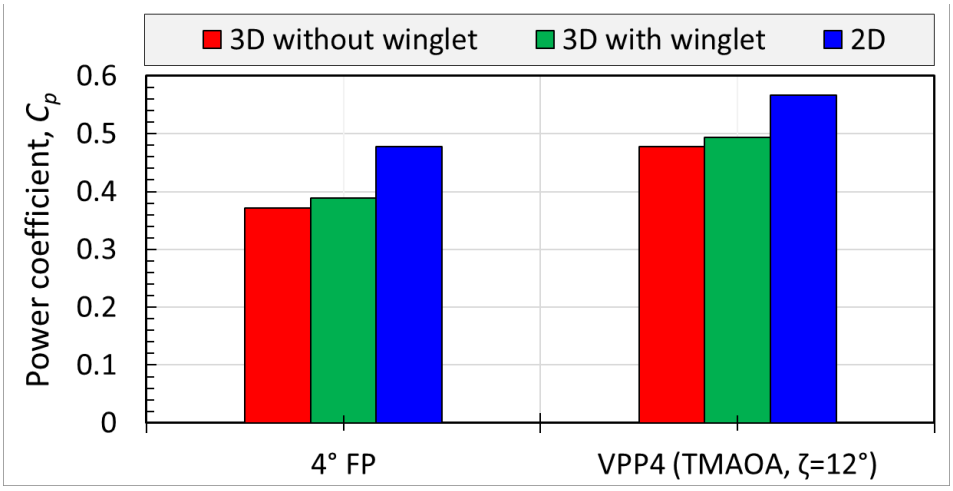

(a)

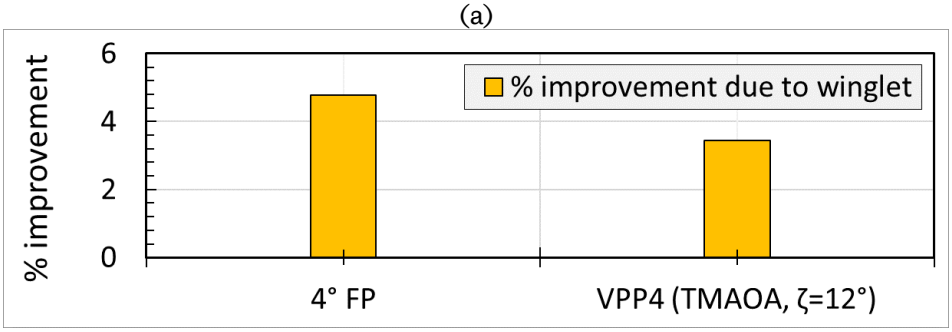

(b)

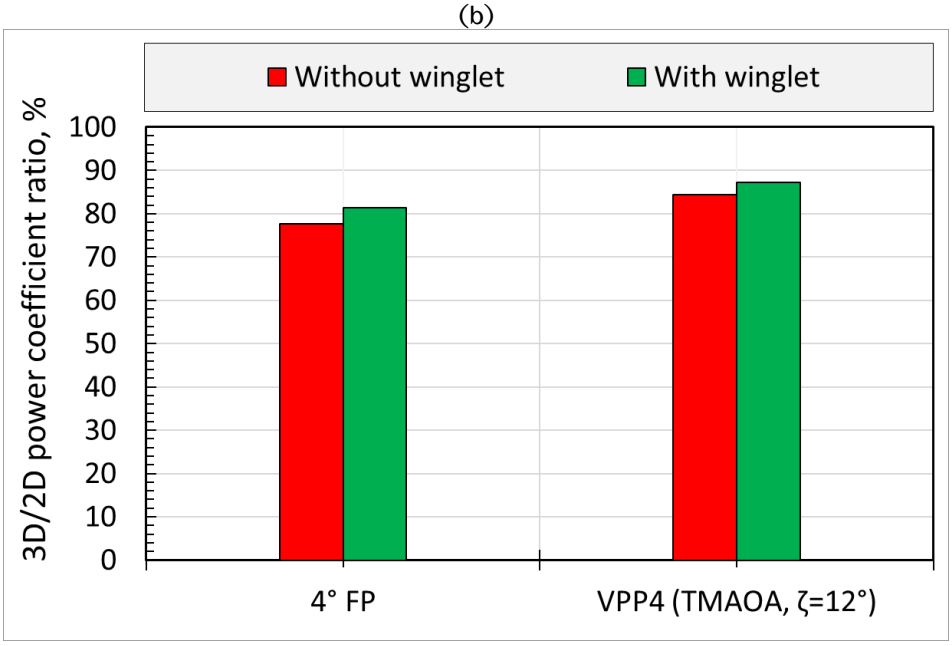

(c)

Figure 8.22 Comparison between the 4° FP and VPP4 (TMAOA, ζ=12°) in terms of (a) the effect of the winglet on the 3D power coefficient, (b) the percentage improvement on the 3D power coefficient due to the winglet, and (c) the ratio between the 2D and 3D power coefficient with and without the winglet.

8.8 Conclusions

The following conclusions are drawn:

- For a fixed pitch VAWT, the outward fixed pitch angle improves the downstream contribution to the power coefficient. In addition, the well-selection of the fixed pitch angle assist in maximising the cycle-averaged power coefficient of a fixed pitch VAWT. Under the current setup, the use of 4° outward fixed pitch improves the cycle-averaged power coefficient by about 11.7 % in contrast with the 0° fixed pitch configuration.
- For a variable pitch VAWT, the shape of the variable pitch profile has a big influence on the performance of the turbine. Under the current setup, the piecewise variable pitch profile that eliminates the high AOA in the upstream part of the cycle shows superior performance. Based on the 2D data, the proposed variable pitch profile is found to have an improvement in the power coefficient of about 32.5% and 18.6% in contrast with the zero fixed pitch and 4° fixed pitch configurations, respectively.
- The well-selection of the targeted maximum AOA leads to improve the performance of the variable pitch VAWT for the different variable pitch profiles. However, the value of the best-targeted maximum AOA and the percentage improvement in the power coefficient depend on the selected variable pitch profile.
- For a variable pitch VAWT, the inward preset fixed pitch angle assists in improving the upstream contribution to the power coefficient. However, the zero preset fixed pitch configuration shows the best overall performance under the current setup.
- The power required to overcome the aerodynamic torque under the pitch motion is negligible taking into account the performance enhancement due to the variable pitch.
- The performance of the VAWT in both the upstream and downstream part of the cycle is interconnected and the design aspect that will improve a certain part will not necessarily improve the other. Therefore, it is important to consider the overall turbine performance as the objective function of the turbine design rather than improving the contribution of a certain part to the overall performance.

- By reducing the AOA, the variable pitch assists in reducing the 3D tip losses, which boosts the overall 3D performance in contrast with the FP configuration.

9 CONCLUSIONS AND FUTURE WORKS

9.1 Graphical summary

The main tasks that have been performed in order to improve the turbine performance in this study are illustrated in Figure 9.1 along with their effect on the cycle-averaged power coefficient, C_P. In order to have consistent comparisons, all the values of the 3D power coefficient are considered without the modelling of the supporting arms. The parameters λ_I, λ_{II}, and λ_{III} represent the relative improvements in the power coefficient relative to the corresponding reference configurations (I), (II), and (III) that are clarified in Figure 9.1. It should be noticed that the superior improvement of 34.5% in the 3D power coefficient for the proposed optimised fixed pitch configuration is mainly due to the relatively large aspect ratio, in contrast with that of the reference case (I).

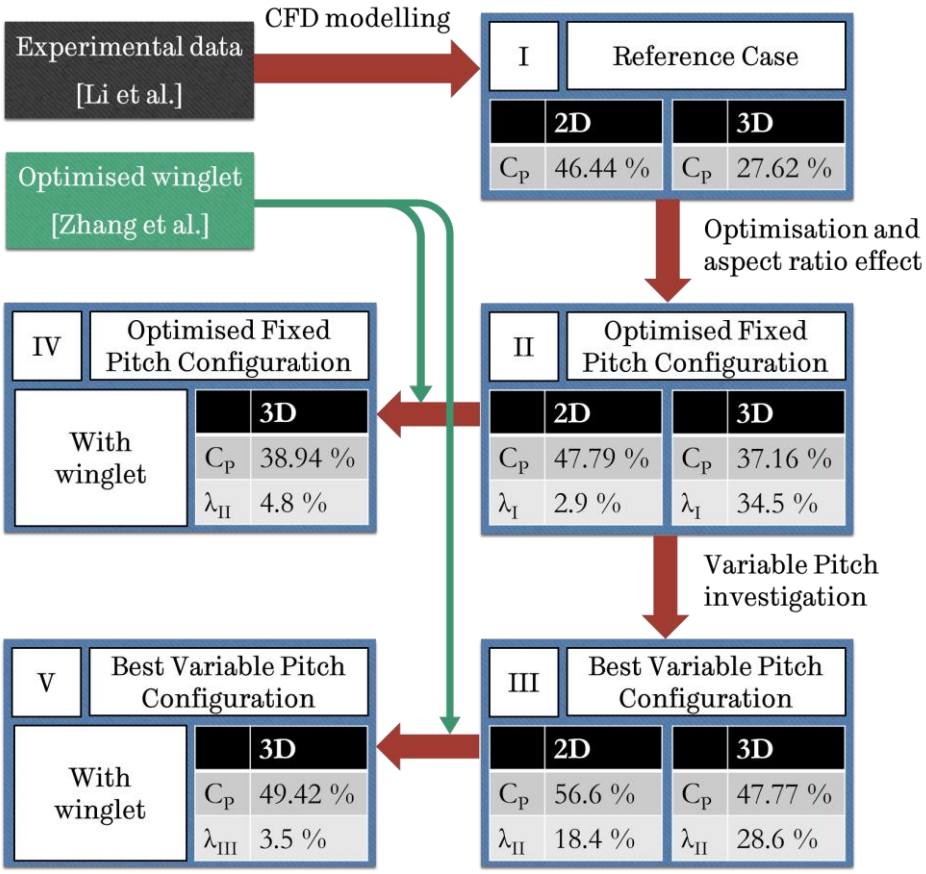

Figure 9.1 A schematic that summarises the influence of the different parts of the current study in the improvement of the performance of the proposed VAWT design. More details about the experimental data and the optimised winglet are available in the work carried out by Li et al. [180] and Zhang et al. [79], respectively.

9.2 Conclusions

The aims of the thesis study are not limited to the identifying of the best fixed pitch and variable pitch VAWT configurations, but these extend to provide a much better understanding of how a certain configuration is able to have a better performance than another. This needs a deep insight on the turbine performance and hence a high fidelity modelling of the VAWT such as the Computational Fluid Dynamics (CFD). The different aspects of the 2D and 3D CFD modelling of VAWT are investigated. Both the 2D and 3D models are numerically verified and validated and a novel procedure for the analysis of the VAWT is proposed. The Response Surface Optimisation algorithm is implemented in order to determine the optimal fixed pitch configuration. The different aspects of the variable pitch configurations are discussed and their influence on the VAWT performance is investigated. The best variable pitch configuration is proposed. In order to improve the 3D performance, the effect of a winglet-shaped tip device is quantified. Through the course of this study, several conclusions are drawn and these are classified into four main groups as clarified in the following subsections.

9.2.1 The CFD modelling of the VAWT

The first scope of this study is to investigate the best modelling strategy for the VAWT based on both the 2D and 3D CFD simulations. Two highly recommended turbulence models in the literature, namely the SST k-ω model and the SST k-ω with the γ transition model, are considered in this investigation. The verifications and validations of the 2D and 3D CFD models are investigated in depth in Chapters 4 and 5. The novelty of this investigation is in the kind of data that is used in the validations of the CFD predictions based on the selected turbulence models. While the available studies in the literature rely on some integral data, this investigation assesses the CFD predictions against instantaneous pressure data captured by a high-frequency pressure scanner. This provides a much better judgment on the behaviour of the CFD predictions of the selected turbulence models. Based on this investigation, the following conclusions are drawn:

- In the 2D case under the current setup, it is found that the selection of the turbulence model has a significant influence on both the behaviour of the results and its sensitivity to any changes in the numerical aspects of the CFD model.

- In contrast with the SST k-ω model, the 2D predictions based on the SST k-ω with the γ transition model are found to be very sensitive to the changes in the numerical aspects, especially in the downstream part of the cycle. These numerical aspects include the mesh refinement, the temporal resolution, and the temporal and spatial discretisations.
- The trends of 2D predictions of the pressure coefficient and the power coefficient based the SST k-ω with the γ transition turbulence model deviates from the experimental data, especially in the regions where the wake interactions exist. It is concluded that the use of the SST k-ω with the γ transition turbulence model is associated with the over-prediction of the separation. However, this behaviour is not observed in the 3D case. While these conclusions are limited to the current test case, deep attention should be given when using the SST k-ω with the γ transition turbulence model in the 2D simulation of VAWTs even within the transition range of Reynolds number.
- Despite the periodic motion of the VAWT, the solution is found to be not fully periodic due to the phase difference between the vortices released from the turbine blades and that released from the considerably large turbine shaft. Therefore, it is suggested that only the results in the upstream part of the cycle should be considered in the assessment of the sensitivity of the results to the changes in the numerical aspects of the CFD model when the turbine shaft is very large.
- Based on both the quantitative and qualitative assessment of the CFD predictions against the experimental data, the SST k-ω model is recommended because of its consistent predictions in both the 2D and 3D cases under the current setup. In the upstream part of the cycle, the deviations between the CFD predictions and the experimental data of the cycle-average torque coefficient are minimal and are about 2% and 3%, for the 2D and 3D cases, the respectively. However, both the 2D and 3D CFD predictions are considerably over-predicted in the downstream part of the cycle where strong wake interactions exist.
- In comparisons with the 2D predictions, the trend of the 3D predictions has a much better agreement with the experimental data. However, the 2D CFD modelling still

provide a fair agreement with the experimental data and is found to be a very useful tool for the design optimisation and extensive parametric studies that would be very computationally expensive if carried out using 3D simulations. However, the 3D modelling is still essential for testing the final designs and for testing of the 3D aspects of the VAWT that include the supporting structure, blade tip devices, and non-straight blades. The turbine performance is generally reduced in the spanwise direction towards the blade tip and this is partially due to tip flow leakage that leads to a loss in the pressure difference between the suction and pressure sides near the tip.

- From the extensive mesh sensitivity study, it is found that the dimensionless wall distance, y+, is the most influential mesh attribute. Despite the associated increase in the mesh elements count and the computational cost, it is recommended to impose y+ less than or equal to unity around the blade profile so that a relatively accurate solution could be obtained.
- A computationally affordable 3D CFD model is achievable by constructing a space-efficient mesh that utilises both the multi-block structured mesh topologies and the CutCell mesh technique. The use of multi-block structured mesh topologies is found to be very useful for the control of the mesh in the regions near the rotor, especially the control of the mesh distribution in the spanwise direction. In addition, the CutCell mesh technique assists in reducing the mesh elements required for the extend domain away from the rotor due to its ability to impose high growth rates without scarifying the quality of the elements.
- The majority of the validation of the CFD models in the literature are based on the comparison with the experimental data of some integral quantity, such as the cycle-averaged power coefficient or the time-averaged wake velocity. However, the validations of the CFD model in the current study are based on a comparison with detailed experimental data of the instantaneous pressure distribution at the mid-span section and its contribution to the power. The use of the instantaneous data is found to be more informative and this assists in obtaining a better assessment of the quality of the CFD predictions. In addition, the use of the data at the mid-span section enables a fair base of comparisons between the experimental data and the

2D CFD data due to the fact that the 3D effects are minimal at the mid-span section. Hence, it is recommended to rely on the instantaneous data in the validation of the numerical models.

9.2.2 The analysis of the VAWT performance

In order to obtain a better understanding of how the VAWT performs under the different operating conditions, a novel procedure for the analysis of the VAWT performance is proposed based on the CFD flow-field data and this relies on a new proposed method for the estimation of the Angle of Attack (AOA). This is discussed in details in Chapter 6 and the following conclusions are drawn:

- The distribution of the AOA over the entire cycle has significant effects on the overall power coefficient of the VAWT and this makes an accurate estimation of the AOA essential. Hence, a new method for the estimation of the AOA is proposed and is validated against a set of prescribed AOAs in static aerofoil simulations.
- The proposed method for the AOA estimation assists in reducing the normalised Root Mean Square Error (RMSE) by about 33.8% relative to the normalised RMSE obtained by an existing method in the literature.
- In contrast with the majority of the AOA estimation methods in the literature, the proposed method for the AOA estimation is found to be very useful as it enables the calculation of the AOA during the simulations with minimal post-processing.
- In the proposed procedure, the interpretation of the instantaneous power coefficient of the VAWT based on the estimated AOA and the lift and drag coefficients is found to very useful in obtaining a better understanding of how a certain VAWT configuration performs better than another.

9.2.3 The optimisation of the FP-VAWT

Based on the 2D CFD simulations, the Response Surface Optimisation (RSO) methodology is implemented in order to optimise the three most-influential design parameters of the FP-VAWT. These parameters include the solidity, fixed pitch angle and tip speed ratio (TSR). Based on the 3D CFD simulations, the 3D aspects of the VAWT are investigated including the aspect ratio and the implementation of an appropriate winglet. The novelty of this investigation is in the utilisation of the Response

Surface Optimisation methodology combined with the high-fidelity CFD simulations in order to optimise the FP-VAWT. Such optimisation has not been carried out before and has been found to be an effective tool for identifying the optimal design as well as exploring the effects of the different design parameters on the performance of the FP-VAWT over the entire design space. In addition, the effects of the implementation of the winglet in improving the performance of VAWT at different aspect ratios that are presented in this investigation has not been revealed before. This is discussed in detail in Chapter 7 and the following conclusions are drawn:

- Due to the complex non-linear relations between the input parameters and the performance of the VAWT, several Response Surface refinements are required. However, after the successive refinements of the Response Surface, the constructed surrogate model is found to have a very good agreement with the CFD data in the optimal region of the design space.
- The Design of Experiment (DoE) table, based on the utilisation of the enhanced rotatable Central Composite Design (CCD) along with the additional corner design points, is observed to provide good coverage of the design space, especially in the central region of the design space.
- Instead of imposing predefined manufacture constraints, it is found to be more robust to adjust the optimal design candidate without any significant change in the performance.
- Under the current setup, constraints and manufacture adjustments, the optimal 2D design of a fixed pitch VAWT is associated with a solidity of 0.315, a pitch angle of 4° and an optimal TSR of 2.6.
- Based on the 3D simulations, it is observed that the 3D power coefficient significantly increases with the increase of the aspect ratio based on the turbine blade height. It is recommended to use the largest possible aspect ratio along with the consideration of the several factors that affect the selection of the aspect ratio such as the installation space constraints, desired rated power, structural design limitations, and manufacture constraints.
- The 3D power coefficient is found to be enhanced by the implementation of an appropriate winglet, especially for a VAWT with low aspect ratio.

9.2.4 The effects of the fixed and variable pitch on the performance of VAWT

For the fixed pitch configuration, the influence of the fixed pitch angle on the VAWT performance is investigated in terms of the contribution of the upstream and downstream part of the cycle to the power coefficient in addition to the cycle-averaged power coefficient. For the variable pitch configuration, the effect of the targeted maximum AOA (TMAOA) on the VAWT performance is discussed for four different variable pitch profiles (VPPs). The influence of both the inward and outward preset fixed pitch on the VAWT performance is evaluated. The power required to overcome the aerodynamic torque during the pitch motion is quantified. Also, the characteristics of a good VPP are identified and the best fixed pitch and variable pitch configurations are identified. The novelty of this work is in the investigations of the TMAOA for different VPPs and the quantification of the power required for the pitch motion. Such investigations have not been carried out before and the effects of the TMAOA on the performance of VP-VAWT for different VPPs are found to be significant. The above-mentioned aspects of the fixed pitch and variable pitch VAWT are discussed in detail in Chapter 8. Under the current setup and operating condition, the following conclusions are drawn:

- For a fixed pitch VAWT configuration, the cycle-averaged power coefficient of a fixed pitch VAWT can be improved by the selection of the most appropriate fixed pitch angle.
- For a variable pitch VAWT, the performance of the turbine significantly depends on the shape of the implemented VPP. In this investigation, a significant improvement in the performance is achieved by implementing the piecewise VPP that eliminates the high AOA in the upstream part of the cycle.
- The performance of the variable pitch VAWT can be improved by selecting the most appropriate TMAOA. However, the most appropriate TMAOA and its percentage improvement in the performance depend on the selected VPP.
- For a variable pitch VAWT, the best overall performance is associated with the zero preset fixed pitch configuration. Although, the inward preset fixed pitch angle is found to improve the upstream contribution to the power coefficient.

- In contrast with the performance enhancement due to the variable pitch, the power required to overcome the aerodynamic torque due to the pitch motion is negligible.
- The performance of the VAWT in the upstream and downstream part of the cycle is interconnected. Therefore, a certain design aspect that improves the performance in a certain part of the cycle does not necessarily improve the performance in the other part and it is not guaranteed to improve the overall performance.
- In contrast with the fixed pitch configuration, the variable pitch reduces the 3D tip losses due to the reduced maximum AOA and hence the overall 3D performance is improved.

9.3 Recommendations and future works

Very interesting research findings regarding the analysis of the aerodynamics of VAWT and how to improve its performance have been discussed in this thesis. This allows for several recommendations on interesting research and future works that are summarised as follows:

- It is recommended to use the instantaneous data based on the pressure measurements in the assessment of the different numerical models.
- While two turbulence models are considered in this study, it would be beneficial to extend the assessments of the CFD predictions to include further turbulence models and the other scale resolving methods.
- It is recommended to conduct further benchmark tests that provide the detailed pressure distributions around the blade of the VAWT at different azimuthal angles for several Tip Speed Ratios (TSRs) and Reynolds number. Such benchmark data will be beneficial for further assessment of the numerical models at different operating conditions.
- In contrast with the conventional parametric studies, the use of the Response Surface Optimisation is recommended, especially when the number of the design parameters is large.

- It is recommended to optimise the geometry of the supporting arms considering both of the aerodynamic and structure aspects in order to reduce the aerodynamic losses while maintaining a sufficient strength.
- It would be beneficial to conduct an acoustic study to explore the effects of variable pitch in the aero-acoustic noise production from blades in addition to the noise from the pitching mechanism.
- While the power required to overcome the aerodynamic torque due to the pitch motion is quantified in the current study, it is recommended to quantify the corresponding power required to overcome the inertial load and mechanical friction. However, this will depend on the structural design of the rotor and the pitch mechanism.
- It would be interesting to implement the proposed procedure of the analysis of the VAWT and the proposed method of estimation of the AOA in the investigations of cycloidal propulsion systems.

REFERENCES

[1] International Energy Agency, “World Energy Outlook-Executive Summary,” Paris, France, 2018.

[2] W. Tong, *Wind power generation and wind turbine design*. WIT Press publisher, 2010.

[3] Vaisala Inc., “Vaisala global wind speed map,” 2015. [Online]. Available: www.vaisala.com. [Accessed: 19-Oct-2016].

[4] Y. A. Katsigiannis and G. S. Stavrakakis, “Estimation of wind energy production in various sites in Australia for different wind turbine classes: A comparative technical and economic assessment,” *Renew. Energy*, vol. 67, pp. 230–236, 2014.

[5] K. Johnson, “Doldrums: Siemens’ new wind turbine tackles low-wind areas - environmental capital - WSJ,” *The Wall Street Journal*, 2009. [Online]. Available: on.wsj.com/1nnCJpM. [Accessed: 08-Feb-2020].

[6] R. H. Barnes, E. V. Morozov, and K. Shankar, “Improved methodology for design of low wind speed specific wind turbine blades,” *Compos. Struct.*, vol. 119, pp. 677–684, 2015, doi: 10.1016/j.compstruct.2014.09.034.

[7] “Global Vertical Axis Wind Turbine Market Report, History and Forecast 2014-2025, Breakdown Data by Manufacturers, Key Regions, Types and Application,” Dataintelo market research report, 2019.

[8] S. Bhuyan and A. Biswas, “Investigations on self-starting and performance characteristics of simple H and hybrid H-Savonius vertical axis wind rotors,” *Energy Convers. Manag.*, vol. 87, pp. 859–867, Nov. 2014.

[9] S. Bhattacharjee and S. Acharya, “Performative analysis of an eccentric solar–wind combined system for steady power yield,” *Energy Convers. Manag.*, vol. 108, pp. 219–232, Jan. 2016, doi: 10.1016/J.ENCONMAN.2015.11.023.

[10] A. Tummala, R. K. Velamati, D. K. Sinha, V. Indraja, and V. H. Krishna, “A review on small scale wind turbines,” *Renewable and Sustainable Energy Reviews*, vol. 56. Elsevier Ltd, pp. 1351–1371, 01-Apr-2016, doi: 10.1016/j.rser.2015.12.027.

[11] R. Devi and J. Singh, “Design and Development of Prototype Highway Lighting with Road Side Wind Energy Harvester,” 2014.

[12] E. H. Bani-Hani, A. Sedaghat, M. Al-Shemmary, A. Hussain, A. Alshaieb, and H. Kakoli, “Feasibility of Highway Energy Harvesting Using a Vertical Axis Wind Turbine,” *Energy Eng. J. Assoc. Energy Eng.*, vol. 115, no. 2, pp. 61–74, 2018.

[13] O. Charrouf, A. Betka, S. Abdeddaim, and A. Ghamri, “Artificial Neural Network power manager for hybrid PV-wind desalination system,” *Math. Comput. Simul.*, vol. 167, pp. 443–460, Jan. 2020, doi: 10.1016/j.matcom.2019.09.005.

[14] J. Yan, L. Lu, T. Ma, Y. Zhou, and C. Y. Zhao, “Thermal management of the waste energy of a stand-alone hybrid PV-wind-battery power system in Hong Kong,” *Energy Convers. Manag.*, vol. 203, Jan. 2020, doi: 10.1016/j.enconman.2019.112261.

[15] M. Osman, M. A. Farahat, and M. E. Lotfy, “Optimal Design of Hybrid Energy System Drives Small-Scale Reverse Osmosis Desalination Plant,” *Int. J. Sustain. Energy*

Environ. Res., vol. 8, no. 1, pp. 48–61, 2019.

[16] F. Balduzzi, A. Bianchini, E. A. Carnevale, L. Ferrari, and S. Magnani, "Feasibility analysis of a Darrieus vertical-axis wind turbine installation in the rooftop of a building," *Appl. Energy*, vol. 97, pp. 921–929, 2012.

[17] A. Bianchini, F. Balduzzi, P. Bachant, G. Ferrara, and L. Ferrari, "Effectiveness of two-dimensional CFD simulations for Darrieus VAWTs: a combined numerical and experimental assessment," *Energy Convers. Manag.*, vol. 136, pp. 318–328, Mar. 2017, doi: 10.1016/J.ENCONMAN.2017.01.026.

[18] P. Rutter and J. Keirstead, "A brief history and the possible future of urban energy systems," *Energy Policy*, vol. 50, pp. 72–80, 2012, doi: 10.1016/j.enpol.2012.03.072.

[19] J. Manwell, J. McGowan, and A. Rogers, *Wind energy explained: theory, design and application*, Second ed. John Wiley & Sons, 2010.

[20] B. Sorensen, "History of, and recent progress in, wind-energy utilization," *Annu. Rev. energy Environ.*, vol. 20, pp. 387–424, 1995.

[21] R. Hills, *Power from wind: a history of windmill technology*. Cambridge University Press, 1996.

[22] D. G. J. Marie, "Turbine having its rotating shaft transverse to the flow of the current," U.S. Patent No. 1,835,018, 1931.

[23] S. J. Savonius, "Rotor Adapted to Be Driven by Wind or Flowing Water," U.S. Patent No. 1,697,574, 1929.

[24] H. Vowles, "An inquiry into origins of the windmill," *Trans. Newcom. Soc.*, pp. 1–14, 1930, doi: 10.1179/tns.1930.001.

[25] L. Shuqin, "Magnetic suspension and self-pitch for vertical-axis wind turbines," *Fundam. Adv. Top. Wind Power*, 2011, doi: 16250.

[26] W. Tjiu, T. Marnoto, S. Mat, M. H. Ruslan, and K. Sopian, "Darrieus vertical axis wind turbine for power generation II: Challenges in HAWT and the opportunity of multi-megawatt Darrieus VAWT development," *Renew. Energy*, vol. 75, pp. 560–571, Mar. 2015.

[27] Z. Q. Yao and C. L. Yang, "Numerical simulation of unsteady flow for variable-pitch vertical axis wind turbine," *Appl. Mech. Mater.*, vol. 291–294, pp. 490–495, 2013.

[28] R. Gosselin, G. Dumas, and M. Boudreau, "Parametric study of H-Darrieus vertical-axis turbines using CFD simulations," *J. Renew. Sustain. Energy*, vol. 8, no. 5, pp. 1–22, Sep. 2016.

[29] Q. Li *et al.*, "Effect of solidity on aerodynamic forces around straight-bladed vertical axis wind turbine by wind tunnel experiments (depending on number of blades)," *Renew. Energy*, vol. 96, pp. 928–939, 2016.

[30] A. Rezaeiha, H. Montazeri, and B. Blocken, "Towards optimal aerodynamic design of vertical axis wind turbines: Impact of solidity and number of blades," *Energy*, vol. 165, pp. 1129–1148, Dec. 2018, doi: 10.1016/j.energy.2018.09.192.

[31] D. Kishore Valappil, N. Somasekharan, S. Krishna, V. Laxman, and V. Ratna Kishore, "Influence of Solidity and Wind Shear on the Performance of VAWT using a Free

Vortex Model," *Int. J. Renew. Energy Res.*, vol. 7, no. 2, pp. 787–796, 2017.

[32] L. Du, G. Ingram, and R. G. Dominy, "Experimental study of the effects of turbine solidity, blade profile, pitch angle, surface roughness, and aspect ratio on the H-Darrieus wind turbine self-starting and overall performance," *Energy Sci. Eng.*, vol. 7, no. 6, pp. 2421–2436, Dec. 2019, doi: 10.1002/ese3.430.

[33] P. L. Delafin, T. Nishino, L. Wang, and A. Kolios, "Effect of the number of blades and solidity on the performance of a vertical axis wind turbine," *J. Phys. Conf. Ser.*, vol. 753, no. 2, pp. 1–8, 2016, doi: 10.1088/1742-6596/753/2/022033.

[34] I. S. Hwang, Y. H. Lee, and S. J. Kim, "Optimization of cycloidal water turbine and the performance improvement by individual blade control," *Appl. Energy*, vol. 86, no. 9, pp. 1532–1540, 2009, doi: 10.1016/j.apenergy.2008.11.009.

[35] A. Sagharichi, M. Zamani, and A. Ghasemi, "Effect of solidity on the performance of variable-pitch vertical axis wind turbine," *Energy*, vol. 161, pp. 753–775, Oct. 2018, doi: 10.1016/j.energy.2018.07.160.

[36] A. Subramanian *et al.*, "Effect of airfoil and solidity on performance of small scale vertical axis wind turbine using three dimensional CFD model," *Energy*, vol. 133, pp. 179–190, 2017, doi: 10.1016/j.energy.2017.05.118.

[37] S. B. Qamar and I. Janajreh, "A comprehensive analysis of solidity for cambered darrieus VAWTs," *Int. J. Hydrogen Energy*, vol. 42, no. 30, pp. 19420–19431, Jul. 2017, doi: 10.1016/j.ijhydene.2017.06.041.

[38] A. Rezaeiha, I. Kalkman, and B. Blocken, "Effect of pitch angle on power performance and aerodynamics of a vertical axis wind turbine," *Appl. Energy*, vol. 197, pp. 132–150, 2017.

[39] S. Chandramouli, S. R. Bose, T. P. Premsai, P. Prithviraj, M. Vivek, and K. Ratna, "Numerical Analysis of Effect of Pitch Angle on a Small Scale Vertical Axis Wind Turbine," *Int. J. Renew. Energy Res.*, vol. 4, no. 4, pp. 929–935, 2014, doi: 10.13140/RG.2.1.2869.7447.

[40] Y. Guo, X. Li, L. Sun, Y. Gao, Z. Gao, and L. Chen, "Aerodynamic analysis of a step adjustment method for blade pitch of a VAWT," *J. Wind Eng. Ind. Aerodyn.*, vol. 188, pp. 90–101, May 2019, doi: 10.1016/j.jweia.2019.02.023.

[41] S. Armstrong, A. Fiedler, and S. Tullis, "Flow separation on a high Reynolds number, high solidity vertical axis wind turbine with straight and canted blades and canted blades with fences," *Renew. Energy*, vol. 41, pp. 13–22, 2012, doi: 10.1016/j.renene.2011.09.002.

[42] W. Roynarin, "Optimisation of vertical axis wind turbines," PhD dissertation, Northumbria University, 2004.

[43] M. T. Asr, E. Z. Nezhad, F. Mustapha, and S. Wiriadidjaja, "Study on start-up characteristics of H-Darrieus vertical axis wind turbines comprising NACA 4-digit series blade airfoils," *Energy*, vol. 112, pp. 528–537, 2016, doi: 10.1016/j.energy.2016.06.059.

[44] H. M. S. M. Mazarbhuiya, A. Biswas, and K. K. Sharma, "Blade thickness effect on the aerodynamic performance of an asymmetric NACA six series blade vertical

axis wind turbine in low wind speed," *Int. J. Green Energy*, vol. 17, no. 2, pp. 171–179, 2020, doi: 10.1080/15435075.2020.1712214.

[45] Y. Wang, S. Shen, G. Li, D. Huang, and Z. Zheng, "Investigation on aerodynamic performance of vertical axis wind turbine with different series airfoil shapes," *Renew. Energy*, vol. 126, pp. 801–818, Oct. 2018, doi: 10.1016/j.renene.2018.02.095.

[46] M. H. Mohamed, "Performance investigation of H-rotor Darrieus turbine with new airfoil shapes," *Energy*, vol. 47, no. 1, pp. 522–530, 2012, doi: 10.1016/j.energy.2012.08.044.

[47] M. H. Mohamed, A. Dessoky, and F. Alqurashi, "Blade shape effect on the behavior of the H-rotor Darrieus wind turbine: Performance investigation and force analysis," *Energy*, vol. 179, pp. 1217–1234, Jul. 2019, doi: 10.1016/j.energy.2019.05.069.

[48] S. Orhan AKANSU, T. Dagdevïr, and N. Kahraman, "Numerical investigation of the effect of blade airfoils on a vertical axis wind turbine," *J. Therm. Sci. Technol.*, vol. 37, no. 1, pp. 115–125, 2017.

[49] I. Andrić *et al.*, "Numerical analysis of VAWT wind turbines: Joukowski vs classical NACA rotor's blades," *Energy Procedia*, vol. 158, pp. 1194–1201, 2018, doi: 10.1016/j.egypro.2019.01.306.

[50] M. Jafari, A. Razavi, and M. Mirhosseini, "Effect of airfoil profile on aerodynamic performance and economic assessment of H-rotor vertical axis wind turbines," *Energy*, vol. 165, pp. 792–810, Dec. 2018, doi: 10.1016/j.energy.2018.09.124.

[51] H. Cao, X. Wu, H. Ye, S. Hu, L. Lu, and J. Peng, "Optimization Research on Lift-Type Vertical Axis Wind Turbine Airfoil by CFD," *J. Phys. Conf. Ser.*, vol. 1064, no. 1, pp. 1–6, Aug. 2018, doi: 10.1088/1742-6596/1064/1/012072.

[52] N. Ma *et al.*, "Airfoil optimization to improve power performance of a high-solidity vertical axis wind turbine at a moderate tip speed ratio," *Energy*, vol. 150, pp. 236–252, May 2018, doi: 10.1016/j.energy.2018.02.115.

[53] C. Liang and H. Li, "Effects of optimized airfoil on vertical axis wind turbine aerodynamic performance," *J. Brazilian Soc. Mech. Sci. Eng.*, vol. 40, no. 88, pp. 1–9, 2018, doi: 10.1007/s40430-017-0926-2.

[54] J. Herrmann and G. Bangga, "Multi-objective optimization of a thick blade root airfoil to improve the energy production of large wind turbines," *J. Renew. Sustain. Energy*, vol. 11, p. 43304, 2019, doi: 10.1063/1.5070112.

[55] C. Liang and H. Li, "Aerofoil optimization for improving the power performance of a vertical axis wind turbine using multiple streamtube model and genetic algorithm," *R. Soc. Open Sci.*, vol. 4, pp. 1–15, 2018, doi: 10.1098/rsos.180540.

[56] G. Bedon, S. De Betta, and E. Benini, "Performance-optimized airfoil for Darrieus wind turbines," *Renew. Energy*, vol. 94, pp. 328–340, Aug. 2016, doi: 10.1016/j.renene.2016.03.071.

[57] G. Bedon, U. Schmidt Paulsen, H. Aagaard Madsen, F. Belloni, M. Raciti Castelli, and E. Benini, "Computational assessment of the DeepWind aerodynamic performance with different blade and airfoil configurations," *Appl. Energy*, vol.

185, pp. 1100–1108, Jan. 2017, doi: 10.1016/j.apenergy.2015.10.038.

[58] C. Song, G. Wu, W. Zhu, and X. Zhang, "Study on Aerodynamic Characteristics of Darrieus Vertical Axis Wind Turbines with Different Airfoil Maximum Thicknesses Through Computational Fluid Dynamics," *Arab. J. Sci. Eng.*, vol. 45, no. 2, pp. 689–698, Feb. 2019, doi: 10.1007/s13369-019-04127-8.

[59] O. S. Mohamed, A. A. Ibrahim, A. K. Etman, A. A. Abdelfatah, and A. M. R. Elbaz, "Numerical investigation of Darrieus wind turbine with slotted airfoil blades," *Energy Convers. Manag. X*, vol. 5, Jan. 2020, doi: 10.1016/j.ecmx.2019.100026.

[60] P. S. Srihari, P. S. Narayana, K. Lakshman Rao, J. D. Venkatesh, and P. Rajesh, "Influence of slat and flaps arrangement on the performance of modified Darrieus wind turbine," in *AIP Conference Proceedings*, 2019, vol. 2200, pp. 1–10, doi: 10.1063/1.5141182.

[61] Y. Li, C. Zhao, C. Qu, S. Zhao, F. Feng, and K. Tagawa, "Effect of Auxiliary Blade on Aerodynamic Characteristics of Vertical Axis Wind Turbine by Numerical Simulation," *Int. J. Rotating Mach.*, vol. 2019, pp. 1–17, 2019, doi: 10.1155/2019/8098160.

[62] Y. Yan, E. Avital, J. Williams, and J. Cui, "Performance Improvements for a Vertical Axis Wind Turbine by Means of Gurney Flap," *J. Fluids Eng.*, vol. 142, no. 2, pp. 1–15, Feb. 2020, doi: 10.1115/1.4044995.

[63] A. Bianchini, F. Balduzzi, D. Di Rosa, and G. Ferrara, "On the use of Gurney Flaps for the aerodynamic performance augmentation of Darrieus wind turbines," *Energy Convers. Manag.*, vol. 184, pp. 402–415, Mar. 2019, doi: 10.1016/j.enconman.2019.01.068.

[64] I. C. M. Lositaño and L. A. M. Danao, "Steady wind performance of a 5 kW three-bladed H-rotor Darrieus Vertical Axis Wind Turbine (VAWT) with cambered tubercle leading edge (TLE) blades," *Energy*, vol. 175, pp. 278–291, May 2019, doi: 10.1016/j.energy.2019.03.033.

[65] Z. Wang and M. Zhuang, "Leading-edge serrations for performance improvement on a vertical-axis wind turbine at low tip-speed-ratios," *Appl. Energy*, vol. 208, pp. 1184–1197, Dec. 2017, doi: 10.1016/J.APENERGY.2017.09.034.

[66] A. S. Siddiqui *et al.*, "Performance evaluation of H-type Darrieus VAWT with J-shaped blade geometry at variable pitch angles," in *AIP Conference Proceedings*, 2019, vol. 2119, pp. 1–10, doi: 10.1063/1.5115369.

[67] M. H. Mohamed, "Criticism study of J-Shaped darrieus wind turbine: Performance evaluation and noise generation assessment," *Energy*, vol. 177, pp. 367–385, Jun. 2019, doi: 10.1016/j.energy.2019.04.102.

[68] B. Shahizare, N. Nik-Ghazali, W. T. T. Chong, S. Tabatabaeikia, N. Izadyar, and A. Esmaeilzadeh, "Novel investigation of the different omni-direction-guide-vane angles effects on the urban vertical axis wind turbine output power via three-dimensional numerical simulation," *Energy Convers. Manag.*, vol. 117, pp. 206–217, Jun. 2016, doi: 10.1016/j.enconman.2016.03.034.

[69] W. T. Chong, S. C. Poh, A. Fazlizan, and K. C. Pan, "Vertical axis wind turbine with omni-directional-guide-vane for urban high-rise buildings," *J. Cent. South Univ.*

Technol., vol. 19, no. 3, pp. 727–732, Mar. 2012, doi: 10.1007/s11771-012-1064-8.

[70] X. Jin, Y. Wang, W. Ju, J. He, and S. Xie, "Investigation into parameter influence of upstream deflector on vertical axis wind turbines output power via three-dimensional CFD simulation," *Renew. Energy*, vol. 115, pp. 41–53, 2018, doi: 10.1016/j.renene.2017.08.012.

[71] D. Velasco, O. López Mejia, and S. Laín, "Numerical simulations of active flow control with synthetic jets in a Darrieus turbine," *Renew. Energy*, vol. 113, pp. 129–140, 2017, doi: 10.1016/j.renene.2017.05.075.

[72] A. Rezaeiha, H. Montazeri, and B. Blocken, "Active flow control for power enhancement of vertical axis wind turbines: Leading-edge slot suction," *Energy*, vol. 189, Dec. 2019, doi: 10.1016/j.energy.2019.116131.

[73] Y. Yan, E. Avital, J. Williams, and J. Cui, "CFD analysis for the performance of micro-vortex generator on aerofoil and vertical axis turbine," *J. Renew. Sustain. Energy*, vol. 11, no. 4, pp. 1–24, Jul. 2019, doi: 10.1063/1.5110422.

[74] S. Zanforlin and S. Deluca, "Effects of the Reynolds number and the tip losses on the optimal aspect ratio of straight-bladed Vertical Axis Wind Turbines," *Energy*, vol. 148, pp. 179–195, Apr. 2018, doi: 10.1016/j.energy.2018.01.132.

[75] Q. Li *et al.*, "Effect of rotor aspect ratio and solidity on a straight-bladed vertical axis wind turbine in three-dimensional analysis by the panel method," *Energy*, vol. 121, pp. 1–9, 2017, doi: 10.1016/j.energy.2016.12.112.

[76] I. Rabei and M. Guțu, "Analysis of the influence of the aspect ratio on the vertical axis wind rotor performance," *IOP Conf. Ser. Mater. Sci. Eng.*, vol. 564, pp. 1–7, 2019, doi: 10.1088/1757-899X/564/1/012076.

[77] S. Brusca, • R Lanzafame, and • M Messina, "Design of a vertical-axis wind turbine: how the aspect ratio affects the turbine's performance," *Int J Energy Env. Eng*, vol. 5, pp. 333–340, 2014, doi: 10.1007/s40095-014-0129-x.

[78] F. Amato, M. R. Castelli, E. Benini, and G. Bedon, "Numerical Analysis of the Influence of Tip Devices on the Power Coefficient of a VAWT," in *Proceedings of World Academy of Science, Engineering and Technology*, 2013, pp. 387–394.

[79] T. Zhang *et al.*, "Winglet design for vertical axis wind turbines based on a design of experiment and CFD approach," *Energy Convers. Manag.*, vol. 195, pp. 712–726, 2019.

[80] Z. Wu, Y. Cao, S. Nie, and Y. Yang, "Effects of rain on vertical axis wind turbine performance," *J. Wind Eng. Ind. Aerodyn.*, vol. 170, pp. 128–140, Nov. 2017, doi: 10.1016/J.JWEIA.2017.08.010.

[81] C. Li, S. Zhu, Y. Xu, and Y. Xiao, "2.5D large eddy simulation of vertical axis wind turbine in consideration of high angle of attack flow," *Renew. Energy*, vol. 51, pp. 317–330, Mar. 2013, doi: 10.1016/J.RENENE.2012.09.011.

[82] H. Lei, D. Zhou, Y. Bao, Y. Li, and Z. Han, "Three-dimensional Improved Delayed Detached Eddy Simulation of a two-bladed vertical axis wind turbine," *Energy Convers. Manag.*, vol. 133, pp. 235–248, Feb. 2017, doi: 10.1016/J.ENCONMAN.2016.11.067.

[83] M. F. Ismail and K. Vijayaraghavan, "The effects of aerofoil profile modification on a vertical axis wind turbine performance," *Energy*, vol. 80, pp. 20–31, Feb. 2015.

[84] M. S. Campobasso, J. Drofelnik, and F. Gigante, "Comparative assessment of the harmonic balance Navier–Stokes technology for horizontal and vertical axis wind turbine aerodynamics," *Comput. Fluids*, vol. 136, pp. 354–370, Sep. 2016, doi: 10.1016/J.COMPFLUID.2016.06.023.

[85] S. Wang, D. B. Ingham, L. Ma, M. Pourkashanian, and Z. Tao, "Numerical investigations on dynamic stall of low Reynolds number flow around oscillating airfoils," *Comput. Fluids*, vol. 39, no. 9, pp. 1529–1541, Oct. 2010, doi: 10.1016/J.COMPFLUID.2010.05.004.

[86] Z. Wang, Y. Wang, and M. Zhuang, "Improvement of the aerodynamic performance of vertical axis wind turbines with leading-edge serrations and helical blades using CFD and Taguchi method," *Energy Convers. Manag.*, vol. 177, pp. 107–121, 2018.

[87] P. Kozak, "Blade pitch optimization methods for vertical-axis wind turbines," Illinois Institute of Technology, 2016.

[88] A. Bianchini, F. Balduzzi, G. Ferrara, and L. Ferrari, "Virtual incidence effect on rotating airfoils in Darrieus wind turbines," *Energy Convers. Manag.*, vol. 111, pp. 329–338, Mar. 2016, doi: 10.1016/J.ENCONMAN.2015.12.056.

[89] J. M. Edwards, L. A. Danao, and R. J. Howell, "Novel Experimental Power Curve Determination and Computational Methods for the Performance Analysis of Vertical Axis Wind Turbines," *J. Sol. Energy Eng.*, vol. 134, pp. 1–11, 2012, doi: 10.1115/1.4006196.

[90] Z. Zhao *et al.*, "Variable pitch approach for performance improving of straight-bladed VAWT at rated tip speed ratio," *Appl. Sci.*, vol. 8, no. 6, 2018, doi: 10.3390/app8060957.

[91] M. Gad-el-Hak, "Flow control: the future," *J. Aircr.*, vol. 38, no. 3, pp. 402–418, May 2001, doi: 10.2514/2.2796.

[92] P. Chougule and S. Nielsen, "Overview and design of self-acting pitch control mechanism for vertical axis wind turbine using multi body simulation approach," *J. Phys. Conf. Ser.*, vol. 524, pp. 1–10, 2014.

[93] C. M. Xisto, J. C. Páscoa, J. A. Leger, and M. Trancossi, "Wind energy production using an optimized variable pitch vertical axis rotor," in *Proceedings of ASME 2014 International Mechanical Engineering Congress & Exposition*, 2014, pp. 1–8.

[94] R. Firdaus, T. Kiwata, T. Kono, and K. Nagao, "Numerical and experimental studies of a small vertical-axis wind turbine with variable-pitch straight blades," *J. Fluid Sci. Technol.*, vol. 10, no. 1, pp. 1–15, 2015, doi: 10.1299/jfst.2015jfst0001.

[95] C. Xisto, J. Páscoa, and M. Trancossi, "Numerical analysis of design parameters with strong influence on the aerodynamic efficiency of a small-scale self-pitch VAWT," in *Volume 1: Advances in Aerospace Technology*, 2015, pp. 1–11, doi: 10.1115/IMECE2015-51581.

[96] T. Kiwata, T. Kita, T. Yamada, S. Takata, N. Komatsu, and S. Kimura, "Performance

of vertical axis wind turbine with variable-pitch straight blades by a linkage mechanism," *Trans. Japan Soc. Mech. Eng. Ser. B*, vol. 74, no. 748, pp. 2543–2551, 2010, doi: 10.1299/kikaib.74.2543.

[97] M. Benedict, V. Lakshminarayan, J. Pino, and I. Chopra, "Aerodynamics of a small-scale vertical-axis wind turbine with dynamic blade pitching," *AIAA J.*, vol. 53, no. 12, pp. 1–12, 2015, doi: 10.2514/1.J052979.

[98] R. Shrivastava, "Efficiency improvement of a straight-bladed vertical axis wind turbine," *People's J. Sci. Technol.*, vol. 2, no. 1, pp. 16–19, 2012.

[99] R. Noll, N. Ham, H. Drees, and L. Nichols, "ASI/Pinson 1-kilowatt high-reliability wind-system development: phase I. design and analysis," New Boston, NH (USA)., 1982.

[100] D. W. Erickson, J. J. Wallace, and J. Peraire, "Performance characterization of cyclic blade pitch variation on a vertical axis wind turbine," in *49th AIAA Aerospace Sciences Meeting*, 2011, pp. 1–23.

[101] V. P. Kayan, "Darrieus turbine with controlled blades: the perspective converter of hydrokinetic energy," *Open J. Renew. energy Sustain. Dev.*, vol. 1, no. 2, pp. 9–23, 2014.

[102] P. Cooper and O. C. Kennedy, "Development and analysis of a novel vertical axis wind turbine," in *Proceedings Solar 2004 - Life, The Universe and Renewables*, 2004, pp. 1–9.

[103] L. Zhang *et al.*, "Design and implementation of straight-bladed vertical axis wind turbine with collective pitch control," *Mechatronics Autom. (ICMA), 2015 IEEE Int. Conf.*, pp. 1258–1263, 2015, doi: 10.1109/ICMA.2015.7237666.

[104] A.-C. Bayeul-Lainé, S. Simonet, and G. Bois, "Spectral analysis of unsteady flow simulation in a small VAWT," *14th Int. Symp. Transp. Phenom. Dyn. Rotating Mach.*, pp. 1–10, 2012.

[105] Z. Mao, W. Tian, and S. Yan, "Influence analysis of blade chord length on the performance of a four-bladed Wollongong wind turbine," *J. Renew. Sustain. Energy*, vol. 8, no. 2, pp. 1–12, 2016, doi: 10.1063/1.4943093.

[106] L. Zhang, S. Zhang, K. Wang, X. Liu, and Y. Liang, "Study on synchronous variable-pitch vertical axis wind turbine," *Asia-Pacific Power Energy Eng. Conf. APPEEC*, pp. 1–5, 2011, doi: 10.1109/APPEEC.2011.5748440.

[107] J. Nappo, J. Sui, and R. Ritchie, "Vertical axis wind turbine: an novel solution to a classic mechanical design challenge." [Online]. Available: www.johncnappo.com. [Accessed: 31-Aug-2016].

[108] S. B. Weiss, "Vertical axis wind turbine with continuous blade angle adjustment," Bachelor thesis, Department of Mechanical Engineering, Massachusetts Institute of Technology, 2010.

[109] R. Firdaus, "Numerical and experimental studies of a small vertical-axis wind turbine with variable-pitch straight blades," Dissertation, Graduate School of Natural Science & Technology, Kanazawa University, 2015.

[110] D. Diaz and F. Pinto, "Mechatronic design of a low TSR vertical axis wind turbine

with variable pitch angle," in *ABCM Symposium Series in Mechatronics - Vol. 6*, 2013, pp. 6771–6782.

[111] A. Bayeul-Laine, S. Simonet, A. Dockter, and G. Bois, "Numerical study of flow stream in a mini VAWT with relative rotating blades," in *22nd International Symposium on Transport Phenomena*, 2011, pp. 1–13.

[112] L. Zhang, Y. Liang, E. Li, S. Zhang, and J. Guo, "Vertical axis wind turbine with individual active blade pitch control," in *Asia-Pacific Power and Energy Engineering Conference, APPEEC*, 2012, pp. 1–4, doi: 10.1109/APPEEC.2012.6307108.

[113] L. Liu, C. Liu, and X. Zheng, "Modeling, simulation, hardware implementation of a novel variable pitch control for H-type vertical axis wind turbine," *J. Electr. Eng.*, vol. 66, no. 5, pp. 264–269, Jan. 2015, doi: 10.2478/jee-2015-0043.

[114] I. S. Hwang, Y. H. Lee, and S. J. Kim, "Effectiveness enhancement of a cycloidal wind turbine by individual active control of blade motion," in *Active and Passive Smart Structures and Integrated Systems*, 2007, pp. 1–8, doi: 10.1117/12.715623.

[115] Y. Liang, L. Zhang, E. Li, and F. Zhang, "Blade pitch control of straight-bladed vertical axis wind turbine," *J. Cent. South Univ.*, vol. 23, no. 5, pp. 1106–1114, 2016, doi: 10.1007/s11771-016-0360-0.

[116] L. X. Zhang, Y. Bin Liang, X. H. Liu, and J. Guo, "Effect of blade pitch angle on aerodynamic performance of straight-bladed vertical axis wind turbine," *J. Cent. South Univ.*, vol. 21, no. 4, pp. 1417–1427, 2014, doi: 10.1007/s11771-014-2080-7.

[117] B. K. Kirke and L. Lazauskas, "Enhancing the Performance of Vertical Axis Wind Turbine Using a Simple Variable Pitch System," *Wind Engineering*, vol. 15. Sage Publications, Ltd., pp. 187–195, 1991, doi: 10.2307/43750355.

[118] N. C. K. Pawsey, "Development and evaluation of passive variable-pitch vertical axis wind turbines," PhD dissertation, The University of New South Wales, 2002.

[119] T. Yamada, T. Kiwata, T. Kita, M. Hirai, N. Komatsu, and T. Kono, "Overspeed control of a variable-pitch vertical-axis wind turbine by means of tail vanes," *J. Environ. Eng.*, vol. 7, no. 1, pp. 39–52, 2012.

[120] Z. Zhao *et al.*, "Study on variable pitch strategy in H-type wind turbine considering effect of small angle of attack," *J. Renew. Sustain. Energy*, vol. 9, no. 5, 2017, doi: 10.1063/1.4989795.

[121] I. Paraschivoiu, O. Trifu, and F. Saeed, "H-Darrieus wind turbine with blade pitch control," *Int. J. Rotating Mach.*, vol. 2009, pp. 1–7, 2009, doi: 10.1155/2009/505343.

[122] Y. L. Xu, Y. X. Peng, and S. Zhan, "Optimal blade pitch function and control device for high-solidity straight-bladed vertical axis wind turbines," *Appl. Energy*, vol. 242, pp. 1613–1625, May 2019, doi: 10.1016/j.apenergy.2019.03.151.

[123] R. Gosselin, G. Dumas, and M. Boudreau, "Parametric study of H-Darrieus vertical-axis turbines using uRANS simulations," in *21st Annual Conference of the CFD Society of Canada*, 2013, pp. 1–16.

[124] Y. Staelens, F. Saeed, and I. Paraschivoiu, "A straight-bladed variable-pitch vawt concept for improved power generation," in *ASME Wind Energy Symposium*,

2003, pp. 1–9.

[125] A. Sagharichi, M. J. Maghrebi, and A. Arabgolarcheh, “Variable pitch blades: An approach for improving performance of Darrieus wind turbine,” *J. Renew. Sustain. Energy*, vol. 8, no. 5, 2016, doi: 10.1063/1.4964310.

[126] I. Paraschivoiu, F. Saeed, and V. Desobry, “Prediction capabilities in vertical-axis wind turbine aerodynamics,” *World Wind Energy Conf. Exhib.*, no. October, pp. 3–6, 2002.

[127] P. Kozak, “Effects of unsteady aerodynamics on vertical-axis wind turbine performance,” Master of Science, Illinois Institute of Technology, 2014.

[128] F. Kanyako and I. Janajreh, “Vertical axis wind turbine performance prediction, high and low fidelity analysis,” in *The 2014 IAJC-ISAM International Conference*, 2014, pp. 1–14.

[129] C. E. Soraghan, W. E. Leithead, H. Yue, and J. Feuchtwang, “Double multiple streamtube model for variable pitch vertical axis wind turbines,” in *43rd AIAA Fluid Dynamics Conference and Exhibit*, 2013, pp. 1–12, doi: 10.2514/6.2013-2802.

[130] D. Rathi, “Performance prediction and dynamic model analysis of vertical axis wind turbine blades with aerodynamically varied blade pitch,” MSc thesis, North Carolina State University, 2012.

[131] P. D. Chougule, S. R. K. Nielsen, and B. Basu, “Active blade pitch control for straight bladed darrieus vertical axis wind turbine of new design,” *Key Eng. Mater.*, vol. 569–570, pp. 668–675, Jul. 2013.

[132] Z. Zhao, D. Su, T. Wang, B. Xu, H. Wu, and Y. Zheng, “A blade pitching approach for vertical axis wind turbines based on the free vortex method,” *J. Renew. Sustain. Energy*, vol. 11, no. 5, 2019, doi: 10.1063/1.5099411.

[133] M. Elkhoury, T. Kiwata, and E. Aoun, “Experimental and numerical investigation of a three-dimensional vertical-axis wind turbine with variable-pitch,” *J. Wind Eng. Ind. Aerodyn.*, vol. 139, pp. 111–123, 2015, doi: 10.1016/j.jweia.2015.01.004.

[134] B. Paillard, J. A. Astolfi, and F. Hauville, “URANSE simulation of an active variable-pitch cross-flow Darrieus tidal turbine: Sinusoidal pitch function investigation,” *Int. J. Mar. Energy*, vol. 11, pp. 9–26, 2015, doi: 10.1016/j.ijome.2015.03.001.

[135] B. Paillard, J.-A. Astolfi, and F. Hauville, “CFD simulation and experimental validation of a vertical axis turbine: toward variable pitch cross-flow marine turbine for maximizing hydropower extraction—the SHIVA project,” in *Volume 5: Ocean Space Utilization; Ocean Renewable Energy*, 2011, pp. 619–627, doi: 10.1115/OMAE2011-49749.

[136] P. A. Kozak, D. Vallverdú, and D. Rempfer, “Modeling Vertical-Axis Wind Turbine Performance: Blade Element Method vs. Finite Volume Approach,” in *12th International Energy Conversion Engineering Conference*, 2014, doi: 10.2514/6.2014-3861.

[137] ANSYS Inc., “ANSYS 17.2 capabilities,” 2016.

[138] D. Mann, “Overset mesh with zero gap interface,” *Dynamics 38, CD-adapco publications*, p. 10, 2015.

[139] R. Howell, N. Qin, J. Edwards, and N. Durrani, "Wind tunnel and numerical study of a small vertical axis wind turbine," *Renew. Energy*, vol. 35, no. 2, pp. 412–422, Feb. 2010.

[140] M. S. Siddiqui, N. Durrani, and I. Akhtar, "Quantification of the effects of geometric approximations on the performance of a vertical axis wind turbine," *Renew. Energy*, vol. 74, pp. 661–670, 2015.

[141] N. Franchina, G. Persico, and M. Savini, "2D-3D Computations of a Vertical Axis Wind Turbine Flow Field: Modeling Issues and Physical Interpretations," *Renew. Energy*, pp. 1170–1189, 2019.

[142] L. Daróczy, G. Janiga, K. Petrasch, M. Webner, and D. Thévenin, "Comparative analysis of turbulence models for the aerodynamic simulation of H-Darrieus rotors," *Energy*, vol. 90, pp. 680–690, 2015.

[143] J. Chaiyanupong and T. Chitsomboon, "Effects of turbulence models and grid densities on computational accuracy of flows over a vertical axis wind turbine," *Int. J. Renew. Energy Dev.*, vol. 7, no. 3, pp. 213–222, 2018.

[144] J. McNaughton, F. Billard, and A. Revell, "Turbulence modelling of low Reynolds number flow effects around a vertical axis turbine at a range of tip-speed ratios," *J. Fluids Struct.*, vol. 47, pp. 124–138, 2014.

[145] K. Rogowski, "Numerical studies on two turbulence models and a laminar model for aerodynamics of a vertical-axis wind turbine," *J. Mech. Sci. Technol.*, vol. 32, no. 5, pp. 2079–2088, 2018.

[146] C. Song, Y. Zheng, Z. Zhao, Y. Zhang, C. Li, and H. Jiang, "Investigation of meshing strategies and turbulence models of computational fluid dynamics simulations of vertical axis wind turbines," *J. Renew. Sustain. Energy*, vol. 7, no. 3, 2015.

[147] K. M. Almohammadi, D. B. Ingham, L. Ma, and M. Pourkashanian, "Modeling dynamic stall of a straight blade vertical axis wind turbine," *J. Fluids Struct.*, vol. 57, pp. 144–158, 2015.

[148] A. Rezaeiha, H. Montazeri, and B. Blocken, "On the accuracy of turbulence models for CFD simulations of vertical axis wind turbines," *Energy*, vol. 180, pp. 838–857, 2019.

[149] F. R. Menter, "Best Practice: Scale-Resolving Simulations in ANSYS CFD-Version 2.00," 2015.

[150] H. Y. Peng and H. F. Lam, "Turbulence effects on the wake characteristics and aerodynamic performance of a straight-bladed vertical axis wind turbine by wind tunnel tests and large eddy simulations," *Energy*, vol. 109, pp. 557–568, Aug. 2016, doi: 10.1016/j.energy.2016.04.100.

[151] K. Rogowski, M. O. L. Hansen, R. Maroński, and P. Lichota, "Scale Adaptive Simulation Model for the Darrieus Wind Turbine Related content," *J. Phys. Conf. Ser.*, vol. 753, pp. 1–11, 2016, doi: 10.1088/1742-6596/753/2/022050.

[152] A. Rezaeiha, H. Montazeri, and B. Blocken, "CFD analysis of dynamic stall on vertical axis wind turbines using Scale-Adaptive Simulation (SAS): Comparison against URANS and hybrid RANS/LES," *Energy Convers. Manag.*, vol. 196, pp.

1282–1298, Sep. 2019, doi: 10.1016/j.enconman.2019.06.081.

[153] S. Barber and H. Nordborg, "Comparison of simulations and wind tunnel measurements for the improvement of design tools for Vertical Axis Wind Turbines," *J. Phys. Conf. Ser.*, vol. 1102, pp. 1–11, 2018, doi: 10.1088/1742-6596/1102/1/012002.

[154] A. Dessoky, T. Lutz, G. Bangga, and E. Krämer, "Computational studies on Darrieus VAWT noise mechanisms employing a high order DDES model," *Renew. Energy*, vol. 143, pp. 404–425, Dec. 2019, doi: 10.1016/j.renene.2019.04.133.

[155] H. F. Lam and H. Y. Peng, "Study of wake characteristics of a vertical axis wind turbine by two- and three-dimensional computational fluid dynamics simulations," *Renew. Energy*, vol. 90, pp. 386–398, May 2016, doi: 10.1016/j.renene.2016.01.011.

[156] H. Lei, D. Zhou, Y. Bao, Y. Li, and Z. Han, "Three-dimensional Improved Delayed Detached Eddy Simulation of a two-bladed vertical axis wind turbine," *Energy Convers. Manag.*, vol. 133, pp. 235–248, Feb. 2017, doi: 10.1016/j.enconman.2016.11.067.

[157] T. P. Syawitri, Y. F. Yao, J. Yao, and B. Chandra, "Assessment of stress-blended eddy simulation model for accurate prediction of three-straight-bladed vertical axis wind turbine performance," in *54th 3AF International Conference on Applied Aerodynamics*, 2019, pp. 1–11.

[158] F. Menter, "Stress-blended eddy simulation (SBES)—A new paradigm in hybrid RANS-LES modeling," *Notes Numer. Fluid Mech. Multidiscip. Des.*, vol. 137, pp. 27–37, 2018, doi: 10.1007/978-3-319-70031-1_3.

[159] M. Elkhoury, "Assessment of turbulence models for the simulation of turbulent flows past bluff bodies," *J. Wind Eng. Ind. Aerodyn.*, vol. 154, pp. 10–20, Jul. 2016, doi: 10.1016/j.jweia.2016.03.011.

[160] L. D. Woods, J. F. Gardner, and K. S. Myers, "Simulation of vertical axis wind turbines with variable pitch foils," in *Volume 6B: Energy*, 2013, pp. 1–9, doi: 10.1115/IMECE2013-65694.

[161] A. A. Kader and A. Abdelmawla, "A novel control scheme for pitch regulated vertical axis wind turbine," *Int. Sci. J. Environ. Sci.*, vol. 4, no. 1, pp. 1–8, 2015.

[162] S. P. Farthing, "Vertical axis wind turbine induced velocity vector theory," *Proc. Inst. Mech. Eng. Part a-Journal Power Energy*, vol. 223, no. A2, pp. 103–114, 2009, doi: 10.1243/09576509jpe657.

[163] S. Horb, R. Fuchs, A. Immas, F. Silvert, and P. Deglaire, "Variable pitch control for vertical-axis wind turbines," *Wind Eng.*, vol. 42, no. 2, pp. 128–135, 2018, doi: 10.1177/0309524X18756972.

[164] B.-L. Annie-Claude, D. Aurore, B. Gérard, and S. Sophie, "Numerical simulation in vertical wind axis turbine with pitch controlled blades," in *4 th International Conference on Experiments / Process / System Modeling / Simulation / Optimization*, 2011, pp. 1–8.

[165] J. C. Cheng, S. J. Su, and J. J. Miau, "Application of variable blade pitch control on

improving the performance of vertical axis wind turbine," *Appl. Mech. Mater.*, vol. 229–231, pp. 2339–2342, 2012, doi: 10.4028/www.scientific.net/AMM.229-231.2339.

[166] I. S. Hwang, S. Y. Min, I. O. Jeong, Y. H. Lee, and S. J. Kim, "Efficiency improvement of a new vertical axis wind turbine by individual active control of blade motion," in *Smart Structures and Materials 2006: Smart Structures and Integrated Systems, Proc. SPIE 6173*, 2006, pp. 1–8, doi: 10.1117/12.658935.

[167] A. Sagharichi, M. Zamani, and A. Ghasemi, "Effect of solidity on the performance of variable-pitch vertical axis wind turbine," *Energy*, vol. 161, pp. 753–775, 2018, doi: 10.1016/j.energy.2018.07.160.

[168] A. Mills, M. Benedict, and I. Chopra, "Investigation of the effect of blade kinematics and Reynolds number on the aerodynamic performance of a small-scale vertical axis wind turbine with dynamic blade pitching," in *54th AIAA Aerospace Sciences Meeting*, 2016, pp. 1–11.

[169] B. K. Kirke and L. Lazauskas, "Experimental verification of a mathematical model for predicting the performance of a self-acting variable pitch vertical axis wind turbine," *Wind Eng.*, vol. 17, no. 2, pp. 58–66, 1993.

[170] D. B. Araya and J. O. Dabiri, "A comparison of wake measurements in motor-driven and flow-driven turbine experiments," *Exp. Fluids*, vol. 56, no. 7, pp. 1–15, Jul. 2015, doi: 10.1007/s00348-015-2022-7.

[171] L. Battisti, L. Zanne, S. Dell'Anna, V. Dossena, G. Persico, and B. Paradiso, "Aerodynamic measurements on a vertical axis wind turbine in a large scale wind tunnel," *J. Energy Resour. Technol.*, vol. 133, no. 3, pp. 1–9, 2011, doi: 10.1115/1.4004360.

[172] Vertogen Ltd, "Welcome to Vertogen Ltd - Vertical Wind Turbines." [Online]. Available: https://www.vertogen.eu/. [Accessed: 04-Feb-2020].

[173] B. K. Kirke and B. Paillard, "Predicted and measured performance of a vertical axis wind turbine with passive variable pitch compared to fixed pitch," *Wind Eng.*, vol. 41, no. 1, pp. 74–90, 2017, doi: 10.1177/0309524X16677884.

[174] D. P. Coiro, A. De Marco, F. Nicolosi, S. Melone, and F. Montella, "Dynamic behaviour of the patented kobold tidal current turbine: numerical and experimental aspects," *Acta Polytech.*, vol. 45, no. 3, pp. 1–8, 2005, doi: 10.14311/718.

[175] ANSYS Inc., "Design Exploration User's Guide," Canonsburg, 2013.

[176] J. Kim *et al.*, "Numerical Investigation of Jet Angle Effect on Airfoil Stall Control," *Appl. Sci.*, vol. 9, no. 15, pp. 1–23, Jul. 2019, doi: 10.3390/app9152960.

[177] L. W. Carr, "Progress in analysis and prediction of dynamic stall," *J. Aircr.*, vol. 25, no. 1, pp. 6–17, May 1988, doi: 10.2514/3.45534.

[178] Q. Wang and Q. Zhao, "Numerical study on dynamic-stall characteristics of finitewing and rotor," *Appl. Sci.*, vol. 9, no. 3, pp. 1–15, 2019, doi: 10.3390/app9030600.

[179] T. K. Guha, W. S. Oates, and R. Kumar, "Characterization of piezoelectric

macrofiber composite actuated winglets," *Smart Mater. Struct.*, vol. 24, no. 6, pp. 1–10, 2015, doi: 10.1088/0964-1726/24/6/065043.

[180] Q. Li *et al.*, "Wind tunnel and numerical study of a straight-bladed vertical axis wind turbine in three-dimensional analysis (Part I: For predicting aerodynamic loads and performance)," *Energy*, vol. 106, pp. 443–452, 2016, doi: 10.1016/j.energy.2016.03.089.

[181] I. Paraschivoiu, "Double-multiple streamtube model for Darrieus in turbines," in *Proceedings of the 2nd DOE/NASA wind turbines dynamics workshop*, 1981.

[182] A. M. Biadgo, A. Simonovic, D. Komarov, and S. Stupar, "Numerical and Analytical Investigation of Vertical Axis Wind Turbine," *FME Trans.*, vol. 41, pp. 49–58, 2013.

[183] A. Bianchini, G. Ferrara, and L. Ferrari, "Design guidelines for H-Darrieus wind turbines: Optimization of the annual energy yield," *Energy Convers. Manag.*, vol. 89, pp. 690–707, 2015, doi: 10.1016/J.ENCONMAN.2014.10.038.

[184] J. H. Strickland, B. T. Webster, and T. Nguyen, "A Vortex Model of the Darrieus Turbine: An Analytical and Experimental Study," *J. Fluids Eng.*, vol. 101, no. 4, pp. 500–505, 1979.

[185] G. Tescione, C. J. Simão Ferreira, and G. J. W. van Bussel, "Analysis of a free vortex wake model for the study of the rotor and near wake flow of a vertical axis wind turbine," *Renew. Energy*, vol. 87, pp. 552–563, 2016.

[186] E. Dyachuk and A. Goude, "Numerical Validation of a Vortex Model against ExperimentalData on a Straight-Bladed Vertical Axis Wind Turbine," *Energies*, vol. 8, no. 10, pp. 11800–11820, 2015.

[187] L. B. Wang, L. Zhang, and N. D. Zeng, "A potential flow 2-D vortex panel model: Applications to vertical axis straight blade tidal turbine," *Energy Convers. Manag.*, vol. 48, no. 2, pp. 454–461, Feb. 2007, doi: 10.1016/J.ENCONMAN.2006.06.017.

[188] M. Ghasemian, Z. N. Ashrafi, and A. Sedaghat, "A review on computational fluid dynamic simulation techniques for Darrieus vertical axis wind turbines," *Energy Convers. Manag.*, vol. 149, pp. 87–100, Oct. 2017, doi: 10.1016/J.ENCONMAN.2017.07.016.

[189] X. Jin, G. Zhao, K. Gao, and W. Ju, "Darrieus vertical axis wind turbine: Basic research methods," *Renew. Sustain. Energy Rev.*, vol. 42, pp. 212–225, 2015.

[190] J. F. Wendt, Ed., *Computational Fluid Dynamics: An Introduction*, 3rd ed. Berlin: Springer, 2009.

[191] ANSYS Inc., "ANSYS FLUENT User's Guide," Canonsburg, 2013.

[192] ANSYS Inc., "ANSYS FLUENT Theory Guide," Canonsburg, 2013.

[193] F. R. Menter, R. B. Langtry, S. R. Likki, Y. B. Suzen, P. G. Huang, and S. Völker, "A Correlation-Based Transition Model Using Local Variables—Part I: Model Formulation," *J. Turbomach.*, vol. 128, no. 3, p. 413, 2006.

[194] R. Lanzafame, S. Mauro, and M. Messina, "Wind turbine CFD modeling using a correlation-based transitional model," *Renew. Energy*, vol. 52, pp. 31–39, Apr. 2013, doi: 10.1016/j.renene.2012.10.007.

[195] S. Mauro, R. Lanzafame, M. Messina, and D. Pirrello, “Transition turbulence model calibration for wind turbine airfoil characterization through the use of a Micro-Genetic Algorithm,” *Int. J. Energy Environ. Eng.*, vol. 8, no. 4, pp. 359–374, Dec. 2017, doi: 10.1007/s40095-017-0248-2.

[196] P. J. Roache, “Quantification of Uncertainty in Computational Fluid Dynamics,” *Annu. Rev. Fluid Mech.*, vol. 29, no. 1, pp. 123–160, Jan. 1997, doi: 10.1146/annurev.fluid.29.1.123.

[197] W. G. Ferreira, “Efficient Global Optimization Driven by Ensemble of Metamodels : New Directions Opened by Least Squares Approximation,” University of Campinas, 2016.

[198] G. G. Wang and S. Shan, “Review of metamodeling techniques in support of engineering design optimization,” *J. Mech. Des.*, vol. 129, no. 4, pp. 370–380, Apr. 2007, doi: 10.1115/1.2429697.

[199] C. Gonçalves, J. J. Carvalho, M. A. Azenha, and M. F. Alpendurada, “Optimization of supercritical fluid extraction of pesticide residues in soil by means of central composite design and analysis by gas chromatography-tandem mass spectrometry,” *J. Chromatogr. A*, vol. 1110, no. 1–2, pp. 6–14, Mar. 2006, doi: 10.1016/j.chroma.2006.01.089.

[200] A. Rezaeiha, H. Montazeri, and B. Blocken, “Towards accurate CFD simulations of vertical axis wind turbines at different tip speed ratios and solidities: Guidelines for azimuthal increment, domain size and convergence,” *Energy Convers. Manag.*, vol. 156, pp. 301–316, Jan. 2018.

[201] A. Rezaeiha, I. Kalkman, and B. Blocken, “CFD simulation of a vertical axis wind turbine operating at a moderate tip speed ratio: Guidelines for minimum domain size and azimuthal increment,” *Renew. Energy*, vol. 107, pp. 373–385, 2017.

[202] X. Zhang, Z. Li, X. Yu, and W. Li, “Aerodynamic Performance of Trailing-Edge Modification of H-Type VAWT Blade Considering Camber Effect,” *Int. J. Aeronaut. Sp. Sci.*, pp. 1–12, 2019, doi: 10.1007/s42405-019-00241-x.

[203] ANSYS Inc., “ANSYS Meshing User’s Guide,” Canonsburg, 2010.

[204] A. Inc., “ANSYS CFD-Post User’s Guide,” Canonsburg, 2017.

[205] A. Sharma and M. Visbal, “Numerical investigation of the effect of airfoil thickness on onset of dynamic stall,” *J. Fluid Mech.*, vol. 870, pp. 870–900, Jul. 2019.

[206] R. E. Sheldahl and P. C. Klimas, “Aerodynamic characteristics of seven symmetrical airfoil sections through 180-degree angle of attack for use in aerodynamic analysis of vertical axis wind turbines.,” *Sandia Natl. Labs, Albuquerque, NM*, no. No. SAND-80-2114, 1981.

[207] R. Islam Rubel, R. R. I, U. M. K, and I. M. Z, “Comparison of Aerodynamics Characteristics of NACA 0015 & NACA 4415 Aerofoil Blade,” *Int. J. Res.*, vol. 5, no. 11, p. 187, 2017.

[208] L. Du, “Numerical and experimental investigations of Darrieus wind turbine start-up and operation,” Durham University, 2016.

[209] A. J. Fiedler and S. Tullis, “Blade offset and pitch effects on a high solidity vertical

axis wind turbine," *Wind Eng.*, vol. 33, no. 3, pp. 237–246, 2009.

[210] G. Lai, J. Liu, and F. Zeng, "Application of multi-objective genetic algorithm in ship shafting alignment optimization," in *Proceedings - 2017 10th International Symposium on Computational Intelligence and Design, ISCID 2017*, 2018, vol. 2, pp. 275–278.

[211] M. T. Retamales, "Comparison between OpenFOAM , ANSYS and Experimental Data for Benchmarking by," Grenoble, 2014.

[212] H. Youngren and M. Drela, "Xfoil subsonic airfoil development system." Open source software, 2005.

[213] J. Morgado, R. Vizinho, M. A. R. Silvestre, and J. C. Páscoa, "XFOIL vs CFD performance predictions for high lift low Reynolds number airfoils," *Aerosp. Sci. Technol.*, vol. 52, pp. 207–214, May 2016.

APPENDICES

APPENDIX A

UDF library

This Appendix provides the source code for the User Defined Functions (UDFs) that have been utilised in the thesis. This includes a UDF to define the constant rotation velocity in addition to four UDFs to define the pitch rate for the different Variable Pitch Profiles (VPPs). More information about the mathematical formulation of VPP1, VPP2, VPP3, and VPP4 are presented in Section 8.3. Furthermore, a UDF is included for the estimation of the AOA and to report the azimuthal angle and the geometric pitch angles. More details about the implemented method for the estimation of the AOA is presented in Section 6.2. In addition, the source code of the UDF that has been used to calculate the aerodynamic torque against the variable pitch motion is provided in this appendix. More details about the mathematical formulation of the torque calculations are presented in Section 8.6. In addition, the UDF that has been used to identify the cell ID for the reference points is provided. Finally, the UDF used to calculate the shear and pressure contributions to the torque of a VAWT is provided. The calculation method of the shear and pressure contributions to the torque of a VAWT is explained in detail in Appendix C.

The UDF that has been used to define the pitch rate for the turbine rotation

```
#include "udf.h"
/*****************************************************************
UDF to define rotation of the turbine
*****************************************************************
omega_r= angular velocity of the turbine rotor
-ve sign indicates clockwise direction
*****************************************************************/
DEFINE_TRANSIENT_PROFILE(Rotational_Velocity,time)
{
   double omega_r;
   omega_r = -20.22222222;
   return omega_r;
}
```

The UDF that has been used to define the pitch rate for VPP1 and TMAOA=12°.

```
#include "udf.h"
/*****************************************************************
UDF to define the pitch profile of turbine blades for VPP1
*****************************************************************/
```

```
//
/*************** angular velocity for blade No.1 *****************/
DEFINE_TRANSIENT_PROFILE(Angular_Velocity_b1,time)
{
double omega_b1;
double omega_r = 20.22222222;
double VP_Magnitude = 12.257019; // check
double  tc=0.31070682;
double ti, n;
n=floor(time/tc);
ti=time-n*tc;
omega_b1=0;
omega_b1 = omega_r*VP_Magnitude/180*M_PI*cos(omega_r*time+0*M_PI);
return omega_b1;
}
/*************** angular velocity for blade No.2 *****************/
DEFINE_TRANSIENT_PROFILE(Angular_Velocity_b2,time)
{
double omega_b2;
double omega_r = 20.22222222;
double VP_Magnitude = 12.257019; // check
double  tc=0.31070682;
double ti, n;
n=floor(time/tc);
ti=time-n*tc;
omega_b2=0;
omega_b2=omega_r*VP_Magnitude/180*M_PI*cos(omega_r*time+2.0/3*M_PI);
return omega_b2;
}
/*************** angular velocity for blade No.3 *****************/
DEFINE_TRANSIENT_PROFILE(Angular_Velocity_b3,time)
{
double omega_b3;
double omega_r = 20.22222222;
double VP_Magnitude = 12.257019; // check
double  tc=0.31070682;
double ti, n;
n=floor(time/tc);
ti=time-n*tc;
omega_b3=0;
omega_b3=omega_r*VP_Magnitude/180*M_PI*cos(omega_r*time+4.0/3*M_PI);
return omega_b3;
}
```

The UDF that has been used to define the pitch rate for VPP2 and TMAOA=12°

```
#include "udf.h"
/*****************************************************************
UDF to define the pitch profile of turbine blades for VPP2
*****************************************************************/
//
/*************** angular velocity for blade No.1 *****************/
DEFINE_TRANSIENT_PROFILE(Angular_Velocity_b1,time)
{
double omega_b1;
double omega = 20.22222222;
double TSR=2.6;
double tc=0.31070682;
double t1, t2, t3, t4, ti, n;
double tb1;
t1=0.12422918*tc;
```

```
t2=0.44243756*tc;
t3=0.55756241*tc;
t4=0.87577081*tc;
tb1=time+tc*0.0;
n=floor(tb1/tc);
ti=tb1-n*tc;
omega_b1=0;
if (ti>=t1)
{if (ti<t2)
{omega_b1=omega*(TSR*cos(omega*ti)+1)/(2*TSR*cos(omega*ti)+TSR*TSR+1);};}
if (ti>=t3)
{if (ti<t4)
{omega_b1=omega*(TSR*cos(omega*ti)+1)/(2*TSR*cos(omega*ti)+TSR*TSR+1);};}
return omega_b1;
}
/*************** angular velocity for blade No.2 *****************/
DEFINE_TRANSIENT_PROFILE(Angular_Velocity_b2,time)
{
double omega_b2;
double omega = 20.22222222;
double TSR=2.6;
double tc=0.31070682;
double t1, t2, t3, t4, ti, n;
double tb2;
t1=0.12422918*tc;
t2=0.44243756*tc;
t3=0.55756241*tc;
t4=0.87577081*tc;
tb2=time+tc*1/3;
n=floor(tb2/tc);
ti=tb2-n*tc;
omega_b2=0;
if (ti>=t1)
{if (ti<t2)
{omega_b2=omega*(TSR*cos(omega*ti)+1)/(2*TSR*cos(omega*ti)+TSR*TSR+1);};}
if (ti>=t3)
{if (ti<t4)
{omega_b2=omega*(TSR*cos(omega*ti)+1)/(2*TSR*cos(omega*ti)+TSR*TSR+1);};}
return omega_b2;
}
/*************** angular velocity for blade No.3 *****************/
DEFINE_TRANSIENT_PROFILE(Angular_Velocity_b3,time)
{
double  omega_b3;
double  omega = 20.22222222;
double  TSR=2.6;
double  tc=0.31070682;
double t1, t2, t3, t4, ti, n;
double tb3;
t1=0.12422918*tc;
t2=0.44243756*tc;
t3=0.55756241*tc;
t4=0.87577081*tc;
tb3=time+tc*2/3;
n=floor(tb3/tc);
ti=tb3-n*tc;
omega_b3=0;
if (ti>=t1)
{if (ti<t2)
{omega_b3=omega*(TSR*cos(omega*ti)+1)/(2*TSR*cos(omega*ti)+TSR*TSR+1);};}
```

```
if (ti>=t3)
{if (ti<t4)
{omega_b3=omega*(TSR*cos(omega*ti)+1)/(2*TSR*cos(omega*ti)+TSR*TSR+1);};}
return omega_b3;
}
```

The UDF that has been used to define the pitch rate for VPP3 and TMAOA=12°

```
#include "udf.h"
/*********************************************************************
UDF to define the pitch profile of turbine blades for VPP3
*********************************************************************/
//
/*************** angular velocity for blade No.1 *****************/
DEFINE_TRANSIENT_PROFILE(Angular_Velocity_b1,time)
{
double omega_b1;
double omega_r = 20.22222222;
double VP_Magnitude = 12.257019; // check
double tc=0.31070682;
double t1, t2, ti, n;
t1=0.0*tc;
t2=0.5*tc;
n=floor(time/tc);
ti=time-n*tc;
omega_b1=0;
if (ti>=t1)
{if (ti<t2)
{omega_b1 = omega_r*VP_Magnitude/180*M_PI*cos(omega_r*time+0*M_PI);};}
return omega_b1;
}
/*************** angular velocity for blade No.2 *****************/
DEFINE_TRANSIENT_PROFILE(Angular_Velocity_b2,time)
{
double omega_b2;
double omega_r = 20.22222222;
double VP_Magnitude = 12.257019; // check
double tc=0.31070682;
double t1, t2, ti, n;
t1=1.0/6*tc;
t2=2.0/3*tc;
n=floor(time/tc);
ti=time-n*tc;
omega_b2 = omega_r*VP_Magnitude/180*M_PI*cos(omega_r*time+2.0/3*M_PI);
if (ti>=t1)
{if (ti<t2)
{omega_b2=0;};}
return omega_b2;
}
/*************** angular velocity for blade No.3 *****************/
DEFINE_TRANSIENT_PROFILE(Angular_Velocity_b3,time)
{
double omega_b3;
double omega_r = 20.22222222;
double VP_Magnitude = 12.257019; // check
double tc=0.31070682;
double t1, t2, ti, n;
t1=1.0/3*tc;
t2=5.0/6*tc;
n=floor(time/tc);
ti=time-n*tc;
```

```
omega_b3=0;
if (ti>=t1)
{if (ti<t2)
{omega_b3 = omega_r*VP_Magnitude/180*M_PI*cos(omega_r*time+4.0/3*M_PI);};}
return omega_b3;
}
```

The UDF that has been used to define the pitch rate for VPP4 and TMAOA=12°

```
#include "udf.h"
/*********************************************************************
UDF to define the pitch profile of turbine blades for VPP4
*********************************************************************/
//
/*************** angular velocity for blade No.1 *****************/
DEFINE_TRANSIENT_PROFILE(Angular_Velocity_b1,time)
{
double omega_b1;
double omega = 20.22222222;
double TSR=2.6;
double tc=0.31070682;
double t1, t2, ti, n;
double tb1;
t1=0.12422918*tc;
t2=0.44243756*tc;
tb1=time+tc*0.0;
n=floor(tb1/tc);
ti=tb1-n*tc;
omega_b1=0;
if (ti>=t1)
{if (ti<t2)
{omega_b1=omega*(TSR*cos(omega*ti)+1)/(2*TSR*cos(omega*ti)+TSR*TSR+1);};}
return omega_b1;
}
/*************** angular velocity for blade No.2 *****************/
DEFINE_TRANSIENT_PROFILE(Angular_Velocity_b2,time)
{
double omega_b2;
double omega = 20.22222222;
double TSR=2.6;
double tc=0.31070682;
double t1, t2, ti, n;
double tb2;
t1=0.12422918*tc;
t2=0.44243756*tc;
tb2=time+tc*1/3;
n=floor(tb2/tc);
ti=tb2-n*tc;
omega_b2=0;
if (ti>=t1)
{if (ti<t2)
{omega_b2=omega*(TSR*cos(omega*ti)+1)/(2*TSR*cos(omega*ti)+TSR*TSR+1);};}
return omega_b2;
}
/*************** angular velocity for blade No.3 *****************/
DEFINE_TRANSIENT_PROFILE(Angular_Velocity_b3,time)
{
double omega_b3;
double omega = 20.22222222;
double TSR=2.6;
double  tc=0.31070682;
```

```
double t1, t2, ti, n;
double tb3;
t1=0.12422918*tc;
t2=0.44243756*tc;
tb3=time+tc*2/3;
n=floor(tb3/tc);
ti=tb3-n*tc;
omega_b3=0;
if (ti>=t1)
{if (ti<t2)
{omega_b3=omega*(TSR*cos(omega*ti)+1)/(2*TSR*cos(omega*ti)+TSR*TSR+1);};}
return omega_b3;
}
```

The UDF that has been used to estimate the AOA and to report the azimuthal angle and the geometric pitch angles

---

```
#include "udf.h"
/*********************************************************************
UDF for to calculate:
- the effective AOA
- the azimuthal and pitch angles
*********************************************************************/
DEFINE_EXECUTE_AT_END(execute_at_end_1)
{
Domain *d = Get_Domain(1); /* Get domain pointer */
double fc_trail_b1[ND_ND];     // Matrix to hold the position of a reference
point
double fc_lead_b1[ND_ND];      // "
double fc_trail_b2[ND_ND];     // "
double fc_lead_b2[ND_ND];      // "
double fc_trail_b3[ND_ND];     // "
double fc_lead_b3[ND_ND];      // "
double fc_trail_r[ND_ND];      // "
double fc_lead_r[ND_ND];       // "
double angle_b1;                        // Absolute angle of blade 1
double angle_b2;                        // Absolute angle of blade 2
double angle_b3;                        // Absolute angle of blade 2
double angle_r;                         // Azimuthal angle
double alpha_b1;                        // Pitch angle of blade 1
double alpha_b2;                        // Pitch angle of blade 2
double alpha_b3;                        // Pitch angle of blade 2
double aoa_b1_o;                        // AOA of blade 1 at the outer
reference point
double aoa_b1_i;                        // AOA of blade 1 at the inner
reference point
/* ↓ x & y component of absolute, blade, and relative velocity ↓ */
/* ↓ Velocity components at outer reference point ↓ */
double vx_abs_o, vy_abs_o, vx_blade_o, vy_blade_o, vx_rel_o, vy_rel_o;
/* ↓ Velocity components at inner reference point ↓ */
double vx_abs_i, vy_abs_i, vx_blade_i, vy_blade_i, vx_rel_i, vy_rel_i;
/* Angular velocity & raduis */
double omega_r = 20.22222222, r = 0.9;
/* ↓ Cell thread, face thread & cell IDs ↓ */
/* ↓ Attention is required after any change in the mesh ↓ */
int ID_b1 = 114;        // Face thread ID of blade 1 chord line
int ID_b2 = 112;        // Face thread ID of blade 2 chord line
int ID_b3 = 113;        // Face thread ID of blade 3 chord line
```

```
int ID_r = 11;          // Face thread ID of rotor reference line
int ID_b1C = 15;        // Cell thread ID of  blade 1 subdomain
int ID_b2C = 16;        // Cell thread ID of  blade 2 subdomain
int ID_b3C = 17;        // Cell thread ID of  blade 3 subdomain
int ID_rC = 14;         // Cell thread ID of  rotor subdomain
face_t f_trail_b1 = 1; // Face ID for a reference point
face_t f_lead_b1 = 2;                   // "
face_t f_trail_b2 = 2;                  // "
face_t f_lead_b2 = 1;                   // "
face_t f_trail_b3 = 2;                  // "
face_t f_lead_b3 = 1;                   // "
face_t f_trail_r = 1;                   // "
face_t f_lead_r = 2;                    // "
cell_t c_aoa_b1_o = 88853; // Cell ID of the AOA @ outer reference point
cell_t c_aoa_b1_i = 209903; // Cell ID of the AOA @ inner reference point
/*****************************************************************/
FILE *fp;       // A local pointer to a file
FILE *fpo;      // "
FILE *fpi;      // "
Thread *t_b1;   // A pointer to a face thread
Thread *t_b2;   // "
Thread *t_b3;   // "
Thread *t_r;    // "
Thread *t_b1C; // A pointer to a cell thread
Thread *t_b2C; // "
Thread *t_b3C; // "
Thread *t_rC;  // "
fp = fopen ("angles", "a");    /* open a file to write the Azimuth and Pitch
angles */
fpo = fopen ("angles_o", "a"); /* open a file to write AOA at the outer
reference point */
fpi = fopen ("angles_i", "a"); /* open a file to write AOA at the inner
reference point */
t_b1 = Lookup_Thread(d, ID_b1);
t_b2 = Lookup_Thread(d, ID_b2);
t_b3 = Lookup_Thread(d, ID_b3);
t_r = Lookup_Thread(d, ID_r);
t_b1C = Lookup_Thread(d, ID_b1C);
t_b2C = Lookup_Thread(d, ID_b2C);
t_b3C = Lookup_Thread(d, ID_b3C);
t_rC = Lookup_Thread(d, ID_rC);
F_CENTROID(fc_trail_b1,f_trail_b1,t_b1);      // return the face centroid
coordinates of the reference point
F_CENTROID(fc_lead_b1,f_lead_b1,t_b1);        // "
angle_b1 = -atan2 (fc_lead_b1[1]-fc_trail_b1[1],fc_lead_b1[0]-
fc_trail_b1[0])/M_PI*180;
if (angle_b1 < 0.0) angle_b1 = angle_b1+360;
F_CENTROID(fc_trail_b2,f_trail_b2,t_b2);      // return the face centroid
coordinates of the reference point
F_CENTROID(fc_lead_b2,f_lead_b2,t_b2);        // "
angle_b2 = -atan2 (fc_lead_b2[1]-fc_trail_b2[1],fc_lead_b2[0]-
fc_trail_b2[0])/M_PI*180;
if (angle_b2 < 0.0) angle_b2 = angle_b2+360;
F_CENTROID(fc_trail_b3,f_trail_b3,t_b3);      // return the face centroid
coordinates of the reference point
F_CENTROID(fc_lead_b3,f_lead_b3,t_b3);        // "
angle_b3 = -atan2 (fc_lead_b3[1]-fc_trail_b3[1],fc_lead_b3[0]-
fc_trail_b3[0])/M_PI*180;
if (angle_b3 < 0.0) angle_b3 = angle_b3+360;
```

```
F_CENTROID(fc_trail_r,f_trail_r,t_r);         // return the face centroid
coordinates of the reference point
F_CENTROID(fc_lead_r,f_lead_r,t_r);                    // "
angle_r = -atan2 (fc_lead_r[1]-fc_trail_r[1],fc_lead_r[0]-
fc_trail_r[0])/M_PI*180;
angle_r = angle_r-15; // corrected angle
if (angle_r < 0.0) angle_r = angle_r+360;
alpha_b1 = -angle_b1+angle_r-180;      // Pitch angle of blade 1
alpha_b2 = -angle_b2+angle_r-240;      // Pitch angle of blade 2
alpha_b3 = -angle_b3+angle_r-120;      // Pitch angle of blade 3
/* ↓ printing the azumithal and pitch angles to file ↓ */
fprintf(fp,"angle_b1= %f angle_b2= %f angle_b3= %f angle_r= %f alpha_b1= %f
alpha_b2= %f alpha_b3= %f\n", angle_b1, angle_b2, angle_b3, angle_r,
alpha_b1, alpha_b2, alpha_b3);
vx_abs_o = C_U(c_aoa_b1_o,t_b1C);
vy_abs_o = C_V(c_aoa_b1_o,t_b1C);
vx_blade_o = -omega_r*r*cos(omega_r*CURRENT_TIME+0*M_PI/180);
vy_blade_o = +omega_r*r*sin(omega_r*CURRENT_TIME+0*M_PI/180);
vx_rel_o = vx_abs_o-vx_blade_o;
vy_rel_o = vy_abs_o-vy_blade_o;
aoa_b1_o = -atan2 (vy_rel_o,vx_rel_o)/M_PI*180;
/* ↓ printing the effective AOA at the outer reference point to file ↓ */
fprintf(fpo,"vx_abs_o = %f vx_blade_o = %f vx_rel_o = %f vy_abs_o = %f
vy_blade_o = %f vy_rel_o = %f aoa_b1_o = %f \n",
 vx_abs_o, vx_blade_o, vx_rel_o , vy_abs_o, vy_blade_o, vy_rel_o,
aoa_b1_o);
vx_abs_i = C_U(c_aoa_b1_i,t_b1C);
vy_abs_i = C_V(c_aoa_b1_i,t_b1C);
vx_blade_i = -omega_r*r*cos(omega_r*CURRENT_TIME+0*M_PI/180);
vy_blade_i = +omega_r*r*sin(omega_r*CURRENT_TIME+0*M_PI/180);
vx_rel_i = vx_abs_i-vx_blade_i;
vy_rel_i = vy_abs_i-vy_blade_i;
aoa_b1_i = -atan2 (vy_rel_i,vx_rel_i)/M_PI*180;
/* ↓ printing the effective AOA at the inner reference point to file ↓ */
fprintf(fpi,"vx_abs_i = %f vx_blade_i = %f vx_rel_i = %f vy_abs_i = %f
vy_blade_i = %f vy_rel_i = %f aoa_b1_i = %f \n",
 vx_abs_i, vx_blade_i, vx_rel_i , vy_abs_i, vy_blade_i, vy_rel_i,
aoa_b1_i);
fclose (fp);
fclose (fpo);
fclose (fpi);
}
```

The UDF that has been used to calculate the aerodynamic torque against the variable pitch motion

---

```
#include "udf.h"
/************************************************************************
UDF for to calculate the aerodynamic torque against the pitch motion
************************************************************************/
DEFINE_EXECUTE_AT_END(execute_at_end_2)
{
FILE *fm;
Domain *d = Get_Domain(1);  /* Get domain pointer */
double f_i_cen[ND_ND]; // Matrix to hold the position of a reference point
double A_i[ND_ND], area_i;
double P_mom=0, Sh_mom=0, Tot_mom=0;
double omega_r = 20.22222222, r = 0.9;
double x_pc, y_pc;             // coordinates of the pitch center
```

```
int ID_b1i = 30;                // Face thread ID of blade 1 profile
Thread *t_b1i;                  // A pointer to a face thread
face_t f_i;
fm = fopen ("Pitch_moment", "a");
t_b1i = Lookup_Thread(d, ID_b1i);
x_pc = -r*sin(omega_r*CURRENT_TIME);
y_pc = -r*cos(omega_r*CURRENT_TIME);
begin_f_loop(f_i, t_b1i)
{
F_AREA(A_i,f_i,t_b1i);
area_i = NV_MAG(A_i);
F_CENTROID(f_i_cen,f_i,t_b1i);
P_mom += F_P(f_i,t_b1i)*(-A_i[1]*(f_i_cen[0]-x_pc)+A_i[0]*(f_i_cen[1]-
y_pc));
}
end_f_loop(f_i, t_b1i)
begin_f_loop(f_i, t_b1i)
{
F_AREA(A_i,f_i,t_b1i);
area_i = NV_MAG(A_i);
F_CENTROID(f_i_cen,f_i,t_b1i);
Sh_mom += (-
F_STORAGE_R_N3V(f_i,t_b1i,SV_WALL_SHEAR)[1]*f_i_cen[0]+F_STORAGE_R_N3V(f_i,
t_b1i,SV_WALL_SHEAR)[0]*f_i_cen[1]);
}
end_f_loop(f_i, t_b1i)
Tot_mom +=P_mom+ Sh_mom;
/* ↓ printing the pitching torque to file ↓ */
fprintf(fm,"P_mom = %2.16f Sh_mom = %2.16f Tot_mom = %2.16f \n", P_mom,
Sh_mom, Tot_mom);
fclose (fm);
}
```

The UDF that has been used to identify the cell ID for the reference points

---

```
#include "udf.h"
/***********************************************************************
UDF to search for the cell ID of the reference points
***********************************************************************/
#include "udf.h"
DEFINE_ON_DEMAND(cell_ID_search)
{
Domain *d=Get_Domain(1);
double CC[ND_ND];
double vf;
cell_t c;
int ID_C = 15;
Thread *t_C;
FILE *fp1;
FILE *fp2;
fp1 = fopen ("cells_P1_in", "a");
fp2 = fopen ("cells_P2_out", "a");
t_C = Lookup_Thread(d, ID_C);
begin_c_loop(c, t_C)
C_CENTROID(CC,c,t_C);
if(CC[0]<-0.0920  && CC[0]>-0.0970 && CC[1]<=-0.7085 && CC[1]>=-0.7135)
{
vf=C_V(c,t_C);
fprintf(fp1,"cb1 = %d x-coord = %f y-coord = %f vf = %f \n",c, CC[0],
CC[1],vf);
}
```

```
end_c_loop(c,t_C)

begin_c_loop(c, t_C)
C_CENTROID(CC,c,t_C);
if(CC[0]<-0.0920 && CC[0]>-0.0970 && CC[1]<=-1.086 && CC[1]>=  -1.0915)
{
vf=C_V(c,t_C);
fprintf(fp2,"cb2 = %d x-coord = %f y-coord = %f vf = %f \n",c, CC[0],
CC[1],vf);
}
end_c_loop(c,t_C)
fclose (fp1);
fclose (fp2);
}
```

The UDF that has been used to calculate the shear and pressure contributions to the torque of a VAWT

```
#include "udf.h"
/*********************************************************************
UDF to calculate the shear and pressure contributions to the torque
*********************************************************************/
DEFINE_EXECUTE_AT_END(execute_at_end)
{
FILE *fm;
Domain *d = Get_Domain(1);  /* Get domain pointer */
double f_i_cen[ND_ND]; // Matrix to hold the position of the face
double A_i[ND_ND], area_i;
double P_mom=0, Sh_mom=0, Tot_mom=0;
int ID_b1i = 29;                        // Face thread ID of blade 1
Thread *t_b1i;                          // A pointer to a face thread
face_t f_i;
fm = fopen ("UDF_mom", "a");
t_b1i = Lookup_Thread(d, ID_b1i);
begin_f_loop(f_i, t_b1i)
{
F_AREA(A_i,f_i,t_b1i);
area_i = NV_MAG(A_i);
F_CENTROID(f_i_cen,f_i,t_b1i);
P_mom += F_P(f_i,t_b1i)*(-A_i[1]*f_i_cen[0]+A_i[0]*f_i_cen[1]);
}
end_f_loop(f_i, t_b1i)
begin_f_loop(f_i, t_b1i)
{
F_AREA(A_i,f_i,t_b1i);
area_i = NV_MAG(A_i);
F_CENTROID(f_i_cen,f_i,t_b1i);
Sh_mom += (-
F_STORAGE_R_N3V(f_i,t_b1i,SV_WALL_SHEAR)[1]*f_i_cen[0]+F_STORAGE_R_N3V(f_i,
t_b1i,SV_WALL_SHEAR)[0]*f_i_cen[1]);
}
end_f_loop(f_i, t_b1i)
Tot_mom +=P_mom+ Sh_mom;
printf("**************************************************************
************************ \n");
printf("P_mom = %2.16f, Sh_mom = %2.16f, Tot_mom = %2.16f \n", P_mom,
Sh_mom, Tot_mom);
printf("**************************************************************
************************ \n");
```

```
fprintf(fm,"P_mom = %2.16f, Sh_mom = %2.16f, Tot_mom = %2.16f \n", P_mom,
Sh_mom, Tot_mom);
fclose (fm);
}
```

APPENDIX B

Effect of TVR

In order to justify the effects of the selected value of the Turbulent Viscosity Ratio (TVR) at the inlet boundary condition on the predicted results. For internal flow with Reynolds number larger than 100,000, TVR= 100 is recommended [211]. However, for external flow, the TVR is typically in the range 1<TVR<10 at the free stream locations [191]. Considering the flow at the exit of the wind tunnel contraction as a fully developed internal flow, a TVR of 100 is chosen as the baseline value in this thesis. However, 2D simulations are carried out considering TVR=1 and TVR=10 in addition to the baseline selected value of TVR=100 in order to test the sensitivity of the results to the value of the TVR. Figure B. 1 and Figure B. 2 show the effects of the tested TVRs on the instantaneous torque coefficient for both the SST k-ω and SST k-ω with the γ transition models, respectively. It is concluded that TVR value at the inlet has no significant effect on the predicted results. This is due to the fact that the value of the TVR gets dramatically increased near the turbine blades regardless of its value at the inlet.

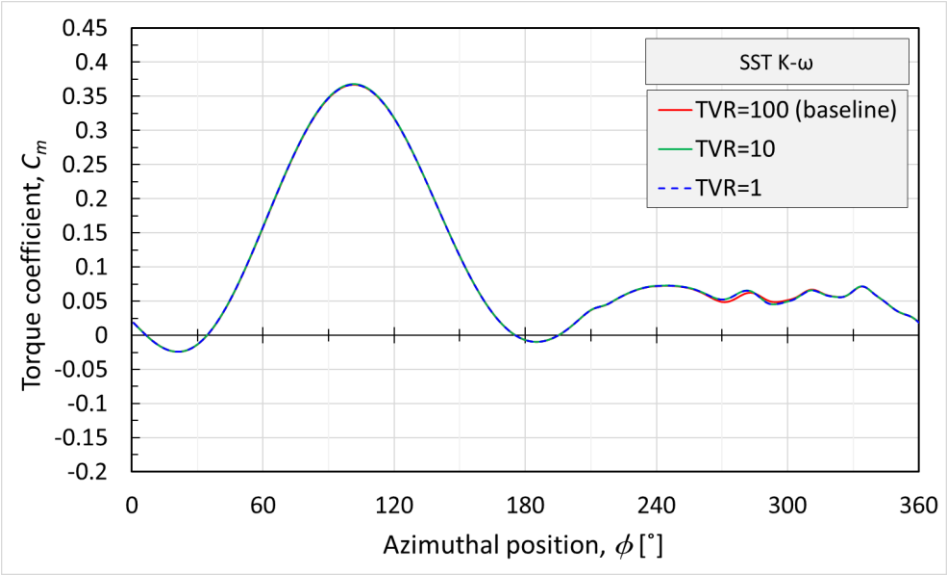

Figure B. 1 The effects of the TVR on the single blade instantaneous torque coefficient, C_m for the SST k-ω turbulence models.

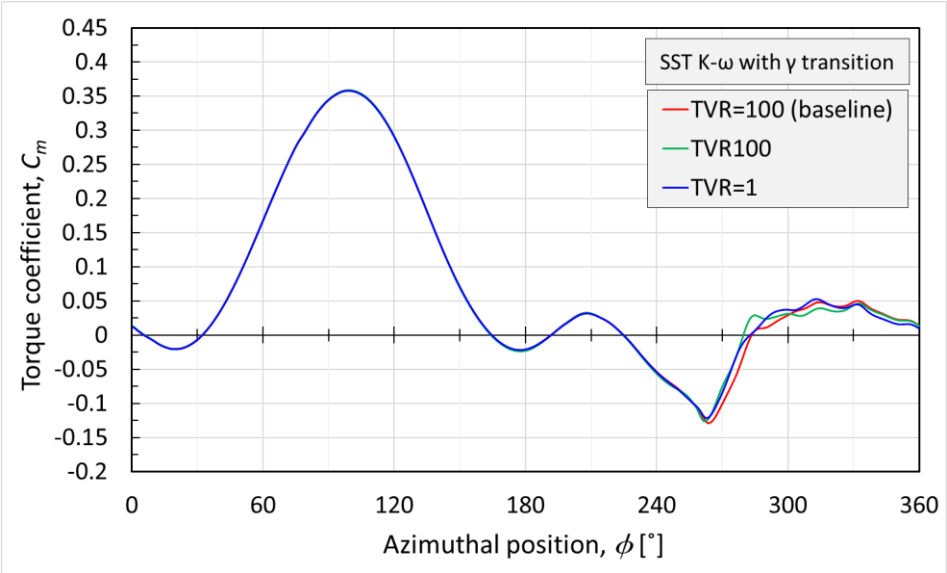

Figure B. 2 The effects of the TVR on the single blade instantaneous torque coefficient, C_m for the SST k-ω with the γ transition turbulence models.

APPENDIX C

Pressure and Shear Contributions to the Torque

When moving through the surrounding air, the aerofoil-shaped blade is subjected to pressure forces and shear forces. Both of these forces affect the driving moment of the turbine blade. In order to assess the contribution of these forces in the driving moment, both the pressure and shear torque contributions to the moment coefficient are analysed in this Appendix.

In the computational mesh, the blade surface or profile is discretised into a finite number of faces. In the 2D mesh structure, these faces are a set of straight edges. Figure C. 1 (a) shows the shape of an arbitrary cell face around the blade. Figure C. 1 (b) and (c) show how the pressure and shear stress act on an arbitrary cell face and how these develop the components of the pressure and shear forces in the x and y directions. Based on Figure C.1 (b) and (c), the pressure torque contributions of the arbitrary cell face, M_P, and the shear torque contributions of the arbitrary cell face, M_τ, are derived as follows:

$$M_P = P * (-A_y * X + A_x * Y) \tag{C.1}$$

$$M_\tau = A * (-\tau_{w_y} * X + \tau_{w_x} * Y) \tag{C.2}$$

where P is the pressure, τ_{w_x} is the shear stress component in the x direction, τ_{w_y} is the shear stress component in the y direction, A is the face area, A_y is the projected area in the y direction, A_x, is the projected area in the x direction, X is the horizontal distance between the face centre and the origin of the domain, and Y is the vertical distance between the face centre and the origin of the domain. In the 2D cases, the face area is calculated based on a unit length of the blade span.

For a discretised blade surface with a number of cell faces, the shear and pressure torque contributions of the blade are calculated as the summation of the corresponding torque contributions of each cell face of the blade surface.

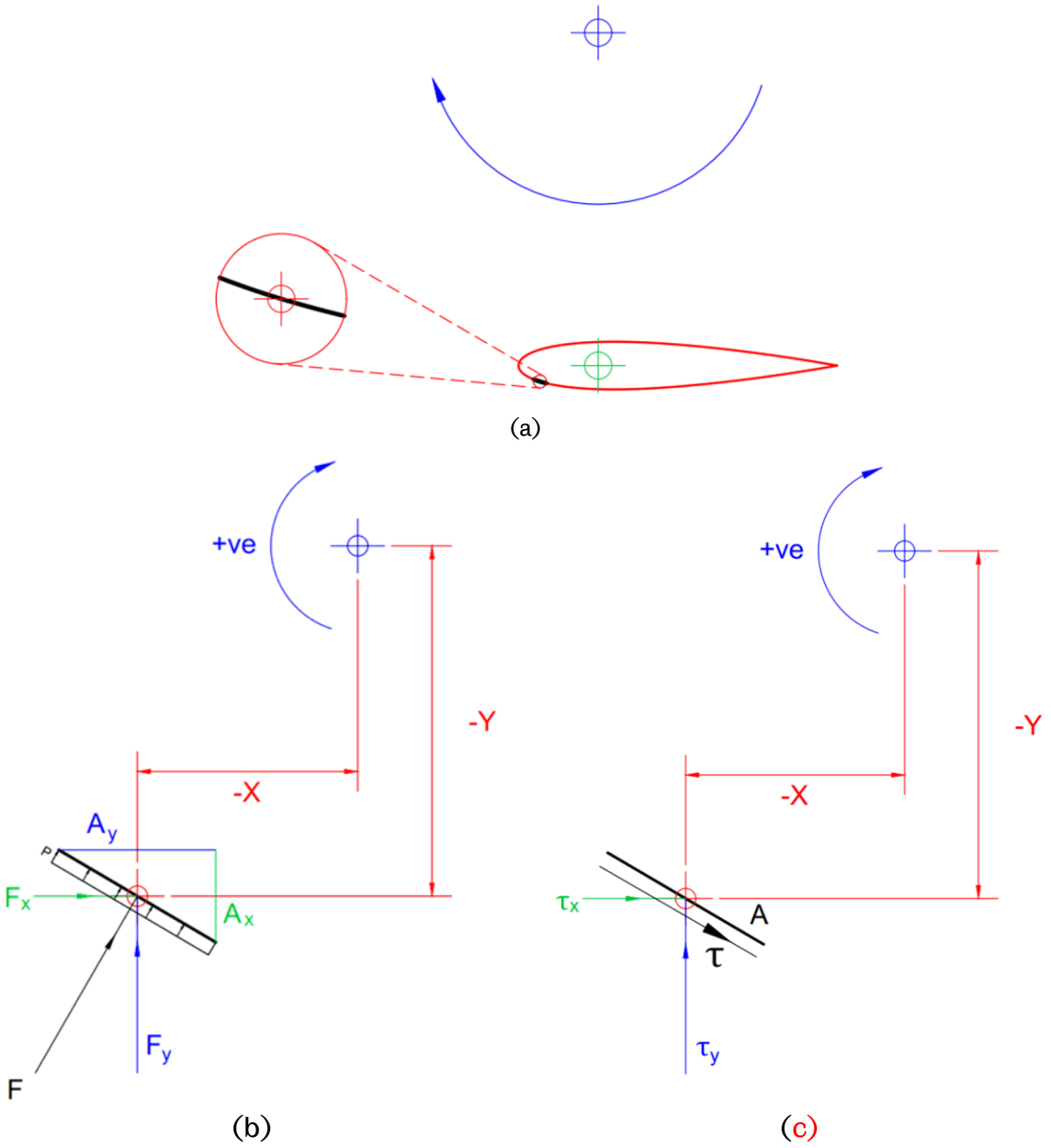

Figure C. 1 Schematic diagrams of (a) the shape of an arbitrary cell face around the blade at an arbitrary location, the forces due to (b) the pressure, and (c) the shear stress on an arbitrary face and the distance between these forces and the domain origin.

The CFD predictions of the shear and pressure torque contributions can be calculated using two methods and both of them represents equations (C.1) and (C.2) and hence give identical results. The first method is by using a UDF for which an example is presented in Appendix A. The second method is by using a Custom Field Function through the GUI of FLUENT as clarified below:

```
(custom-field-function/define'
 (
   (
     (name shear-torque)
```

```
        (display "face-area-magnitude*(-y-wall-shear*x +x-wall-shear*y)")
        (syntax-tree ("*" "face-area-magnitude" ("+" ("*" ("-" "y-wall-
        shear") "x-coordinate") ("*" "x-wall-shear" "y-coordinate"))))
        (code (field-* (field-load "face-area-magnitude") (field-+ (field-*
        (field-- (field-load "y-wall-shear")) (field-load "x-coordinate"))
        (field-* (field-load "x-wall-shear") (field-load "y-coordinate")))))
    )

    (
        (name pressure-torque)
        (display "p*(-y-face-area*x +x-face-area*y)")
        (syntax-tree ("*" "pressure" ("+" ("*" ("-" "y-face-area") "x-
        coordinate") ("*" "x-face-area" "y-coordinate"))))
        (code (field-* (field-load "pressure") (field-+ (field-* (field--
        (field-load "y-face-area")) (field-load "x-coordinate")) (field-*
        (field-load "x-face-area") (field-load "y-coordinate")))))
    )
  )
)
```

Figure C. 2 shows the pressure, shear, and total contributions in the torque coefficient based on the CFD predictions for the reference 2D case that is described in Section 4.1. The data in Figure C. 2 is based on the Custom Field Function. However, it is identical to the data extracted from the UDF. It is clear that the shear forces are acting against the motion through the cycle where the shear torque contribution is always negative. However, the average and maximum amplitude of the shear torque contribution are significantly smaller than that of the pressure torque contributions. Hence, it is concluded that the pressure contribution is more significant than the shear contribution under the current conditions.

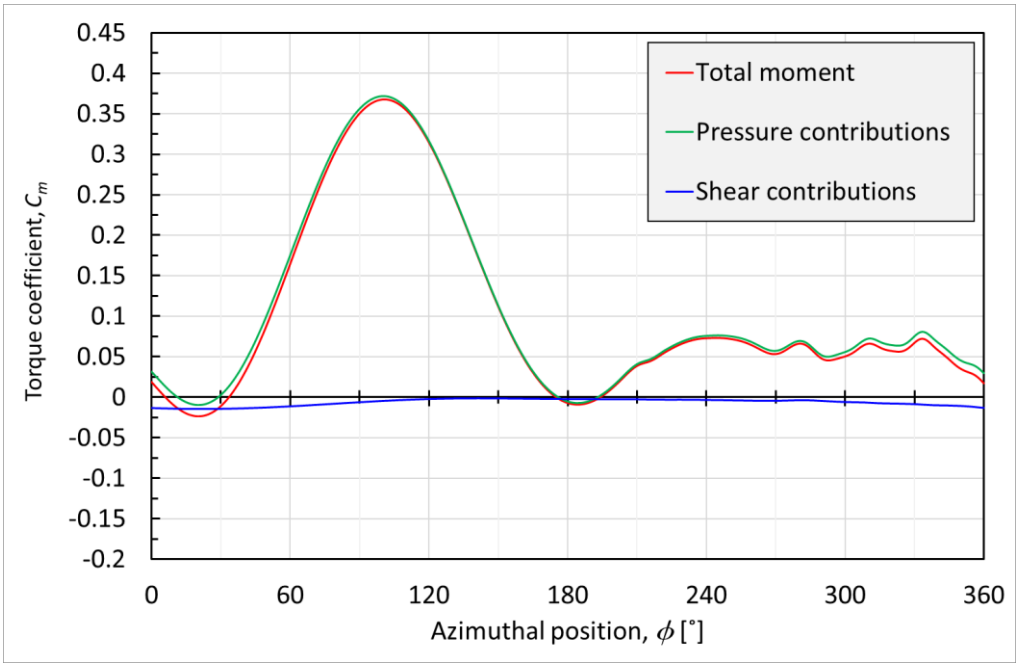

Figure C. 2 A comparison between the pressure, shear, and total contributions in the torque coefficient based on a 2D CFD simulation with the SST k-ω turbulence models.

APPENDIX D

Verification and Validation of the Static Aerofoil Case

Due to the lack of experimental data at the chosen flow conditions, the data from the widely validated XFOIL software [212] is used to validate the CFD model. XFOIL has been developed for the prediction of the aerofoil characteristics at low Reynolds numbers. This is established by incorporating both the integral boundary layer and transition equations along with the potential flow panel method. Morgado et al. [213] compared the XFOIL predictions to both of the experimental and CFD data for the aerofoil characteristics at low Reynolds number and they reported that XFOIL is an excellent analysis tool for the aerodynamic characteristics of the aerofoils. The accurate predictions on using XFOIL makes it reasonable to be used for the verification of other numerical methods, including CFD, especially when there is a lack of experimental data for the desired flow conditions.

The static blade model shares the same numerical aspects as the 2D CFD model of the VAWT in Section 4.2, except that the solver is used in the steady model. A full structured mesh is constructed across the domain as shown in Figure D. 1 (a). This mesh has the same meshing attributes as the 2D CFD model of the VAWT in Section 4.2. Figure D. 1 (b) shows the mesh in the vicinity of the leading edge of the aerofoil where a fine resolution is maintained around the aerofoil with a maximum dimensionless wall distance, y^+ <1 and a growth rate of 1.05.

In order to test the solution sensitivity to the generated mesh, three levels of mesh refinement are constructed with a refinement factor of 2. These meshes include the coarse mesh, baseline mesh, and fine mesh with a total number of elements 116400, 354600, and 1198400, respectively. Figure D. 2 shows the distribution of the pressure coefficient around the aerofoil at AOA=10° for the largest flow velocity of 21 [m/s] for the three meshes and it is found that there is no significant difference observed in the results obtained. The reason why there are no obvious differences between different grids is that the dimensionless wall distance y+, first layer thickness has been kept less than 1, and the mesh growth rate perpendicular to the aerofoil profile is kept small in all the cases. The CFD predictions of the pressure distribution around the aerofoil depend mainly on the near-wall treatment and y+. Therefore, when the computational

mesh is reasonably fine, the mesh refinements in the spanwise direction or outside the inflation layer do not have a significant effect on the computational results. The baseline mesh with 354600 elements is considered for this static aerofoil study in order to reduce the computational cost while maintaining a fine mesh distribution and a reasonable accuracy, in spite of the fact that the coarser mesh could be used with adequate accuracy. However, optimising the computational cost was not prioritised in this study.

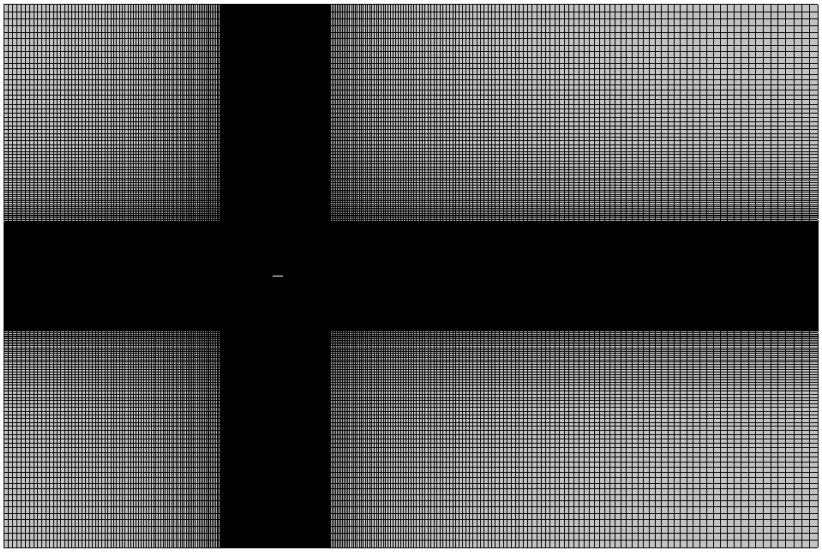

(a)

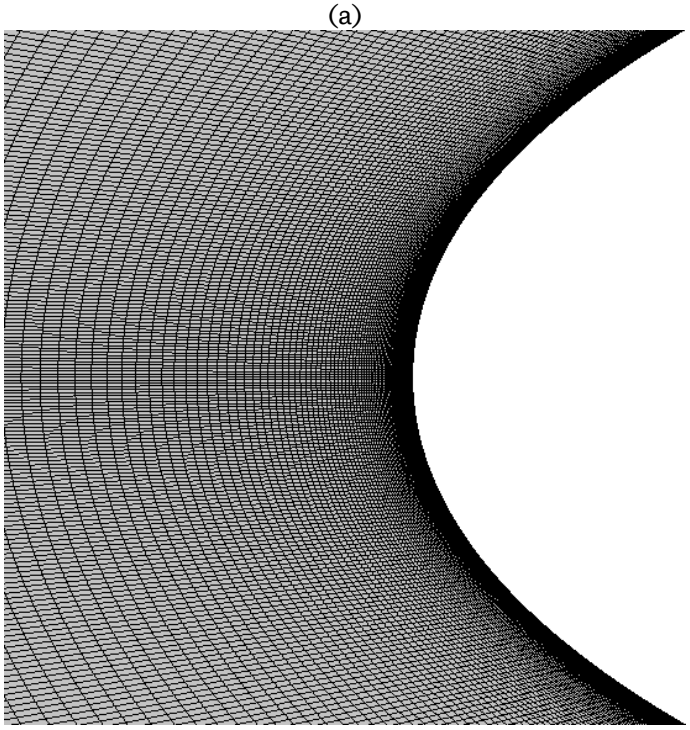

(b)

Figure D. 1 (a) The structured mesh across the domain and (b) Mesh clustering around the leading edge of the aerofoil.

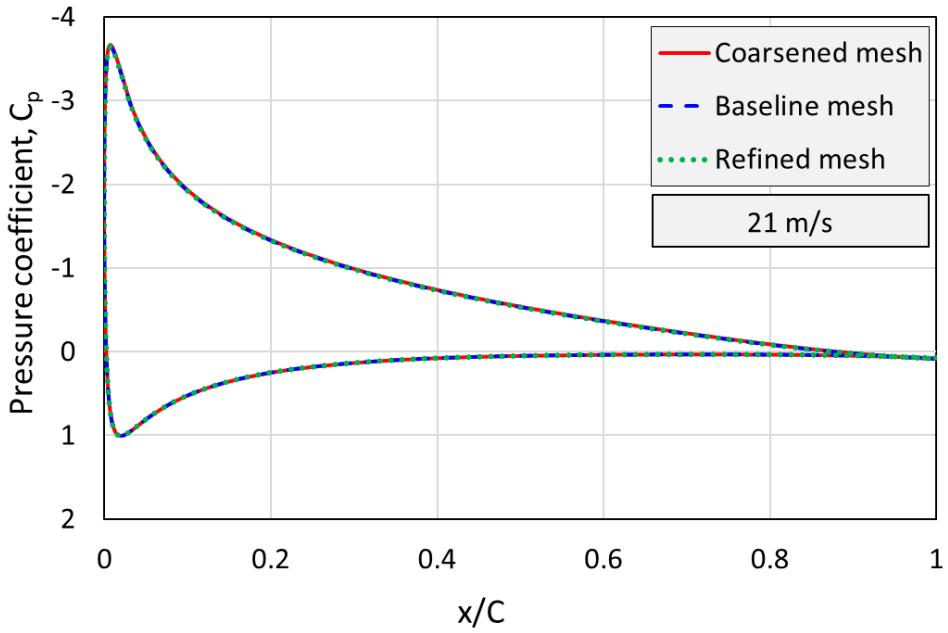

Figure D. 2 The effect of the mesh refinement on the pressure coefficient around the aerofoil at a flow velocity of 21 [m/s] and AOA=10°.

Figure D. 3 shows the comparisons between the CFD and XFOIL predictions of the pressure coefficient around the aerofoil for flow velocities of 7, 14, and 21 [m/s] at AOA=10°. It is observed that the differences between the CFD and XFOIL data are associated with the prediction of the laminar separation bubbles. The reason is that the SST k-ω model in the CFD simulation imposes a fully turbulent flow while the viscous boundary layer module in XFOIL accounts for the laminar to turbulent transition. However, these small separation bubbles have a negligible effect on the velocity field around the aerofoil and hence do not affect the calculation of the AOA.

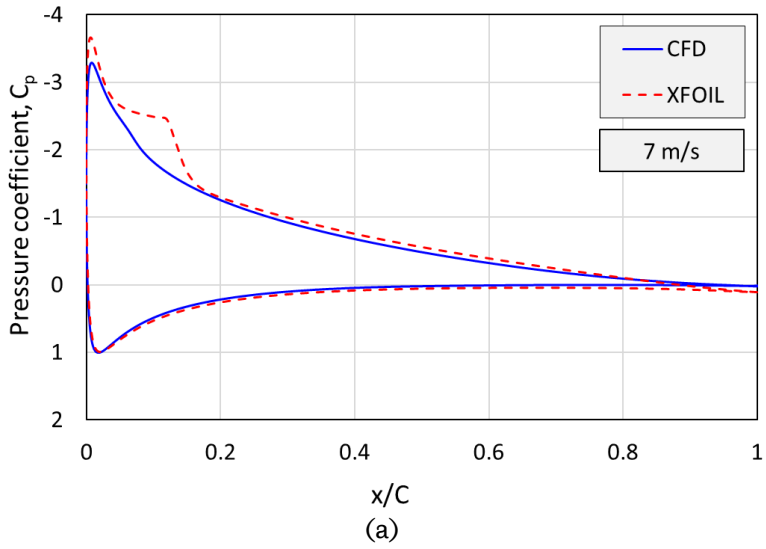

(a)

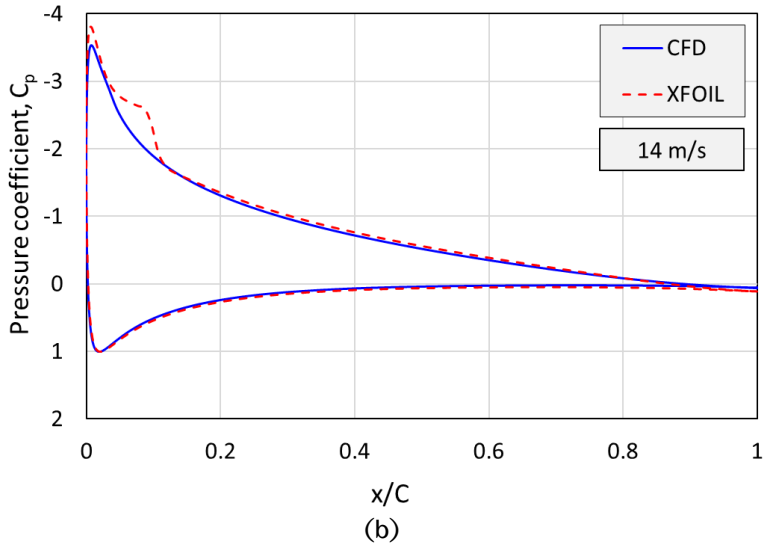

(b)

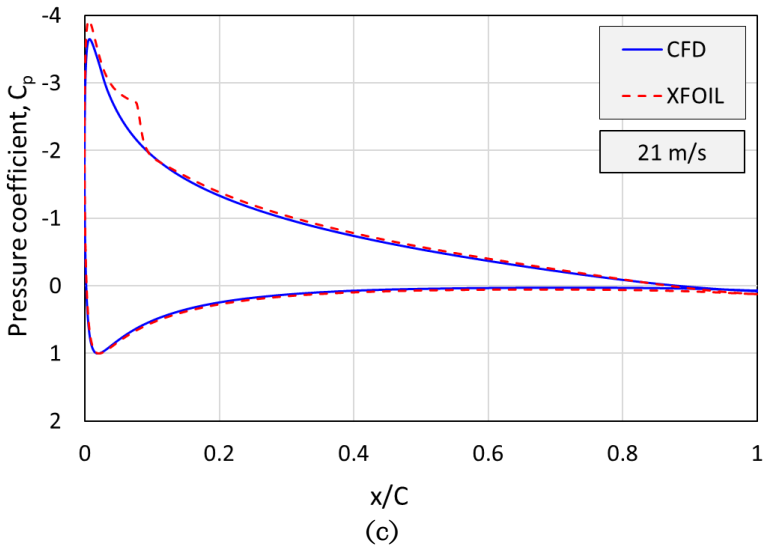

(c)

Figure D. 3 A comparisons between the CFD and XFOIL predictions of the pressure coefficient around the aerofoil at AOA=10° for flow velocities of 7, 14, and 21 [m/s].

APPENDIX E

THE ADDITIONAL SETS OF COMPUTATIONAL MESHES

The topology and attributes of the computational mesh are clarified in Sections 4.2.2 and 4.3.2 for the reference two-bladed configuration in the 2D and 3D case, respectively. The mesh topologies have been modified to suit the proposed three-bladed configuration and the implemented winglet at the blade tip. Despite the change in the mesh topology, the main mesh attributes are maintained the same as that of the reference cases. In this Appendix, the details of the additional sets of mesh are clarified.

THE MESH TOPOLOGY FOR THE 2D MODEL OF THE PROPOSED THREE-BLADED CONFIGURATION

Figure E. 1 show an extremely coarse mesh that is constructed for illustration purpose only and has not been used in the simulations. This set of mesh corresponds to the geometry of the final optimal fixed pitch configuration that is described in Section 07.7. Figure E. 2 shows the actual mesh set that is used for the 2D simulations of the final optimal design. This illustrates the mesh clustering around the rotor and in the wake region.

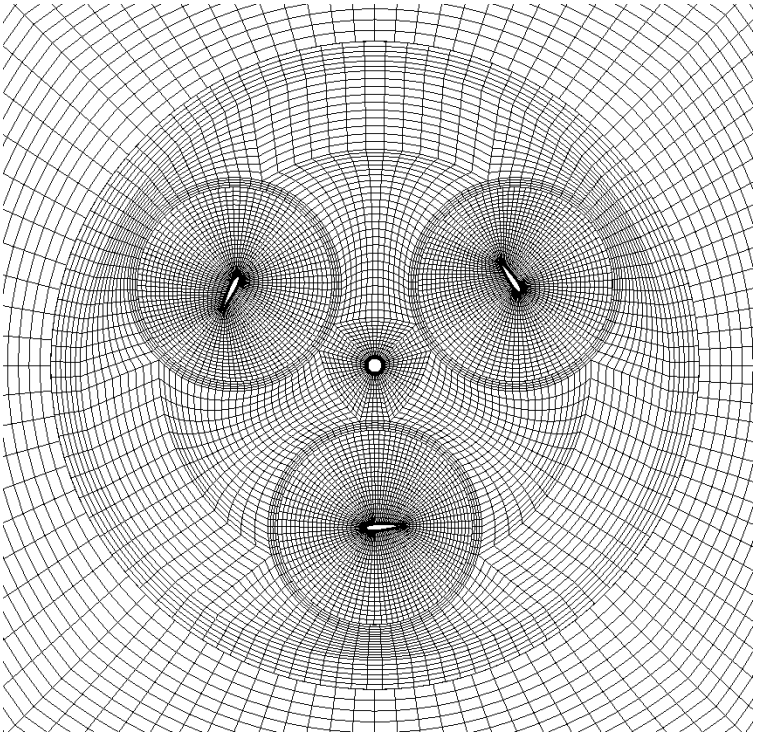

Figure E. 1 The mesh topology for a three-bladed model in an extremely coarse mesh.

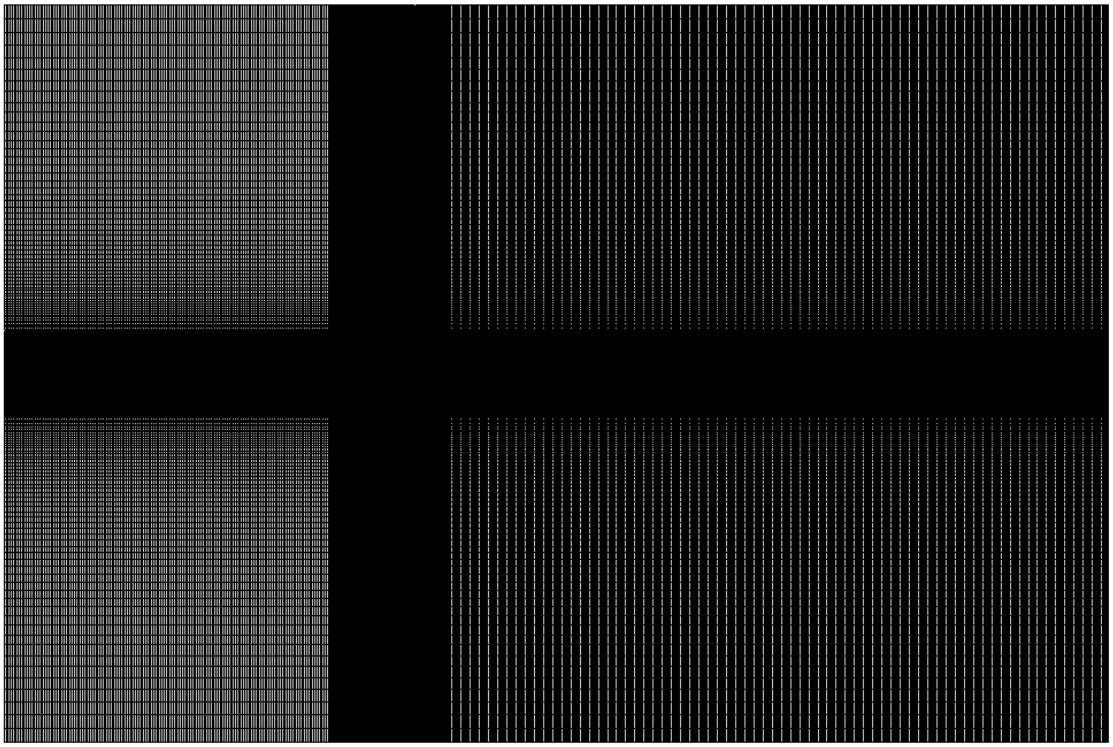

Figure E. 2 The actual 2D mesh set for the final optimal design. This illustrates how the mesh is clustered in the region near the rotor and in the wake region.

THE MESH TOPOLOGY FOR THE 3D MODEL WITH WINGLET

The details of the 3D mesh topologies for reference 3D case is discussed in details in Section 4.3.2. However, the mesh topology near the blade tip has been modified to fit with implemented winglet. Due to the complex geometry of the winglet, A hybrid mesh strategy is implemented that combines the structured mesh topology near the winglet surface and the CutCell mesh around the structured mesh. A non-conformal mesh interface is utilised to connect the two CutCell zone to the structured zone. Figure E. 3 illustrates the 3D hybrid mesh topology and the different inflation layers that assist to maintain an excellent mesh quality near the blade and winglet surfaces.

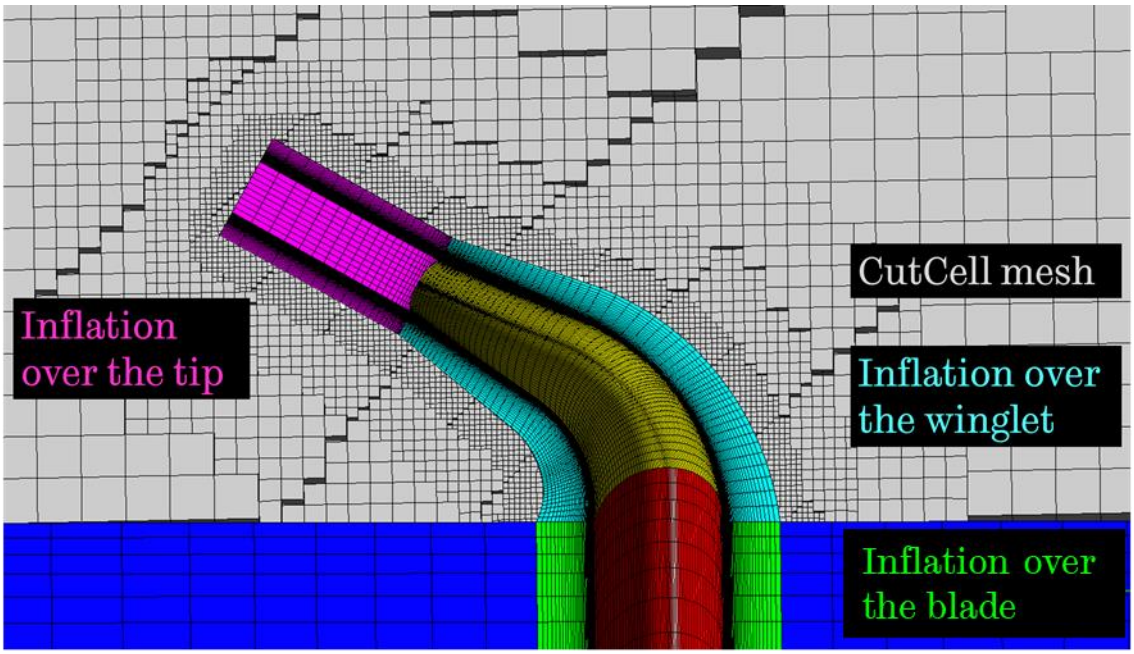

Figure E. 3 The 3D hybrid mesh topology near the winglet showing both the structured topologies and the CutCell mesh.

APPENDIX F

FORTRAN LIBRARY

This Appendix provides the source code for the FORTRAN programs that have been utilised in the thesis. This includes a code for calculating the pitch amplitude for the VPP1 in addition to a code for calculating the piecewise pitch function intervals bounds using the Bisection method for the VPP2. More information about the mathematical formulation of the VPP1 and VPP2 are presented in Section 8.3

FORTRAN code for calculating the pitch amplitude for VPP1

```
      PROGRAM VPP1
c     to calculate the pitch amplitude for VPP1
      REAL tsr, fp_angle, vp_amplitude,required_vp_amplitude, range
      REAL target_aoa, current_vp_amplitude, current_max
      tsr=2.6
      fp_angle=0
      target_aoa=22
      required_vp_amplitude=0
      range=alpha_vp_max(tsr,fp_angle,0.0)

      DO i=1,1000000

      current_vp_amplitude = i*range/1000000
c     current_vp_amplitude = i*range/100000
      current_max= alpha_vp_max(tsr,fp_angle,current_vp_amplitude)

      IF (current_max< target_aoa+0.0001) THEN
      IF (current_max> target_aoa-0.0001) THEN
      required_vp_amplitude= current_vp_amplitude
      PRINT*,required_vp_amplitude, current_max
      END IF
      END IF

      END DO


      END
c     ***********************************************************************
c     subroutine
c     ***********************************************************************
      REAL FUNCTION alpha_vp_max(tsr,fp_angle,vp_amplitude)
      REAL phi,f_alpha_vp_max, alpha_vp, PI
      PI=3.14159265358979323846264338327795

      f_alpha_vp_max=0


      DO i=1,1000
      phi = i*2*PI/1000
      alpha_vp= 180/PI*ATAN(sin(phi)/(tsr+cos(phi)))
     & -vp_amplitude*sin(phi)+fp_angle
```

```
      IF (alpha_vp> f_alpha_vp_max) f_alpha_vp_max=alpha_vp
C     print*,phi,alpha_vp_max

      END DO
      alpha_vp_max=f_alpha_vp_max
      RETURN
      END
```

FORTRAN code to calculate the piecewise pitch function intervals bounds using the Bisection method for VPP2

```
      PROGRAM VPP2
c     to calculate the piecewise intervals bounds using Bisection Method
      REAL PI, error_traget, a, b, c, switch
      PI=3.14159265358979323846264338327795
      error_traget=0.00001
c     a, b, and c are the interval bounds for the Bisection method
c     switch is used to switch the interval bounds

c     ****************************************************************
c     Part 1: first quarter
c     ****************************************************************
      a=0.0
      b=0.313
      IF((f(a)> 0).AND.(f(b)< 0))THEN
      switch=a
      a=b
      b=switch
      ENDIF
c     WRITE(*,*)f(a), f(b)
11     c=(a+b)/2
      IF(abs(f(c))< error_traget) GOTO 12
      IF(f(c)< 0)THEN
      a=c
      ELSE
      b=c
      ENDIF
      GOTO 11
12    WRITE(*,13)c
13    FORMAT(1x,'t1= ',F16.15)

c     ****************************************************************
c     Part 2: second quarter
c     ****************************************************************
      a=0.313
      b=0.5-0.01
      IF((f(a)> 0).AND.(f(b)< 0))THEN
      switch=a
      a=b
      b=switch
      ENDIF
c     WRITE(*,*)f(a), f(b)
21    c=(a+b)/2
      IF(abs(f(c))< error_traget) GOTO 22
      IF(f(c)< 0)THEN
      a=c
      ELSE
      b=c
```

```
      ENDIF
      GOTO 21
22    WRITE(*,23)c
23    FORMAT(1x,'t2= ',F16.15)

c     ****************************************************************
c     Part 3: third quarter
c     ****************************************************************
      a=0.5+0.01
      b=1-0.313
      IF((f(a)> 0).AND.(f(b)< 0))THEN
      switch=a
      a=b
      b=switch
      ENDIF
c     WRITE(*,*)f(a), f(b)
31    c=(a+b)/2
      IF(abs(f(c))< error_traget) GOTO 32
      IF(f(c)< 0)THEN
      a=c
      ELSE
      b=c
      ENDIF
      GOTO 31
32    WRITE(*,33)c
33    FORMAT(1x,'t3= ',F16.15)
c     ****************************************************************
c     Part 4: fourth quarter
c     ****************************************************************
      a=1-0.313
      b=1
      IF((f(a)> 0).AND.(f(b)< 0))THEN
      switch=a
      a=b
      b=switch
      ENDIF
c     WRITE(*,*)f(a), f(b)
41    c=(a+b)/2
      IF(abs(f(c))< error_traget) GOTO 42
      IF(f(c)< 0)THEN
      a=c
      ELSE
      b=c
      ENDIF
      GOTO 41
42    WRITE(*,43)c
43    FORMAT(1x,'t4= ',F16.15)
      STOP
      END
c     ****************************************************************
c     subroutine
c     ****************************************************************
      REAL FUNCTION f(t_T)
      REAL required_vp_amplitude, PI,tsr
      required_vp_amplitude=22
      PI=3.14159265358979323846264338327795
      tsr=2.6
      fp_angle=0
      IF(t_T < 0.5)THEN
      f= 180/PI*ATAN(sin(t_T*2*PI)/(tsr+cos(t_T*2*PI)))
     & -required_vp_amplitude+fp_angle
```

```
 ELSE
 f= 180/PI*ATAN(sin(t_T*2*PI)/(tsr+cos(t_T*2*PI)))
& +required_vp_amplitude+fp_angle
 ENDIF
 RETURN
 END
```